

Development of an *in situ* acoustic emission monitoring technique for tribochemical applications

James Thomas Makin

Submitted in accordance with the requirements for the degree of
Doctor of Philosophy

The University of Leeds
School of Mechanical Engineering

August 2019

The candidate confirms that the work submitted is his own and that appropriate credit has been given where reference has been made to the work of others.

This copy has been supplied on the understanding that it is copyright material and that no quotation from the thesis may be published without proper acknowledgement.

The right of James Thomas Makin to be identified as Author of this work has been asserted by him in accordance with the Copyright, Designs and Patents Act 1988.

Acknowledgements

Firstly, I would like to thank my supervisors, Professor Anne Neville OBE and Professor Ardian Morina for supporting me throughout my PhD. I am extremely grateful to the Integrated Tribology Centre for Doctoral Training (IT-CDT) for funding this research.

I am privileged to have been part of the IT-CDT because through the centre I have made many friends. I would like to thank all of the other members of the CDT in my cohort as well as the other cohorts. Particularly, I would like to thank Rachel, Mahdiyar, Sohail, Nadia and Leon for being the best office mates; always being there for a cup of tea or to discuss the trials and tribulations of PhD life.

I would like to thank Marcello for always being there to talk to; you were always the happiest person in the room at any tribology event. Also, thank you for introducing me to limoncello and the fact that “there is always room for a gin and tonic”. I am so sorry that I will never get to take you up on your offer of visiting you and your family back home in Italy, you were such a huge part of the CDT and you will be sadly missed.

I am also very grateful to the technicians who work tirelessly across The University of Leeds. Jordan, Mick and Andrew thank you for always making sure that the tribometers were functioning well. I would also like to thank the other researchers who are part of iFS who have been invaluable in offering support and advice.

Thank you to my family for their support, particularly my Mum and Dad, who have always supported and believed in me, you have always been there with great words of advice to keep me going.

Finally, I would like to thank my amazing wife Kirsty for her unwavering support and belief in me. Thank you so much for always being there to listen to me talk about my work, I'm sure after the last 4 years you know everything there is to know about tribology and acoustic emissions. I honestly could not have done this without you!

Abstract

Lubricant additives such as MoDTC and ZDDP have been used for decades to change the tribochemical environment of contacts by respectively forming friction modifying or anti-wear tribofilms. The monitoring of these tribofilms is very difficult *in situ* and in real time as the current techniques that are used can have a great impact on the tribocontact. For example, it is necessary to change one of the contacting surfaces to sapphire so that line-of-site methods such as spectroscopy can be used. Alternatively, the tribological tests being conducted can be stopped and then measurements can be taken of the tribofilm. Both techniques mentioned have limitations as to how accurately they represent real tribological interfaces. Acoustic emissions have historically been used for the detection or crack formation and propagation within pressure vessels. Acoustic emissions utilise the piezo electric properties of the sensors which when vibrated produce an electrical charge, it is this charge that can be measured.

The use of acoustic emissions in a tribochemical environment has never been studied before and the link between tribofilms and acoustic emissions is unknown. This study developed and implemented a methodology for monitoring the MoDTC and ZDDP tribofilm formation and growth *in situ* and in real time. Tests were conducted on a high speed pin-on-disk tribometer using steel disk and ball counterfaces. Experiments were conducted at 100°C and 1000 RPM with a maximum contact pressure of 2.29 GPa. The lubricants used for tests were PAO only, PAO + 0.1wt% MoDTC and PAO + 0.55wt% ZDDP. A WSA acoustic emission sensor attached to the tribometer and connected to a bespoke high speed data acquisition system was used to continuously monitor the acoustic emissions produced throughout testing.

This work has shown for the first time that the formation and removal of MoDTC and ZDDP tribofilms can be observed in the acoustic emission data. It has also shown that in a tribochemical environment there is a direct link between the coefficient of friction and the acoustic emission signal, as such it is possible to use the acoustic emission signal to predict the instantaneous coefficient of friction of the contact.

Table of Contents

Acknowledgements	iii
Abstract	iv
Table of Contents	v
List of Tables	ix
List of Figures	x
Abbreviations	xvii
Nomenclature	xviii
Chapter 1 Introduction	1
1.1 Tribology	1
1.1.1 Friction	1
1.1.2 Wear	2
1.1.3 Lubrication	4
1.1.3.1 Hydrodynamic Lubrication	5
1.1.3.2 Elastohydrodynamic Lubrication.....	5
1.1.3.3 Boundary Lubrication	6
1.1.3.4 Mixed Lubrication	7
1.1.3.5 Stribeck Curve.....	8
1.2 Tribochemistry.....	8
1.2.1 Lubricants	8
1.2.1.1 Mineral Oils	9
1.2.1.2 Synthetic Oils	9
1.2.2 Lubricant Additives	9
1.2.2.1 Molybdenum Dithiocarbamate (MoDTC)	10
1.2.2.2 Zinc Dialkyldithiophosphate (ZDDP).....	15
1.3 Experimental Methods in Tribology	18
1.3.1 Laboratory Tribology Tests	18
1.3.1.1 Experimental measurements of friction	20
1.3.1.2 Experimental measurements of wear	20
1.3.2 Surface Analysis	22
1.3.2.1 Contact profilometry	22
1.3.2.2 White Light Interferometry	23
1.3.3 Tribofilm Characterisation	24
1.3.3.1 Raman Spectroscopy	24
1.3.3.2 Energy-dispersive X-Ray spectroscopy.....	25

1.3.4	<i>In situ</i> Analysis	25
1.4	Acoustic Emission	30
1.4.1	Fundamentals of Acoustic Emission	30
1.4.1.1	Measurement Parameters	31
1.4.1.1.1	Absolute Energy	31
1.4.1.1.2	Hit Counts	31
1.4.1.1.3	Root Mean Squared (RMS) average	32
1.4.1.2	Acoustic Emission Sensing Technology	33
1.4.2	Acoustic Emission in the Condition Monitoring of Cracks	35
1.4.3	Acoustic Emission and Tool Wear	36
1.4.4	Acoustic Emission in Tribology	37
1.5	Aim and Objectives	44
1.6	Thesis Outline	45
Chapter 2	Methodologies	47
2.1	High Speed Pin-on-Disk Tribometer	47
2.2	Materials	48
2.2.1	Poly Alpha Olefin (PAO) base stock	48
2.2.2	Lubricant Additives	49
2.2.3	Acoustic Emission Sensor	49
2.2.4	Sample Polishing	50
2.3	Surface Analysis	53
2.3.1	Contact Profilometry	53
2.3.2	White Light Interferometry	53
2.3.3	Optical Microscopy	53
2.4	Tribofilm Analysis	54
2.4.1	Raman Spectroscopy	54
2.4.2	Scanning Electron Microscopy + EDX Analysis	54
Chapter 3	Development of Bespoke Data Acquisition System	55
3.1	Data Acquisition	55
3.1.1	Sampling Speed	55
3.1.2	Signal Strength	57
3.2	Signal Processing	57
3.2.1	Time Domain	58
3.2.2	Frequency Domain	59
3.3	LabVIEW Framework	62

3.3.1	State Machine.....	63
3.3.2	Event Handler.....	64
3.3.3	Producer/Consumer.....	64
3.3.4	Queued Message Handler (QMH).....	65
3.4	Development of QMH Architecture.....	67
3.4.1	Acquisition loop.....	70
3.4.2	Analysis Loop.....	70
3.4.3	Logging Loop.....	71
3.4.4	Data Display Loop.....	71
3.5	Hardware Setup.....	76
3.6	Fixation of Sensor to Tribometer.....	76
3.7	Influence of Varying Acoustic Emission Parameters.....	77
3.7.1	Sampling Time and Interval.....	77
3.7.2	Hit Count Threshold and Width.....	82
3.8	Summary.....	84
Chapter 4 Effect of Initial Surface Roughness on Acoustic Emission Response Under Boundary Lubricated Conditions.....		85
4.1	Acoustic Emission and Coefficient of Friction Data.....	86
4.1.1	SF-120.....	89
4.1.2	SF-320.....	90
4.1.3	SF-600.....	91
4.1.4	SF-800.....	92
4.1.5	SF-1200.....	93
4.1.6	SF-9 μ m.....	94
4.1.7	SF-0.25 μ m.....	95
4.2	Experiment Repeatability.....	96
4.2.1	Average Value.....	96
4.2.2	Peak Value.....	99
4.3	Changes in Surface Roughness.....	102
4.4	Summary.....	106
Chapter 5 Monitoring MoDTC Based Tribofilm Formation and Removal Under Boundary Lubricated Conditions.....		107
5.1	Tribofilm Formation.....	108
5.2	Early Stages of MoS ₂ Tribofilm Formation.....	115
5.3	Frequency Analysis.....	122
5.4	Tribofilm Removal.....	124

5.5	Acoustic Emission and Wear.....	126
5.6	Acoustic Emission and Coefficient of Friction.....	129
5.7	Summary.....	132
Chapter 6	Monitoring ZDDP Based Tribofilm Formation and Removal Under Boundary Lubricated Conditions	134
6.1	Tribofilm Formation	136
6.2	Early Stages of ZDDP Tribofilm Formation	142
6.3	Frequency Analysis.....	145
6.4	Tribofilm Removal	147
6.5	Acoustic Emission and Wear.....	149
6.6	Acoustic Emission and Coefficient of Friction.....	152
6.7	Summary.....	155
Chapter 7	Discussion	156
7.1	Development of a High Speed Data acquisition System	157
7.2	Tribofilm Monitoring.....	158
7.3	Acoustic Emission and Friction	161
7.4	Acoustic Emission and Wear.....	164
7.5	Frequency Analysis.....	165
7.6	Acoustic Emission as an <i>in situ</i> Real Time Methodology	169
7.7	Using Acoustic Emissions as a Predictive Tool for the Coefficient of Friction	169
Chapter 8	Conclusion and Future Work	173
8.1	Conclusion	173
8.2	Future Work	174
8.2.1	Software Development.....	174
8.2.2	Experimental.....	174
Bibliography	176

List of Tables

Table 1 – <i>In situ</i> approaches used for tribological interface studies....	26
Table 2 - Test conditions used in tribotests throughout this work.....	48
Table 3 – Typical properties of PAO.....	49
Table 4 - List of grinding/polishing operations performed on sample disks depending on desired final surface finish.	51
Table 5 - Test parameters used for sampling time and interval tests... 	78
Table 6 - Tribological parameters for tests conducted in this section. 	85
Table 7 - Test parameters used for investigating the effect MoDTC based additives have on acoustic emission.....	108
Table 8 – Test parameters used for investigating the effect ZDDP based additives have on acoustic emission.....	136

List of Figures

Figure 1.1 – Schematic drawing showing two possible outcomes from adhesive interaction between surface asperities.....	3
Figure 1.2 –Schematic illustration of the hydrodynamic lubrication regime.	5
Figure 1.3 – Schematic illustration of the elastohydrodynamic lubrication regime.....	5
Figure 1.4 – Schematic illustration of the boundary lubrication regime.	6
Figure 1.5 – Schematic illustration of the mixed lubrication regime.	7
Figure 1.6 – Illustration of a modified Stribeck curve.	8
Figure 1.7 – Proposed method for the formation MoS ₂ tribofilm from MoDTC additive.....	11
Figure 1.8 - Proposed reaction pathway for decomposition of MoDTC within tribocontacts (R represents other carbon and hydrogen elements attached to the MoDTC molecule being investigated)...	12
Figure 1.9 – MoS ₂ solid structure.....	13
Figure 1.10 – Friction coefficient obtained from changing lubricant from MoDTC to base oil, ZDDP and ZDDP/MoDTC.....	14
Figure 1.11 - Simple representation of the structural formula of ZDDP (R represents the carbon and hydrogen atoms attached to the ZDDP molecule being investigated).	15
Figure 1.12 - Evolution of pad-like structure of ZDDP tribofilm using atomic force microscopy.....	16
Figure 1.13 - Schematic diagram of the pad composition and structure.	16
Figure 1.14 – Effect of dispersant on pre-formed ZDDP tribofilms.....	17
Figure 1.15 - Comparison between tribotest complexity and realism. .	19
Figure 1.16 - Schematic illustrations of different tribometers.....	19
Figure 1.17 - Schematic of line profilometry measurement.....	22
Figure 1.18 - Schematic of white light interferometry measurement....	23
Figure 1.19 - Schematic of Raman spectroscopy measurement.....	24
Figure 1.20 - Schematic of the ultra-thin film interferometry apparatus used to measure sub-nanometre lubricant films.	28
Figure 1.21 - Schematic diagram of the <i>in situ</i> spacer layer interferometry set-up on the MTM	29
Figure 1.22 - Image demonstrating the source of acoustic emission events due to sliding wear.	30

Figure 1.23 - Diagrammatic representation of how absolute energy is calculated from a waveform.....	31
Figure 1.24 - Diagrammatic representation of how AE hits are counted as the signal passes a threshold value.....	32
Figure 1.25 - Diagrammatic representation of how the RMS value would appear on a model sine wave.	33
Figure 1.26 – Schematic of a typical acoustic emission sensor.	34
Figure 1.27 - Schematic showing piezoelectric effect of PZT crystals.	34
Figure 1.28 - Distribution of AE event frequencies.	35
Figure 1.29 - Twin disk experimental apparatus used by Lingard et al. (1993).	38
Figure 1.30 - Frequency spectra for A) aluminium on steel and B) steel on hardened steel.	39
Figure 1.31 - Number of AE counts for varying defects at 1500 RPM... ..	40
Figure 1.32 - Predicted wear volume of slider using AE signal and measure values as a function of time.	41
Figure 1.33 - Log-log graph of integrated AE RMS and ball volume loss showing three distinct linear relationships.	42
Figure 1.34 - Schematic diagram of scratch tester used by Cho and Lee (2000).	43
Figure 1.35 - Scratch test data for CrN coated steel disk with 1 μm coating thickness.....	43
Figure 2.1 - Schematic diagram of HSPOD tribometer and acoustic emission sensor.....	47
Figure 2.2 - Schematic showing the dimensions of the WS α sensor. ..	49
Figure 2.3 - Frequency response of WS α sensor.....	50
Figure 2.4 - Surface roughness, R $_a$, values of test disks depending upon grade of final polish.	52
Figure 2.5 - Calculated lambda ratio dependent upon initial surface roughness.....	52
Figure 3.1 - Image displaying the detrimental effects caused by too low a sample rate.	56
Figure 3.2 - Image showing the resultant sampled signal when an 800 kHz signal is sampled at 1 MS/s.	56
Figure 3.3 - Image showing how the signal information is represented in both the frequency and time domain.	58
Figure 3.4 – Diagram depicting continuous signal comprised of individual burst events, AE traces from an experiment conducted throughout this work.	59
Figure 3.5 - Image showing spectral leakage caused by high frequency discontinuities.....	61

Figure 3.6 - The effects of windowing during performing a FFT.....	62
Figure 3.7 - The addition of two numbers as performed in the graphical interface of LabVIEW.	63
Figure 3.8 - Example of a basic state machine.	63
Figure 3.9 - Example of a basic event handler.....	64
Figure 3.10 - Example of a basic producer/consumer structure.....	65
Figure 3.11 - Example of basic QMH structure	66
Figure 3.12 - Flowchart showing the order execution for QMH data acquisition	67
Figure 3.13 - Block diagram of the complete QMH architecture used in this work.	68
Figure 3.14 - Graphical user interface for QMH acquisition system.....	69
Figure 3.15 - Settings dialog that allows the user to fine tune the data acquisition parameters for each test.....	70
Figure 3.16 - Block diagram for Acquisition Loop.....	72
Figure 3.17 - Block diagram Analysis Loop.	73
Figure 3.18 - Block diagram for Logging Loop.....	74
Figure 3.19 - Block diagram for Data Display Loop.....	75
Figure 3.20 - Annotated photograph of acoustic emission sensor and bespoke fixation device.....	76
Figure 3.21 - Annotated photograph of acoustic emission sensor located on the HSPOD tribometer and material connection between acoustic emission sensor and ball.	77
Figure 3.22 - Comparison of absolute energy and CoF data for four different sampling times and intervals.....	79
Figure 3.23 - Comparison of hit count and CoF data for four different sampling times and intervals.....	80
Figure 3.24 - Comparison of RMS and CoF data for four different sampling times and intervals.....	81
Figure 3.25 - Average hit count \pm SD for different threshold values.....	83
Figure 3.26 - Average hit count \pm SD for different width values.....	83
Figure 4.1 – Absolute energy and coefficient of friction data for tribotest conducted using a standard sample in PAO.....	87
Figure 4.2 – Hit count and coefficient of friction data for tribotest conducted using a standard sample in PAO.	87
Figure 4.3 – RMS and coefficient of friction data for tribotest conducted using a standard sample in PAO.	88
Figure 4.4 – RMS and coefficient of friction data for tribotest conducted using a SF-120 sample in PAO.	89

Figure 4.5 – RMS and coefficient of friction data for tribotest conducted using a SF-320 sample in PAO.	90
Figure 4.6 – RMS and coefficient of friction data for tribotest conducted using a SF-600 sample in PAO.	91
Figure 4.7 – RMS and coefficient of friction data for tribotest conducted using a SF-800 sample in PAO.	92
Figure 4.8 – RMS and coefficient of friction data for tribotest conducted using a SF-1200 sample in PAO.	93
Figure 4.9 - RMS and coefficient of friction data for tribotest conducted using a SF-9 μ m sample in PAO.	94
Figure 4.10 – RMS and coefficient of friction data for tribotest conducted using a SF-0.25 μ m sample in PAO.	95
Figure 4.11 - Average coefficient of friction value from the last 5 minutes of the test for each surface roughness.	97
Figure 4.12 - Average absolute energy value from the last 5 minutes of the test for each surface roughness.	97
Figure 4.13 - Average hit count value from the last 5 minutes of the test for each surface roughness.	98
Figure 4.14 - Average RMS value from the last 5 minutes of the test for each surface roughness.	98
Figure 4.15 - Peak coefficient of friction value for each surface roughness.	100
Figure 4.16 - Peak absolute energy value for each surface roughness.	100
Figure 4.17 - Peak hit count value for each surface roughness.	101
Figure 4.18 - Peak RMS value for each surface roughness.	101
Figure 4.19 - Measurements of surface roughness both pre- and post-test.	102
Figure 4.20 - Comparison of pre- and post-test surfaces using white light interferometry.	106
Figure 5.1 - Coefficient of friction response using PAO + 0.1 wt% MoDTC as the lubricant.	107
Figure 5.2 - Annotated coefficient of friction graph showing measurement parameters.	109
Figure 5.3 - Annotated RMS graph showing measurement parameters.	110
Figure 5.4 - Measurements of the time taken to reach the 'peak' (T_P) and 'drop' (T_D) for coefficient of friction and acoustic emission data.	111
Figure 5.5 - Measurements of the percentage change in magnitude for various parameters relating to coefficient of friction and acoustic emission data.	111

Figure 5.6 - Absolute energy and coefficient of friction data for tribotest conducted in PAO + 0.1wt% MoDTC.	113
Figure 5.7 - Acoustic emission hit count and coefficient of friction data for tribotest conducted in PAO + 0.1wt% MoDTC.	114
Figure 5.8 - RMS and coefficient of friction data for tribotest conducted in PAO + 0.1wt% MoDTC.	114
Figure 5.9 – RMS and coefficient of friction data from a test conducted using PAO + 0.1 wt% MoDTC as a lubricant.	116
Figure 5.10 - Raman spectra obtained from disk wear scars generated at different test durations.	118
Figure 5.11 - Raman spectra obtained from sample disk after 10 second test.	118
Figure 5.12 - Raman spectra obtained from sample disk after 20 second test.	119
Figure 5.13 - Raman spectra obtained from sample disk after 30 second test.	119
Figure 5.14 - Raman spectra obtained from sample disk after 45 second test.	120
Figure 5.15 - Raman spectra obtained from sample disk after 60 second test.	120
Figure 5.16 - Raman spectra obtained from sample disk after 180 second test.	120
Figure 5.17 - Raman spectra obtained from sample disk after 300 second test.	121
Figure 5.18 - FFT analysis taken at ~30 seconds, 5 minutes, 10 minutes and 30 minutes.	123
Figure 5.19 - Graph showing the acoustic emission and coefficient of friction data from a tribofilm removal test conducted in PAO + 0.1wt% MoDTC.	125
Figure 5.20 – Acoustic emission and coefficient of friction data for tribofilm removal test with exaggerated x-axis to show exact moment when the tribofilm is destroyed.	126
Figure 5.21 - Wear volume loss against time for tests conducted in PAO + 0.1wt% MoDTC.	127
Figure 5.22 - Graph showing relationship between the wear volume loss and cumulative absolute energy (No correlation shown)....	128
Figure 5.23 - Graph showing relationship between the wear volume loss and cumulative hit count (No correlation shown).....	128
Figure 5.24 - Graph showing the relationship between the wear volume loss and cumulative RMS (No correlation shown).	129

Figure 5.25 - Graph showing the significant correlation (Pearson's Correlation Coefficient, n=2792, P<0.0001) between CoF and absolute energy values with PAO + 0.1wt% MoDTC as the lubricant.....	131
Figure 5.26 - Graph showing the significant correlation (Pearson's Correlation Coefficient, n=2792, P<0.0001) between CoF and hit count values with PAO + 0.1wt% MoDTC as the lubricant.	131
Figure 5.27 - Graph showing the significant correlation (Pearson's Correlation Coefficient, n=2792, P<0.0001) between CoF and RMS values with PAO + 0.1wt% MoDTC as the lubricant.....	132
Figure 6.1 - Coefficient of friction response using PAO + 0.55 wt% ZDDP as the lubricant. 1000RPM, 2.29 GPa, 100 °C.....	135
Figure 6.2 - Annotated coefficient of friction graph showing measurement parameters.	137
Figure 6.3 - Annotated RMS graph showing measurement parameters. 137	
Figure 6.4 - Measurements of the time taken to reach a plateau for coefficient of friction and acoustic emission data.....	138
Figure 6.5 - Measurements of the percentage change in magnitude for various parameters relating to coefficient of friction and acoustic emission data.	139
Figure 6.6 - Absolute energy and coefficient of friction data for tribotest conducted in PAO + 0.55wt% ZDDP.....	140
Figure 6.7 – Hit count and coefficient of friction data for tribotest conducted in PAO + 0.55wt% ZDDP.	141
Figure 6.8 – RMS and coefficient of friction data for tribotest conducted in PAO + 0.55wt% ZDDP.	141
Figure 6.9 - EDX analysis data of Zn:P ratio against time.	143
Figure 6.10 - Illustrative representation of the relative abundance of Zinc (Zn) and Phosphorus (P) elements in the wear scar of tests samples after varying tribotest durations.....	144
Figure 6.11 - FFT analysis taken at ~30 seconds, 5 minutes, 10 minutes and 30 minutes.....	146
Figure 6.12 - Graph showing the acoustic emission and coefficient of friction data from a ZDDP based tribofilm removal test.	148
Figure 6.13 - Wear volume loss against time for tests conducted in PAO + 0.55wt% ZDDP.	149
Figure 6.14 - Graph showing relationship between the wear volume loss and cumulative absolute energy (No correlation shown)....	150
Figure 6.15 - Graph showing relationship between the wear volume loss and cumulative hit count (No correlation shown).....	151
Figure 6.16 - Graph showing relationship between the wear volume loss and cumulative RMS value (No correlation shown).....	151

Figure 6.17 - Graph showing the significant correlation (Pearson's Correlation Coefficient, n=2438, P<0.0001) between CoF and absolute energy values with PAO + 0.55wt% ZDDP as the lubricant.....	153
Figure 6.18 - Graph showing the significant correlation (Pearson's Correlation Coefficient, n=2438, P<0.0001) between CoF and hit count values with PAO + 0.55wt% ZDDP as the lubricant.....	153
Figure 6.19 - Graph showing the significant correlation (Pearson's Correlation Coefficient, n=2438, P<0.0001) between CoF and RMS values with PAO + 0.55wt% ZDDP as the lubricant.....	154
Figure 7.1 – Mean ZDDP tribofilm thickness for varying slide-roll ratios.	159
Figure 7.2 – ZDDP film thickness for various load and temperature configurations.....	160
Figure 7.3 – Comparison between the magnitude of absolute energy values taken in the last 5 minutes of the test between MoDTC and ZDDP data.....	161
Figure 7.4 - Comparison between the magnitude of hit count values taken in the last 5 minutes of the test between MoDTC and ZDDP data.	162
Figure 7.5 - Comparison between the magnitude of RMS values taken in the last 5 minutes of the test between MoDTC and ZDDP data.	162
Figure 7.6 – Combination plot of absolute energy data (black bar) and reported hardness values (red diamond) for the steel plate, MoDTC tribofilm and ZDDP tribofilm.....	164
Figure 7.7 – Schematic indicating the three key measurements taken from the FFT data.....	166
Figure 7.8 - Comparison of peak centre values of FFT data from various time points during tests conducted in PAO, PAO + 0.1 wt% MoDTC and PAO + 0.55 wt% ZDDP.	167
Figure 7.9 - Comparison of peak width values of FFT data from various time points during tests conducted in PAO, PAO + 0.1 wt% MoDTC and PAO + 0.55 wt% ZDDP.....	168
Figure 7.10 - Comparison of peak amplitudes of FFT data from various time points during tests conducted in PAO, PAO + 0.1 wt% MoDTC and PAO + 0.55 wt% ZDDP.....	168
Figure 7.11 - Measured and predicted coefficient of friction values for a tribotest conducted in PAO + 0.1 wt% MoDTC.....	171
Figure 7.12 - Measured and predicted coefficient of friction values for a tribotest conducted in PAO + 0.55 wt% ZDDP.....	172

Abbreviations

AE	Acoustic Emission
AES	Auger Electron Spectroscopy
AFM	Atomic Force Microscopy
AISI	American Iron and Steel Institute
ATR-FTIR	Attenuated Total Reflection Fourier Transform Infrared Spectroscopy
CCD	Charged Coupled Device
CoF	Coefficient of Friction
DC	Direct Current
EDX	Energy-Dispersive X-Ray Spectroscopy
EELS	Electron Energy Loss Spectroscopy
FFT	Fast Fourier Transform
FIB	Focused Ion Beam
HRC	Rockwell Hardness
HSPOD	High Speed Pin-on-Disk
MoDTC	Molybdenum Dithiocarbamate
N.A.	Numerical Aperture
PAO	Poly Alphaolefin
ppm	Parts Per Million
QMH	Queued Message Handler
RMS	Root Mean Squared
RPM	Revolutions Per Minute
s.e.m.	Standard Error of the Mean
SD	Standard Deviation
SEM	Scanning Electron Microscopy
SFA	Surface Force Apparatus
SLIM	Spacer Layer Imaging Methodology
TDMS	Technical Data Management Streaming
TEM	Transmission Electron Microscopy
WLI	White Light Interferometry
WSD	Wear Scar Diameter
XPS	X-Ray Photoelectron Spectroscopy
ZDDP	Zinc Dialkyl Dithiophosphate

Nomenclature

R_a	Surface roughness (μm)
μ	Coefficient of friction
λ	Lambda ratio
h_{min}	Minimum film thickness (μm)
F	Tangential load (N)
W	Normal load (N)
D	Sliding distance (m)
H	Hardness (Nm^2)

Chapter 1

Introduction

1.1 Tribology

On the 9th March 1966 the word Tribology was first introduced to the world in a seminal report by a Committee of the British Department (Ministry) of Education and Science (Jost, 1966). In it, Tribology was defined as “The science and technology of interacting surfaces in relative motion – and of associated subjects and practices”. Tribology is multi-disciplinary and encompasses the study of friction, lubrication and wear.

Whilst the word Tribology was first introduced in 1966, friction, lubrication and wear have been studied for hundreds if not thousands of years. Leonardo Da Vinci may have died almost 450 years prior to the first usage of the word Tribology (1452-1519), but it is very clear that he was aware of the basic tribological concepts of friction lubrication and wear (Hutchings, 2016). There are fundamental laws of friction known as Amontons’ laws, named after Guillaume Amontons, who in 1699 published a rediscovery of the laws that were first postulated by Leonardo da Vinci some two hundred years previous (Hutchings, 2016). Even further back in time, the ancient Egyptians fully exploited the fundamentals of tribology in the construction of the pyramids by using lubricants and wheels to move heavy masses (Dowson, 1998).

1.1.1 Friction

Friction is defined as the resistance encountered when one body moves tangentially in relation to another (Hutchings and Shipway, 2017a). Friction can be further separated into two distinct areas: dry and viscous. Viscous friction occurs between two lubricated bodies whereas dry friction occurs in the absence of a lubricant (Torbacke et al., 2014).

The aforementioned laws of friction apply only to two bodies under dry friction in the macro scale and are as follows:

- The friction force is directly proportional to the normal load applied
- The friction force is independent of the contact area
- The friction force is independent of the sliding velocity

The magnitude of the frictional force is often described by the value of the coefficient of friction (CoF), this calculated from the first law stated above.

$$F = \mu W$$

Equation 1 - Coefficient of Friction.

Where:

F = Tangential force

W = Normal load (N)

μ = Coefficient of friction

Therefore, the CoF can be easily described as:

$$\mu = \frac{F}{W}$$

In tribological experiments the CoF is calculated by measuring the tangential force using a load cell and setting the normal load that is applied.

1.1.2 Wear

Wear is the progressive loss of material over time between two contacting surfaces. There are numerous equations that have been developed in order to try and predict the wear of materials. However, one of the most well-known equation is known as Archard's equation (Archard, 1953) which defines a dimensionless wear coefficient, k, as:

$$k = \frac{VH}{Wd}$$

Equation 2 - Archard's wear equation.

Where:

V = Wear volume (m³)

H = Hardness (Nm⁻²)

W = Normal Load (N)

d = Sliding Distance (m)

There are different types of wear mechanisms that occur between contacting surfaces. Abrasive and adhesive wear are two such key wear mechanisms.

Prior to explaining the different types of wear mechanisms it is worth noting that the surface of solids represent very complex issues as the variety of defects on any real surface, from bulk flaws to nanoscopic imperfections, have a very large impact on the overall friction and wear characteristics (Stachowiak and Batchelor, 2013). The surfaces of all real materials are made up of peaks and valleys that are known as asperities. The presence of asperities mean that

when two bodies come into contact it is the interaction between the small asperities that is of the utmost importance.

Adhesive wear is when material is transferred from one of the contacting surfaces to the other as a result of cold welding of asperities (Stachowiak and Batchelor, 2013). However, the mechanism behind how contacting asperities lead to wear debris is still not fully understood (Aghababaei et al., 2016). It is thought that the wear process due to asperity contact is either from debris formation caused by fractures (Archard and Hirst, 1956) or gradual smoothing caused by plastic deformation (Holm, 2013). Both mechanisms have been reported in the literature in AFM wear experiments (Sato et al., 2012, Chung and Kim, 2003, Liu et al., 2010, Maw et al., 2002).

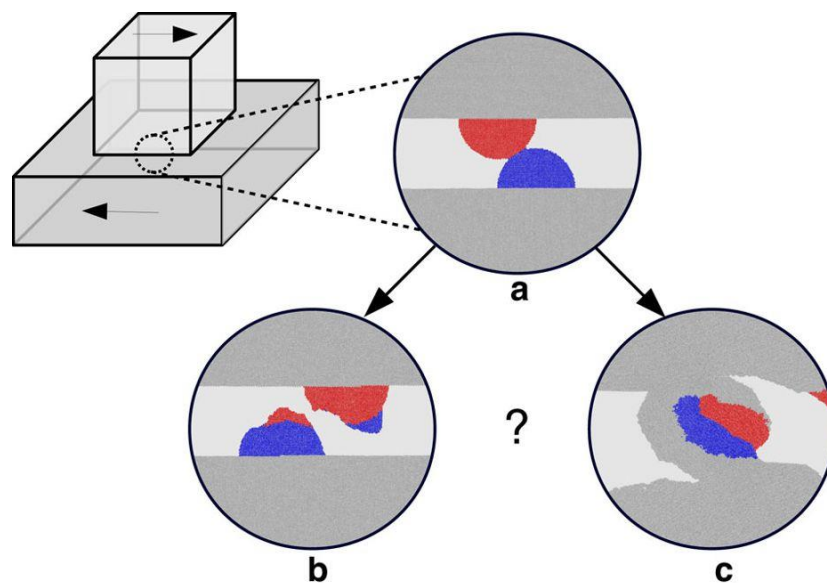


Figure 1.1 – Schematic drawing showing two possible outcomes from adhesive interaction between surface asperities (a). The wear process occurs via either gradual plastic deformation (b) or fracture induced debris formation (c). Taken from Aghababaei et al. (2016).

Abrasive wear occurs when hard particles come into contact with softer materials (Khrushchov, 1974). Abrasive wear may occur due to various surface destructive mechanisms such as harder asperities ploughing or cutting the softer material (Khrushchov, 1974). The agglomeration of transfer particles resulting from adhesive wear can also cause further abrasive wear as they are often work hardened and damage the softer surface (Stachowiak and Batchelor, 2013).

1.1.3 Lubrication

Lubrication can be defined as the interposition of a solid, liquid or gas between two bodies in order to improve the smoothness of movement (i.e. reduce friction) of one surface another and to prevent damage (i.e. wear) (Stachowiak and Batchelor, 2013). The specific lubrication regime in which surfaces interact depends on the following factors (Stachowiak and Batchelor, 2013):

- Operating conditions e.g. temperature, load and sliding speed
- Surface properties e.g. roughness
- Lubricant properties e.g. viscosity and additive

There are four different lubrication regimes; hydrodynamic, elastohydrodynamic, boundary and mixed lubrication (Hutchings and Shipway, 2017, Stachowiak and Batchelor, 2013). Each regime will be discussed briefly below with corresponding schematic illustrations of the regimes. In Figures 1.2-1.5 the dashed blue lines represent the centre lines of the two surface profiles and:

Z = vertical displacement of the respective surface from the centre line

x = horizontal coordinate

h = vertical separation of the centrelines at any x

h_T = vertical separation of the surfaces at any x

U = relative sliding velocity between the surfaces

The minimum value of the separation of the centre lines (h) is referred to as h_{min} .

A useful parameter for comparing relative film thicknesses across all lubrication regimes is the specific film thickness, or Lambda ratio (λ), it can be calculated as follows:

$$\lambda = \frac{h_{min}}{\Sigma R_a}$$

Equation 3 - Lambda ratio equation.

Where:

h_{min} = minimum film thickness, μm

R_a = centre line roughness of the two surfaces, μm

1.1.3.1 Hydrodynamic Lubrication

In the hydrodynamic lubrication regime the interacting surfaces are separated fully by a lubricant film. The resultant behaviour of the contact is determined by the bulk properties of the lubricant, predominantly the viscosity, and the relative velocities of the surfaces.

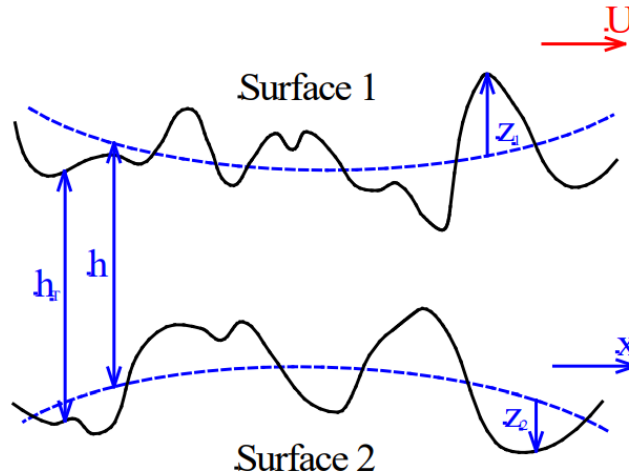


Figure 1.2 –Schematic illustration of the hydrodynamic lubrication regime. Taken from Priest (2014).

In the hydrodynamic lubrication regime h_{\min} is typically greater than $1\mu\text{m}$ and the specific film thickness, λ , is greater than 10 (Priest, 2014).

1.1.3.2 Elastohydrodynamic Lubrication

Elastohydrodynamic lubrication occurs in low conformity, highly loaded tribological interfaces such as bearings. This lubrication regime is a form of hydrodynamic lubrication where the elastic deformations of the contacting bodies and increased lubricant viscosity suppress a more severe contact.

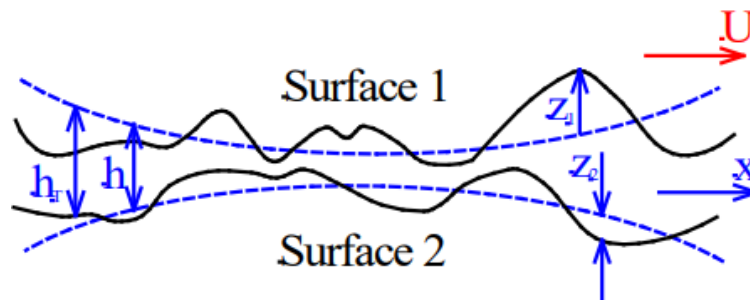


Figure 1.3 – Schematic illustration of the elastohydrodynamic lubrication regime. Taken from Priest (2014).

In the elastohydrodynamic lubrication regime h_{\min} is between $0.1\mu\text{m}$ and $1\mu\text{m}$ and the specific film thickness is greater than 4 or 5 (Priest, 2014).

1.1.3.3 Boundary Lubrication

Boundary lubrication occurs when the average surface roughness is greater than the average lubricant film thickness (Stachowiak and Batchelor, 2013). This results in a lubricant film with a thickness that is insufficient to separate the surfaces of the contacting bodies, leading to direct asperity-asperity contact.

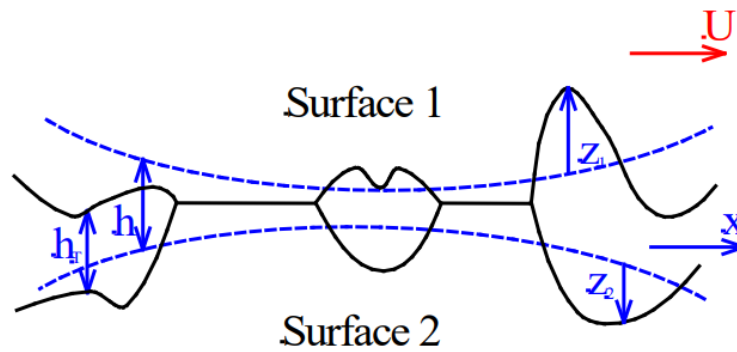


Figure 1.4 – Schematic illustration of the boundary lubrication regime. Taken from Priest (2014).

During boundary lubrication h_{\min} varies from $0.005\mu\text{m}$ to $0.01\mu\text{m}$ and the specific film thickness is less than 1 (Priest, 2014).

Contact between boundary lubricated surfaces is comparable to that of dry contact interfaces as there is no lubricant film that separates the two surfaces. However, thin surface films are formed at the asperity-asperity contacts that provide tribological benefits without separating the two surfaces (Stachowiak and Batchelor, 2013). During boundary lubrication, the wear and friction is determined by the properties of the thin lubricant films formed at the asperity-asperity interfaces as opposed to the bulk properties of the lubricant (Stachowiak and Batchelor, 2013).

The thin boundary film has varying film strength depending on the way it interacts with the surface (Stachowiak and Batchelor, 2013). The film strength is the resistance of the film to stay within the contact and suppress asperity-asperity interaction (Priest, 2014). Boundary lubricant films can be classified based upon the manner in which the film is formed or is adhered to the surface. There are three main types of interactions which are listed below in ascending order with relation to film strength (Priest, 2014, Mortier et al., 2010).

- **Physically adsorbed layers** are formed by short-range inter-molecular forces such as Van der Waal's forces. Typically a layer of lubricant one

or more molecules thick attached to the surface that provides a modest protection against wear.

- **Chemically adsorbed layers** are generally produced by adding long chain fatty acid molecules, such as those found in animal fats, to the lubricant. These fatty acid molecules exhibit a great chemical affinity for metals and can reduce the CoF to the range of 0.1 to 0.15.
- **Films formed by chemical reactions** between components of the lubricant and the surface are the strongest boundary layer films. During severe contact conditions, asperity-asperity interaction leads to frictional heating, this is used constructively to generate resilient surface layers. Lubricant additives such as sulphur react at around 100°C to form highly resistant sulphides which have melting points in excess of 1000°C.

In this work, tests will be conducted in the boundary lubrication regime in order to monitor the effects that the aforementioned thin boundary films have on acoustic emission responses.

1.1.3.4 Mixed Lubrication

A mixed lubrication regime occurs when the lubrication condition varies locally across the contact between hydrodynamic lubrication and boundary lubrication. It is possible for areas within a contact in which asperity-asperity contact occurs and areas where the contact interface is completely separated by a lubricant film.

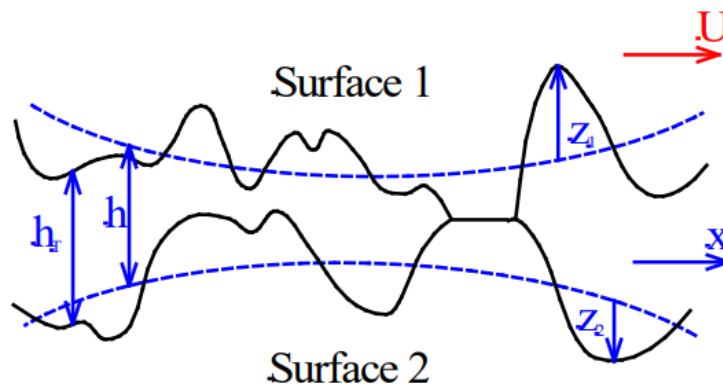


Figure 1.5 – Schematic illustration of the mixed lubrication regime. Taken from Priest (2014).

During mixed lubrication h_{\min} is found to be between $0.05\mu\text{m}$ and $1\mu\text{m}$ with specific film thickness varying from 1 to 5 (Priest, 2014).

1.1.3.5 Stribeck Curve

The Stribeck curve illustrates how the coefficient of friction, CoF, varies in relation to the specific film thickness and therefore the lubrication regime.

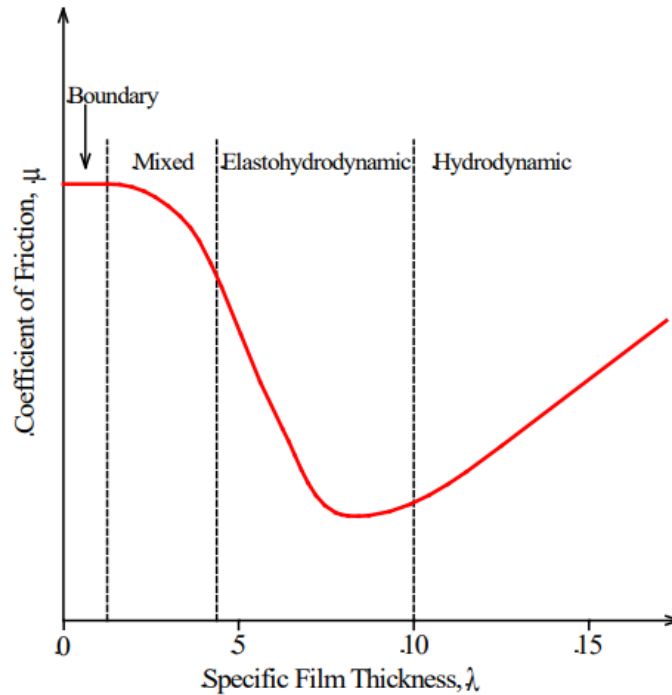


Figure 1.6 – Illustration of a modified Stribeck curve. Taken from Priest (2014).

It can be seen in Figure 1.6 that the coefficient of friction is highest during boundary lubrication, this is due to increased asperity-asperity contact. Conversely, the coefficient of friction is lowest when there is no asperity-asperity contact during elastohydrodynamic lubrication. However, as the specific film thickness increases friction is generated due to viscous shearing of the fluid film, hence the increased coefficient of friction during hydrodynamic lubrication.

1.2 Tribochemistry

1.2.1 Lubricants

Lubricants can be simply defined as substances that reduce friction and wear and allow the smooth running of tribological components.

In Tribology, lubricants are typically composed of a base oil with a small percentage of additives blended in to provide specific performance requirements.

There are a range of different materials that can be used as lubricants to reduce friction and wear, these range from mineral and synthetic oils to greases and even water (Gohar and Rahnejat, 2012).

1.2.1.1 Mineral Oils

Mineral oils are manufactured from crude petroleum oil, the refining process of crude petroleum oil produces several basic grades of mineral oil which can then be blended to create lubricants for different purposes (Priest, 2014).

1.2.1.2 Synthetic Oils

Even when supplemented with additives, mineral oils have a limited operating temperature range. Therefore, it is now commonplace for synthetic oils with enhanced properties to be used in tribology (Mortier et al., 2010). There are many different types of synthetic oils, however, only one type was used in this work; Polyalphaolefin (PAO).

PAO oils have a wide temperature performance range combined with excellent chemical, physical and thermo-oxidative stability. In addition, an increased demand for longer lifetimes and better performance of automotive oils has led to the increased usage of PAO based lubricants (Mortier et al., 2010).

1.2.2 Lubricant Additives

The performance of all lubricants can be enhanced by the inclusion of blended chemical additives (Priest, 2014, Bhushan, 2000). Lubricant additives can be separated by the specific functions that they perform such as:

- Friction modification
- Anti-wear
- Antioxidants
- Detergents
- Dispersants

Friction modifiers operate as their name would suggest, they reduce the friction of the contact by generating a film on the surface. Friction modifiers are particularly important during boundary lubrication (Stachowiak and Batchelor,

2013). One of the most common friction modifiers is molybdenum dithiocarbamate (MoDTC) (Bhushan, 2000). More detailed information regarding the composition and operation of MODTC is covered in Section 1.2.2.1.

Anti-wear additives have been used to enhance the boundary-lubricating properties of engine oils since the 1940s (Mortier et al., 2010). The most widely used anti-wear additive is zinc dialkyl dithiophosphate (ZDDP). More detailed explanation of ZDDP additives, their composition and operation is covered in Section 1.2.2.2.

Antioxidants are additives that delay the oxidation processes in lubricants (Priest, 2014). Interestingly, ZDDP additives were first used as antioxidants before it became apparent that they also reduced wear (Mortier et al., 2010).

Detergents are typically metallic based compounds such as magnesium, barium, calcium and zinc that prevent insoluble deposits forming on surfaces at high temperatures due to oil oxidation (Bhushan, 2000, Priest, 2014).

Dispersants are additives that are used to form a suspension of insoluble oxidised products formed at low temperatures, typically below 100°C (Bhushan, 2000, Priest, 2014).

This work investigates the effect that friction modifiers and anti-wear additives have on acoustic emission response. Only one of each type of additive has been investigated in this work in order to establish an initial link between the tribochemical environment and acoustic emission. The friction modifier (MoDTC) and anti-wear additive (ZDDP) used in this work are discussed in a lot more detail below.

1.2.2.1 Molybdenum Dithiocarbamate (MoDTC)

Organometallic species such as MoDTC are exploited extensively in the internal combustion engine to reduce frictional losses (Morina and Neville, 2007a). Effective lubrication of boundary lubricated systems is ensured by the formation of tribofilms (Morina and Neville, 2007b).

Formation of MoDTC tribofilms is affected by many different parameters such as temperature, MoDTC concentration, the presence of antioxidants and other lubricant additives. Contact parameters such as the stroke length, sliding speed, slide–roll ratio and surface roughness of the sliding pair also affect the formation of tribofilms and the frictional performance of the additive (Graham

et al., 2001a; Grossiord et al., 1999; Morina et al., 2006; Muraki et al., 1997; Muraki and Wada, 2002).

It is generally accepted that MoDTC additives reduce friction in the system by forming a tribofilm containing MoS₂ on the tribological contact (Graham et al., 2001a, 2001b; Martin et al., 1996; Yamamoto and Gondo, 1989). However, the breakdown of MoDTC into MoS₂ films is still under debate, Grossiord et al. (1998) proposed that the breakdown of MoDTC from a chemical point of view occurs as shown in Figure 1.7.

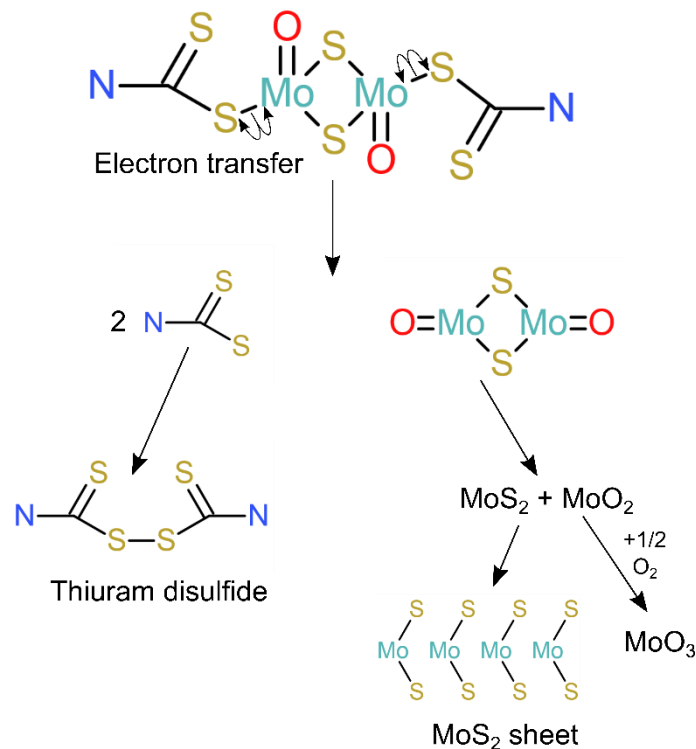


Figure 1.7 – Proposed method for the formation MoS₂ tribofilm from MoDTC additive. Adapted from Grossiord et al. (1998).

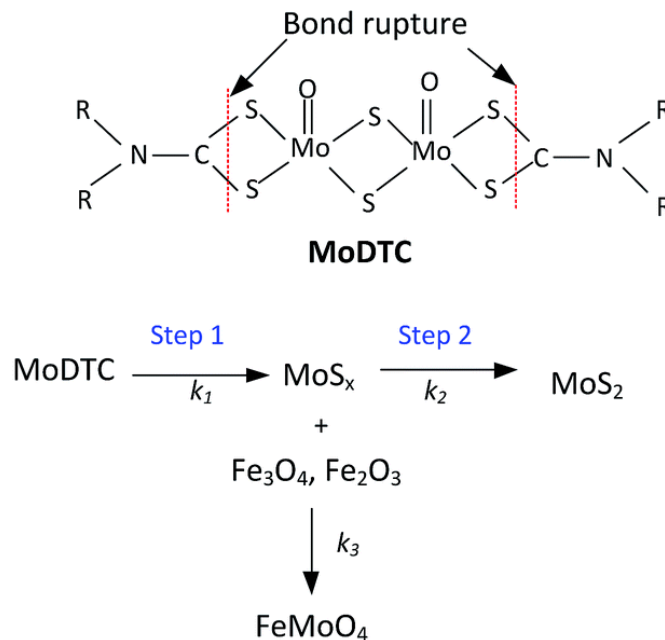
It is suggested that the first stage in the formation of MoS₂ is via electron transfer at the Mo-S chemical bond of MoDTC. This electron transfer from the Mo-S bond leads to the formation of three free radicals. Two of the free radicals correspond to the chain ends of the MoDTC molecule with the final free radical corresponding to the core of MoDTC.

The third stage of this process is the decomposition of the core radical into MoS₂ and MoO₂, which can oxidise in the presence of O₂. The chain end free radicals also recombine, forming thiuram disulphide.

This mechanism is still to be elucidated experimentally in real tribological contacts. The proof of the mechanism being correct is based solely on the observation of MoS₂ tribofilm formation when there is a reduction in friction (Morina et al., 2006).

Recent research conducted by Khaemba *et al.* (2016) proposes a new mechanism for the decomposition of MoDTC as it was found that the method proposed by Grossiord et al. (1998) couldn't be used to explain the MoDTC decomposition products arising from 20°C tests since MoS₂, MoO₂ or MoO₃ were not found in the wear scars following Raman spectroscopy.

It is proposed that the new reaction pathway is caused by the rupturing of the C-S bond through shear stress, shown in Figure 1.8 below. This decomposition forms an intermediate molybdenum compound which undergoes intermolecular sulphonation to form amorphous MoS_x (Khaemba et al., 2016).



Step 1: Dependent on shear stress

Step 2: Dependent on shear stress, temperature and MoDTC concentration

Figure 1.8 - Proposed reaction pathway for decomposition of MoDTC within tribocontacts (R represents other carbon and hydrogen elements attached to the MoDTC molecule being investigated). Taken from Khaemba et al. (2016).

It is believed that FeMoO₄ is formed from a reaction of iron oxides on the steel surfaces with MoS_x. Further to this, Khaemba *et al.* (2016) found that there were peaks belonging to FeMoO₄ not MoO₃ when using Raman spectroscopy. It is suggested that previous reporting of MoO₃ in the tribofilm from XPS tests

is actually a misrepresentation of FeMoO_4 , as both compounds have the same oxidation state (+6) and due to overlapping peaks it is therefore impossible to differentiate between them when using XPS (Khaemba et al., 2016).

The MoS_2 molecule has a layered lattice structure, shown in Figure 1.9. There is powerful covalent bonding between the atomic species in each layer but only weak Van der Waals attraction between the lattice layers themselves (Morina and Neville, 2007b). The presence of MoS_2 in the rubbing contact greatly reduces friction due to interlayer sliding of MoS_2 sheets between the sliding pair, only a few sheets are necessary for low friction to be achieved (Graham et al., 2001c; Onodera et al., 2010). The discrete MoS_2 sheets have been found to have a geometry of approximately 10-20 nm in diameter and 1-2 nm in thickness (Grossiord et al., 1998).

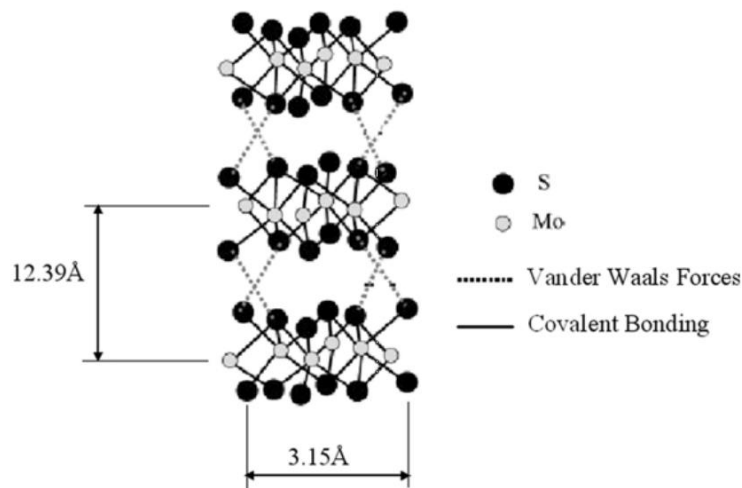


Figure 1.9 – MoS_2 solid structure. Taken from Morina and Neville (2007a).

When an MoDTC containing lubricant is used a distinctive friction trace is typically produced. It can be seen in Figure 1.10 below that the trace shows two distinct regions. In the induction phase there is high friction and a subsequent reduced friction phase occurs when a tribofilm is formed (Morina and Neville, 2007b). The ability of MoDTC additives to form a low friction tribofilm depends on many factors such as the additive type and concentration, as well as the operating temperature, load and surface roughness (Morina and Neville, 2007a).

Low friction MoDTC films are relatively unstable and can be easily removed from the contact (Morina and Neville, 2007b), an instantaneous change in friction values can be observed when the additive is removed from the lubricant (Morina and Neville, 2007a), this can be seen in Figure 1.10 below.

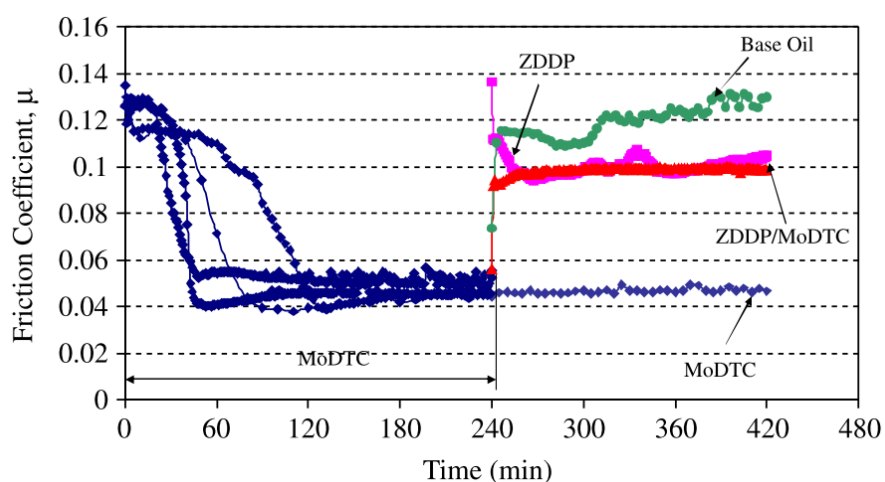


Figure 1.10 – Friction coefficient obtained from changing lubricant from MoDTC to base oil, ZDDP and ZDDP/MoDTC. Taken from Morina and Neville (2007b).

It can be seen in the blue traces in Figure 1.10, that on all four tests conducted the friction was reduced as a tribofilm formed, showing the typical trend that is common for MoS₂ containing tribofilms. It can also be seen in Figure 1.10 that when the MoDTC additive is removed from the system and the oil is replaced with base oil, ZDDP or ZDDP and MoDTC there is an instantaneous increase in the friction coefficient. This drastic rise in friction is due to the instability of the MoS₂ tribofilm and the inherent need for constant replenishment.

Although there is a consensus within the research community about friction reduction via the formation of MoS₂ in the contact area from MoDTC additives, no mechanistic model exists that links additive chemistry in a dynamic tribological system to friction and wear performance. This is mainly because of the difficulty in monitoring surface chemistry changes at the contact region *in situ* and in real time (Khaemba et al., 2015).

Whilst MoDTC is used exclusively as a friction modifier, it also has an effect on the extent of wear of tribocontacts. Morina et al. (2006) found that the wear factor for lubricants containing 250ppm of MoDTC was considerably lower than the wear factor for tests conducted in PAO only. Similar results have also been reported by (Yamamoto and Gondo, 1989) and (Unnikrishnan et al., 2002).

1.2.2.2 Zinc Dialkyldithiophosphate (ZDDP)

ZDDP was originally used in the 1940s as an antioxidant additive before its prowess as an anti-wear additive were discovered (Mortier et al., 2010, Hoshino et al., 2012). ZDDP additives are arguably the most successful lubricant additives used as they have been in continuous use since their discovery and still remain in the majority of current engine oils (Spikes, 2004).

The main constituents of ZDDP are zinc, phosphorus and sulphur; a simple representation of the ZDDP structure can be seen in Figure 1.11 below.

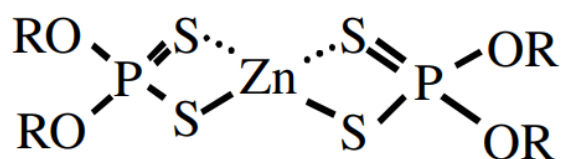


Figure 1.11 - Simple representation of the structural formula of ZDDP (R represents the carbon and hydrogen atoms attached to the ZDDP molecule being investigated). Taken from Spikes (2004).

The nature of ZDDP tribofilms, i.e. the formation and resulting structure of the lubricant film, has been widely studied, this has led to the following definitive knowledge on ZDDP tribofilms.

For a long time it was thought that ZDDP tribofilms formed exclusively in the boundary and mixed lubrication regimes (Spikes, 2004). However, Zhang and Spikes (2016) showed that ZDDP tribofilms form even when there is no asperity contact during full film lubrication, suggesting that the main cause of ZDDP tribofilm formation is the applied shear stress.

When under sliding contact and boundary lubrication conditions, ZDDP forms relatively thick lubricant films, typically 50-150 nm in thickness (Mortier et al., 2010). ZDDP tribofilms can be described as having a glass like polyphosphate structure, the composition of this film is variable and dependent upon the oil formulation and contact conditions (Mortier et al., 2010, Aktary et al., 2002). On steel surfaces, ZDDP tribofilms initially form as separated islands which over time, gradually develop into an almost continuous, but still separate, pad-like film (Mortier et al., 2010, Spikes, 2004) the evolution of the pad-like structure can be seen in Figure 1.12 below.

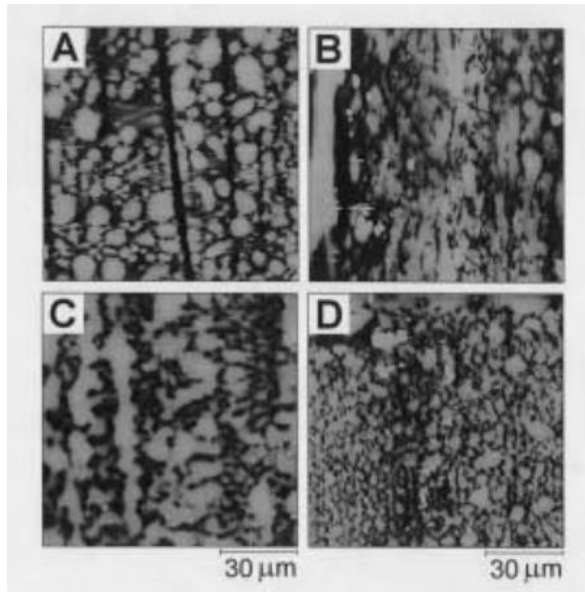


Figure 1.12 - Evolution of pad-like structure of ZDDP tribofilm using atomic force microscopy. (A) 10 min, (B) 40 min, (C) 60 min and (D) 120 min. Taken from Aktary et al. (2002).

It can be seen in Figure 1.12D that even though over time the pad-like structure (shown in white) forms a continuous film, the pads are still separated by deep valleys (Spikes, 2004). The composition of the pads is mainly glassy phosphate which is graded in nature with a thin outer layer of zinc polyphosphate that grades to a bulk film of ortho- or pyrophosphate (Spikes, 2004, Mortier et al., 2010).

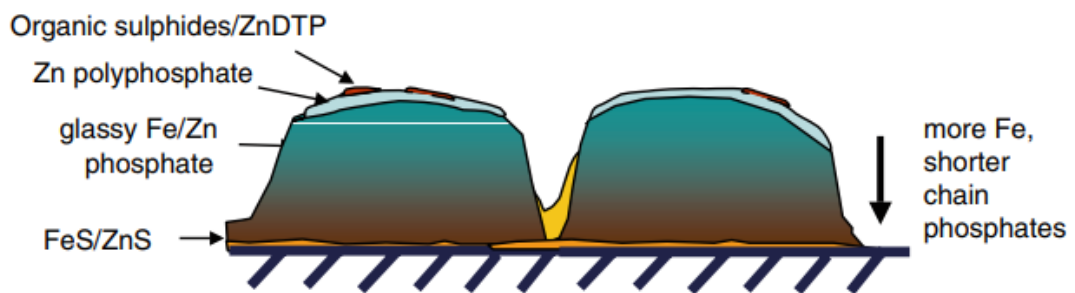


Figure 1.13 - Schematic diagram of the pad composition and structure. Taken from Spikes (2004).

It is thought that ZDDP tribofilms prevent direct mechanical contact between the surfaces and therefore the adhesion between surface asperities is considerably reduced (Dawczyk et al., 2019). The ZDDP tribofilms contain only very small amounts of ferrous species, thus any wear that occurs after a ZDDP film is formed involves little ferrous material loss (Dawczyk et al., 2019). It has also been suggested that the ZDDP tribofilm acts as a cushion, reducing the

stress caused by asperity peaks (Hutchings and Shipway, 2017b) and that ZDDP may react with ferrous wear particles embedded in the tribofilm reducing their abrasive capabilities (Martin, 1999). ZDDP tribofilms are very tenacious and resistant to wear with studies showing that once formed, wear of the tribofilm takes a long time, even when base oil is used to replace the ZDDP containing oil (Bancroft et al., 1997). However, dispersants, another common lubricant additive are known to have a detrimental effect on the anti-wear properties of ZDDP additives (Zhang et al., 2014). Zhang et al. (2014) showed that the thickness of pre-formed ZDDP tribofilms could be substantially reduced by replaced ZDDP containing oil with a dispersant, this can be seen below in Figure 1.14.

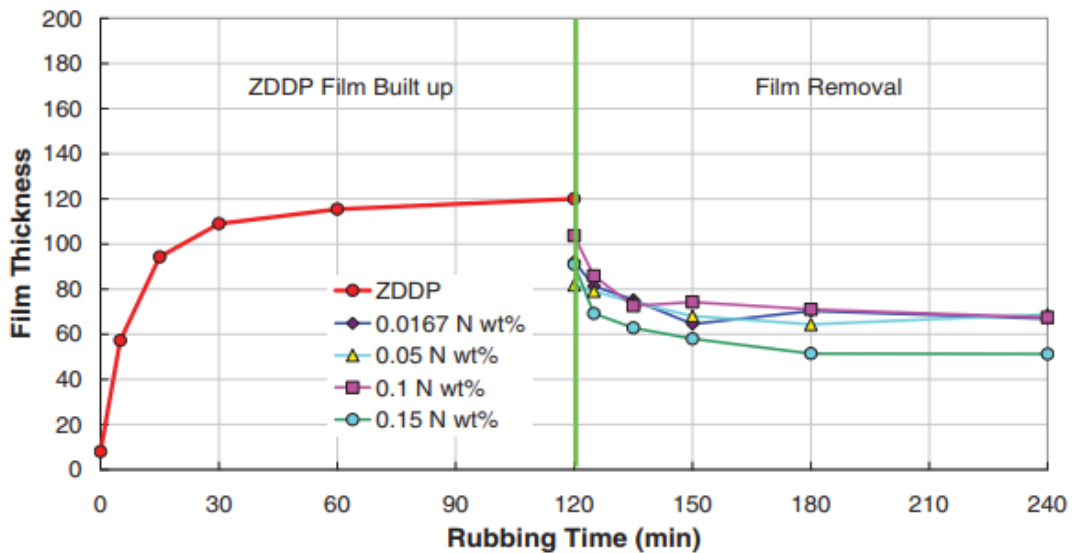


Figure 1.14 – Effect of dispersant on pre-formed ZDDP tribofilms. Taken from Zhang et al. (2014).

It is clear that ZDDPs have a dramatic effect on the amount of wear produced in a contact. However, ZDDP additives are known to cause an increase in friction during mixed lubrication (Taylor and Spikes, 2003). It was shown by Morina et al. (2003) that ZDDP film formation increases the coefficient of friction but that for less severe conditions i.e. higher starting λ stable friction values are reached more quickly. The high friction properties of ZDDP tribofilms are generally undesirable, however, certain applications such as continuous variable ratio transmissions utilise ZDDP additives to achieve much sought after high friction (Kano et al., 1999).

As well as forming tribofilms, in certain conditions, ZDDP can form thermal films. Thermal films are formed when metals such as steel and copper are immersed in a heated ZDDP solution at a temperature typically above 100 °C (Spikes, 2004). The thermal films have a similar composition to ZDDP tribofilms with a thin outer layer of polyphosphate that grades to a bulk film of ortho- or pyrophosphate (Bancroft et al., 1997). The rate of thermal film formation is proportional to the temperature and films as thick as 200 nm have been reported on steel samples (Aktary et al., 2001), the surface morphology of ZDDP thermal films also vary over time (Li et al., 2008). Bancroft et al. (1997) showed that ZDDP thermal films are relatively resistant to wear by enduring for at least 12 hours when rubbed in base oil.

1.3 Experimental Methods in Tribology

1.3.1 Laboratory Tribology Tests

The purpose of a bench tribometer is to provide a controlled simulation of friction and wear responses to various contact conditions (Stachowiak and Batchelor, 2004). Figure 1.15 shows that by simplifying complex tribocontacts it is possible to decrease the costs associated with performing the tests as well as increase the amount of control over the interface.

Laboratory tribology tests, shown as “model test” in Figure 1.15 use specimens that have relatively simple geometries that represent a certain aspect of a larger tribosystem. Laboratory tribometers are designed to cover a specific range of operating conditions or wear mechanisms and they are usually unsuitable for tests operated outside their intended range (Stachowiak and Batchelor, 2004). The class of tribometers that has been most extensively researched are those used for the study of dry or partially lubricated sliding contacts (Stachowiak and Batchelor, 2004).

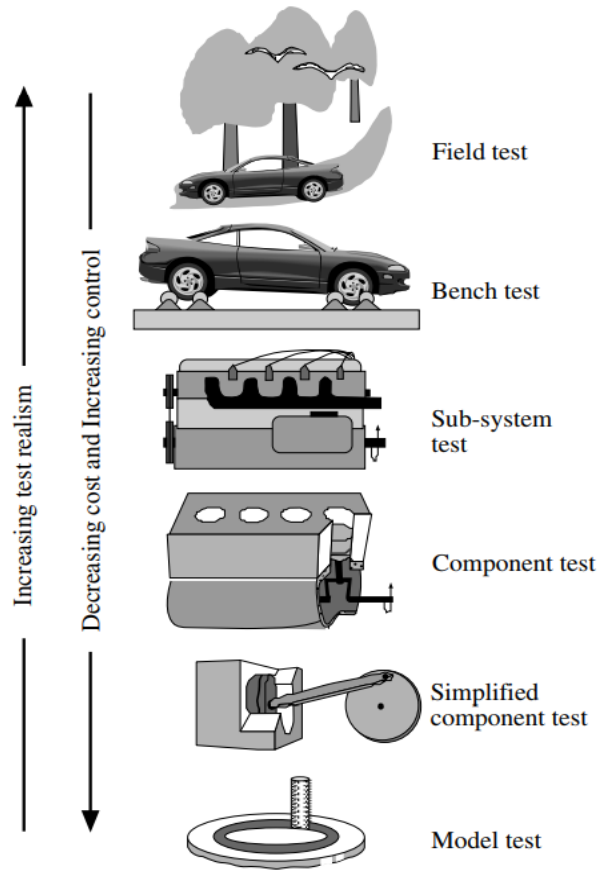


Figure 1.15 - Comparison between tribotest complexity and realism. Taken from axén et al. (2001).

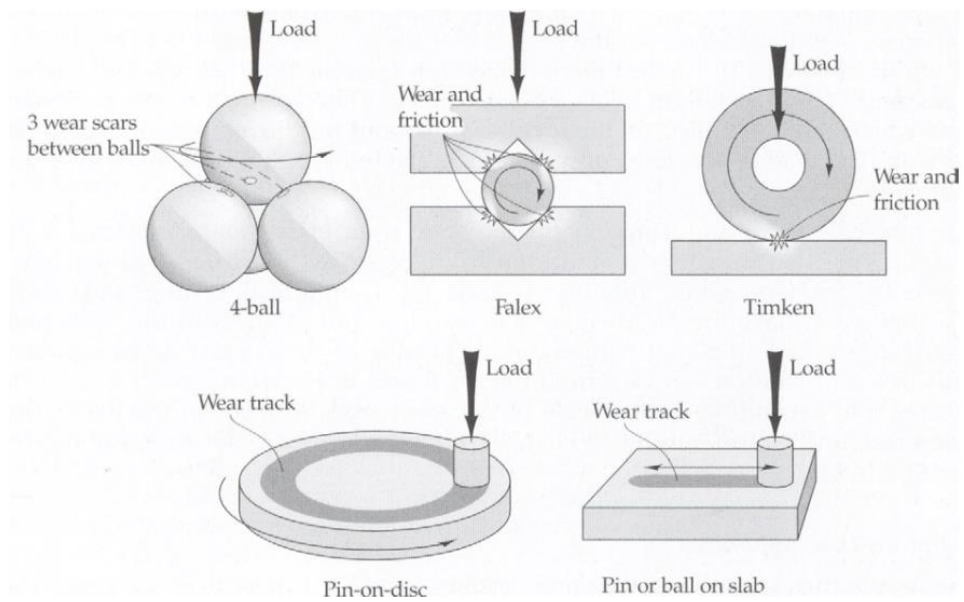


Figure 1.16 - Schematic illustrations of different tribometers. Taken from Stachowiak and Batchelor (2004).

Figure 1.16 shows five different common tribometers that are used in the study of friction and wear. The four-ball, Falex and Timken tribometers are typically used for standard lubricant tests that are specified by either industrial organisations or by scientific institutions (Stachowiak and Batchelor, 2004). Research work is more typically conducted using either pin-on-disk or pin-on-slab (pin-on-plate) tribometers. The pin-on-disk tribometer operates by applying a load to a pin that is pressed against a rotating disk. The dimensions of the pin and the disk can be varied depending upon the test being conducted, for example the pin can be flat or have a radius. The pin-on-plate tribometer is used when reciprocating sliding is being studied, it operates in a similar manner to the pin-on-disk with the load being applied to the pin. However, the plate is moved in a reciprocating manner as opposed to unidirectionally as on the pin-on-disk.

The tribological experiments in this work are conducted on a unidirectional pin-on-disk tribometer, this equipment was chosen so that acoustic emission phenomena could be suitably investigated without complications arising from changes in the tribometer direction.

1.3.1.1 Experimental measurements of friction

Equation 1 (Page 2) shows that there are only two components that define friction, these are the normal load and the tangential force. In laboratory tribotests both of these parameters are relatively easy to measure, thus allowing the calculation of the coefficient of friction. During laboratory based tribotests the normal load is very simple to measure, as the force is often applied through the use of hanging weights. The tangential force is measured as the force the test specimen acts upon a load cell as the test is running. For a pin-on-disk tribometer there is an arm attached to the pin holder that is in contact with a fixed load cell, as the disk is rotated the arm applies a force to the load cell.

1.3.1.2 Experimental measurements of wear

Post-test analysis of wear is relatively simple depending upon the tribocontact materials. It is often the case that one of the tribocontacts will wear more than the other, for example a groove could be created in a plate specimen with limited wear of the pin that acted upon it. Conversely, it is possible for the pin to be worn away significantly with limited wear being shown upon the counterface.

There are numerous post-test methodologies that can be employed to determine the extent of the wear caused during testing. Historically, one method used was to weigh the samples pre- and post-test which provides a quantifiable mass loss (Gåhlin and Jacobson, 1998). Unfortunately, there are numerous drawbacks to this technique as the precision of the balance used would typically require that the samples measured experience a high mass loss relative to the total component weight (Gåhlin and Jacobson, 1998). Another drawback to this method is that it does not provide any information regarding the distribution of wear over a component (Gåhlin and Jacobson, 1998).

An alternative to measuring the mass loss is to measure dimensional changes of the contact, these could be one, two or three dimensional. Bergman et al. (1997) monitored the wear via one dimensional measurements of the length of the pin in pin-on-disk tests using a high resolution displacement transducer. Khan et al. (2016) utilised optical microscopy and contact profilometry to perform two dimensional measurements of the diameter and average wear depth of wear scars. Furustig et al. (2016) used atomic force microscopy to perform two dimensional measurements of the wear scars of steel disks to a very high precision, with lateral and vertical resolutions of 0.2 nm and 0.01 nm respectively. Stevenson et al. (2018) used white light interferometry to perform three dimensional mapping of wear scars which they used to report a total wear volume. However, one downside to the use of white light interferometry is that it can introduce optical artefacts (Spencer et al., 2013).

As previously mentioned, each of these methodologies was used to measure the total amount of wear post-test. It is also possible to measure the wear *in situ* whilst the test is running. Wahl and Sawyer (2008) mounted a reciprocating tribometer onto a white light interferometer in order to monitor the wear surface whilst the test progressed. Penkov et al. (2017) used a high precision 3D laser microscope attached to a micro-tribotester to enable *in situ* monitoring and evaluation of wear. Alternatively, atomic force microscopy techniques have been extensively employed to act as both the tribometer and the measuring device whereby the microscope tip acts as the abrading surface whilst simultaneously imaging the damage (Bhushan et al., 1995, Patton and Bhushan, 1996, Miyake and Kaneko, 1992).

1.3.2 Surface Analysis

The tribological behaviour of a contact is dependent upon the material properties of the test specimens (Stachowiak and Batchelor, 2004). As such, the characterisation of test specimens is essential in order to provide a sufficient control when completing multiple tests. Polymers, ceramics and metals all require different sample preparation prior to characterisation. As only steel tests specimens are used in this work, polymers and ceramics will not be discussed.

Wear and friction are intrinsically linked to the surfaces of the materials being characterised, it is therefore necessary that tribological contacts are sufficiently characterised. One of the key ways in which surfaces are characterised both pre- and post-test is to measure the surface roughness. There are multiple ways in which the surface roughness can be measured, this can be through direct contact with the surface using a contact profilometer or a non-contact method such as white light interferometry (WLI).

1.3.2.1 Contact profilometry

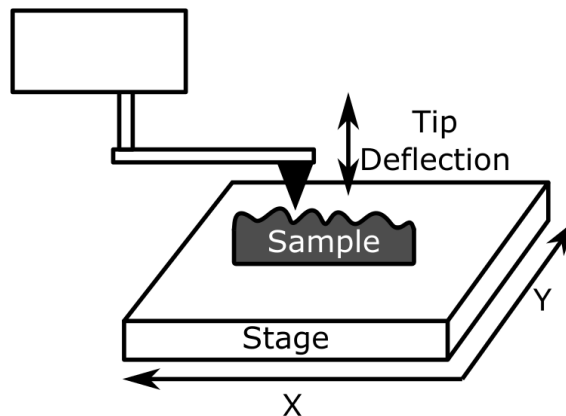


Figure 1.17 - Schematic of line profilometry measurement.

Contact profilometry utilises a fine tipped probe that is physically moved across the surface of the sample in order to acquire the surface height. Any deflection in the vertical displacement of the tip is measured using a linear variable displacement transducer that converts linear displacement into a measurable signal. As the probe is scanned across the surface the changes in the probe height are representative of the material surface.

Using contact profilometry is extremely sensitive and provides high resolution in the Z direction (sub-nanometer) however the horizontal resolution is dictated

by the probe tip size. A too-large probe tip would simply be driven over very small surface defects without reporting a change.

As the probe tip is in contact with the surface, it can become contaminated therefore, samples need to be cleaned prior to measurement.

1.3.2.2 White Light Interferometry

WLI is a non-contact optical method that is used to measure the surface profiles of 3D structures. As the name suggests, WLI utilises the phenomena of interference to measure the surface of the sample.

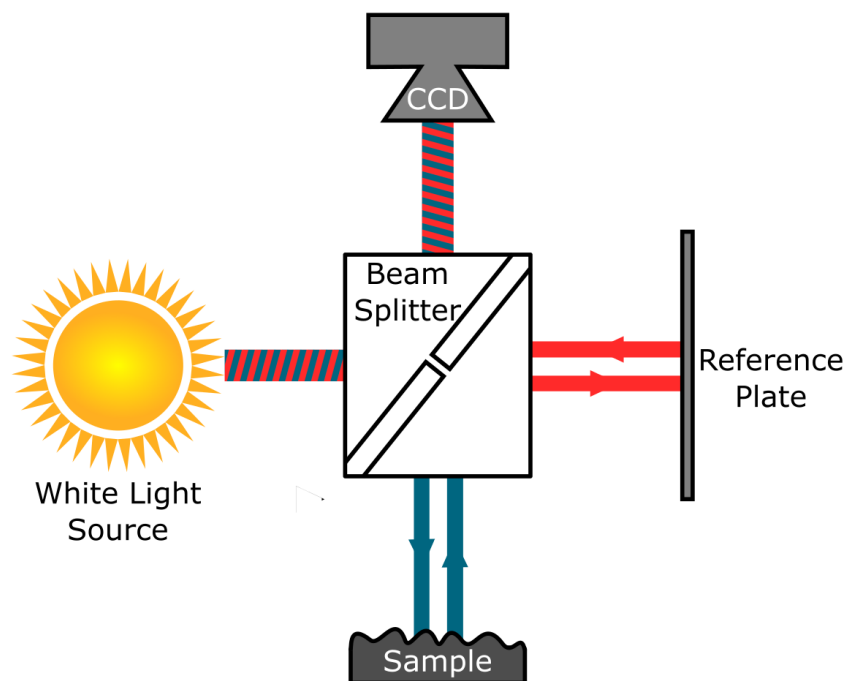


Figure 1.18 - Schematic of white light interferometry measurement.

WLI works by splitting a beam of white light into two, one beam is then directed to the sample surface and the other to a reference plane. The beams are then recombined, creating an interference pattern. The recombined interference pattern is then analysed by determining the differences in the paths the two beams travelled and therefore the height variations present on the measured surface. A 3D reconstruction of the sample surface can be created using the interference patterns.

WLI is a very accurate method for the analysis of surfaces with the vertical and horizontal resolution often reported as being sub-nanometre.

1.3.3 Tribofilm Characterisation

In order to determine whether a tribofilm has been formed post-test alternative techniques must be employed in order to determine whether a tribofilm has been formed and to measure certain aspects such as thickness, and chemical composition.

1.3.3.1 Raman Spectroscopy

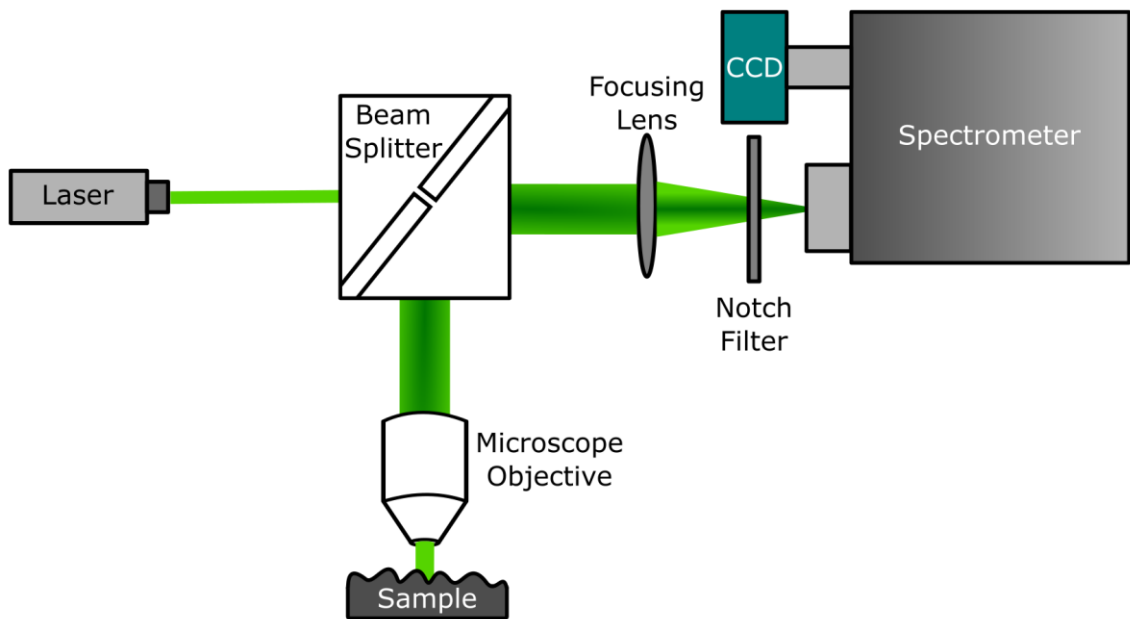


Figure 1.19 - Schematic of Raman spectroscopy measurement.

When determining whether a tribofilm has formed when using MoDTC as a lubricant additive, it is common that Raman spectroscopy is used post-test to detect the presence of MoS₂ on the surface. Typically, a Raman spectrometer, as shown in Figure 1.19 contains at least four major components: a monochromatic light source usually a laser, a sample area with collection optics, a spectrometer and a detector such as a charged coupled device (CCD).

Raman spectroscopy utilises the inelastic scattering of a laser light source. The laser light is directed to the sample where it interacts with certain molecular vibrations inherent within the present molecules. This interaction results in the energy of the laser photons being shifted up or down in comparison with the original frequency; it is this shift in energy which allows certain molecules and functional groups to be identified within a sample.

Previous Raman spectroscopic studies of MoS₂ have identified four first-order Raman active modes, found at 32 cm⁻¹, 286 cm⁻¹, 383 cm⁻¹ and 408 cm⁻¹ namely E_{2g}², E_{1g}, E_{1g}¹, and A_{1g} respectively, that can be used to determine whether there is any MoS₂ present on the surface being examined (Wieting and Verble, 1971).

1.3.3.2 Energy-dispersive X-Ray spectroscopy

ZDDP tribofilms cannot be detected by Raman spectroscopy; one alternative is to use a Scanning Electron Microscope (SEM) fitted with an Energy-dispersive X-ray (EDX) spectrometer attachment. The EDX analytical technique operates in a similar manner to the Raman spectrometer in that it relies on the interaction of atoms with electromagnetic radiation. However, EDX analysis relies on the interaction between the sample and an X-ray source rather than light. EDX spectrometers can be attached to a SEM as the electron beam that is used to scan across the surface can be used as the excitation source for the EDX analysis (Goldstein et al., 2017). When the sample surface is excited using the electron beam it is possible that an electron in an inner shell of the atom is ejected thus leaving an electron hole (Goldstein et al., 2017). An electron from an outer higher energy shell would then fill the 'electron hole' with the difference in energy between the two shells being released in the form of an X-ray (Goldstein et al., 2017).

Therefore, using an EDX spectrometer it is possible to measure the number and energy of X-rays being emitted from the sample surface. It is possible to determine the chemical composition of the sample being measured due to the fact that all atoms have a different structure and the released X-rays are characteristic of the energy difference between the two shells (Goldstein et al., 2017, Torbacke et al., 2014).

Unlike Raman spectroscopy, EDX analysis can only identify individual atoms such as Zn and P as opposed to molecules such as MoS₂. Morina et al. (2006) successfully used EDX analysis to investigate the effect of ZDDP/MoDTC ratio on tribofilm formation as well as the effect of temperature on ZDDP tribofilm formation.

1.3.4 *In situ* Analysis

The previously discussed analysis techniques are typically used to characterise samples post-test and *ex situ* by removing the samples from the tribometer at the end of the test to measure key parameters such as wear and

tribofilm composition etc. One obvious flaw in this methodology is that it is not possible to monitor these parameters directly throughout the duration of the test as the test has to be stopped and the samples removed prior to examination.

One way of combatting the flaws of *ex-situ* examination is the implementation of *in situ* analysis techniques.

There are multiple directions in which *in situ* analysis can be approached, a modified tribometer could be installed within the analysis equipment such as the *in situ* Raman tribometer developed by Rai (2015). Alternatively, changes to the sample geometry, composition, and testing environment can be made to allow *in situ* measurements to take place (Sawyer and Wahl, 2008). Transparent materials such as sapphire can be used to enable observations of the contact interface by allowing certain electromagnetic radiation to pass through, such as light or X-rays (Sawyer and Wahl, 2008, Rai, 2015, Wahl and Sawyer, 2008). However, the materials used to allow this are not often the typical counterface material for the application this would therefore affect the results (Sawyer and Wahl, 2008). Additionally, it is very common for the geometry of samples used to be determined based upon their measurability rather than suitability to the application being replicated (Sawyer and Wahl, 2008). Sawyer and Wahl (2008) compiled a list of different *in situ* techniques alongside their spatial resolutions and practical limitations, this can be seen in Table 1.

Table 1 – *In situ* approaches used for tribological interface studies. Replicated from Sawyer and Wahl (2008).

Technique	Measurement	Spatial Resolution	Limitations	Reference
Optical Microscopy	Tribofilm formation and motion, contact size	~ 1 μm	One counterface must be optically transparent	(Krick et al., 2012)
Interferometry (contact)	Contact separation	~ 1 μm	One counterface must be optically transparent	(Gunsel et al., 1993)
Interferometry (wear track)	Wear	~ 1 μm	Index of refraction or reflectivity changes can distort results	(Keith, 2010)

Raman microscopy	Composition/chemistry, film thickness	~ 1 μm	One counterface must be optically transparent	(Bongaerts et al., 2008, Scharf and Singer, 2003, Singer et al., 2002)
ATR-FTIR spectroscopy	Chemical bonding	mm to cm (width of crystal)	One counterface must be IR-transparent	(Piras et al., 2002b, Piras et al., 2002a)
TEM + EELS + AFM / Nano indentation	Microstructural transformation, interfacial film formation composition, chemistry	0.1 nm	Interface region must be electron-transparent; vacuum environment	(Wang et al., 2009)
SEM/EDX	Surface morphology, composition	10 nm	Contact charging, contamination in low vacuum environments	(Lim and Brunton, 1985, Rabe et al., 2004)
SEM + FIB	Cross section of sliding surface w/o separation	0.1 nm	Potential beam damage from FIB sectioning	(Eswara-Moorthy et al., 2014)
SFA + x-ray diffraction or neutron reflectivity	Structure	μm 's	Requires synchrotron access	(Idziak et al., 1996, Idziak et al., 1994, Golan et al., 2002)
AFM	Friction, surface topography, contact stiffness, wear	~ 1 μm	Difficult to ascertain contact size, chemistry	(Sch et al., 1998, Grierson et al., 2005)
AES	Composition	10 nm	Cannot probe inside contact zone	(Le Mogne et al., 1999, Pepper, 1974)
XPS	Composition, chemical state	10s of μm	Cannot probe inside contact zone	(Le Mogne et al., 1999)
Contact Resistance	Coating thickness, damage, interfacial film formation			(Oyarce et al., 2009, Laedre et al., 2013)

Note: ATR-FTIR, attenuated total reflection Fourier transform infrared spectroscopy; TEM, transmission electron microscopy; AFM, atomic force microscopy; EELS, electron energy loss spectroscopy; SEM, scanning electron microscopy; EDX, energy dispersive x-ray spectroscopy; FIB, focused ion beam; SFA, surface force apparatus; AES, Auger electron spectroscopy; XPS, x-ray photoelectron spectroscopy.

Ultra-thin film interferometry has been used to study the film-forming properties of lubricants (Gunsel et al., 1993, Ratoi et al., 2003, Glovnea et al., 2003, Fujita and Spikes, 2005, Spikes, 1999, Ratoi et al., 2014). This technique is capable of measuring lubricant films in high pressure and shear rate conditions to nanometer thicknesses, similar conditions to those found in real machine component contacts.

Whilst it is possible to measure the film thickness of the lubricant and potential changes in rheology, this methodology is not capable of providing chemical characterisation for the lubricant. Furthermore, this methodology requires one of the contact counterfaces to be transparent in order to allow optical interference patterns to be observed. This limits the applicability of this methodology as it cannot take into account the effect of metal-on-metal contacts and the influence of generated third body wear particles.

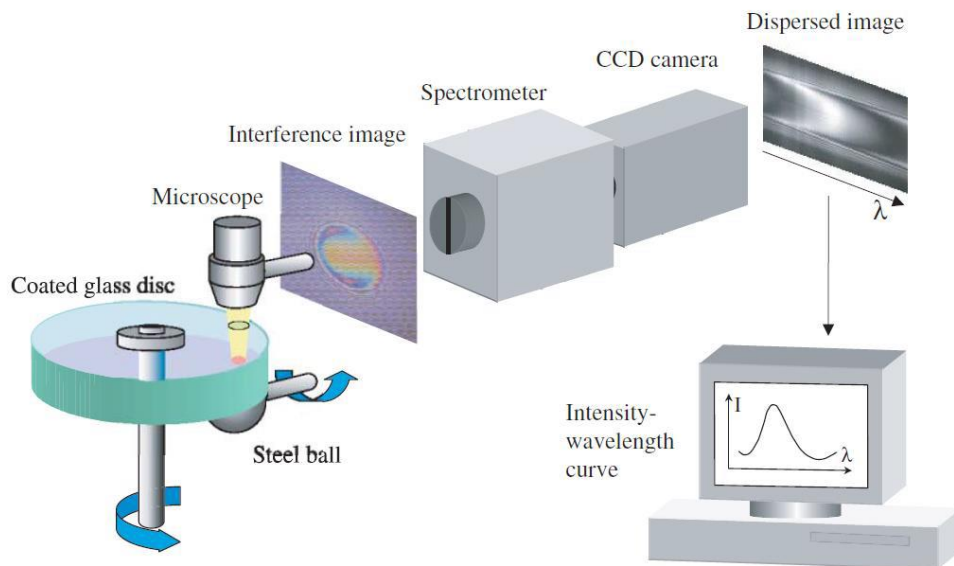


Figure 1.20 - Schematic of the ultra-thin film interferometry apparatus used to measure sub-nanometre lubricant films. Taken from Glovnea et al. (2003).

Spacer Layer Imaging Methodology (SLIM) has been utilised by Fujita and Spikes (2004) to measure and compare the formation of both ZDDP thermal and tribofilms. The SLIM technique utilises optical interferometry that is caused by loading the wear track of the ball specimen against a spacer-layer coated glass window, it is capable of determining the thickness of a film present on the contact (Cann et al., 1996). The SLIM technique uses a modified mini traction machine (PCS Instruments) which has the spacer layer equipment and necessary camera attached.

The SLIM technique assumes that the spacer-layer coated glass surface conforms elastically to the ball specimen and that non-conformity of the ball does not affect measurements of the tribofilm thickness (Spikes and Cann, 2001). One downside to his technique is that it is dependent upon knowledge of the refractive index of the lubricant being measured in order to convert the measured film thickness to a true value. Further, the SLIM technique does not measure the film thickness whilst the ball and plate are in contact, the test is stopped and the ball is then loaded against the glass window, this is therefore not a truly accurate representation of the tribofilm present in the contact area.

Topolovec-Miklozic et al. (2007) used both atomic force microscopy and SLIM techniques to measure the thickness and roughness of ZDDP tribofilms. It was found that the SLIM approach underestimated the roughness of the tribofilm and the authors recommended that AFM methods should be used to study the morphology of the tribofilm.

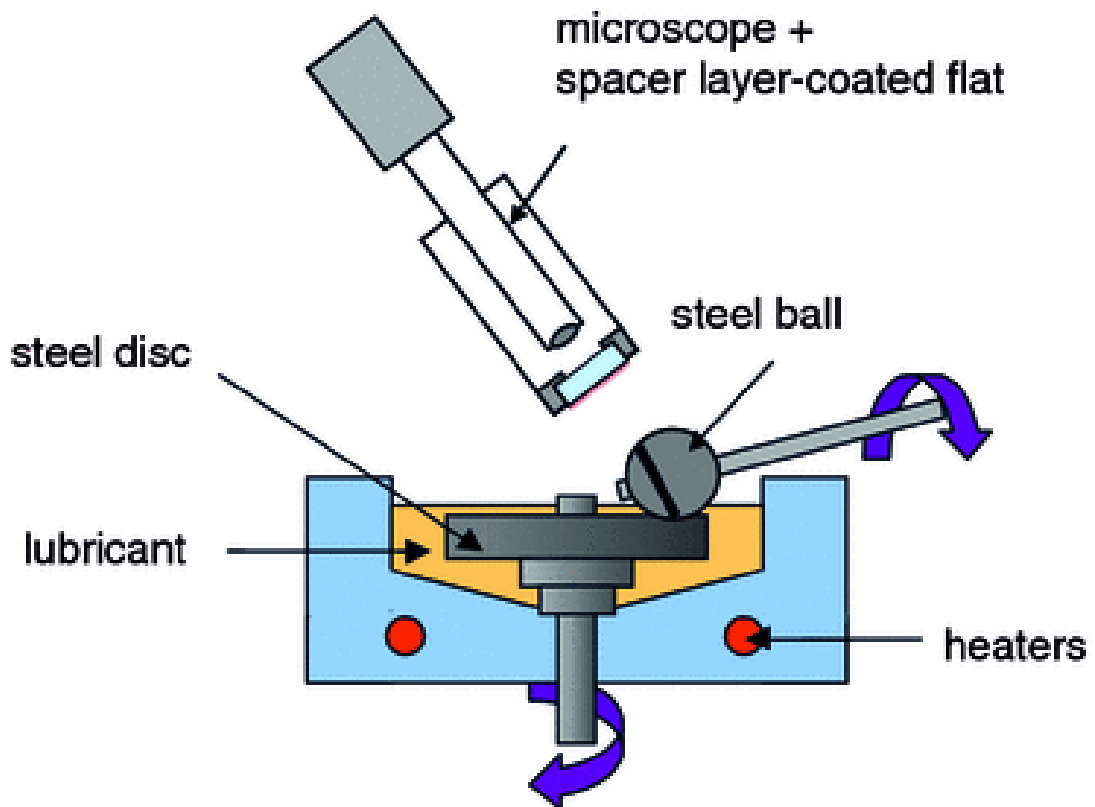


Figure 1.21 - Schematic diagram of the *in situ* spacer layer interferometry set-up on the MTM, along with the coated glass window loaded on a stationary steel ball wear track. Taken from Topolovec-Miklozic et al. (2008) .

It can be seen that there are many different *in situ* analysis techniques for tribological applications and whilst they all have associated limitations,

implementation of *in situ* analysis still provides an important improvement on *ex-situ* analysis. This improvement is provided a number of ways, such as the fact that eliminating the requirement for removing the sample from the test environment will reduce the possibility of surface contamination. Secondly, the relationship between friction, wear and the contact interface can be more directly investigated. Finally, by measuring contacts in real time and *in situ* it is possible to remove the need for highly speculative explanations regarding what is happening at the surface as it will be measured directly (Wahl and Sawyer, 2008).

1.4 Acoustic Emission

1.4.1 Fundamentals of Acoustic Emission

Acoustic emission is the phenomena whereby transient elastic waves are generated by the sudden rapid release of energy within a material (Hanchi and Klamecki, 1991). This release can occur from numerous potential mechanisms, such as induced stress or strain and deformation processes (Boness and McBride, 1991, Hanchi and Klamecki, 1991, Kustas et al., 1994, Li, 2002, Ravi and Sethuramiah, 1995). The same interaction between sliding surfaces causes adhesion, deformation and material removal resulting in friction and wear (Benabdallah and Aguilar, 2008).

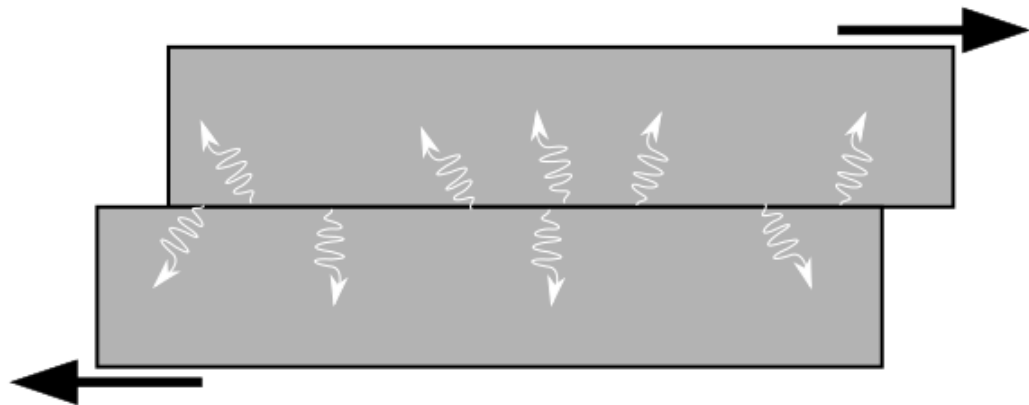


Figure 1.22 - Image demonstrating the source of acoustic emission events due to sliding wear.

The stress waves that are produced by surfaces coming into contact then propagate out away from the contact interface. These propagating stress waves can be detected on the surface through the use of an appropriate sensor, a portion of the stress waves fall within the frequency range of the order of 10 – 1000 kHz (Kustas et al., 1994). Frequencies within this range can

be detected by piezoelectric materials which transform the vibrational energy into a voltage that can be read by a data acquisition unit.

Unlike other non-destructive testing techniques, AE measures events stimulated from within the material itself and as such it is widely used as a fault detection methodology (Kustas et al., 1994). However, it has been shown that the analysis of the acoustic emission signals can give an insight into wear mechanisms and the interface of a contact (Lingard et al., 1993, Sun et al., 2005, Wang and Wood, 2009).

1.4.1.1 Measurement Parameters

There are a range of different measurement parameters that can be utilised when using acoustic emission techniques. The three most common measurement parameters are absolute energy, hit count and root mean square (RMS) of the signal, each parameter will be briefly discussed below.

1.4.1.1.1 Absolute Energy

The absolute energy is a measurement of the amount of energy released when the acoustic emission is produced. To measure the absolute energy is relatively easy, it is the integral of the acoustic emission signal that is produced which is simply the area under the curve, this can be clearly seen in Figure 1.23.

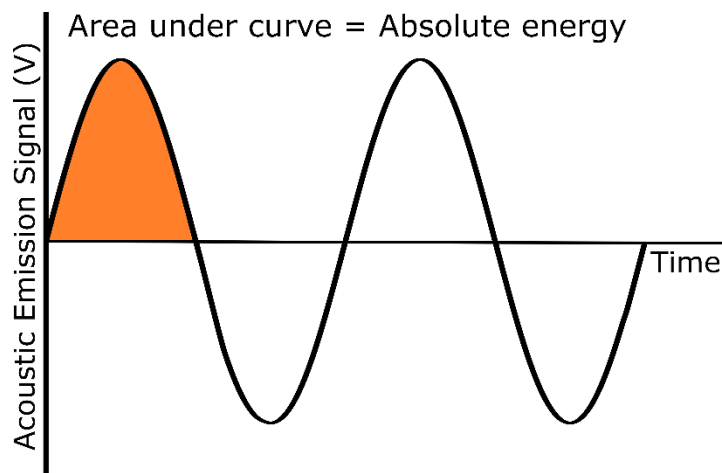


Figure 1.23 - Diagrammatic representation of how absolute energy is calculated from a waveform.

To validate the calculations used to measure the absolute energy, a known idealised signal can be integrated to verify that the resultant absolute energy is correct.

1.4.1.1.2 Hit Counts

AE hits are defined as an emission burst lasting typically a fraction of a millisecond (Lingard et al., 1993) and are traditionally used to detect discrete short term events such as an increment of crack propagation in brittle material.

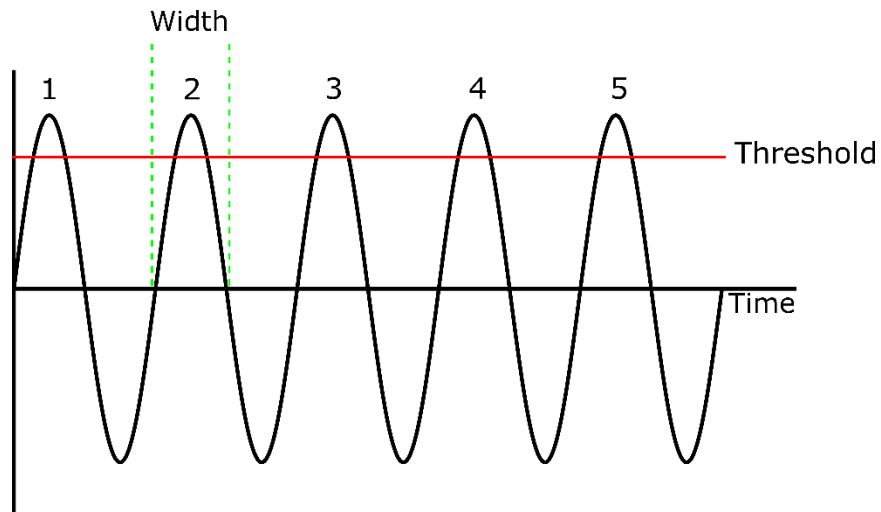


Figure 1.24 - Diagrammatic representation of how AE hits are counted as the signal passes a threshold value.

It is shown in Figure 1.24 how each AE hit is counted as the measured signal amplitude crosses the threshold value, this is a model example shown on a sine wave. The width is used to determine what time scale is used when measuring the number of times the signal crosses the threshold value. In this model example the width equates to one threshold cross per peak.

1.4.1.1.3 Root Mean Squared (RMS) average

For deformation proceeding steadily at a lower level, multiple individual emission waves of low amplitude are thought to merge and overlap producing a continuous emission which appears on initial observation similar to electronic noise (Lingard et al., 1993). Further signal processing allows continuous signals to be studied and correctly analysed. AE RMS is the arithmetic average of the input signal over a certain time base.

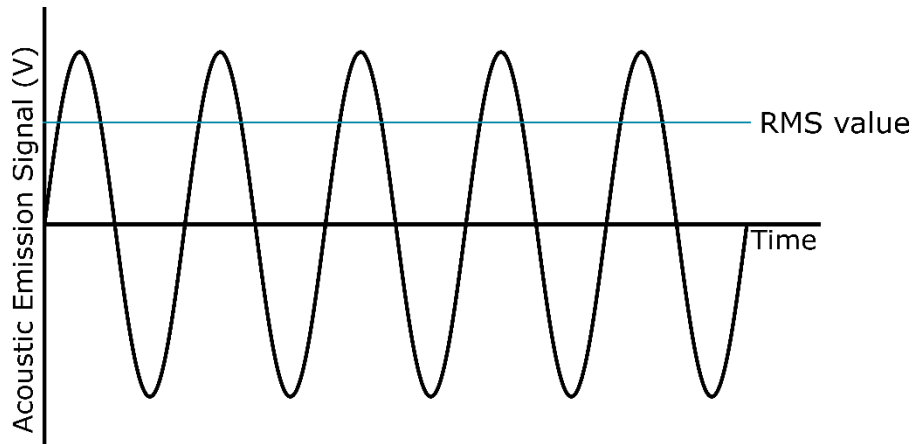


Figure 1.25 - Diagrammatic representation of how the RMS value would appear on a model sine wave.

Figure 1.25 shows an example of the representative RMS signal that would arise from the model sine wave shown. In a more complex signal the time/sample length is taken into account. If a signal was to be averaged over its entirety a straight line as seen in Figure 1.25, to avoid this the signal is instead averaged over a smaller time base so that all relevant signal features are captured.

In this work the time base used for the RMS calculations was determined by the sampling speed and intervals used in the bespoke data acquisition system. This is discussed in more detail in Chapter 3.

1.4.1.2 Acoustic Emission Sensing Technology

Acoustic emission sensors are comprised of several parts, illustrated in Figure 1.26; the case, damping material, electrodes and the piezoelectric element. Each of these parts plays a fundamental role in the measurement of acoustic emission signals. A damping material is used to dampen the signal around the resonant frequency of the element. The case is used as a practical way in which the integral parts of the sensor can be housed in a convenient package (NDT Resource Center, 2019).

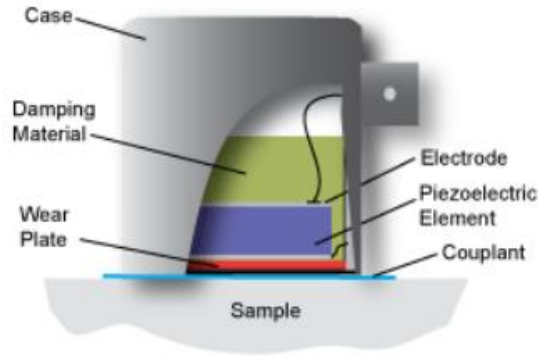


Figure 1.26 – Schematic of a typical acoustic emission sensor. Taken from NDT Resource Center (2019).

The most important part of any acoustic emission sensor is the piezoelectric element; these are typically made from lead zirconate titanate (PZT) crystals. PZT utilise the piezoelectric effect whereby when they are deformed i.e. from an acoustic emission, they produce a small voltage, it is this voltage that is then measured and recorded as the acoustic emission signal, a diagrammatic representation of this can be seen below in Figure 1.27.

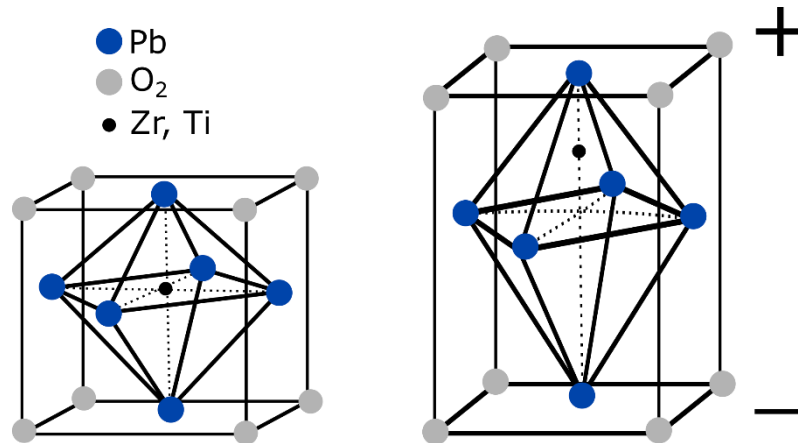


Figure 1.27 - Schematic showing piezoelectric effect of PZT crystals.

There is a wide range of commercial sensors available on the market, major differences being in bandwidth and frequency responses. As such it is imperative that the correct sensor is chosen for the application. Figure 1.28 shows the frequencies at which AE events have been recorded by various authors, it can be seen that acoustic emissions are produced over a very large range of frequencies and that it would be most beneficial to capture as much of that range as possible.

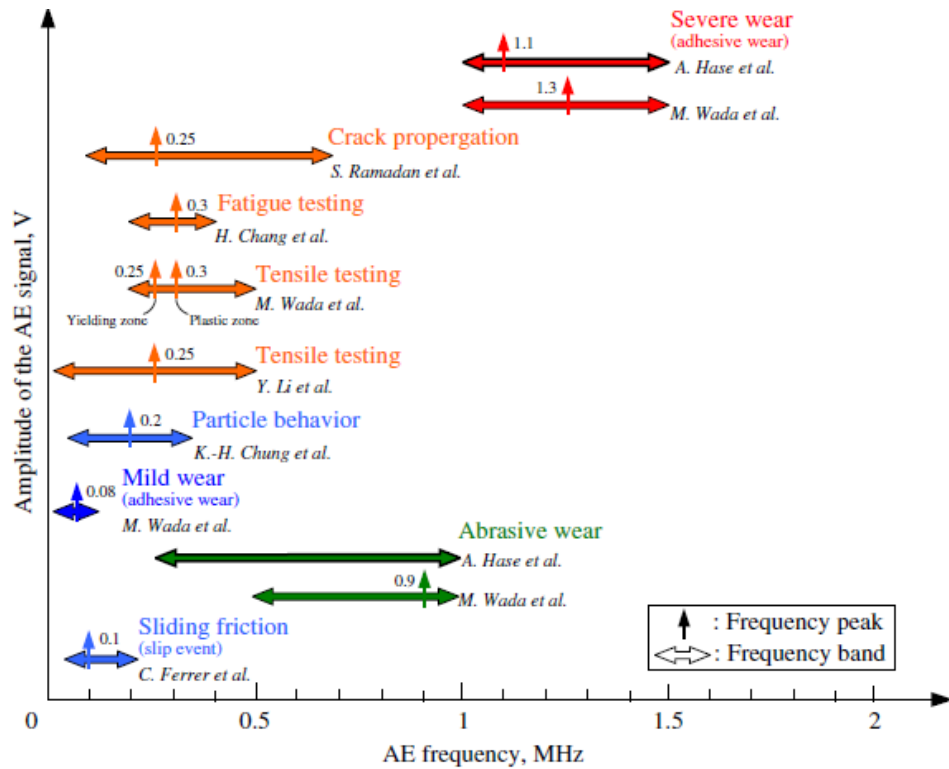


Figure 1.28 - Distribution of AE event frequencies. Taken from Hase et al. (2012).

It has also been shown by Lingard et al. (1993) that emission frequencies in the range of 50 kHz to 2MHz are more useful in determining stress waves generated by rubbing surfaces. Frequencies in this range are distinct from the lower frequency, large scale mechanical vibrations and noise that may also occur within a tribometer.

1.4.2 Acoustic Emission in the Condition Monitoring of Cracks

Traditionally, acoustic emission monitoring has been used for the detection, location and monitoring of fatigue cracks in a multitude of metal structures (Roberts and Talebzadeh, 2003).

Harris and Dunegan (1974) used acoustic emission techniques to detect fatigue-crack propagation in aluminium and steel. Gong et al. (1992) used acoustic emissions to identify active cracks, find new cracks and validate the effectiveness of repairs across 36 steel railroad bridges.

McBride et al. (1993) used acoustic emission monitoring for enhanced fatigue crack detection in aging aircraft airframes, they found that continuous monitoring eliminates the possibility of improper conclusions and also improves the location of crack advance sources.

Ennaceur et al. (2006) identified that the count, amplitude, rise time and average frequency are important parameters for the identification of crack propagation mechanisms.

As well as the study of metal structures, acoustic emission methodologies have been used to study crack propagation in other materials such as concrete (Luo et al., 2004, Ohtsu, 1996, Shiotani et al., 1999).

Shiotani et al. (2001) and Ohtsu (2006) found that the number of acoustic emission hits and the maximum amplitude of the acoustic emission signal could be used to estimate the degree of damage in concrete structures.

1.4.3 Acoustic Emission and Tool Wear

Tool wear is complex and occurs in many different ways in metal cutting processes (Li, 2002). When a tool is worn it adversely affects the workpiece that is being machined and as such it is necessary that tool condition monitoring systems are developed. Acoustic emission techniques are one of the most effective indirect measurement tools that have been widely used in the metalworking industry as a solution to the enduring problem of when to change a tool (Maia et al., 2015, Li, 2002).

Several sources of acoustic emissions in metal cutting processes were identified by Liang and Dornfeld (1989), these are:

- a) Plastic deformation during the cutting process in the workpiece
- b) Plastic deformation in the chip
- c) Collisions between chip and tool
- d) Chip breakage
- e) Frictional contact between the tool flank face and the workpiece resulting in flank wear
- f) Frictional contact between the tool rank face and the chip resulting in crater wear
- g) Tool fracture

Hase et al. (2014) correlated the acoustic emission signals produced when turning an AISIA O1 steel with cermet tools to cutting phenomena. It was found that the primary shear angle, the chip form and the process in which the chip formed significantly affected the acoustic emission signal that was produced.

Bhuiyan et al. (2016) used acoustic emission sensors for tool condition monitoring, specifically investigating the frequency associated with tool wear and plastic deformation. It was found that the amplitude of the acoustic emission signal increases with tool wear as well as increases in the frequency of the signal with increased material removal.

Sampath and Vajpayee (1986) developed a linear regression model that relates the flank wear of a carbide turning insert with cumulative acoustic emission hit count values. This work was then expanded upon by Vajpayee and Sampath (1988) who used the hit count as a reliable parameter for predicting tool flank wear in real time.

Similarly, Cho and Komvopoulos (1997) using the RMS of the acoustic emission signal to estimate tool life found that the estimation agreed well with measurements of wear from the tool nose.

Nevertheless, the use of acoustic emission in the monitoring of tool wear is not without its drawbacks as the mechanisms of several phenomena in cutting are still poorly defined. For example, it is not well known what frequencies are produced when voids coalesce and dislocations move (Maia et al., 2015).

1.4.4 Acoustic Emission in Tribology

Multiple signal processing methods have been used in conjunction with one another by a number of authors to analyse the acoustic emission responses in relation to more traditional tribological parameters such as friction and wear (Boness et al., 1990, Jiaa and Dornfeld, 1990, Lingard and Ng, 1989, Mechefske and Sun, 2001).

Fan et al. (2010) created a theoretical model to correlate acoustic emissions to sliding friction based on the elastic asperity contact of materials. They found that a number of tribological parameters affected the acoustic emission signal such as the load supported by asperities, the sliding speed and the number of asperity contacts.

Boness and McBride (1991) demonstrated that the primary source of acoustic emissions between sliding surfaces was the asperity contact. They established a relationship between the integrated RMS signal and the total wear volume of tribotests conducted using light and heavy paraffin as a lubricant. A similar relationship between integrated RMS signal and wear volume was also established for fuel-wetted surfaces by Boness (1993).

Lingard et al. (1993) used the twin disk experimental setup shown below in Figure 1.29 to measure the contact between a rotating 40 mm specimen of either low carbon mild steel or hardened medium carbon nickel-chrome steel against a stationary 40 mm specimen. The stationary specimen was either 2100 series aluminium alloy, 70/30 brass or low carbon mild steel.

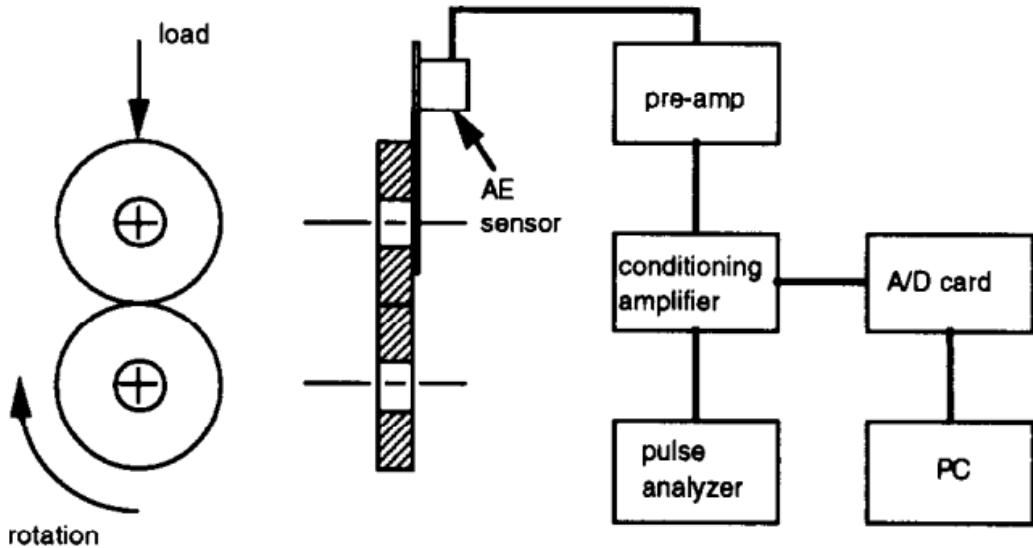


Figure 1.29 - Twin disk experimental apparatus used by Lingard et al. (1993).

It was found by Lingard et al. (1993) using Fourier transforms that certain peak frequencies were associated with each contact pairing, this is shown for aluminium on steel and steel on hardened steel pairings in Figure 1.30 below.

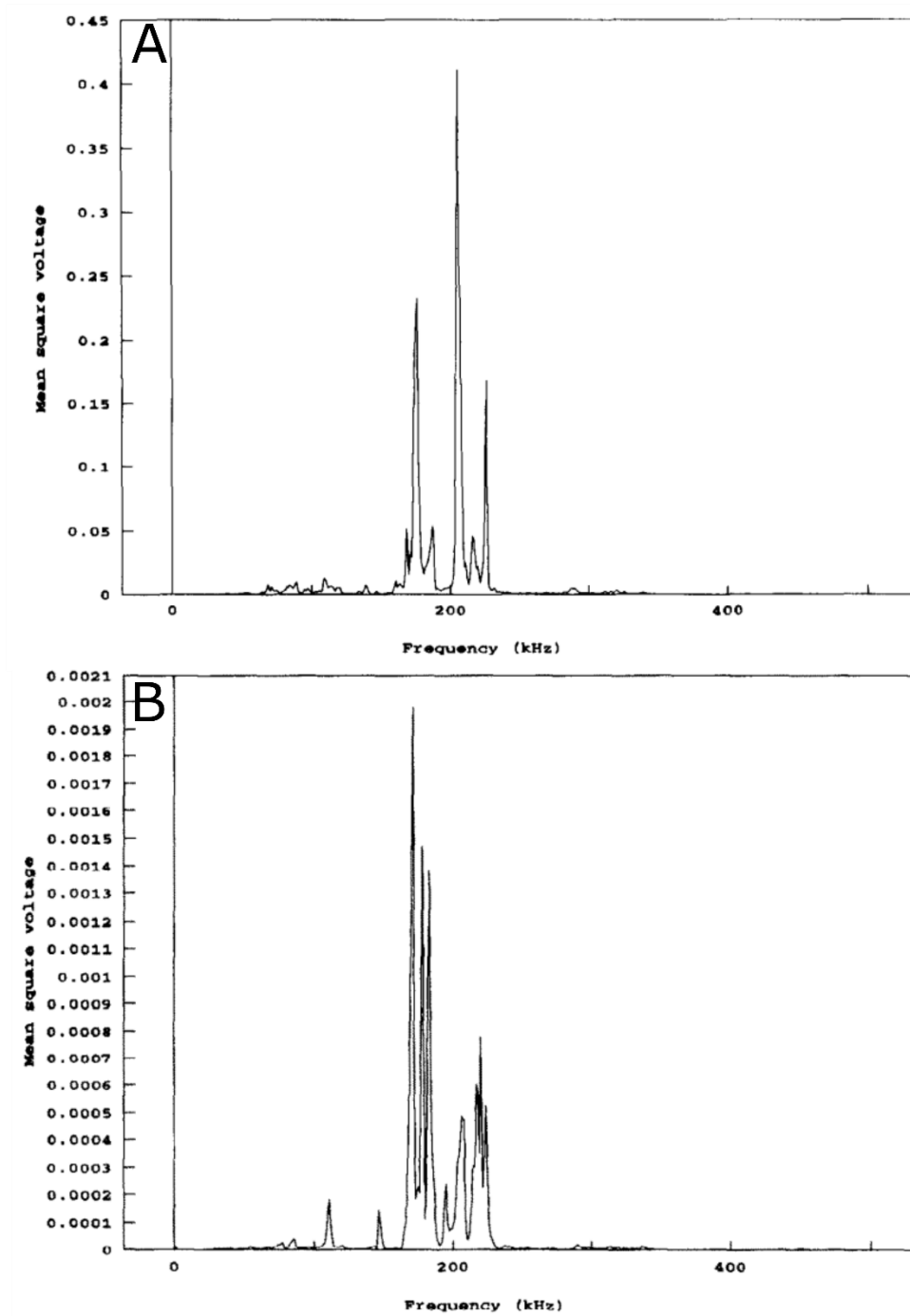


Figure 1.30 - Frequency spectra for A) aluminium on steel and B) steel on hardened steel. Taken from Lingard et al. (1993) .

It can be seen that there is difference in the peak frequencies of the two spectra shown in Figure 1.30, it is also worth noting that the magnitude of the two spectra are wildly different with a peak frequency for A being at approximately 0.4 V and for B it is only 0.002 V. It was also found that the range of frequencies is very large with complex variations in intensities dependent upon test conditions and duration.

Hisakado and Warashina (1998) used a pin-on-disk tribometer to test the acoustic emission characteristics of an iron pin on a hardened steel bearing disk. Constant load and sliding speed, 5.04N and 0.12 ms⁻¹ were applied for all experiments. Tests were conducted under three lubricated conditions wet, half wet and dry; wet was determined using a pool of lubricant whereas half wet corresponded to a thin layer of lubricant being applied to the pin. All tests were performed on for three disks of varying surface roughness. It was found that under all lubricated conditions AE hits were found to increase as the mean friction coefficient increased.

Morhain and Mba (2003) used a test rig designed to simulate the early stage of bearing defects; the test rig investigated the split Cooper spherical roller type 01C/40GR. The use of this bearing allowed the authors to cause pre-test defects to the bearings with minimal disruption to the test rig. A wideband (100-1000 kHz) AE sensor was used utilising pre amplification ranging from 40-60 dB.

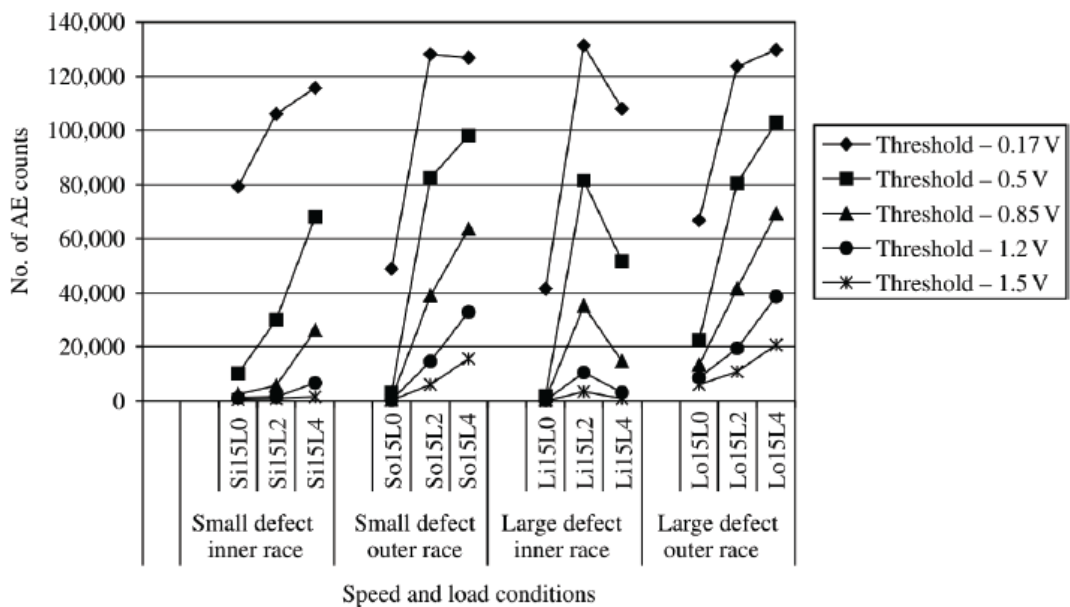


Figure 1.31 - Number of AE counts for varying defects at 1500 RPM. Taken from Morhain and Mba (2003).

Figure 1.31 illustrates the relationship between defect size and AE counts for both the inner and outer raceway at different load cases and threshold values. For all cases on outer race defects there is a clear trend of increasing counts with load regardless of threshold value. The above discussed tests were repeated for multiple speed and load conditions and as such Morhain and Mba (2003) validated the use of AE hits as a robust technique for detecting bearing

damage. Further to this it was also shown that RMS correlated with changes in speed and load.

Matsuoka (2001) formulated a relationship between the AE RMS signal and the wear coefficient for hard disk drives, it is shown below.

$$V_{RMS} = \alpha\sqrt{kNv} + \beta$$

Equation 4 - Relationship between AE RMS and wear coefficient

Where: V_{RMS} is the AE RMS voltage, k is the wear coefficient according to Archard's equation, N is the normal force, v is the relative sliding speed, and α and β are constants.

Utilising Equation 4 and multiple tests to calibrate α and β , it was possible for Matsuoka (2001) to predict the wear of the slider and compare it to experimental data, this can be seen below in Figure 1.32.

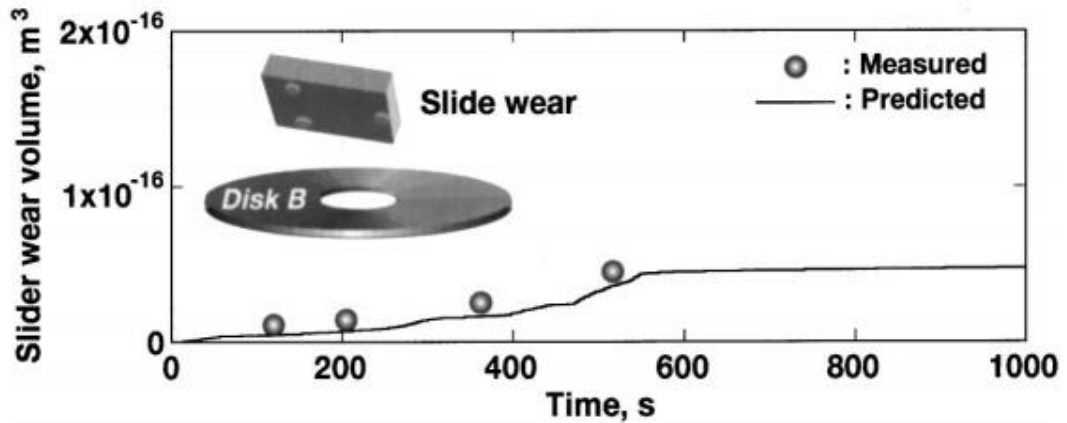


Figure 1.32 - Predicted wear volume of slider using AE signal and measure values as a function of time. Taken from Matsuoka (2001).

It can be seen that Matsuoka (2001) successfully developed a method for indirectly estimating and monitoring the wear of hard disk drives by sliders *in situ* through the correlation of AE RMS values and wear.

A correlation between different wear mechanisms and integrated AE RMS was found by Sun et al. (2005). Experiments were performed under dry contact conditions using a pin-on-disk tribometer; each wear mechanism was identified using scanning electron microscopy. Figure 1.33 below, shows the ball volume loss against integrated RMS signal.

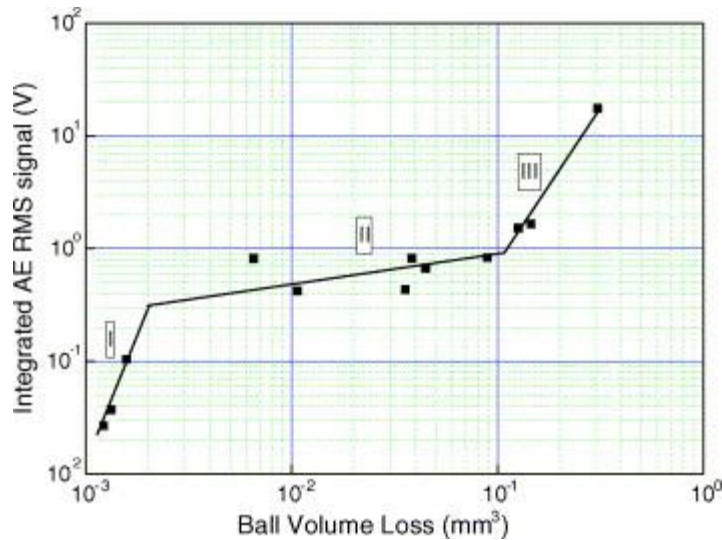


Figure 1.33 - Log-log graph of integrated AE RMS and ball volume loss showing three distinct linear relationships. Taken from Sun et al. (2005).

It can be seen that there are three different linear relationships between the integrated AE RMS signal and the pin volume loss. Sun et al. (2005) state that the three separate regions are running-in, oxidation and delamination.

A large scale piece of research was performed by Yahiaoui et al. (2015) in which three different tribological systems were investigated using wideband AE sensors. The three systems that were investigated were: Rotary sliding contact between WC-Co pin and alumina flat, Reciprocating sliding flat-on-flat contact between thermoplastic polyurethane and steel counterface and fretting contact between alumina pin and flat. It was shown that the acoustic emission signals follow changes in friction coefficient but the absolute values vary depending on tribometer set up and materials.

Cho and Lee (2000) were able to observe sudden AE variations that coincided with thin coating failure prior to any noticeable change in coefficient of friction. Single pass scratch testing was used to evaluate the bonding strength of CrN coatings with 0.2% plain carbon steels. A wideband AE sensor was attached to the scratch tester, as show in Figure 1.34.

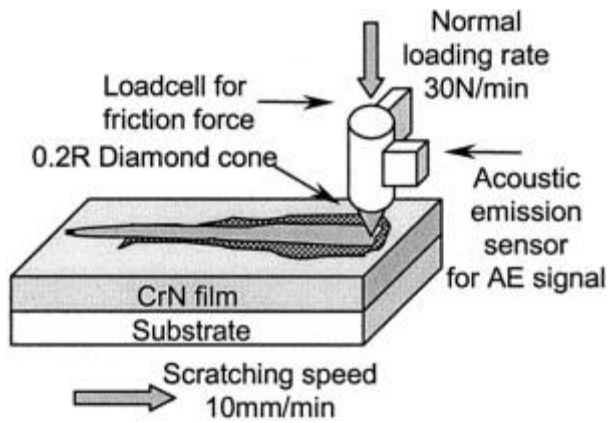


Figure 1.34 - Schematic diagram of scratch tester used by Cho and Lee (2000).

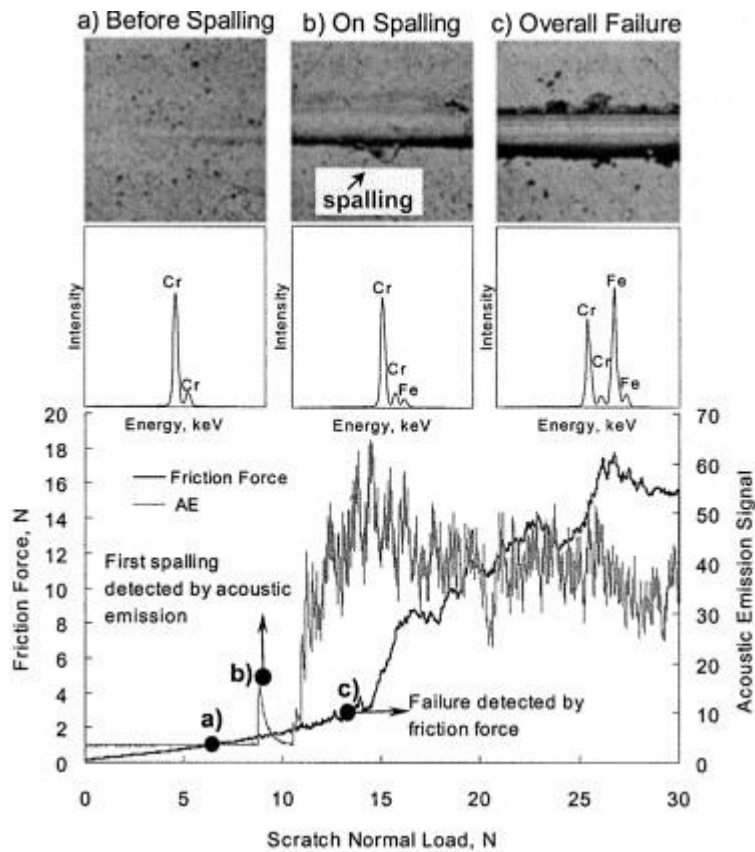


Figure 1.35 - Scratch test data for CrN coated steel disk with 1 μm coating thickness. Taken from Cho and Lee (2000).

It can be seen in Figure 1.35 that at point (b) there is an increase in AE signal before there is any dramatic change in the frictional force. It was also found that the average scratch normal load required for detection of spalling was 7.52 N for AE methods in comparison to 13.52 for frictional methods, this highlights sensitivity of acoustic emission techniques.

Saeidi et al. (2016) used acoustic emissions produced by a flat-on-flat tribometer to detect scuffing. Using wavelet transforms they developed an automatic system that can be used with an 88% accuracy to detect catastrophic failure due to scuffing.

Hase et al. (2012) used acoustic emissions to examine the two main types of mechanical wear, adhesive and abrasive wear. It was found that the frequency and the amplitude of the acoustic emission signal is symptomatic of the type of wear that occurs. With adhesive wear having a peak frequency at around 1.1 MHz and abrasive wear having multiple peaks in the region of 0.25 MHz to 1 MHz.

Geng et al. (2019) investigated the friction and wear of dry sliding steel-steel contacts conducted on a high frequency reciprocating rig. It was found that certain acoustic emission frequencies are highly correlated to the coefficient of friction and that acoustic emission can be a powerful tool for monitoring tribological behaviour.

It can be seen that there has been extensive research into the use of acoustic emissions as sensing techniques whether that is with respect to tool wear and monitoring, fault detection as well as friction and wear prediction. However, as of yet no work has been produced that links the tribochemical effects of lubricant additives to the generation of acoustic emission events. This work aims to establish the applicability of using acoustic emission measurements to monitor and measure tribochemical phenomena such as tribofilm generation and removal.

1.5 Aim and Objectives

The aim of this work is to show that there is a link between acoustic emissions and the tribochemical environment; leading to an ability to detect the formation and removal of tribofilms using commercially available acoustic emission sensors. It has previously been shown in the literature that there is a link between acoustic emissions and friction and wear in dry and lubricated contacts. It is also known that the use of additives affects the friction and wear experienced during tribological testing. Therefore, it is hypothesised that there will be a link between the tribochemical environment and the acoustic emissions produced, this will be explored through the following objectives:

- To develop a high speed data acquisition system using LabVIEW that is accurate, efficient and flexible to the needs of this work.

- To study the acoustic emission response to lubricated pin-on-disk tribometer tests and investigate the effect initial surface roughness has on the acoustic emission response.
- To investigate the acoustic emission response to MoDTC based tribofilm formation and removal.
- To investigate the acoustic emission response to ZDDP based tribofilm formation and removal.
- To investigate the relationship between measured acoustic emission parameters and the coefficient of friction

1.6 Thesis Outline

This thesis is composed of eight chapters, the structure of which will be briefly discussed. Chapter 1 provides an introduction to the fundamentals of tribology, friction, lubrication and wear. In this chapter a review of available literature on acoustic emission and tribochemistry is also presented.

Chapter 2 clarifies the experimental arrangements, sample preparation procedures and materials used throughout this work. Detailed information regarding the tribological parameters such as the materials, specimens, lubricant and additives, tribotest conditions is also shown. Surface analysis techniques used in this work are discussed and justified.

Chapter 3 is the first substantive results chapter in this work. The results shown in this chapter represent the development of a bespoke high speed data acquisition system that is used throughout this work for accurate and efficient data capture and processing.

Chapter 4 explores the effect that initial surface roughness has on the acoustic emission response generated by the tribological contact whilst operated in boundary lubrication conditions. In total, eight different initial surface roughnesses were used to investigate what effect this would have on acoustic emissions.

Chapter 5 presents the data gathered when investigating the acoustic emission response generated during MoDTC tribofilm formation and removal. Raman spectroscopy was used to confirm the formation of a MoDTC based tribofilm.

Chapter 6 presents the data gathered when investigating the acoustic emission response to ZDDP tribofilm formation and removal. SEM and EDX analysis was used to confirm the formation of a ZDDP tribofilm.

Chapter 7 discusses the main findings of the experiments conducted in this work. Comparisons between data sets and justifications of findings is also reported. Finally, a conclusion and suggestions of future work are presented in Chapter 8.

Chapter 2

Methodologies

2.1 High Speed Pin-on-Disk Tribometer

As previously discussed, both friction and wear occur when two or more interfaces come into contact. Often, these faces have complex geometries and the wear occurs over a large time frame, typically hundreds of thousands of cycles. It is therefore, very difficult to replicate the exact environment in the laboratory when investigating the cause of the wear. In order to overcome the need for bespoke equipment for every test and extended testing time frames, laboratory bench tribometers are used. All tribological tests in this work were conducted using a High Speed Pin-On-Disk (HSPOD) tribometer (Denison T62), shown in Figure 2.1, under unidirectional sliding conditions at a temperature of 100 °C.

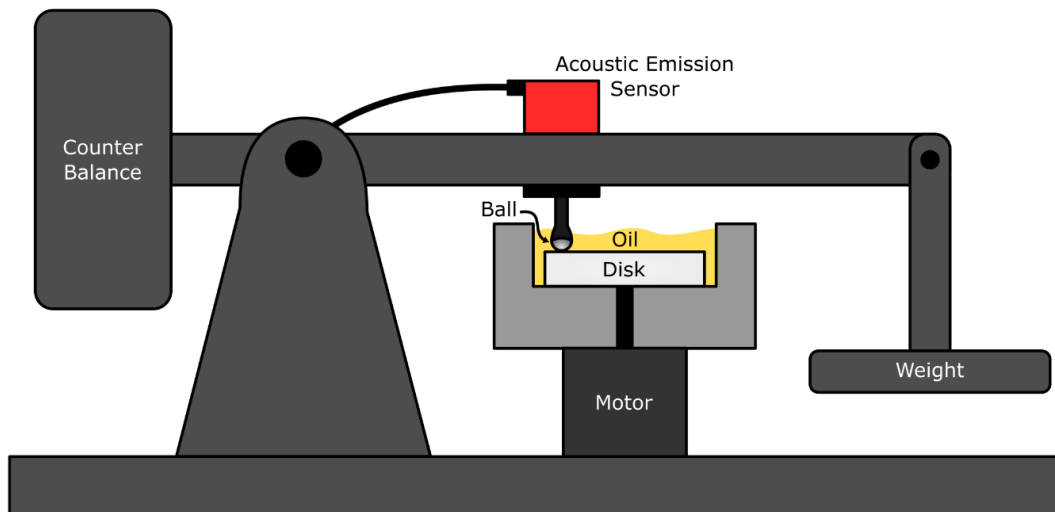


Figure 2.1 - Schematic diagram of HSPOD tribometer and acoustic emission sensor.

The sample disk is secured to a rotating platform which is submerged in an oil reservoir, the disk can then be rotated from beneath via an electric DC motor. The counterface is provided by a ball bearing that is attached to the loading arm via a ball holder. The load is applied through a dead weight suspended from a cantilever arm. The temperature of the test is controlled through heaters placed within the reservoir.

Prior to testing, all components that come into contact with the test oil are ultrasonically cleaned in acetone for fifteen minutes in order to remove contaminants.

The tribotest conditions used throughout this work can be seen in Table 2.

Table 2 - Test conditions used in tribotests throughout this work.

Test Condition	Parameters
Base oil	Polyalphaolefin
Additive Concentration	0.1 wt% MoDTC, 0.55 wt% ZDDP
Temperature	100 °C
Contact Pressure	2.29 GPa
Sliding Speed	1000 RPM (1.75 ms ⁻¹)
Test Duration	5 – 180 minutes
Material	Disk: AISI 1074, Ball: AISI 52100
Hardness	Disk: 60-64 HRC, Ball: 60-67 HRC
Young's Modulus	190-210 GPa (ball and disk)
Roughness	Disk: R _a = 110 nm, Ball: R _a = 10 nm
Lambda Ratio (λ)	0.12-1.29

2.2 Materials

Steel thrust washers (Simply Bearings Ltd.) were used as the testing specimens in this work, they have a thickness of 1mm and inner and outer diameters of 25 mm and 42 mm respectively. The thrust washers are made from AISI 1074 spring steel with a Rockwell hardness of 60 – 64 HRC and a nominal surface roughness, R_a of ~100 nm. The counterface for this work is provided by AISI 52100 6.5 mm diameter steel ball bearings (Simply Bearings Ltd.), the hardness of the ball bearings is 60 – 67 HRC and they have a nominal surface roughness, R_a of 10 nm.

2.2.1 Poly Alpha Olefin (PAO) base stock

Synthetic oil base stocks of PAO provided by Afton Chemicals was used throughout this work. PAO is a high performance base stock that is used in

many industrial and automotive lubricant applications. Typically, PAO has the properties listed in Table 3 below.

Table 3 – Typical properties of PAO. Taken from (Mortier et al., 2010)

Property	Value
Visual Appearance	Transparent Liquid
Pour Point	-68 °C
Flash Point	226 °C
Viscosity index	122
Viscosity at 40°C	0.1267 Pa.s
Viscosity at 100 °C	0.0026 Pa.s

2.2.2 Lubricant Additives

All additive containing lubricants used consist of a base stock of PAO blended with the relevant additive. For MoDTC additive tests the ‘raw’ MoDTC additive was blended with the PAO base stock in the university prior to testing. Whereas, for ZDDP tests a pre-formulated blend of 0.55wt% ZDDP was acquired from Afton Chemicals.

2.2.3 Acoustic Emission Sensor

A WS α 100-1000 KHz wideband AE sensor (Physical Acoustics) was used throughout this work. The WS α sensor was chosen due to its relatively small size, dimensions shown below in Figure 2.2, and also the flat frequency response of the sensor, shown in red in Figure 2.3.

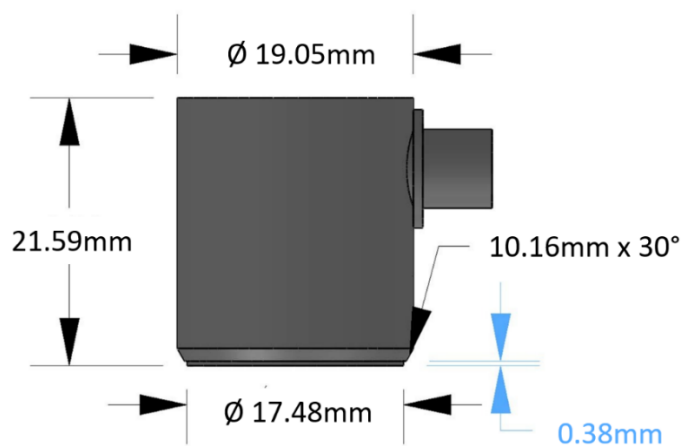


Figure 2.2 - Schematic showing the dimensions of the WS α sensor. Adapted from Physical Acoustics (2019).

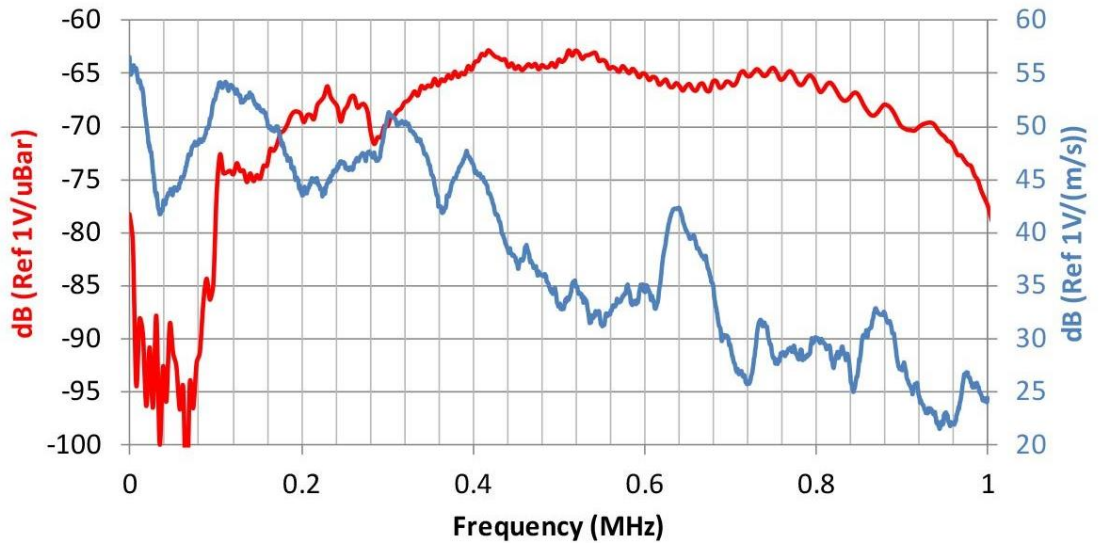


Figure 2.3 - Frequency response of WSA sensor. Taken from Physical Acoustics (2019)

A wideband and flat frequency response, as can be seen in red in Figure 2.3, is desirable for experimental applications where the exact frequency of the acoustic emission source is not known (Vallen Systeme GmbH, 2017). A flat frequency response ensures that the sensor is equally sensitive to all frequencies across its measuring range (100 – 1000 kHz) and that the amplitude of no frequencies will be exaggerated or reduced.

2.2.4 Sample Polishing

Whilst the standard thrust washers purchased from Simply Bearings Ltd have a surface roughness, R_a , of 110 nm it was necessary to perform a range of grinding and polishing steps to the disks so that a range of surface roughnesses could be tested.

A Buehler Beta Grinder-Polisher was used with a range of grinding and polishing papers to produce different surface roughnesses for test disks. Silicon Carbide abrasive paper disks (MetPrep) ranging in roughness from P120-P1200 where used for the grinding of test samples, with roughness decreasing as the P values increases. Diamond suspensions of 9 μm and 0.25 μm (Kemet International Ltd.) were used in conjunction with a MicroFloc polishing cloth (Buehler Test and Measurement GmbH) for the final polishing of the sample disks.

All grinding and polishing steps were performed by hand at a speed of 300 RPM and a load of ~ 10 N. Sample disks were secured to a bespoke holder

which ensured equal load distribution across the sample disk throughout the polishing process.

Polished samples were categorised by the grade of the last grinding paper used on that sample, for example a disk labelled SF-120 was last ground using a P120 grinding paper. Depending upon the desired finish, sample disks were subject to up to 5 sequential grinding/polishing operations. Table 4 shows the grinding and polishing operations performed on each sample disk.

Table 4 - List of grinding/polishing operations performed on sample disks depending on desired final surface finish.

		Grinding paper grade						
		P120	P320	P600	P800	P1200	MicroFloc + 9µm Suspension	MicroFloc + 0.25µm Suspension
Sample Finish	SF-120	X						
	SF-320		X					
	SF-600			X				
	SF-800			X	X			
	SF-1200			X	X	X		
	SF-9µm			X	X	X	X	
	SF-0.25µm			X	X	X	X	X

Once each sample had been produced the initial surface roughness was measured using a contact profilometer, the methodology of which will be discussed in Section 2.3.1. This showed that by performing the sample preparations as described in Table 4 a wide range of surface roughnesses can be achieved, this is shown below in Figure 2.4. The roughest sample, SF-120, has an initial R_a surface roughness of 240 nm. Comparatively, the smoothest sample, SF-0.25µm, has an initial surface roughness of only 5.6 nm.

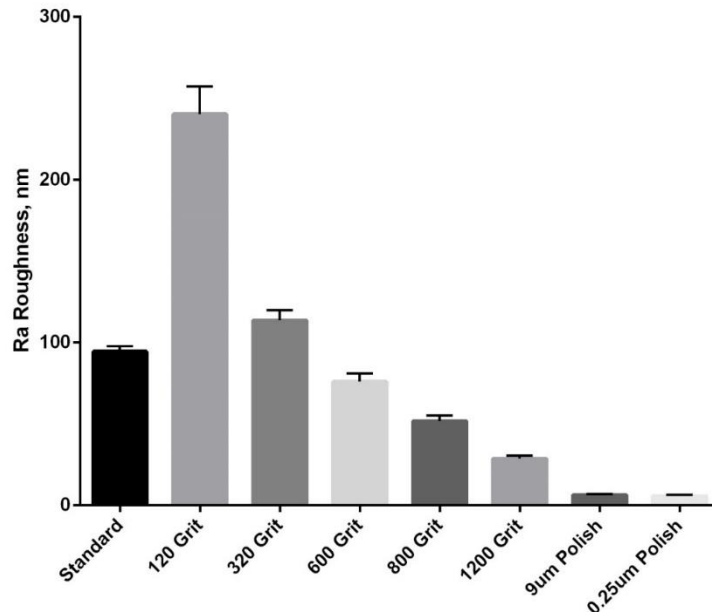


Figure 2.4 - Surface roughness, R_a , values of test disks depending upon grade of final polish.

Equation 3 (Page 4) shows the formula for calculating the lambda ratio and it can be seen that the surface roughness of the samples has a direct impact on the lambda ratio of the contact and as such the lubrication regime in which the test operates. Figure 2.5 shows just how drastically the initial surface roughness can affect the lambda ratio in which the tribotests operate. For the sample with the largest initial surface roughness, SF-120, the lambda ratio is 0.12. However, for the smoothest sample, SF-0.25 μ m, the lambda ratio is 1.29 and as previously discussed in Chapter 1 lambda ratios above 1 indicate a mixed lubrication regime rather than boundary lubrication.

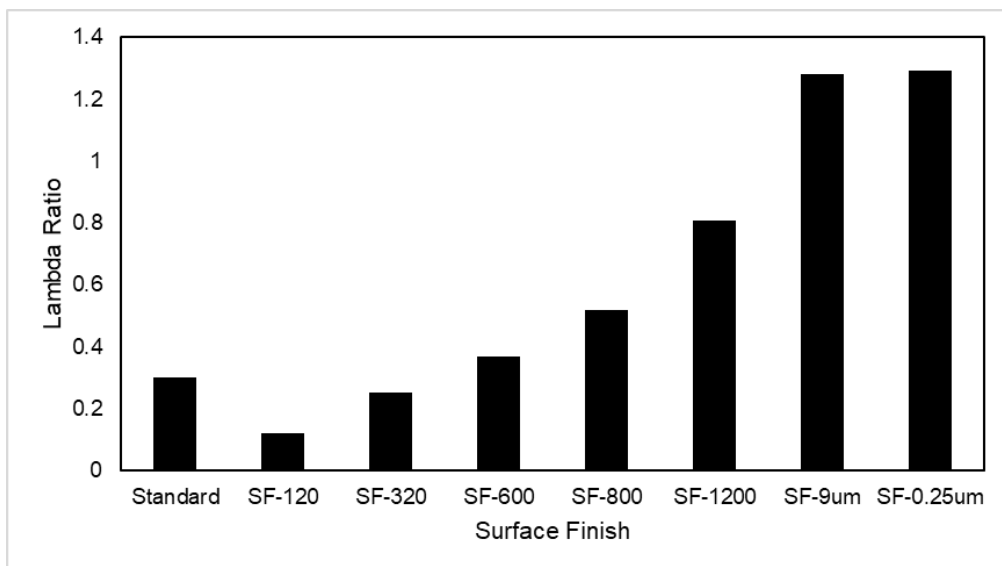


Figure 2.5 - Calculated lambda ratio dependent upon initial surface roughness.

2.3 Surface Analysis

2.3.1 Contact Profilometry

As previously discussed in Chapter 1, contact profilometry is a useful method that can be used to measure the surface roughness of a sample. In this work a form talysurf line profilometer (Taylor Hobson) was used to measure the surface roughness, R_a of disk specimens both before and after tribotests. The profilometer in this work is fitted with a 2 μm tip radius diamond conisphere probe, in line with ISO 3274. A 2 μm probe was chosen as it is key when measuring the surface finish of a sample to use a measuring probe with the smallest tip radius feasible so that no surface features are overlooked.

To avoid contamination of the measurement tip all samples were rinsed in acetone using an ultrasonic bath prior to measurement.

2.3.2 White Light Interferometry

An NPFlex white light interferometer (Bruker) was used throughout this work to produce 3D maps of sample surfaces both pre- and post-test. This allows for a clear visualisation of the effect that tribotests have on the sample surface. In order to eliminate any adverse reflections from tribofilms or residue lubricant prior to any measurements, samples were rinsed in acetone using an ultrasonic bath.

2.3.3 Optical Microscopy

A Leica DM600M optical microscope was used to take optical micrographs of sample surface pre- and post-test. Built in analytical functions allow for the measurement of wear scar diameters on the ball which can then be used to calculate a wear volume loss using the following equation.

$$\text{Volume Loss} = \pi \frac{WSD^4}{64D}$$

Equation 5 - Volume Loss equation.

Where:

WSD = Wear Scar Diameter

D = Ball Diameter

2.4 Tribofilm Analysis

2.4.1 Raman Spectroscopy

Raman spectroscopy analysis was used to determine the presence of MoS₂ and related reaction products formed during tribotests. After tests, samples were rinsed in heptane in an ultrasonic bath prior to Raman analysis. As discussed by Khaemba et al. (2016) Raman analysis can be performed on un-rinsed samples, however by rinsing the samples with heptane a better signal of the MoDTC decomposition products can be observed.

Raman analysis was conducted using a Renishaw InVia spectrometer (UK). The spectrometer has a spectral resolution of 1 cm⁻¹ and a lateral resolution of 800 nm. Raman spectra were acquired with an Olympus 50x objective with a numerical aperture (N.A) of 0.75 in a backscattering configuration. All spectra were obtained using a 488 nm wavelength laser at 1 mW laser power with 1 second exposure time. Ten accumulations were obtained in order to increase the signal to noise ratio (Khaemba et al., 2016). The Raman parameters used throughout this work were selected as Khaemba et al. (2015) had previously shown that they produced no laser damage to MoDTC tribofilms.

2.4.2 Scanning Electron Microscopy + EDX Analysis

Energy dispersive X-ray analysis was used to determine the presence of a ZDDP tribofilm, through the detection of Zn and P atoms, post-test. Similarly to the sample preparation prior to Raman analysis, samples were rinsed in heptane in an ultrasonic bath prior to EDX analysis. As ZDDP forms a tenacious tribofilm the heptane does not affect it, it does however remove residue oil from the surface (Morina and Neville, 2007a).

SEM images were collected and EDX analysis was conducted using a Hitachi TM303plus benchtop SEM fitted with an Oxford Instruments Aztec EDX detector.

Chapter 3

Development of Bespoke Data Acquisition System

Commercial data acquisition systems are available for the measurement and monitoring of acoustic emission signals. Unfortunately, the commercial system that was originally available at The University of Leeds (Vallen Systeme AMSY-6) did not satisfy specific needs required for this work.

The AMSY-6 system does not offer the flexibility that a bespoke system offers, additionally the commercial system only provided very rigid filters for the signal and as the work being conducted is novel it was not known what filters would be necessary in advance.

It was therefore decided that the best approach to the data acquisition throughout this work was through a bespoke LabVIEW based acquisition system. This system would be scalable, flexible and capable of continuous monitoring. The challenges associated with creating a data acquisition system are discussed below.

3.1 Data Acquisition

3.1.1 Sampling Speed

When using data acquisition systems, it is important that the signal is sampled at an appropriate rate. To determine the minimum sampling frequency that should be used the Nyquist sampling theorem is used. This theorem explains the relationship between the frequency of the measured signal and the sampling rate (Nyquist, 1928). It is stated that the sample rate, f_s , must be at least two times greater than the highest frequency component of interest in the measured signal, the Nyquist frequency, f_N (National Instruments, 2019a).

$$f_s > 2f_N$$

Equation 6 - The sample rate must be greater than two times the Nyquist frequency

Sampling an acquired signal below f_s can lead to detrimental problems with the measurement. The various problems that arise are discussed below.

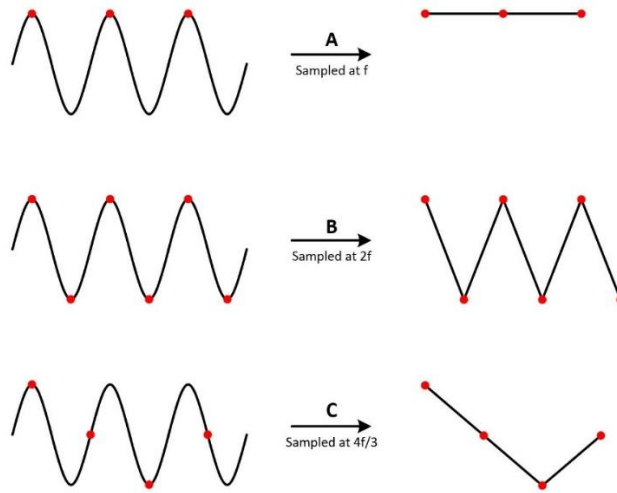


Figure 3.1 - Image displaying the detrimental effects caused by too low a sample rate. The input signal is shown on the left with the measured signal shown on the right hand side. Taken from National Instruments (2019a).

Figure 3.1 shows graphically how the sample rate affects the resultant signal, three different sampling rates are shown. For case A, the signal of frequency f is sampled at that same frequency. On the right hand side it can be seen that sampling at this rate distorts the signal into appearing as a constant value. For case B, the signal is now sampled twice as quickly, at a rate of $2f$. This sampling rate is equal to f_s as previously defined, and as such the highest frequency component of the signal is captured and no aliasing occurs. Finally, for case C, the signal is sampled at $4f/3$ this is below the f_s and as such aliasing occurs and the distorted signal shown on the right hand side is recorded.

Aliasing occurs if a signal is sampled at a rate that is smaller than twice the Nyquist frequency, this causes false lower frequency components to appear in the sampled data (National Instruments, 2019a).

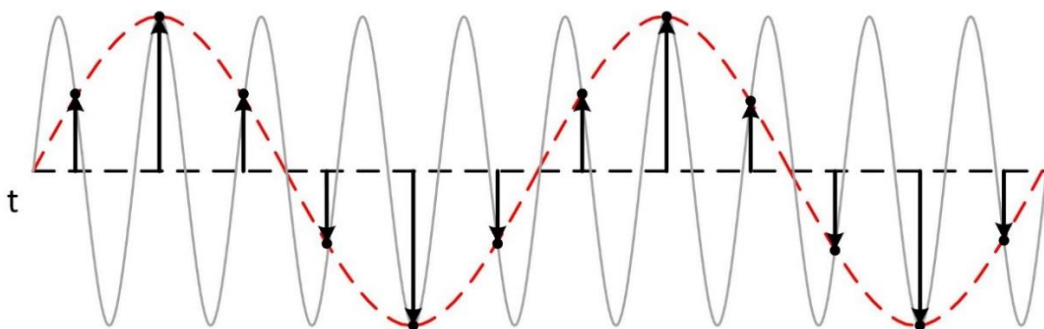


Figure 3.2 - Image showing the resultant sampled signal when an 800 kHz signal is sampled at 1 MS/s. Taken from National Instruments (2019a).

Figure 3.2 demonstrates the aliasing that occurs when an 800 kHz signal is sampled at 1 MS/s. The dotted red line indicates the aliased signal, the effect

of which causes the appearance of a 200 kHz sine wave that is non-existent in the original signal. It is clear the problems that would be faced if aliasing occurred in an experimental setting.

3.1.2 Signal Strength

The signal produced by acoustic emission sensors is very small in magnitude; much too small to be measured at a high enough resolution by most data acquisition systems. As such, pre-amplifiers are commonly used in these applications. Pre-amplifiers are electronic circuits that amplify the measured signal prior to sampling.

Pre-amplifiers often use decibels, dB, to indicate the increase in signal magnitude. Decibels are logarithmic units used to express the ratio of two values, in this case an input and output voltage. Decibels can be calculated using the equation below.

$$A[dB] = 20 \log \left(\frac{V_o}{V_i} \right)$$

Equation 7 - Equation used to calculate the amplitude of the signal in decibels where V_o is the output voltage and V_i is the input voltage.

Pre-amplifiers often have a set value or range of values by which they can increase the signal, for example an AEP4H pre-amplifier produced by Vallen Systeme GmbH can either have a value of 34 dB or 40 dB.

Due to the logarithmic nature of decibels the fold increase in a signal can be dramatic. A 34 dB amplification corresponds to approximately a 50 fold increase in input voltage whereas a 40 dB amplification corresponds to approximately a 100 fold increase in input voltage.

In this work a 40 dB AEP4H pre-amplifier (Vallen Systeme GmbH) was used, providing a sufficient increase in the acoustic emission signal magnitude.

3.2 Signal Processing

As previously discussed acoustic emission measurements require high-speed data capture to ensure that the signal is not aliased and no erroneous data is produced when sampling. With a correctly sampled amplified signal, the question that remains is how to correctly analyse the acquired signal.

The acquired signal consists of a time domain and a frequency domain, it is important that when analysing the data that both domains are considered as some information such as the frequency of the signal being measured is only present in one of the domains.

The time domain represents how the signal values change over the duration of the test whereas the frequency domain indicates what frequencies are present in the signal at any given time point.

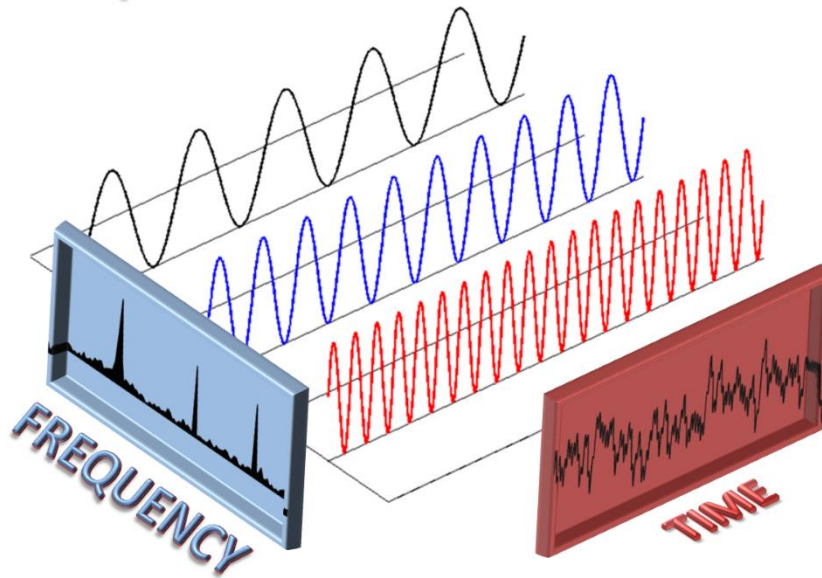


Figure 3.3 - Image showing how the signal information is represented in both the frequency and time domain. Taken from G. Kalhara et al. (2017).

Figure 3.3 shows how a signal comprised of 3 sine waves appears in both the time and frequency domains. It is clear from the image how important analysing both domains is as key information may be hidden in these domains.

3.2.1 Time Domain

As previously discussed in Section 1.4.1.1 there are a range of different measurement parameters that can be utilised when using acoustic emission. The parameters mentioned in Section 1.4.1.1 , absolute energy, hit count and RMS, are all time domain parameters in that they are used to analyse the acoustic emission signal with respect to time.

Generally, acoustic emission signals can be separated into two categories: burst emissions and continuous emissions (Benabdallah and Aguilar, 2008). Continuous emissions are however still comprised of individual burst events, as shown in Figure 3.4.

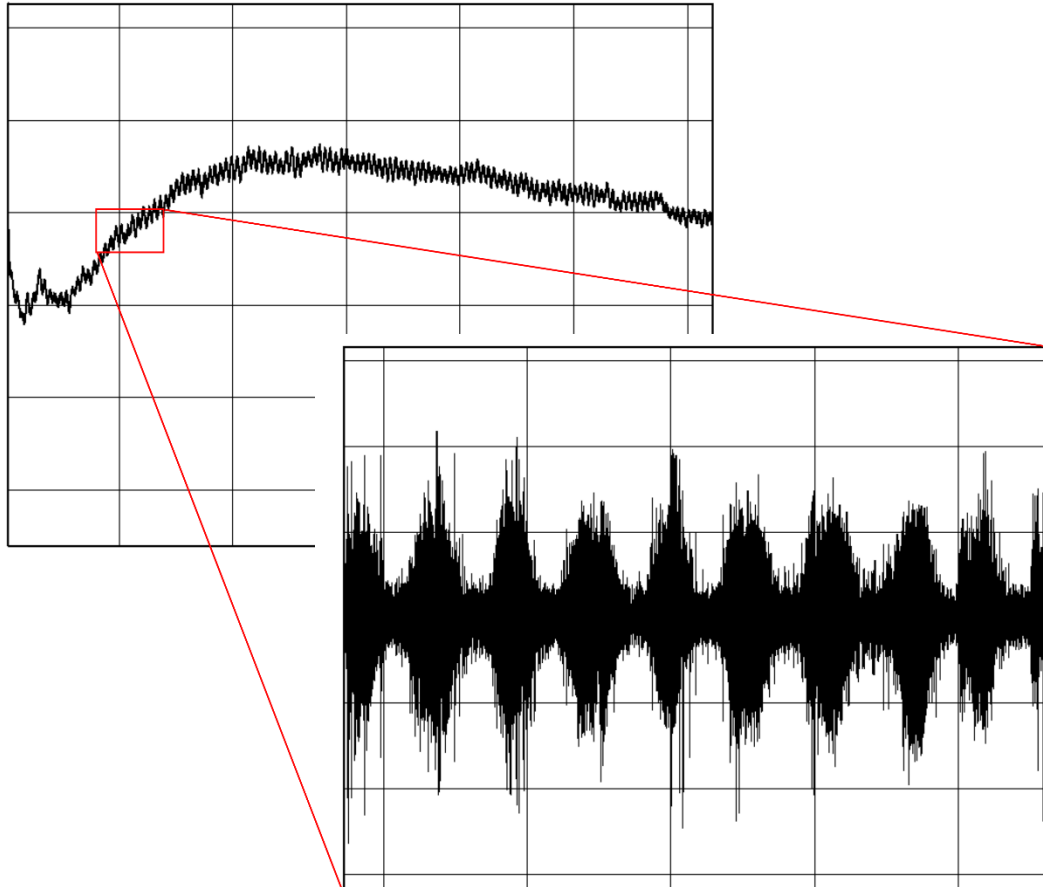


Figure 3.4 – Diagram depicting continuous signal comprised of individual burst events, AE traces from an experiment conducted throughout this work.

The most common measurements used for burst emissions are known as hits or counts, which consist of counting the number of times the AE signal crosses a pre-set trigger or threshold value. Measurements of the arithmetic average also known RMS voltage are generally used to quantify continuous emissions (Lingard et al., 1993).

3.2.2 Frequency Domain

There are many different methods of exploring the frequency domain of a signal, one of the most common methods is through the use of Fourier transforms. The Fourier transform is a complex mathematical function that can be used to essentially break a signal down into its component parts i.e. sine waves of different amplitudes and frequencies (National Instruments, 2019b), the equation for which can be seen below.

Equation 8 - Fourier Transform

$$X_k = \sum_{n=0}^{N-1} x_n e^{-i2\pi k \frac{n}{N}}$$

Where:

X_k = Spectrum of x at frequency k

N = number of time samples

X_n = input signal amplitude

k = frequency

The Fast Fourier Transform (FFT) is a computationally efficient method for performing the Fourier transform on a signal (Li, 2002).

There are other techniques available when analysing the frequency domain of a signal such as Short-term Fourier transforms (STFT) and wavelet transforms. Both STFT's and wavelet transforms can be used to analyse the frequency components of a signal as they change over time.

Simplistically, STFT's are composed of multiple FFT's where the window function is moved through the time domain, this allows the frequency components of the signal to be visualised as they change with respect to time.

Wavelet transforms, whilst being composed from a different mathematical function to FFT's, contain similar information to STFT's in that the way in which the frequency of a signal changes over time can be visualised.

This work investigates for the first time the effect that lubricant additives have on the acoustic emission response of a steel on steel tribocontact using a bespoke data acquisition system developed by the author. As such only FFT analysis was performed on the acoustic emission signal, this allowed the scope of this work to focus on the development of the acquisition system and tribological experimentation without the additional complexities associated with more in depth frequency analysis.

As the measured signal is broken down into its corresponding sum of sine waves it is possible to see at which frequencies the amplitude is highest. This allows troubleshooting of the signal such as noise removal as well as in depth analysis such as comparisons between the amplitude of frequencies at key points within a test.

The problem with continuous data such as an acoustic emission signal is that the signal is interpreted by the FFT as one period of a periodic signal. For the FFT both the frequency and the time domain are circular topologies, so both endpoints of the time waveform are interpreted as though they are connected (National Instruments, 2019b). In this instance, discontinuities show in the FFT as high frequency components not present in the original signal. High frequency discontinuities are often higher than the Nyquist frequency and as such are aliased between zero and half of the sampling rate (National Instruments, 2019a). Therefore, the spectrum shown from a FFT is a smeared version of the actual spectrum where it looks as if the energy at one frequency has spread into other frequencies, this is known as spectral leakage (National Instruments, 2019b).

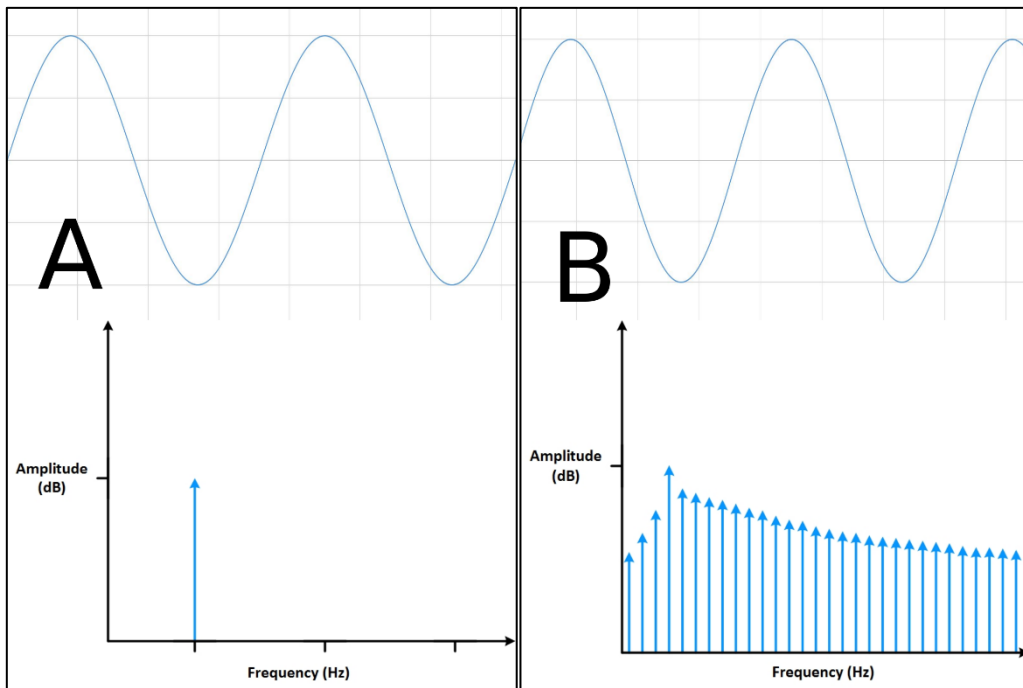


Figure 3.5 - Image showing spectral leakage caused by high frequency discontinuities. A) shows the ideal case whereas B) shows dramatic spectral leakage. Adapted from National Instruments (2019b).

Figure 3.5 indicates the problems that are caused by spectral leakage, even though signals A and B have the same frequency and amplitude sample B is not an integer period so discontinuities arise at the start and end points causing spectral leakage.

Spectral leakage cannot be completely removed but it can be mitigated through the use of windowing. Windowing is a method whereby the signal is

encapsulated and the amplitudes of the end points are both gradually reduced to zero, this can be seen in Figure 3.6.

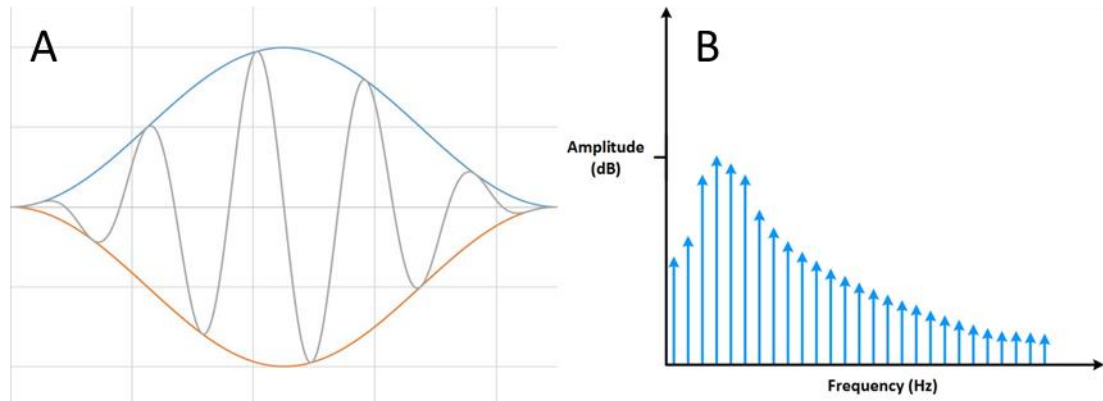


Figure 3.6 - The effects of windowing during performing a FFT. A) shows the window placed around the signal and B) shows the resultant frequency spectrum with reduced spectral leakage. Adapted from National Instruments (2019b).

It can be seen that the resultant spectrum in Figure 3.6B shows much less spectral leakage compared to that in Figure 3.5B, this is shown by the more defined peak amplitude and increased suppression of the surrounding frequencies.

There are multiple different windowing types each with their own advantages and disadvantages. However, in order to focus this work on tribochemistry and not signal processing the pros and cons of each windowing type will not be discussed. In this work a Hanning window was used as it has good frequency resolution and reduced spectral leakage (National Instruments, 2019b), it also has very quick processing speeds which is very useful in this work. The shape of the Hanning window is shown in Figure 3.6A.

3.3 LabVIEW Framework

LabVIEW is National Instruments' development environment that is "designed specifically to accelerate the productivity of engineers" (National Instruments, 2019c). LabVIEW uses a graphical programming interface that allows users to visualise exactly what sort of engineering system they require; no coding skills are necessary but can be implemented if desired. Figure 3.7 below demonstrates this graphical interface by showing how simple addition is performed in the program.

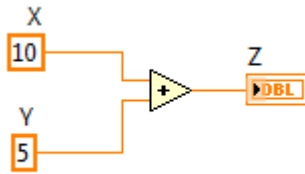


Figure 3.7 - The addition of two numbers as performed in the graphical interface of LabVIEW.

There is a large number of different programming architectures that can be utilised in LabVIEW. The three fundamental designs that are used and expanded upon in this work are the State Machine, Event Handler and Producer/Consumer. The basics of these three fundamental design patterns will be shown below.

3.3.1 State Machine

A State Machine is used in applications where distinguishable states exist. Each state can lead to one or multiple further states, each state can also end the process flow. A state machine requires either in-state calculation or user input to determine which state to transition to.

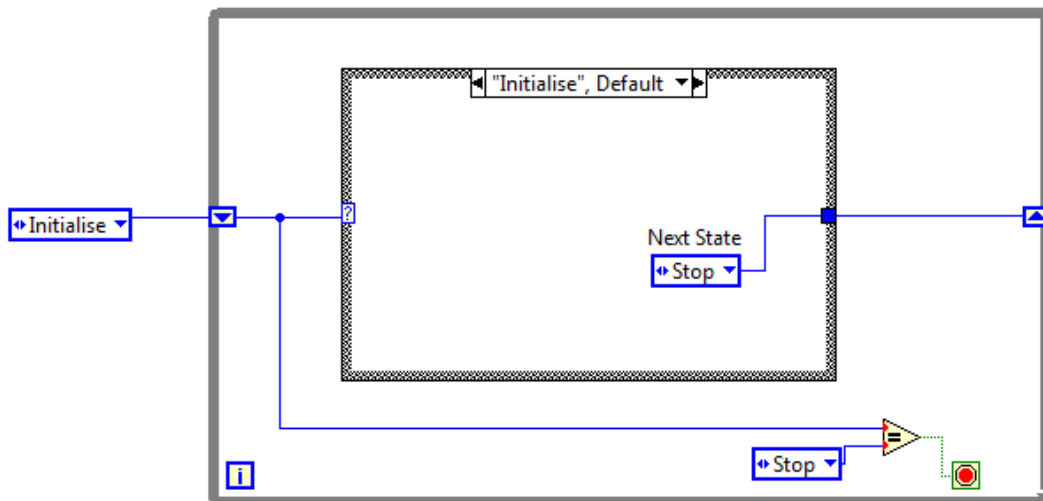


Figure 3.8 - Example of a basic state machine.

It can be seen in Figure 3.8 how state machine architecture can be utilised in LabVIEW. It can be seen that the initial state is Initialise and that inside the internal case structure the next state will be Stop. This is obviously a redundant piece of code but it does highlight the importance of state machines and what

they could be used for. For example, a user could use different states to determine the order in which other, more complicated code is executed.

3.3.2 Event Handler

The event handler architecture is an efficient way to deal with user interactions. The Event Handler is to be used for detecting when events occur on the user interface such as moving/clicking the mouse, changing the value of a control or pressing a key.

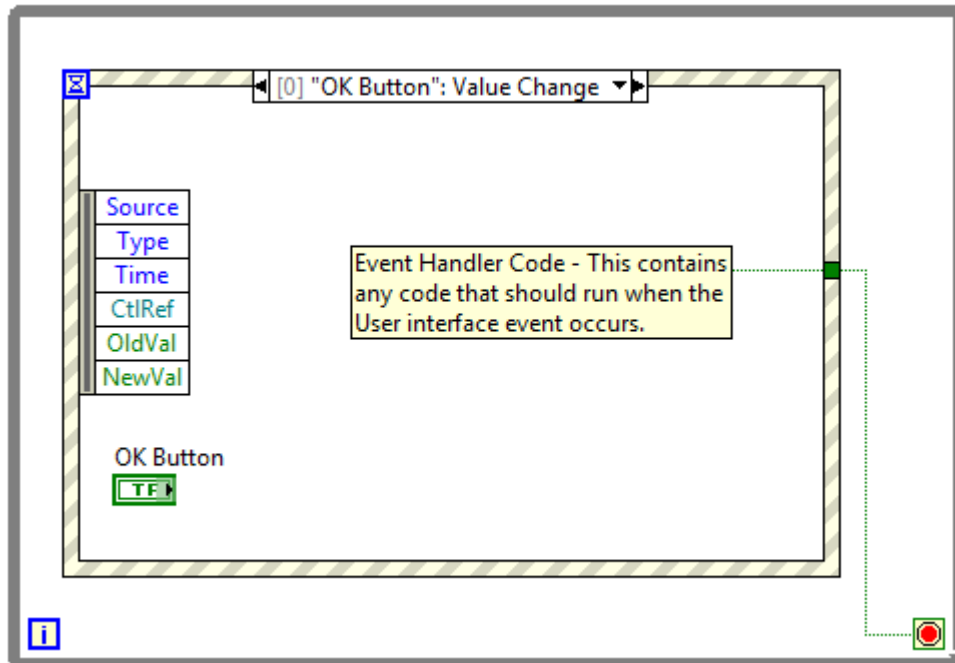


Figure 3.9 - Example of a basic event handler.

Figure 3.9 shows the basics of an Event Handler, in this case the 'event' is the change in value of the Boolean OK button. When the button is pressed an assortment of code would then be executed as long as it is within the confines of the Event Handler bounding box. It is evident even from this basic example the power that an Event Handler has within a system.

3.3.3 Producer/Consumer

The Producer/Consumer architecture is used when data needs to be shared between parallel loops that are running at different rates. As the name suggests, the architecture is comprised of two categories of loops, a producer and a consumer. This architecture uses data queues to communicate between the loops and allow data buffering.

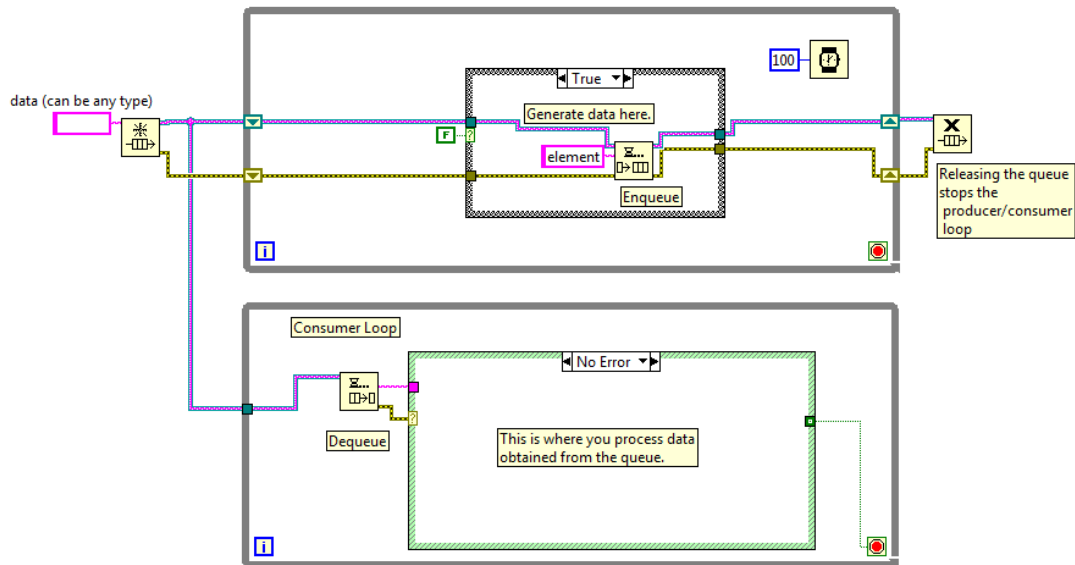


Figure 3.10 - Example of a basic producer/consumer structure.

Figure 3.10 shows a basic Producer/consumer structure, the top loop acts as the producer and is where data is generated and then added to a queue. The bottom loop then de-queues this data to then process it. The use of queues allows data to be buffered and ensures that no data is overwritten or missed.

3.3.4 Queued Message Handler (QMH)

Three fundamental LabVIEW architectures have been discussed as a primer to the actual architecture that is used in this current work and will be used in future work. The architecture that is used is called a Queued Message Handler (QMH). It joins together aspects from all three previously discussed designs to create a highly efficient and robust architecture.

Figure 3.11 shows the basic QMH template from LabVIEW 2013. The top loop is the Producer loop, this contains an event structure that sends messages to the Consumer loop. The Consumer receives and processes the messages in a State Machine. A message can be triggered by either user interface events or from other states in the State Machine. A QMH can also be configured to provide feedback from the Consumer to the Producer using User Events.

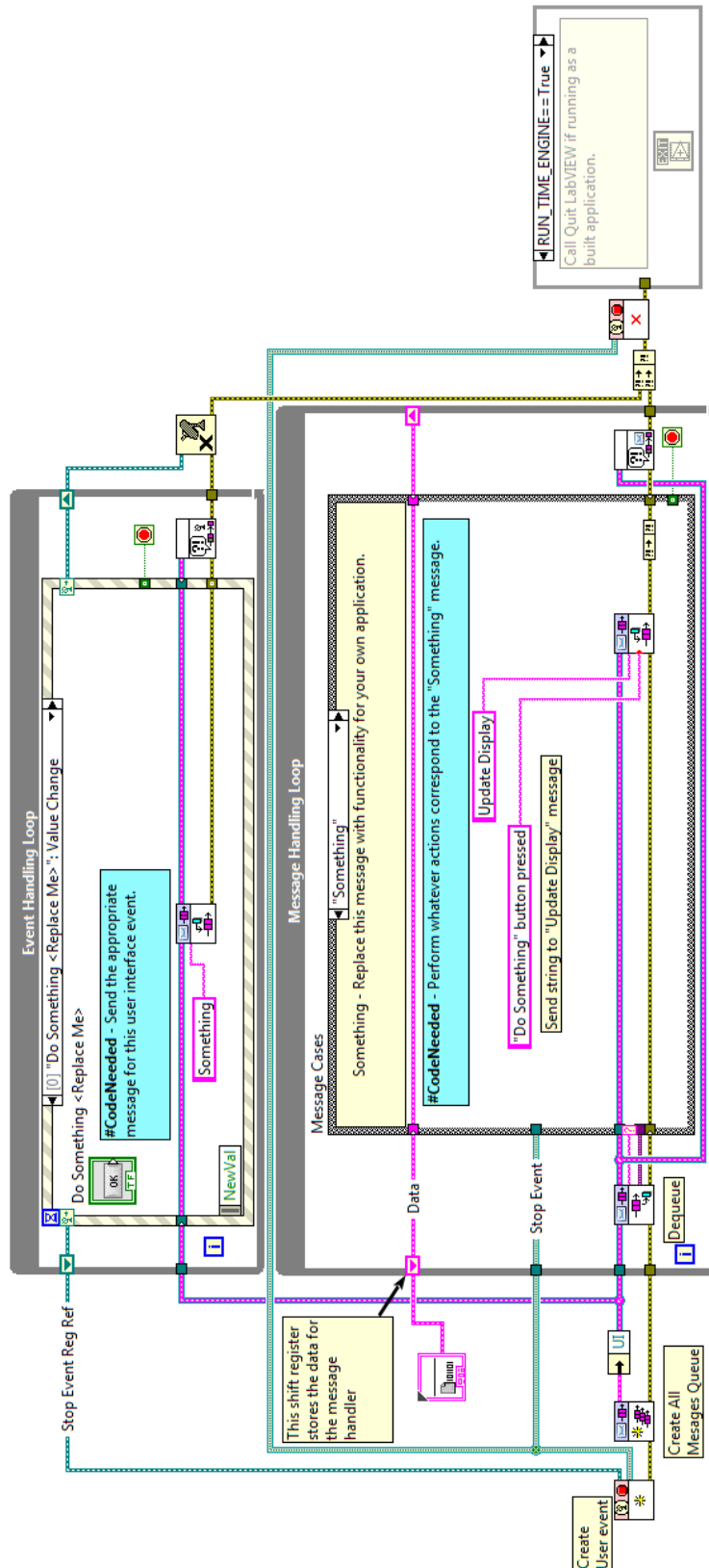


Figure 3.11 - Example of basic QMH structure taken from LabVIEW Template.

3.4 Development of QMH Architecture

The data acquisition system developed for this work uses the basic QMH architecture shown in Figure 3.11 but it is enhanced through the implementation of four additional loops which run simultaneously.

Each of the additional loops used in the QMH architecture serve a specific purpose, the functions of which are: Acquisition, Analysis, Logging and Display. Figure 3.12 shows a flowchart for the QMH architecture indicating data flow and execution order.

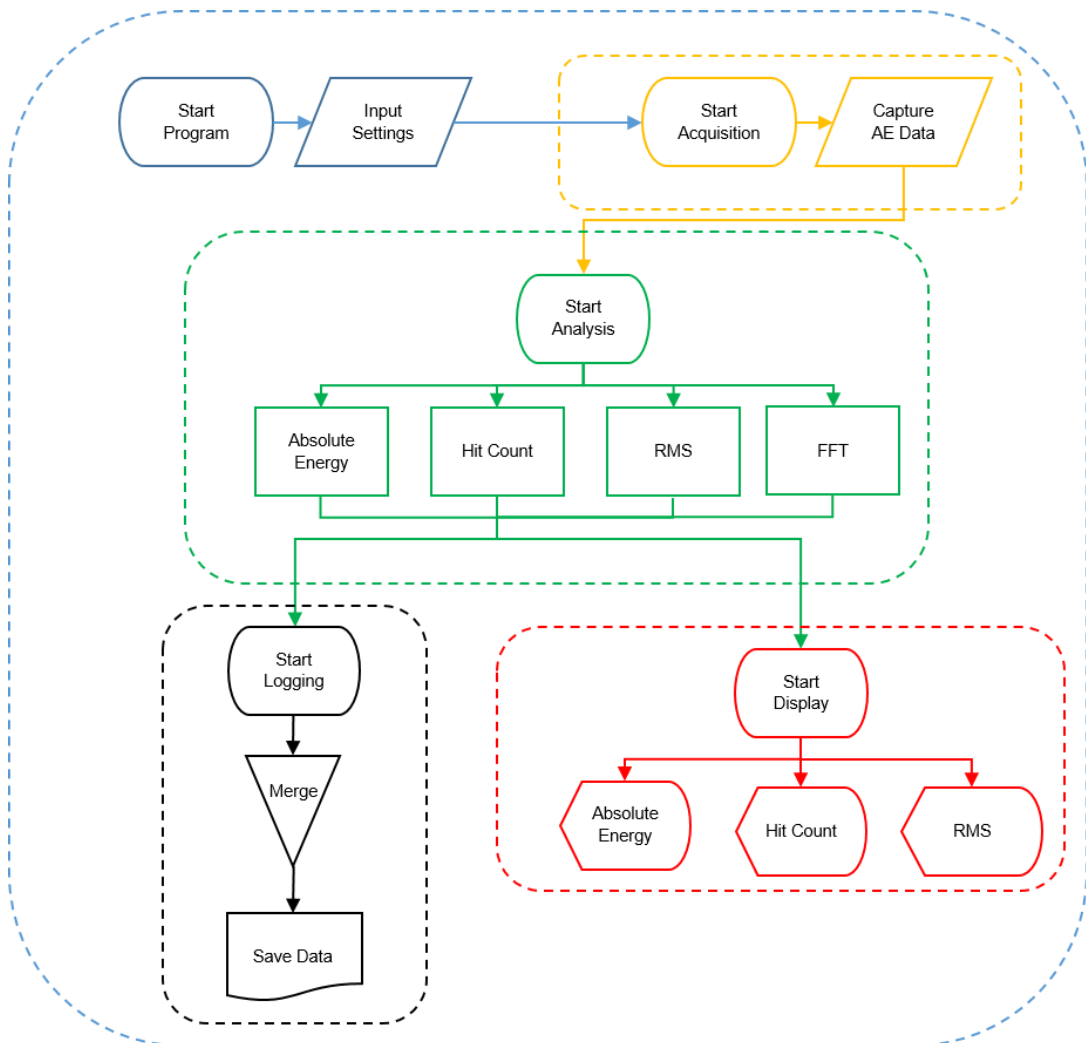


Figure 3.12 - Flowchart showing the order execution for QMH data acquisition

The functional LabVIEW block diagram for the QMH architecture can be seen in Figure 3.13.

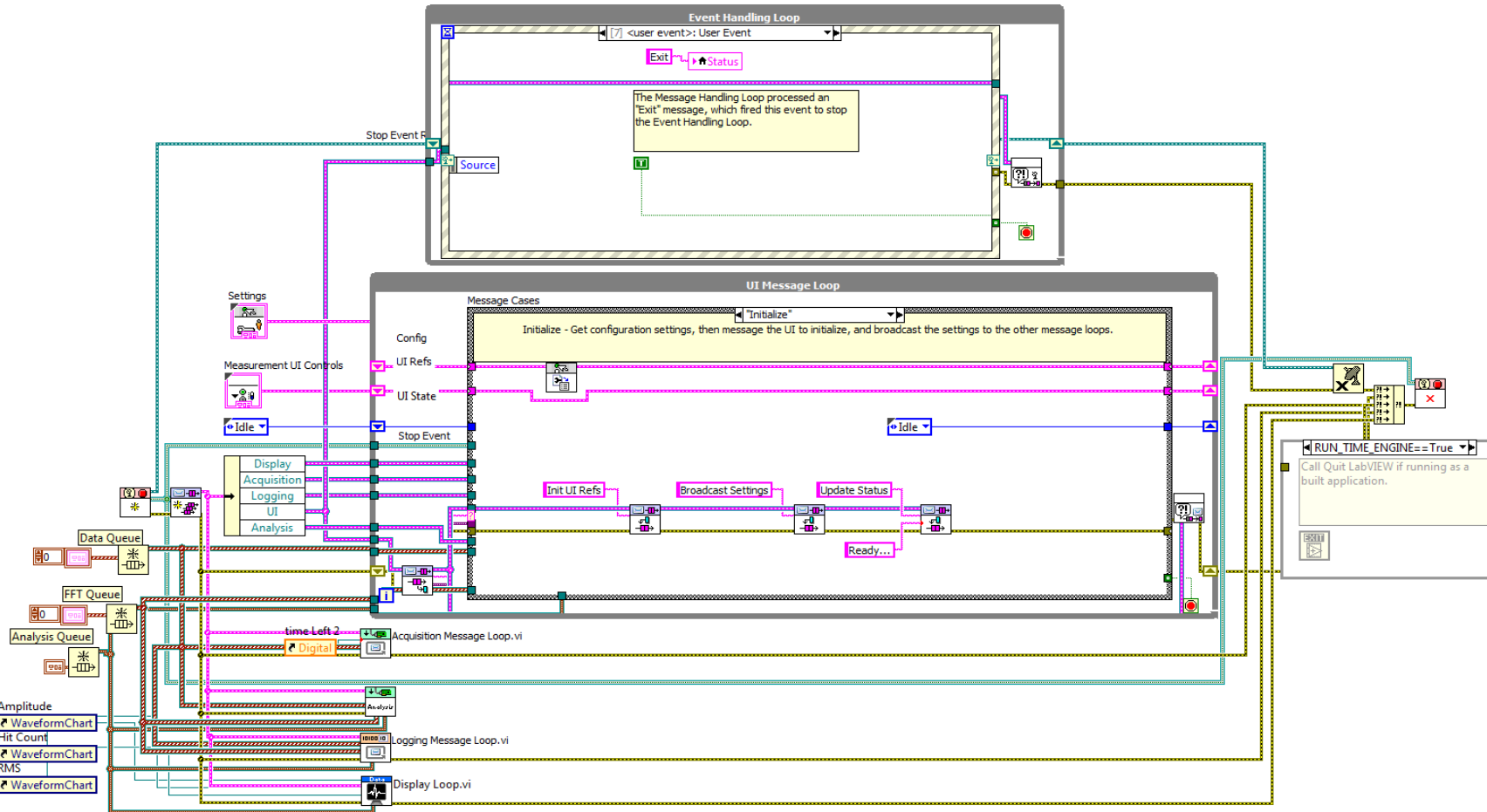


Figure 3.13 - Block diagram of the complete QMH architecture used in this work.

It can be seen that this program is much more complex than the template shown previously in Figure 3.11. This is due to the additional functionality provided by the 4 simultaneously running loops. As such, each section of the flowchart will be explained over the following pages, including the block diagrams of each loop at each stage.

Initially when the user starts the program they are faced with graphical user interface shown in Figure 3.14. From here the program can be started and both the hardware and software settings can be edited.



Figure 3.14 - Graphical user interface for QMH acquisition system.

Figure 3.15 shows the dialog box containing all of the settings required by the data acquisition system. From here key parameters such as sample rate, bandpass cut-offs and threshold values can be changed. It is in this dialog box where the file path for data logging is inserted. It is also possible to change all global settings whilst a test is running, a feature that is not possible in commercial systems

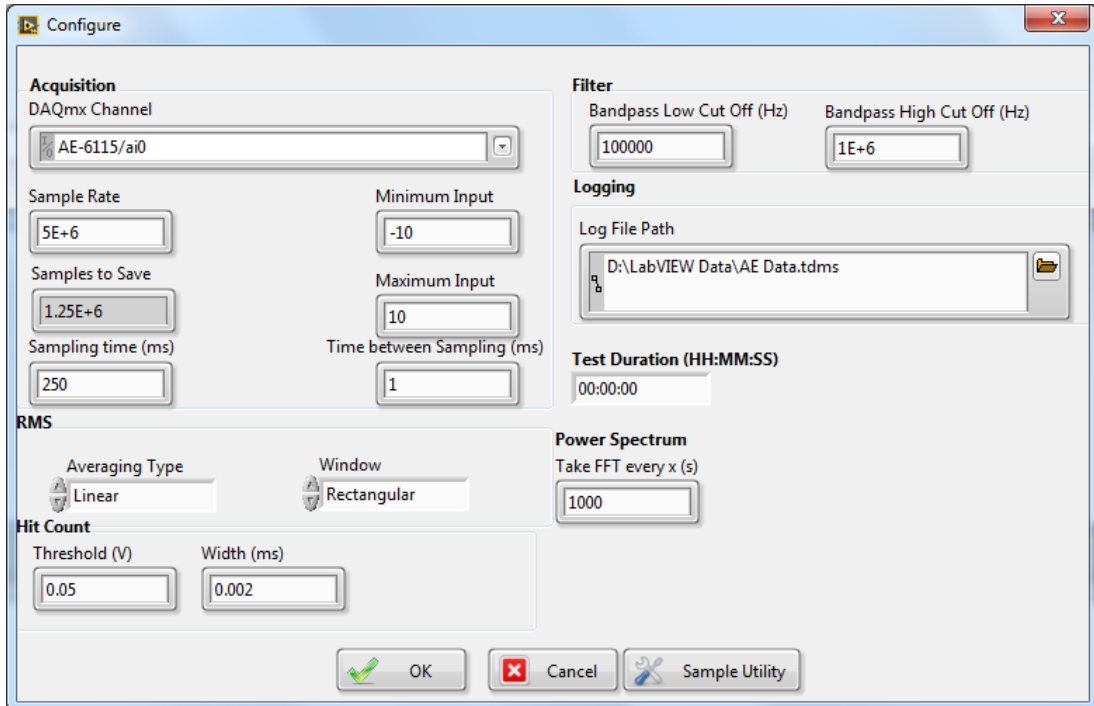


Figure 3.15 - Settings dialog that allows the user to fine tune the data acquisition parameters for each test.

3.4.1 Acquisition loop

Figure 3.16 shows the “start” state of the acquisition loop used in this work. In this loop the hardware interfaces with the software and the measurements of the raw acoustic emission signal are conducted. As per the settings, the acoustic emission signal is captured at a speed of 5 MHz. A sampling speed of 5 MHz was chosen to avoid aliasing the signal as described previously by the Nyquist equation shown in Equation 6 (Page 54).

The only data that is present in the acquisition loop is the raw signal direct from the acoustic emission sensor; from here the data is then passed to the analysis loop.

3.4.2 Analysis Loop

Figure 3.17 shows the “analyse” state of the analysis loop. In the analysis loop, raw data is taken from the acquisition loop and is then processed in order to quantify the key acoustic emission parameters: absolute energy, hit count and RMS.

To calculate the absolute energy, the raw signal is integrated for each time point as specified in the settings by the ‘Sampling time’ variable. To calculate the hit count the ‘Threshold’ and ‘Width’ variables are used to count the number

of times the raw acoustic emission signal exceeds the 'Threshold' within the 'Width' timeframe. To calculate the RMS of the acoustic emission signal, simple arithmetic is applied to the signal in order to average it. The arithmetic that is required is performed by the built in LabVIEW function 'Basic DC/RMS'. Finally, a FFT is performed on the raw data at the time interval determined by the 'Power Spectrum' variable, this provides a snapshot into the frequency domain of the signal at regular intervals during the test. Performing an FFT at different timepoints throughout the test also allows for much faster data processing as an FFT requires a lot of processing power and if one was performed continuously on each piece of data the data acquisition system would grind to a halt. Once the data has been analysed it is then passed through to both the logging loop and the data display loop.

3.4.3 Logging Loop

Figure 3.18 shows the "log" state of the logging loop. In the logging loop, the processed data is passed from the analysis loop to be stored in an appropriate format. The absolute energy, hit count and RMS values are grouped together in a single file with the FFT data stored separately, this allows both sets of data to be monitored at different rates. Both sets of data are stored as Technical Data Management Streaming (TDMS) files, TDMS data files combine the benefits of many different data storage options to provide high-speed data storage that has a small disk footprint. This means that a lot more data could be captured per test as the small storage footprint ensured that the hard drive would not reach capacity. Furthermore, the TDMS file allows high-speed storage which ensured that the data was captured much more efficiently than if other data types were used.

3.4.4 Data Display Loop

Figure 3.19 shows the "display" state of the display loop. In the display loop, the processed data is passed from the analysis loop to be displayed in real time in the user interface. Only the absolute energy, hit count and RMS values are displayed throughout the test as the FFT data is too large to display continuously and doing so would result in slowing down the system.

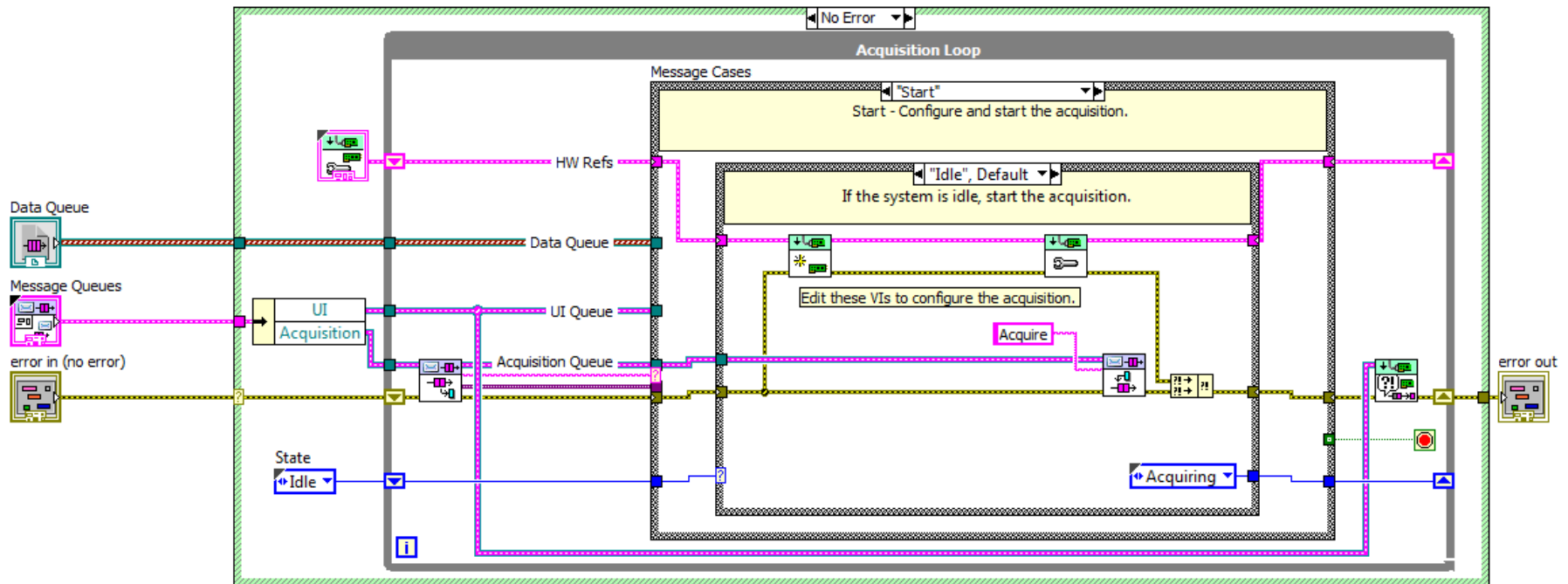


Figure 3.16 - Block diagram for Acquisition Loop.

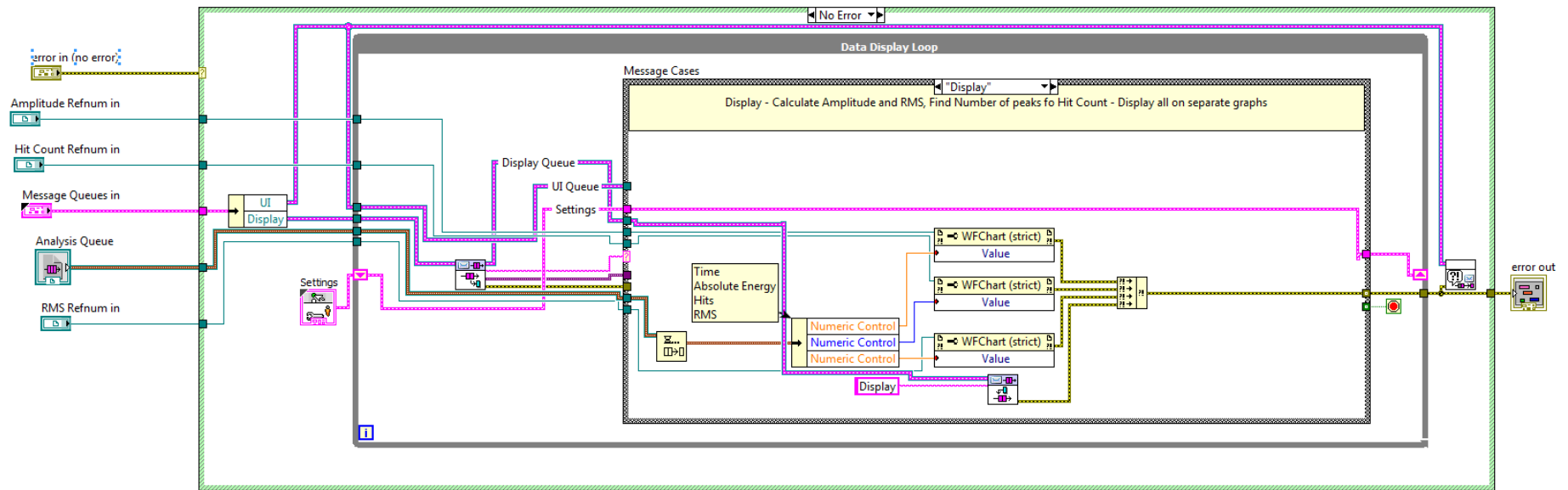


Figure 3.19 - Block diagram for Data Display Loop

3.5 Hardware Setup

In this work a PCI-6115 12 bit, 10 MS/s/channel simultaneous sampling multifunction DAQ (National Instruments) coupled with a BNC-2110 adapter was used for the data acquisition. The PCI-6115 card was installed within a bespoke high performance desktop computer (Dell Precision 5810 workstation). The BNC-2110 adapted was attached to the desktop PC and allows for easy connections of the relevant cables to the PCI-6115.

The PCI-6115 is capable of receiving 4 high speed inputs, each capable of sampling speeds of 10 MHz simultaneously, but in this work only one input was used.

3.6 Fixation of Sensor to Tribometer

In order to get repeatable results the location of the acoustic emission sensor is required to be the same during every test. To ensure this a bespoke holder was created so that the sensor can be screwed directly in the ball holder of the tribometer. The sensor holder was designed by the author and manufactured at The University of Leeds.

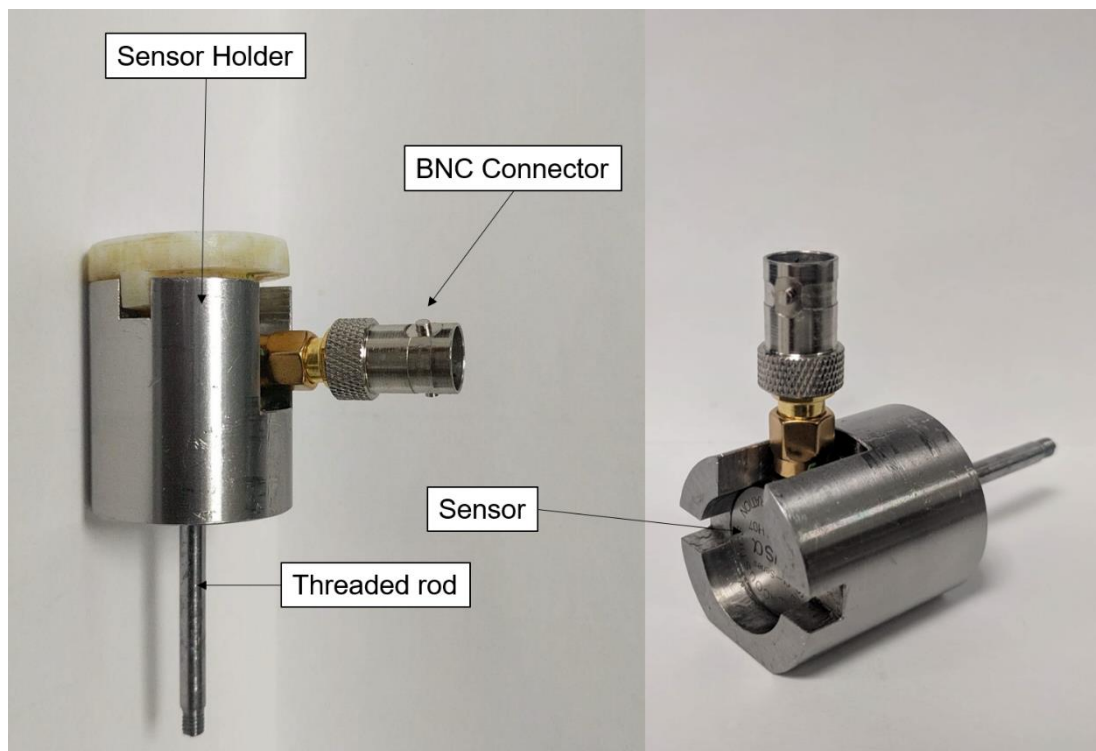


Figure 3.20 - Annotated photograph of acoustic emission sensor and bespoke fixation device.

The sensor holder, shown in Figure 3.20, is made from machined aluminium to reduce the weight. The weight of the device is taken into account for contact pressure calculations. Figure 3.21 shows the acoustic emission sensor attached to the HSPOD tribometer. It can also be seen that by using a holder that is screwed directly into the ball holder ensures that there is constant material contact from the tribocontact interface and the acoustic emission sensor, this allows the acoustic emission signal to travel directly to the sensor, with limited dampening effects.

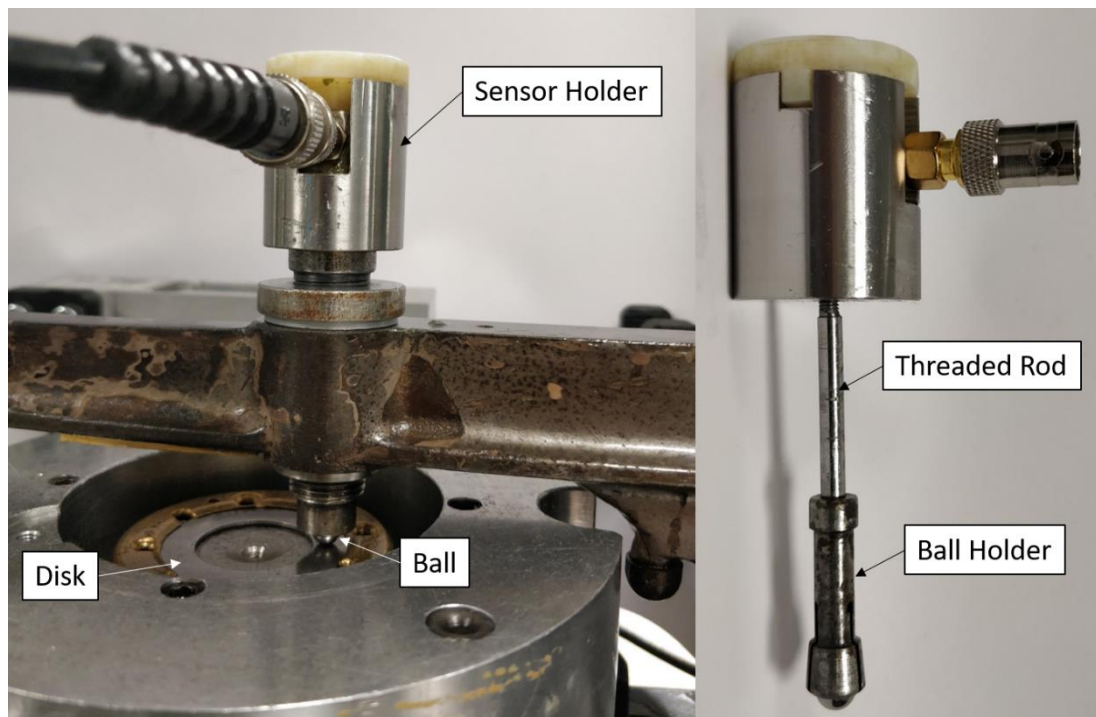


Figure 3.21 - Annotated photograph of acoustic emission sensor located on the HSPOD tribometer and material connection between acoustic emission sensor and ball.

3.7 Influence of Varying Acoustic Emission Parameters

Prior to beginning testing it was necessary to ensure that the various acoustic emission parameters were fine tuned for the HSPOD system. The variables that needed to be compared were sampling time and interval, hit count threshold and width values.

3.7.1 Sampling Time and Interval

In order to determine the most appropriate sampling time and interval values to use during this research a range of tests were conducted in which those

values were altered and the results were analysed. Tests were conducted with a load of 5 kg in PAO, a high load was required as this promoted extreme friction and wear behaviour during the test. The extreme friction and wear behaviour ensured that throughout the tests there would be dynamic changes in the CoF values and hopefully this would be reflected in the acoustic emission data. The values used for sampling time and interval comparison are shown in Table 5.

Table 5 - Test parameters used for sampling time and interval tests.

Test	Sampling Time	Sampling Interval
A	1000 ms	1 ms
B	250 ms	100 ms
C	250 ms	1 ms
D	25 ms	1 ms

Each test shown in Table 5 was completed separately, with new sample disks and ball bearings being used for each test. For each test the absolute energy, hit count and RMS signal will be reported and can be seen in Figure 3.22, Figure 3.23 and Figure 3.24, respectively.

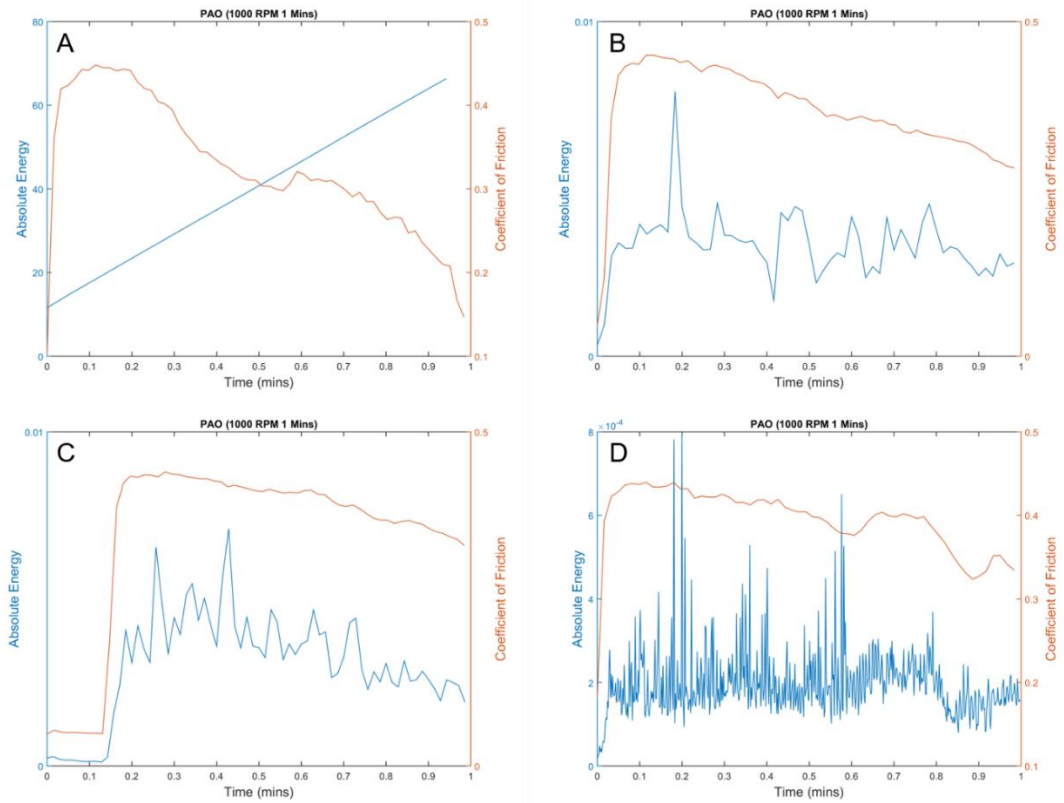


Figure 3.22 - Comparison of absolute energy and CoF data for four different sampling times and intervals (shown as time/interval): A) 1000/1, B) 250/100, C) 250/1 and D) 25/1.

Figure 3.22 shows the absolute energy and CoF data for the four different sampling times and intervals being compared. For a sampling time of 1000 ms it can be seen in A that there is no relationship between the acoustic emission measurement and the coefficient of friction. Both B and C have a sampling time of 250 ms but B has a time interval of 100 ms whereas the time interval for C is 1 ms. It is clear that there are more data points shown in C and also the overall trend of the acoustic emission signal appears to mimic that of the coefficient of friction whereas for B it does not. Finally, D shows the acoustic emission data for a sampling interval of 25 ms, it is clear that there is a lot more data points being shown, however, the sheer amount of data is causing the overall trend of the signal to be obscured slightly and further post processing such as averaging would be required to produce a cleaner signal.

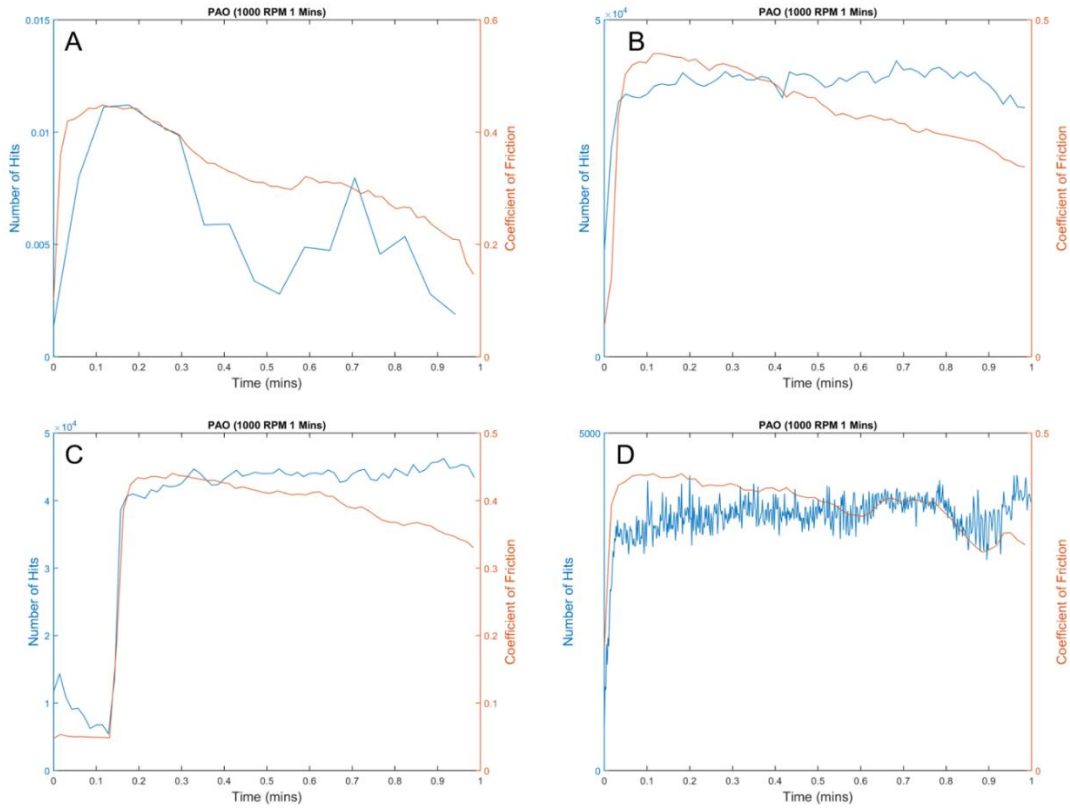


Figure 3.23 - Comparison of hit count and CoF data for four different sampling times and intervals (shown as time/interval): A) 1000/1, B) 250/100, C) 250/1 and D) 25/1.

Figure 3.23 shows the hit count and CoF data for the four different sampling times and intervals being compared. For a sampling time of 1000 ms it can be seen in A that there is a clear relationship between the acoustic emission measurement and the coefficient of friction, however, there are only 15 data points shown for the full minute test. If there was a rapid change in the signal, this would not be picked up by the acoustic emission signal. Both B and C have a sampling time of 250 ms but B has a time interval of 100 ms whereas the time interval for C is 1 ms. The reduced time interval of 1 ms has resulted in an increased number of data points as shown in C. Finally, D shows the acoustic emission data for a sampling interval of 25 ms, it is clear that there is a lot more data points being shown, however, the sheer amount of data is causing the overall trend of the signal to be obscured slightly and further post processing such as averaging would be required to produce a cleaner signal.

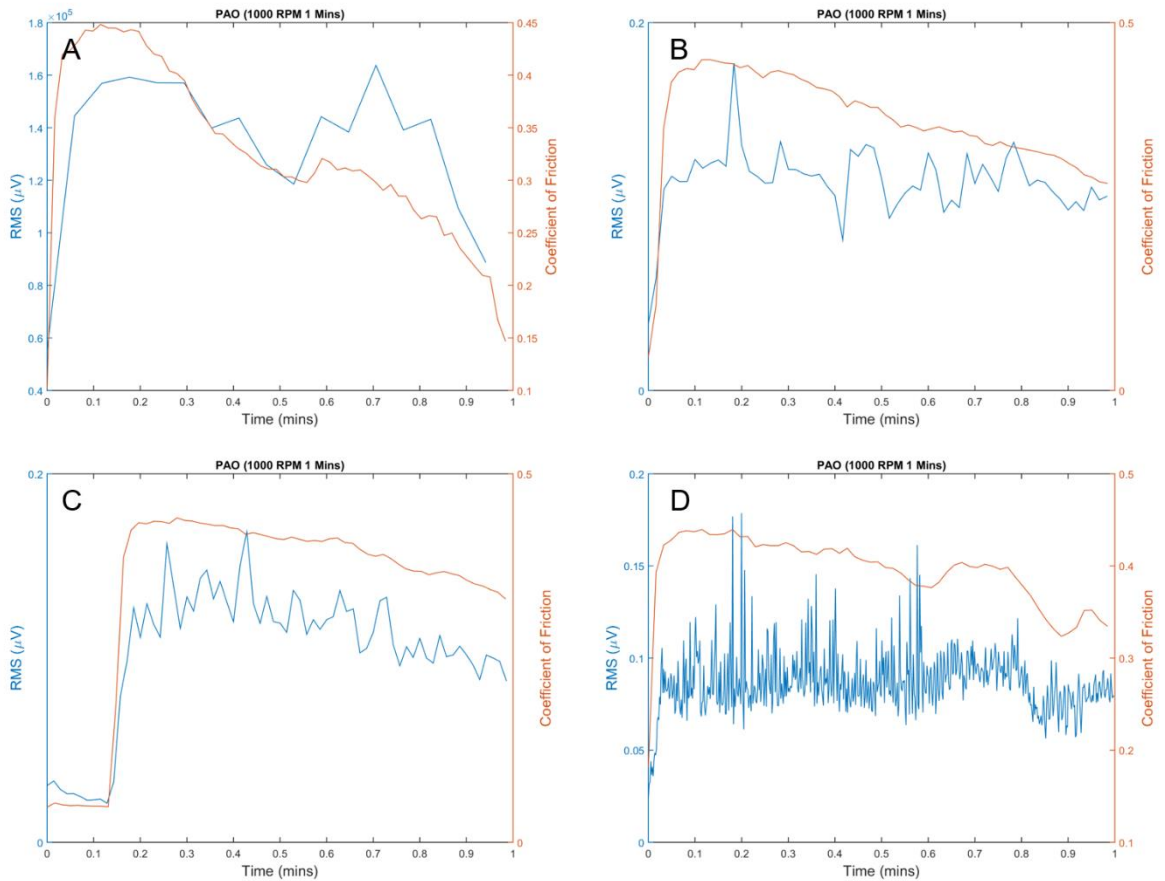


Figure 3.24 - Comparison of RMS and CoF data for four different sampling times and intervals (shown as time/interval): A) 1000/1, B) 250/100, C) 250/1 and D) 25/1.

Figure 3.24 shows the RMS and CoF data for the four different sampling times and intervals being compared. For a sampling time of 1000 ms it can be seen in A that there is a clear relationship between the acoustic emission measurement and the coefficient of friction, however, there are only 15 data points shown for the full minute test. If there was a rapid change in the signal, this would not be picked up by the acoustic emission signal. Both B and C have a sampling time of 250 ms, B has a time interval of 100 ms whereas the time interval for C is 1 ms. It is clear that there are more data points shown in C and also the overall trend of the acoustic emission signal appears to mimic that of the coefficient of friction whereas for B it does not. Finally, D shows the acoustic emission data for a sampling interval of 25 ms, it is clear that there is a lot more data points being shown, however, the sheer amount of data is causing the overall trend of the signal to be obscured slightly and further post processing such as averaging would be required to produce a cleaner signal. Based on the above three figures it was decided that the sampling duration and interval would be set at 250 ms and 1 ms respectively. These settings

reflect the need to have accurate and representative data that is not oversaturated, as is the case with a sampling time and interval of 25 ms and 1 ms respectively.

3.7.2 Hit Count Threshold and Width

Similarly, in order to determine the most appropriate hit count threshold and width values a test was conducted in which the acoustic emission variables were altered and the results were then analysed. The test was conducted at a load of 2.5 kg in PAO. The test was allowed to run for a 30 minutes running in period before any measurements were taken, this was to ensure that the raw acoustic emission signal remained as constant as possible whilst the variable values were changed. Following the running in period the acoustic emission variables were then changed and an acquisition was taken for 30 seconds. The average hit count was then calculated for the 30 second measurement period, this was then repeated three times for each variable change.

As depicted in Figure 1.24 in Section 1.4.1.1.2, there are two key parameters associated with the acoustic emission hit count measurements, these are the threshold and the width. The threshold is the amplitude that the raw acoustic emission signal must cross in order to trigger the count of a hit. The width is the window in which the hits can be counted.

In order to determine the best threshold value the width was set at 1 and the threshold was then varied from 0.01 – 0.2. The average hit count is shown for each threshold value in Figure 3.25. Further, to determine the best width value the threshold was set at 0.05 and the width value was then varied from 1 – 10. The average hit count is shown for each width value in Figure 3.26.

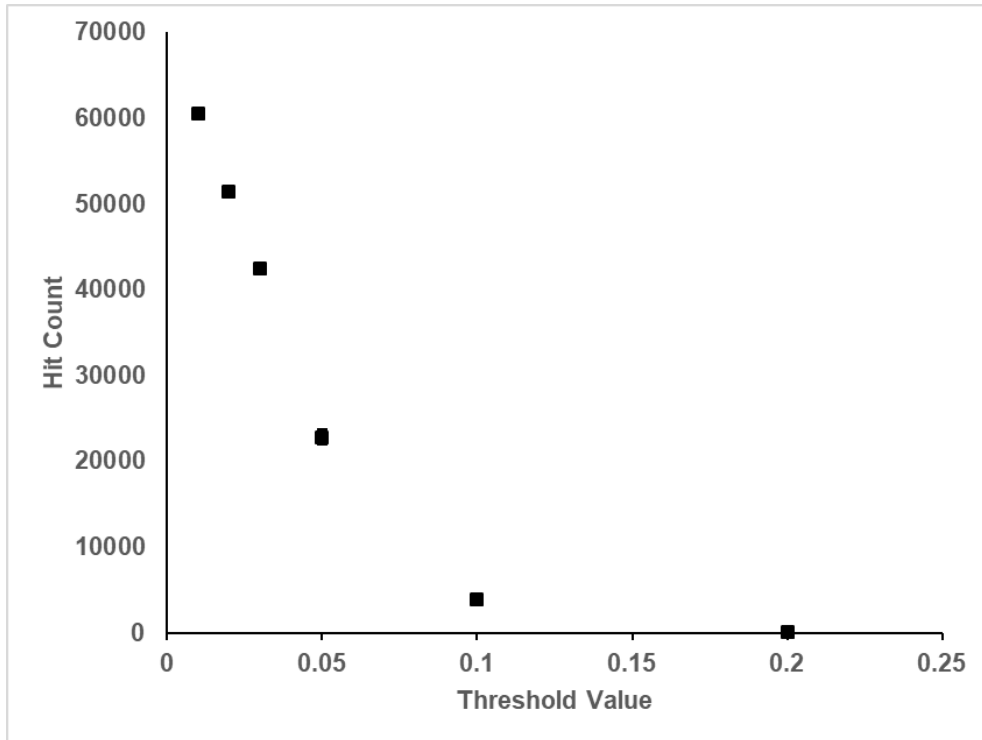


Figure 3.25 - Average hit count \pm SD for different threshold values.

Figure 3.25 shows how the hit threshold value affects the measured hit count, for a threshold value of 0.01 an extremely large hit count of 60000 is reported. As the threshold value is increased the hit count decreases. At a threshold value of 0.1 and above the reported hit count is very small ~4000 and ~20 for thresholds of 0.1 and 0.2 respectively.

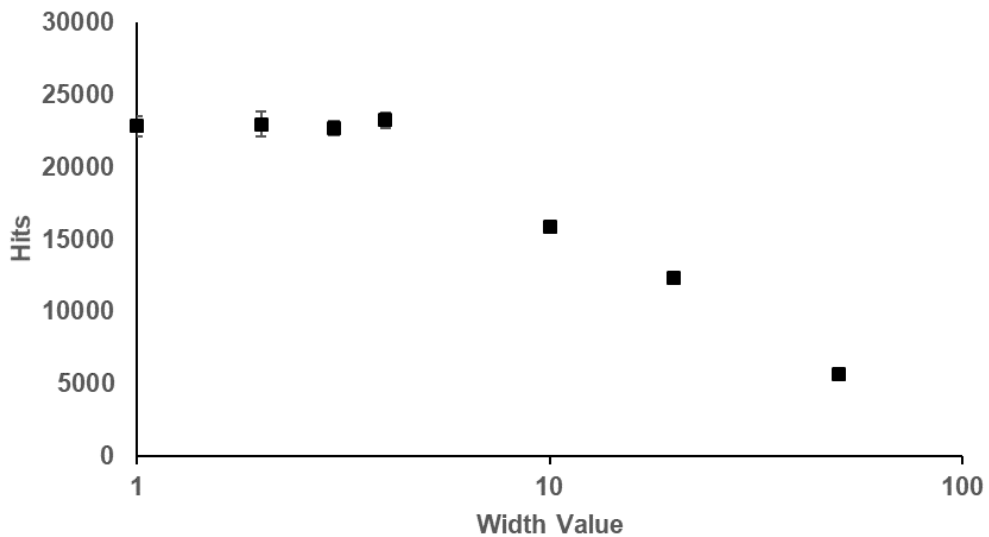


Figure 3.26 - Average hit count \pm SD for different width values.

Figure 3.26 shows the impact that changing the width value has on the hit count. It can be seen that for width values of 1–5 the reported hit count remains

relatively unchanged. However, width values >5 result in a drastic reduction in the reported hit count.

Based on the information provided in Figure 3.25 and Figure 3.26 the hit count threshold and width values throughout the rest of this work were determined to be 0.05 for the threshold and 1 for the width. This combination of values provide a large enough hit count so that any relatively small changes can be seen in the data, but the number isn't so large as to distort the impact of any such changes.

3.8 Summary

In this chapter the development of a bespoke LabVIEW based data acquisition has been documented alongside the investigation into the effects of key acquisition parameters. The findings of this chapter can be summarised as follows:

- A bespoke LabVIEW data acquisition system has been developed that allows for data capture through a scalable and flexible system that can grow in tandem with project complexity
- Acoustic emission variables key to this work have been identified

Chapter 4

Effect of Initial Surface Roughness on Acoustic Emission Response Under Boundary Lubricated Conditions

It is believed that the source of acoustic emissions during tribological tests comes from asperity-asperity interactions between the two contacting faces and the resulting processes associated with the asperity-asperity interaction. This chapter will investigate the extent in which the initial surface roughness impacts the acoustic emission response. Consequently, by changing the initial surface roughness of the test samples, the lambda ratio in which the test operates will also change. The effect of this will also be investigated.

The methods used in this section are described in detail in Chapter 2. However, the key tribotest parameters used during this work are shown in Table 6. The parameters shown in Table 6 were chosen after multiple trial experiments in which the contact pressure was varied. Increasing the contact pressure reduces the lambda ratio for the tests, this is of key importance for the smoothest samples. However, increasing the contact pressure also causes increased wear, this is more prominent on the roughest samples. As such the parameters listed below provide the best compromise between lambda ratio and friction/wear results.

Table 6 - Tribological parameters for tests conducted in this section.

Test Condition	Parameters
Base oil	Polyalphaolefin
Temperature	100 °C
Contact Pressure	1.68 GPa
Sliding Speed	1000 RPM (1.75 ms ⁻¹)
Test Duration	20 Minutes
Material	Disk: AISI 1074, Ball: AISI 52100
Hardness	Disk: 60-64 HRC, Ball: 60-67 HRC
Young's Modulus	190-210 GPa (ball and disk)
Roughness (R _a)	Ball: 10 nm, Disk: 5.6 – 240 nm
Lambda Ratio (λ)	0.12 – 1.28

As previously discussed in Section 2.2.4, test disks were polished using a Buehler Beta Grinder-Polisher in order to achieve a range of different surface roughnesses. The surface roughness of each sample was measured using a contact profilometer as described in Chapter 2. It was found that the roughest sample, SF-120, had an initial R_a surface roughness of 240 nm. Comparatively, the smoothest sample, SF-0.25 μm , had an initial surface roughness of only 5.6 nm.

4.1 Acoustic Emission and Coefficient of Friction Data

For each test specimen, the acoustic emission and coefficient of friction data were measured simultaneously throughout the entirety of the test. The data shown in Figures 4.1-4.10 are a single representation of the multiple test repeats; the repeatability of the tests is discussed in Section 4.2. It is also worth noting that each of the graphs are shown on the same scale to ensure comparisons can be made between the different test conditions.

Figures 4.1-4.3 show the absolute energy, hit count and RMS data compared to the CoF data for a tribotest conducted using PAO as the lubricant and a standard sample as the counterface. It can be seen in all three figures that the acoustic emission data and the coefficient of friction data show similar responses, remaining relatively constant throughout the test. Further, at approximately 9 minutes there is a spike in the coefficient of friction data, this is also clearly shown by all three acoustic emission parameters.

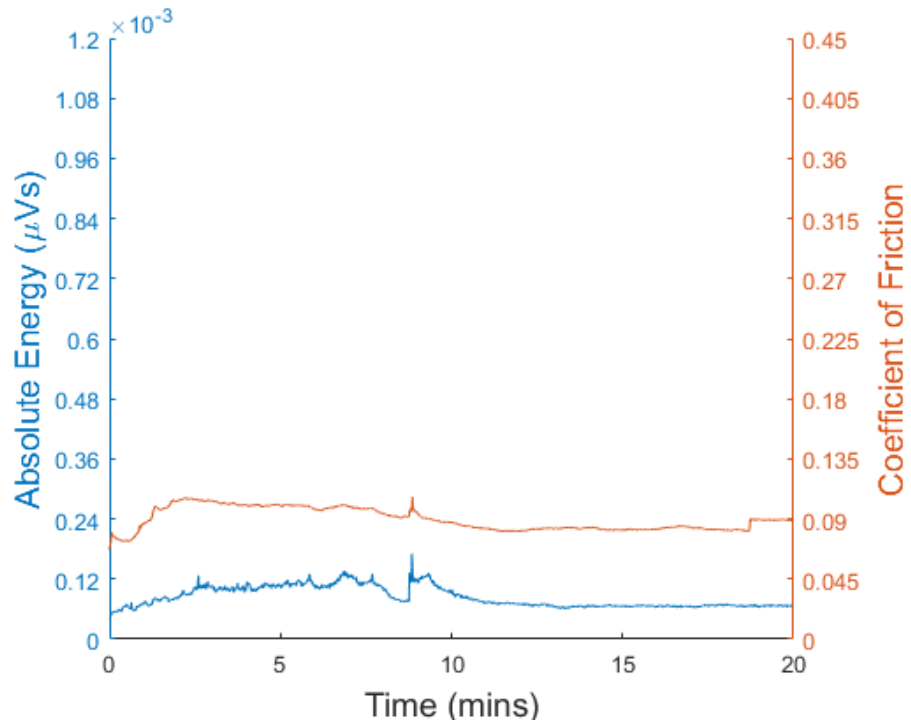


Figure 4.1 – Absolute energy and coefficient of friction data for tribotest conducted using a standard sample in PAO. (Contact Pressure: 1.68 GPa, Speed: 1000 RPM and Temperature 100 °C).

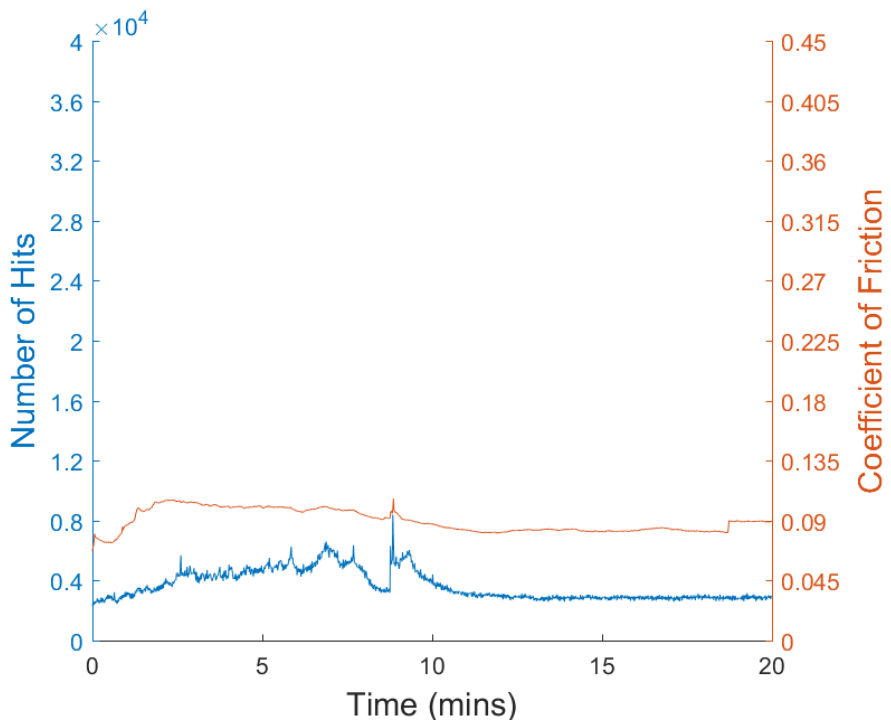


Figure 4.2 – Hit count and coefficient of friction data for tribotest conducted using a standard sample in PAO. (Contact Pressure: 1.68 GPa, Speed: 1000 RPM and Temperature 100 °C).

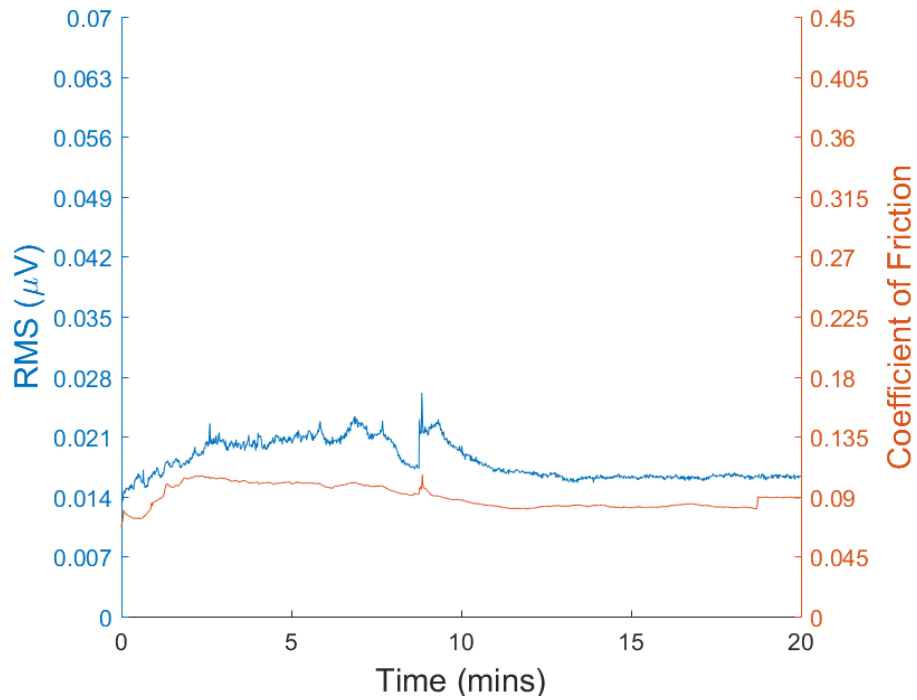


Figure 4.3 – RMS and coefficient of friction data for tribotest conducted using a standard sample in PAO. (Contact Pressure: 1.68 GPa, Speed: 1000 RPM and Temperature 100 °C).

For each specified surface finish at least 3 specimens were created and tested. Further, for each test, 3 separate graphs representing the various acoustic emission parameters were produced, which as has been shown above show very similar responses. Therefore, in order to avoid repetition, only the RMS data for one representative sample for each surface finish will be shown in this chapter.

4.1.1 SF-120

Figure 4.4 shows the coefficient of friction and RMS data for a tribotest conducted in PAO using a SF-120 disk as the counterface. It can be seen that for both the friction and the RMS data there is initially a very large spike as soon as the test starts but the magnitudes of both data reduces dramatically for the remainder of the test. It is worth noting that at approximately 5 minutes there is a second large spike shown in both the acoustic emission and the coefficient of friction data, showing that the two parameters are inextricably linked. The cause of this spike could be due to third body wear particles forming as the rough surface is worn, although more testing is required to fully evaluate the phenomena.

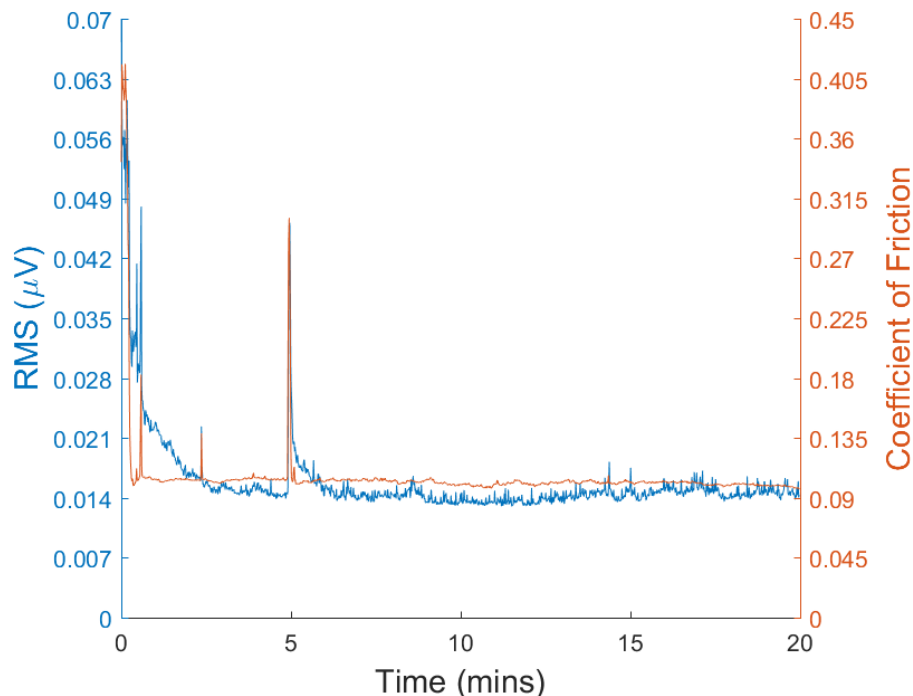


Figure 4.4 – RMS and coefficient of friction data for tribotest conducted using a SF-120 sample in PAO. (Contact Pressure: 1.68 GPa, Speed: 1000 RPM and Temperature 100 °C).

The initial spike in the data shown in Figure 4.4 is due to the large initial surface roughness. The rough surface is then believed to smooth as the test continues and the disk is worn. This is represented in the acoustic emission and coefficient of friction data from 5 minutes onwards. However, it appears that the effect the surface roughness has on the acoustic emission data is much more profound than that shown in the coefficient of friction data. The RMS data takes a lot longer to reach a plateau from the spike than the coefficient of

friction, indicating that the acoustic emission signal is more sensitive to external stimuli.

4.1.2 SF-320

Figure 4.5 shows the coefficient of friction and RMS data for a tribotest conducted in PAO using a SF-320 disk as the counterface. It can be seen that for both the coefficient of friction and the acoustic emission data there is initially a very large spike as soon as the test starts but the magnitudes of both data reduces dramatically and maintains a relatively steady state for the remainder of the test.

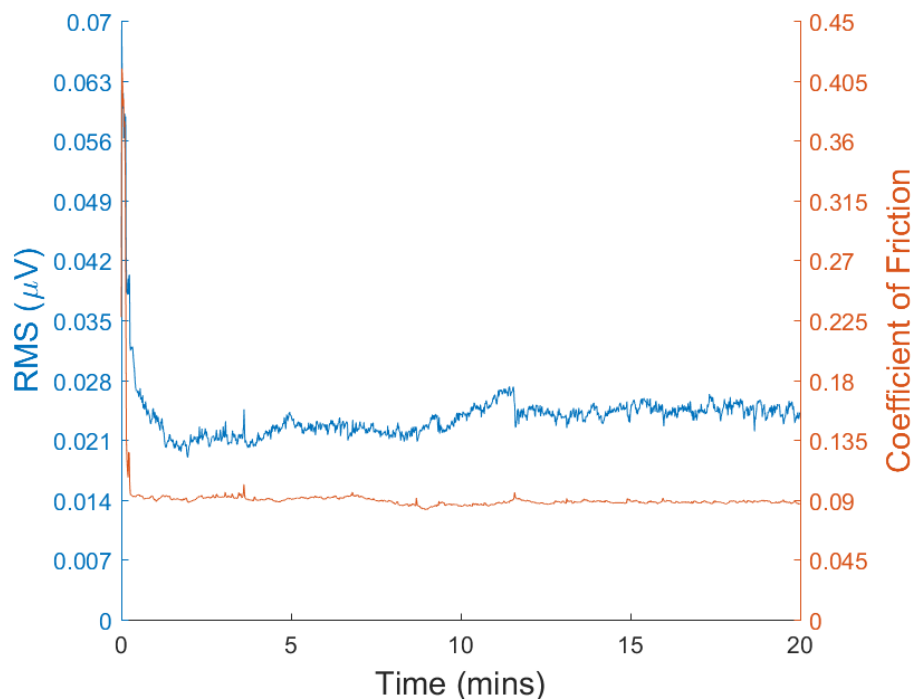


Figure 4.5 – RMS and coefficient of friction data for tribotest conducted using a SF-320 sample in PAO. (Contact Pressure: 1.68 GPa, Speed: 1000 RPM and Temperature 100 °C).

Similarly to Figure 4.4, the initial spike in the data shown in Figure 4.5 is due to the large initial surface roughness, the rough surface then smooths as the test continues and the disk is worn, this is represented in the acoustic emission and coefficient of friction data from ~2 minutes onwards. Once again, it appears that the effect the surface roughness has on the acoustic emission data is much more profound than that shown in the coefficient of friction data as the RMS data takes a lot longer to reach a plateau from the spike than the coefficient of friction. This indicates that the acoustic emission signal is more sensitive to external stimuli.

4.1.3 SF-600

Figure 4.6 shows the coefficient of friction and RMS data for a tribotest conducted in PAO using a SF-600 disk as the counterface. It can be seen that for both the coefficient of friction and the acoustic emission data there is initially a very large spike as soon as the test starts but the magnitudes of both data reduces dramatically and maintains a relatively steady state for the remainder of the test.

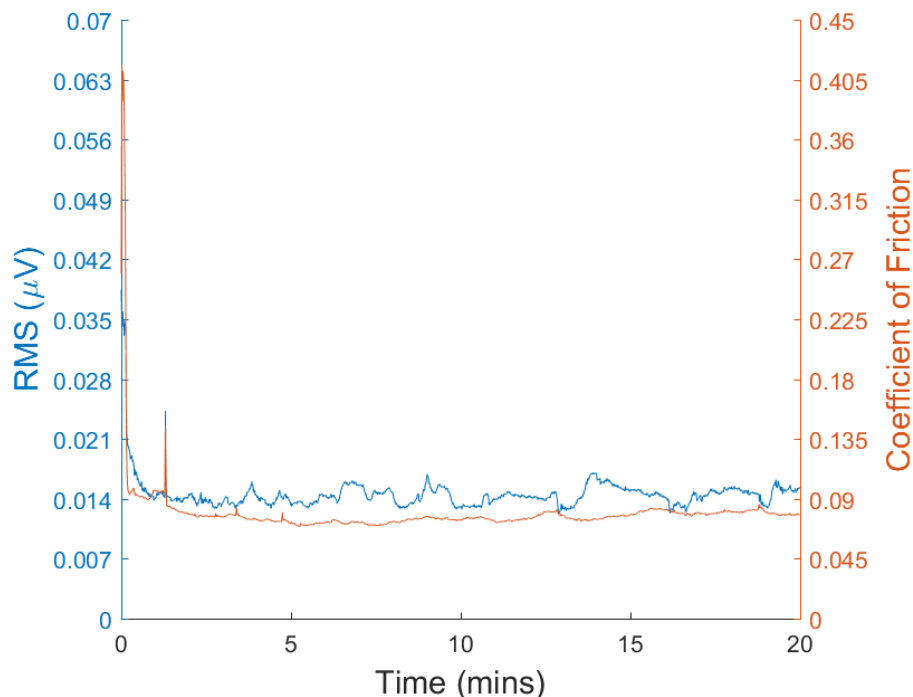


Figure 4.6 – RMS and coefficient of friction data for tribotest conducted using a SF-600 sample in PAO. (Contact Pressure: 1.68 GPa, Speed: 1000 RPM and Temperature 100 °C).

Similarly to Figure 4.4 and Figure 4.5, the initial spike in the data shown in Figure 4.6 is due to the large initial surface roughness, the rough surface then smooths as the test continues and the disk is worn, this is represented in the acoustic emission and coefficient of friction data. Unlike the previous two sets of data, it appears that the effect the surface roughness has on the acoustic emission data is the same as that shown in the coefficient of friction data. The RMS data reaches a plateau from the spike in a similar time frame as the coefficient of friction. This is unlike the data shown for the previous two surface roughnesses and may be due to reduced asperity wear at the start of the test caused by a smoother initial surface roughness.

4.1.4 SF-800

Figure 4.7 shows the coefficient of friction and acoustic emission data for a tribotest conducted in PAO using a SF-800 disk as the counterface. The acoustic emission data has a quick increase in the first 30 seconds followed by a gradual decrease for the remainder. Whereas, the coefficient of friction data initially goes down and is followed by a slight rise at around 2 minutes into the test.

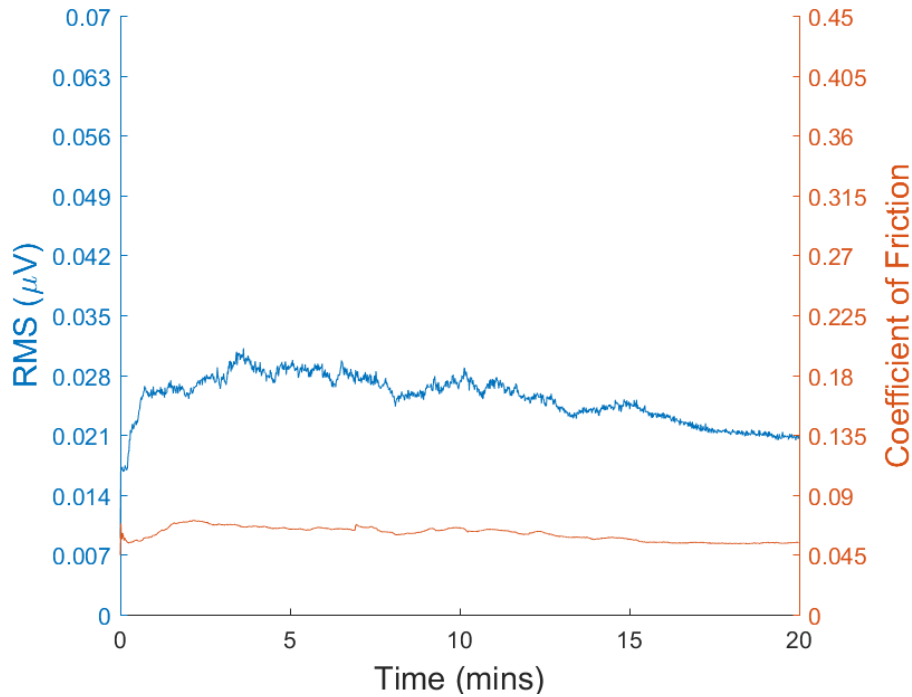


Figure 4.7 – RMS and coefficient of friction data for tribotest conducted using a SF-800 sample in PAO. (Contact Pressure: 1.68 GPa, Speed: 1000 RPM and Temperature 100 °C).

Unlike the previous three tests, there is no initial spike in coefficient of friction or acoustic emission data and it is more representative of the standard sample data shown in Figure 4.3.

4.1.5 SF-1200

Figure 4.8 shows the coefficient of friction and acoustic emission data for a tribotest conducted in PAO using a SF-1200 disk as the counterface. Similarly to the SF-800 data, it can be seen that both the friction and the RMS follow the same trend for the entirety of the test. Both the acoustic emission data and coefficient of friction data show a slight rise in the first minute of the test followed by a plateau for the remainder.

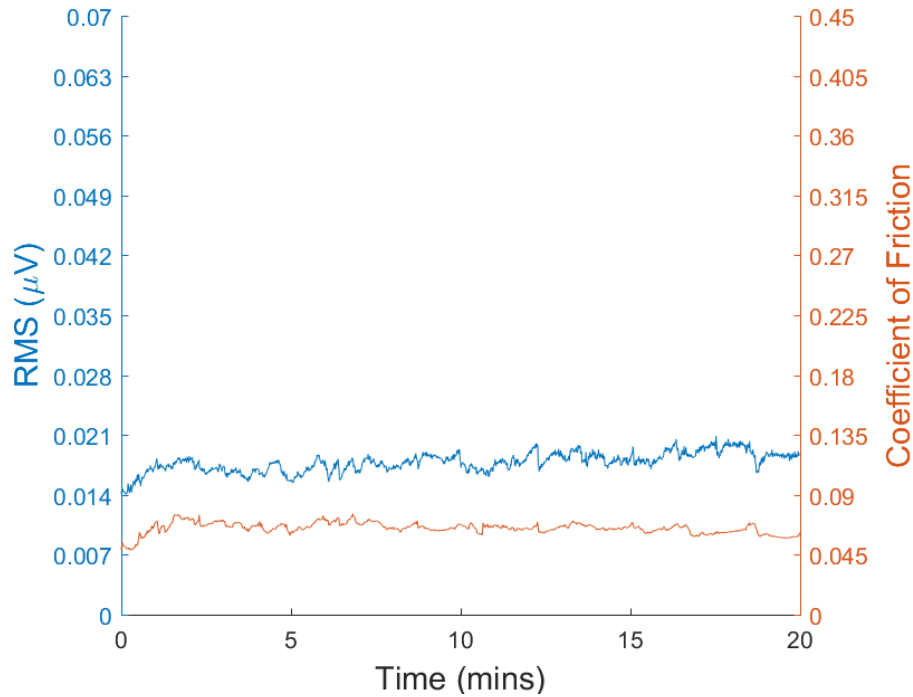


Figure 4.8 – RMS and coefficient of friction data for tribotest conducted using a SF-1200 sample in PAO. (Contact Pressure: 1.68 GPa, Speed: 1000 RPM and Temperature 100 °C).

The data in Figure 4.8 shows that there is a direct link between the coefficient of friction and acoustic emission data as they show the exact same trend, any increase or decrease in one data set is shown in the other.

4.1.6 SF-9 μm

Figure 4.9 shows the coefficient of friction and RMS data for a tribotest conducted in PAO using a SF-9 μm disk as the counterface. It can be seen that for both the friction and the RMS data there is a large spike at approximately 30 seconds, the magnitudes of both data then reduce dramatically and remain steady for the remainder of the test.

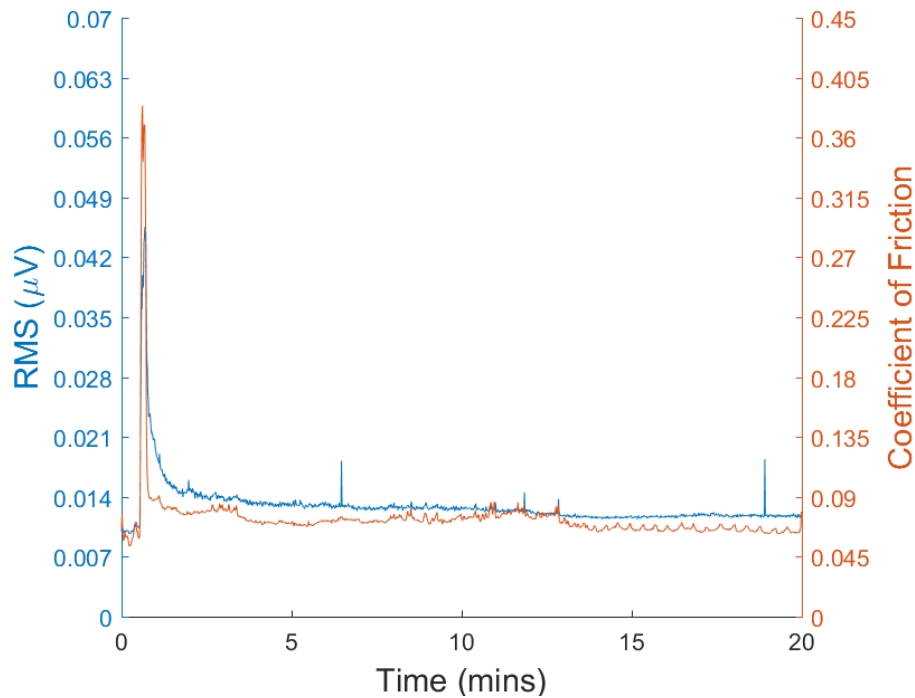


Figure 4.9 - RMS and coefficient of friction data for tribotest conducted using a SF-9 μm sample in PAO. (Contact Pressure: 1.68 GPa, Speed: 1000 RPM and Temperature 100 $^{\circ}\text{C}$).

The large spike at approximately 30 seconds is believed to be due to the surface being so smooth that any contact with the counter ball produces wear particles which can induce higher friction and therefore increased acoustic emission signals

4.1.7 SF-0.25 μ m

Figure 4.10 shows the coefficient of friction and RMS data for a tribotest conducted in PAO using a SF-0.25 μ m disk as the counterface. It can be seen that for both the friction and the RMS data there is a large spike at the very beginning of the test, the magnitudes of both data then reduce dramatically and remain steady for the remainder of the test.

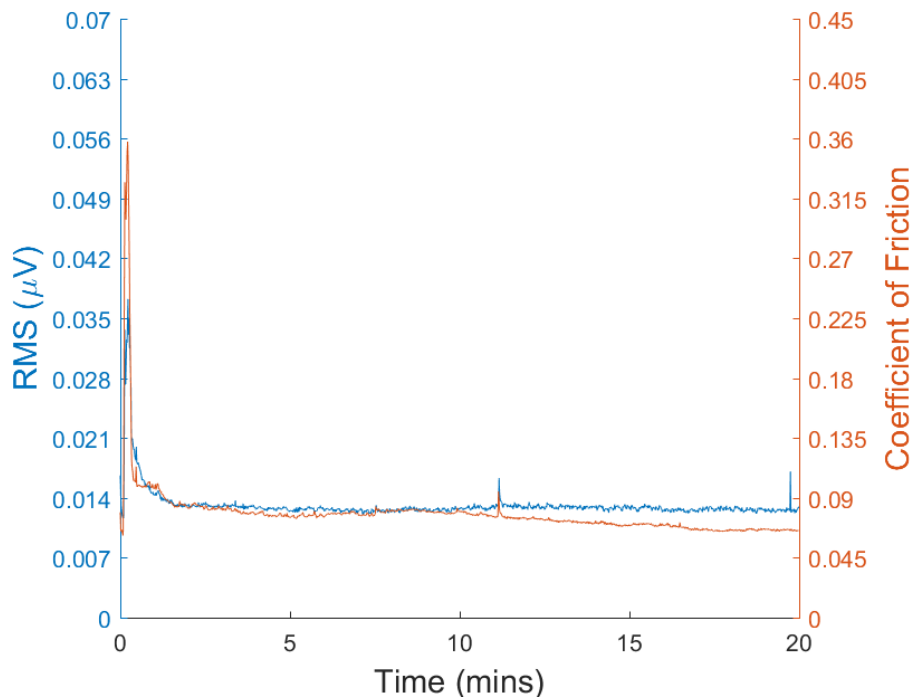


Figure 4.10 – RMS and coefficient of friction data for tribotest conducted using a SF-0.25 μ m sample in PAO. (Contact Pressure: 1.68 GPa, Speed: 1000 RPM and Temperature 100 °C).

Similarly to Figure 4.9, it is believed that the initial spike in acoustic emission and coefficient of friction data is due to initial wear of the smooth sample surface.

Figures 4.4-4.10 show that irrespective of the differing initial surface roughness of the sample, the acoustic emission and coefficient of friction data show broadly the same trend. This indicates that there is a direct link between the coefficient of friction and acoustic emission data for tests conducted in PAO.

4.2 Experiment Repeatability

Across multiple tests key measurements were taken of the coefficient of friction and acoustic emission data to quantify the repeatability of the results. An average value was taken over the last 5 minutes of the tests to analyse the steady state coefficient of friction and acoustic emission values. The peak values were also measured from the beginning of the tests. Data is shown for each different surface finish as well as for a standard sample as a reference point.

4.2.1 Average Value

Figures 4.11-4.14 show the average coefficient of friction and acoustic emission values \pm standard error of the mean taken from the last 5 minutes of multiple tests ($n=3$).

Figure 4.11 shows the coefficient of friction data. It can be seen that as the initial surface roughness of the samples reduces, so does the coefficient of friction. The average coefficient of friction values from the final 5 minutes of the test decrease from 0.096 to 0.066 for samples SF-120 and SF-9 μ m respectively. It is worth noting however that for the smoothest of the samples (SF-0.25 μ m) the average coefficient of friction value is slightly higher at 0.072.

Figure 4.12 shows the absolute energy data, it can be seen that the data does not show any particular trend regarding the initial surface roughness. The highest average absolute energy value is 0.000138 μ Vs which corresponds to surface finish SF-800. The lowest average absolute energy value is 0.00003377 μ Vs which corresponds to surface finish SF-0.25 μ m.

Figure 4.13 shows the hit count data, it can be seen that this data shows the same trend as the absolute energy data. The highest average hit count value is 6988 which corresponds to surface finish SF-800. The lowest average hit count value is 1973 which corresponds to surface finish SF-0.25 μ m.

Finally, Figure 4.14 also displays the same trend as shown by the other acoustic emission parameters. The highest RMS is 0.0222 μ V which corresponds to surface finish SF-800. The lowest average RMS is 0.0116 μ V which corresponds to surface finish SF-0.25 μ m.

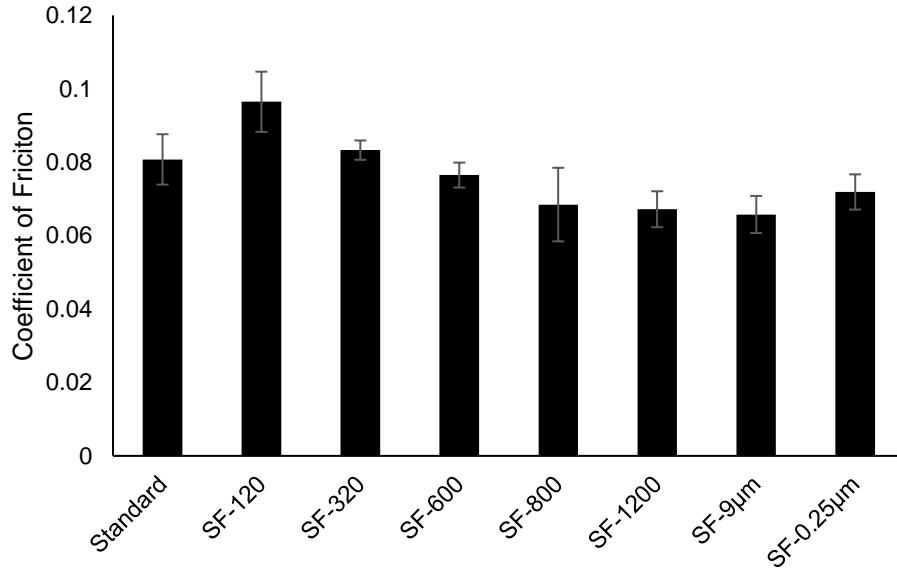


Figure 4.11 - Average coefficient of friction value from the last 5 minutes of the test for each surface roughness. (Data shown as mean ± s.e.m. n=3).

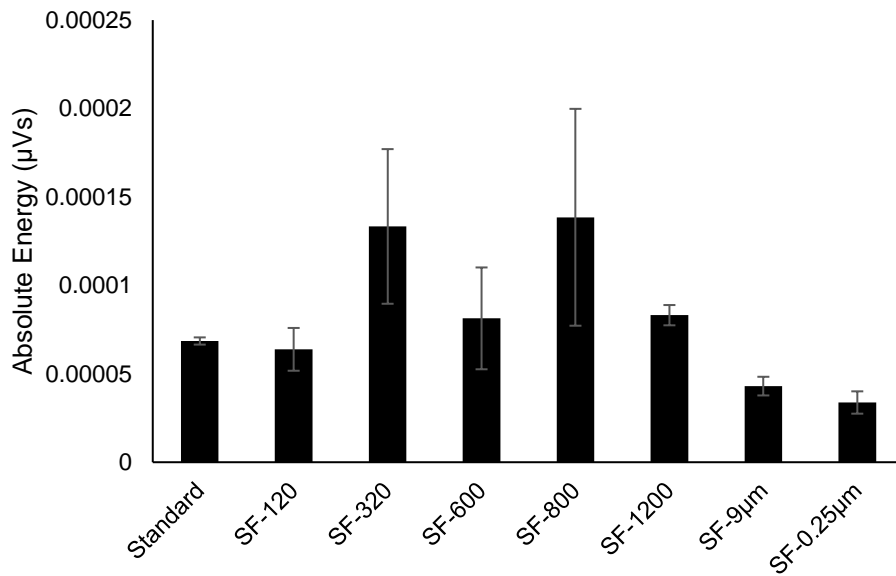


Figure 4.12 - Average absolute energy value from the last 5 minutes of the test for each surface roughness. (Data shown as mean ± s.e.m. n=3).

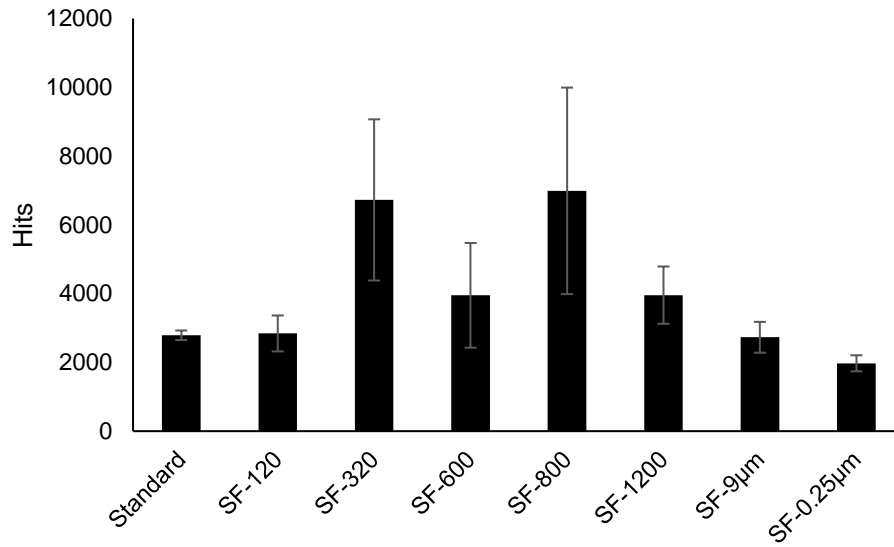


Figure 4.13 - Average hit count value from the last 5 minutes of the test for each surface roughness. (Data shown as mean ± s.e.m. n=3).

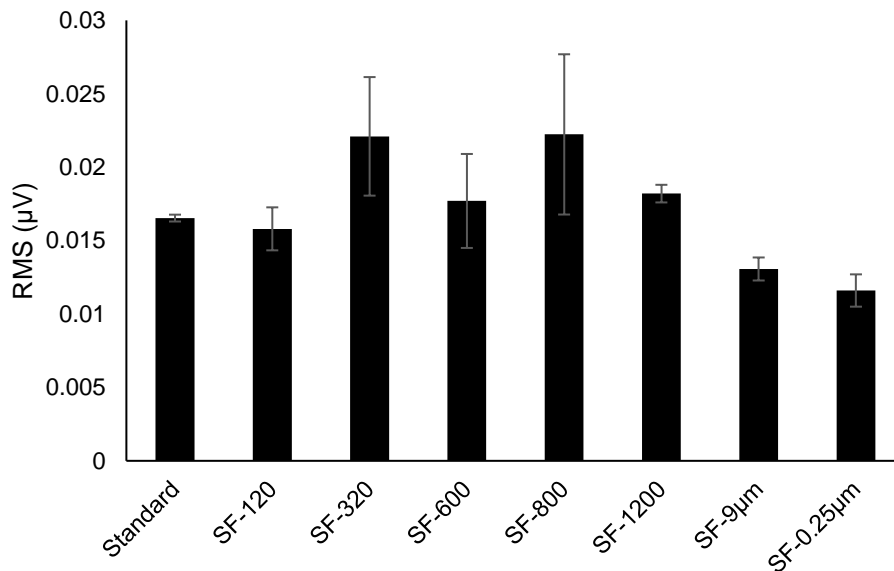


Figure 4.14 - Average RMS value from the last 5 minutes of the test for each surface roughness. (Data shown as mean ± s.e.m. n=3).

It can be seen in Figures 4.11-4.14 that the initial surface roughness has a profound effect on the average coefficient of friction taken during the last 5 minutes of the test. Figure 4.11, shows that as the initial surface roughness of the sample decreases, so does the average coefficient of friction. No such relationship can be seen for the acoustic emission data. Figures 4.12-4.14 all show the same trend, in that there is no discernible pattern present in the acoustic emission data that relates back to the initial surface roughness of the sample.

4.2.2 Peak Value

Figures 4.15-4.18 show the maximum recorded values for the coefficient of friction and acoustic emission \pm standard error of the mean taken from the last 5 minutes of multiple tests ($n=3$).

Figure 4.15 shows the peak value present in the coefficient of friction data. It can be seen that for four out of the seven surface roughnesses measured, the maximum value for coefficient of friction is ~ 0.4 . However, for SF-800 and SF-1200 the maximum value measured is considerably lower, 0.185 and 0.086, respectively.

Figure 4.16 shows the maximum recorded absolute energy data for the different initial surface roughnesses. There appears to be a positive correlation between the initial surface roughness and peak recorded value, as the initial surface roughness decreases so does the peak recorded value. The maximum value can be seen to decrease from 0.00115 μVs to 0.00013 μVs for surfaces SF-120 and SF-1200 respectively. The maximum value then increases to 0.0046 μVs for SF-9 μm and then reduces again to 0.00027 μVs for the SF-0.25 μm sample.

Figure 4.17 shows the maximum recorded hit count data for the varying initial surface roughnesses. As shown in the absolute energy data, there appears to be a positive correlation between the initial surface roughness and peak recorded value. The maximum value can be seen to decrease from 35271 to 6311.5 for surfaces SF-320 and SF-1200 respectively. However, the maximum hit count value recorded for the SF-120 samples is slightly lower than the value recorded for SF-320 samples. As before, the maximum value then increases to 17751 for SF-9 μm and then reduces again to 14413 for the SF-0.25 μm sample.

Finally, Figure 4.18 also displays the same trend as shown by the other acoustic emission parameters. The maximum value can be seen to decrease from 0.0667 μV to 0.0226 μV for surfaces SF-120 and SF-1200 respectively. The maximum value then increases to 0.0388 μV for SF-9 μm and then reduces again to 0.0328 μV for the SF-0.25 μm sample.

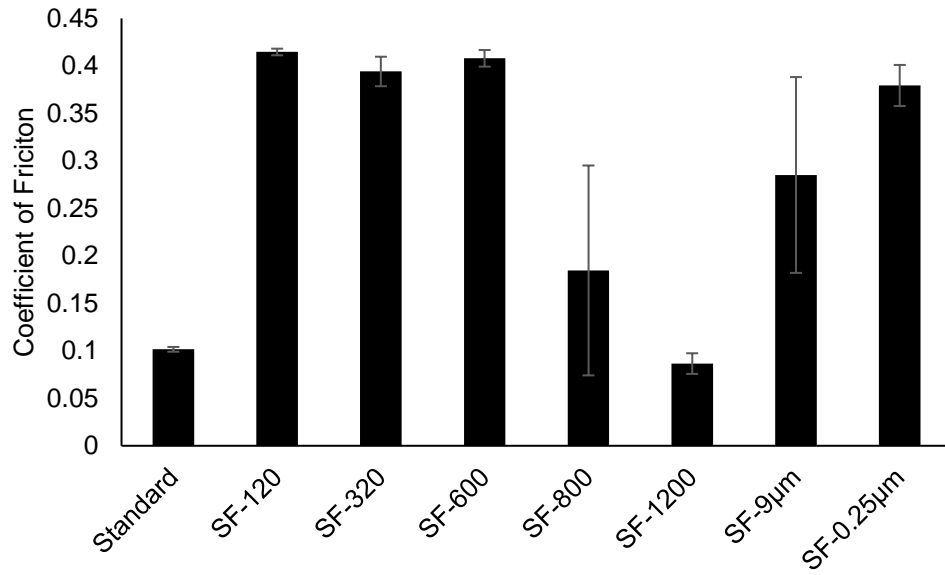


Figure 4.15 - Peak coefficient of friction value for each surface roughness. (Data shown as mean \pm s.e.m. n=3).

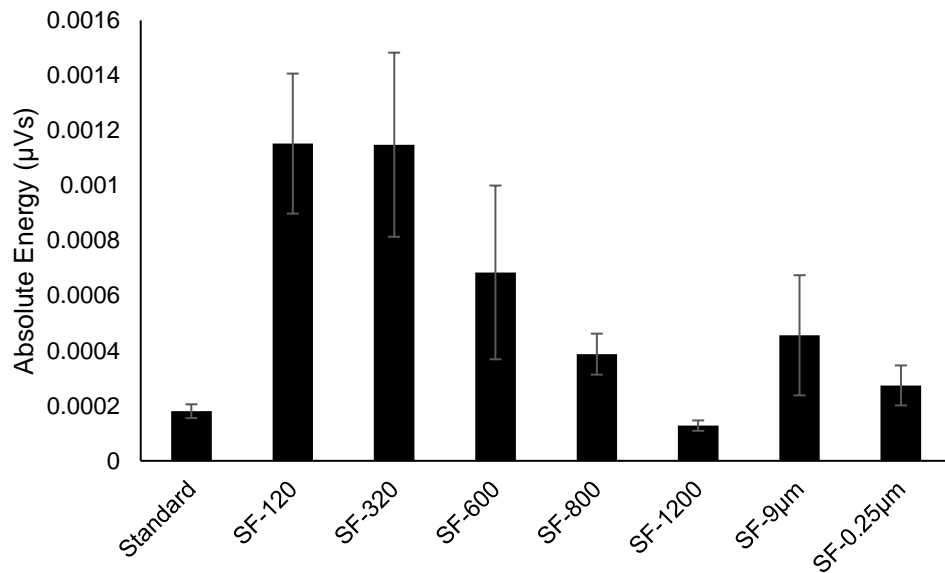


Figure 4.16 - Peak absolute energy value for each surface roughness. (Data shown as mean \pm s.e.m. n=3).

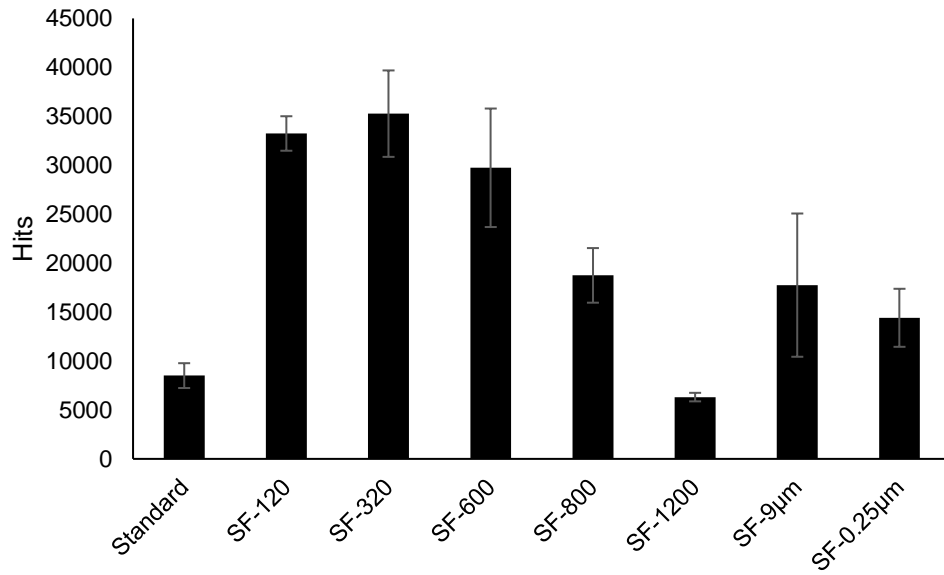


Figure 4.17 - Peak hit count value for each surface roughness. (Data shown as mean \pm s.e.m. n=3).

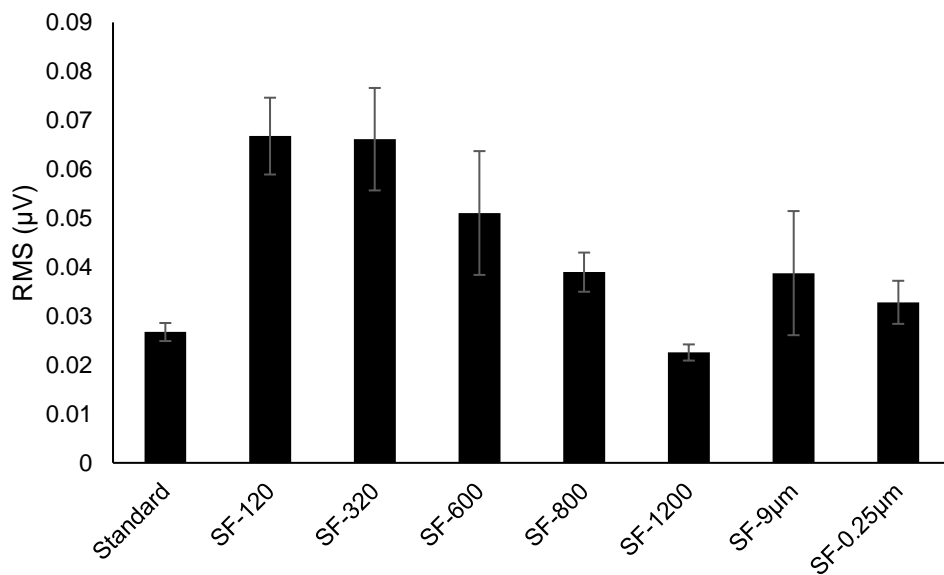


Figure 4.18 - Peak RMS value for each surface roughness. (Data shown as mean \pm s.e.m. n=3).

It can be seen in Figures 4.15-4.18 that the initial surface roughness has a profound effect on the maximum values recorded for the acoustic emission parameters.

Figures 4.16-4.18 broadly show the same trend that as the initial surface roughness of the samples is reduced so is the maximum value of the acoustic emission parameter. This relationship does not hold true for the two smoothest

sample preparations, SF-9 μm and SF-0.25 μm . This is most likely due to the lubrication regime in which the tests are operating in, the two smoothest samples initially have respective lambda ratios of 1.28 and 1.29 (shown in Figure 2.5), meaning that initially these tests take place in the mixed lubrication regime. The higher peak values shown in Figures 4.16-4.18 for samples SF-9 μm and SF-0.25 μm may be due to the transition from mixed lubrication to boundary lubrication as the surfaces become rougher.

No such relationship can be seen for the coefficient of friction data. Figure 4.15 shows that there is no discernible pattern present in the data that links the maximum recorded value with the initial surface roughness of the sample.

4.3 Changes in Surface Roughness

Measurements were taken of the samples pre- and post-test in order to establish the effect that running the tribotest had on the surface roughness. Post-test measurements were taken within the wear scars only so that the direct effect of the tribotest could be measured. Measurements were taken using a form talysurf profilometer (Taylor Hobson) in line with the methodology discussed in Chapter 2.

Figure 4.19 shows the results from these tests with pre-test data shown in black and post-test data shown in grey.

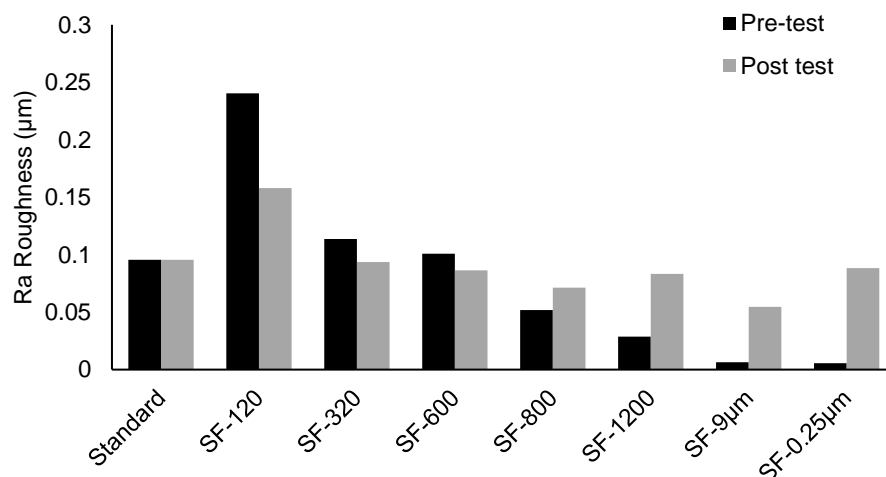


Figure 4.19 - Measurements of surface roughness both pre- and post-test.

There is little to no change in the pre- and post-test surface roughness for the standard sample. However, it can be seen that for the three roughest samples

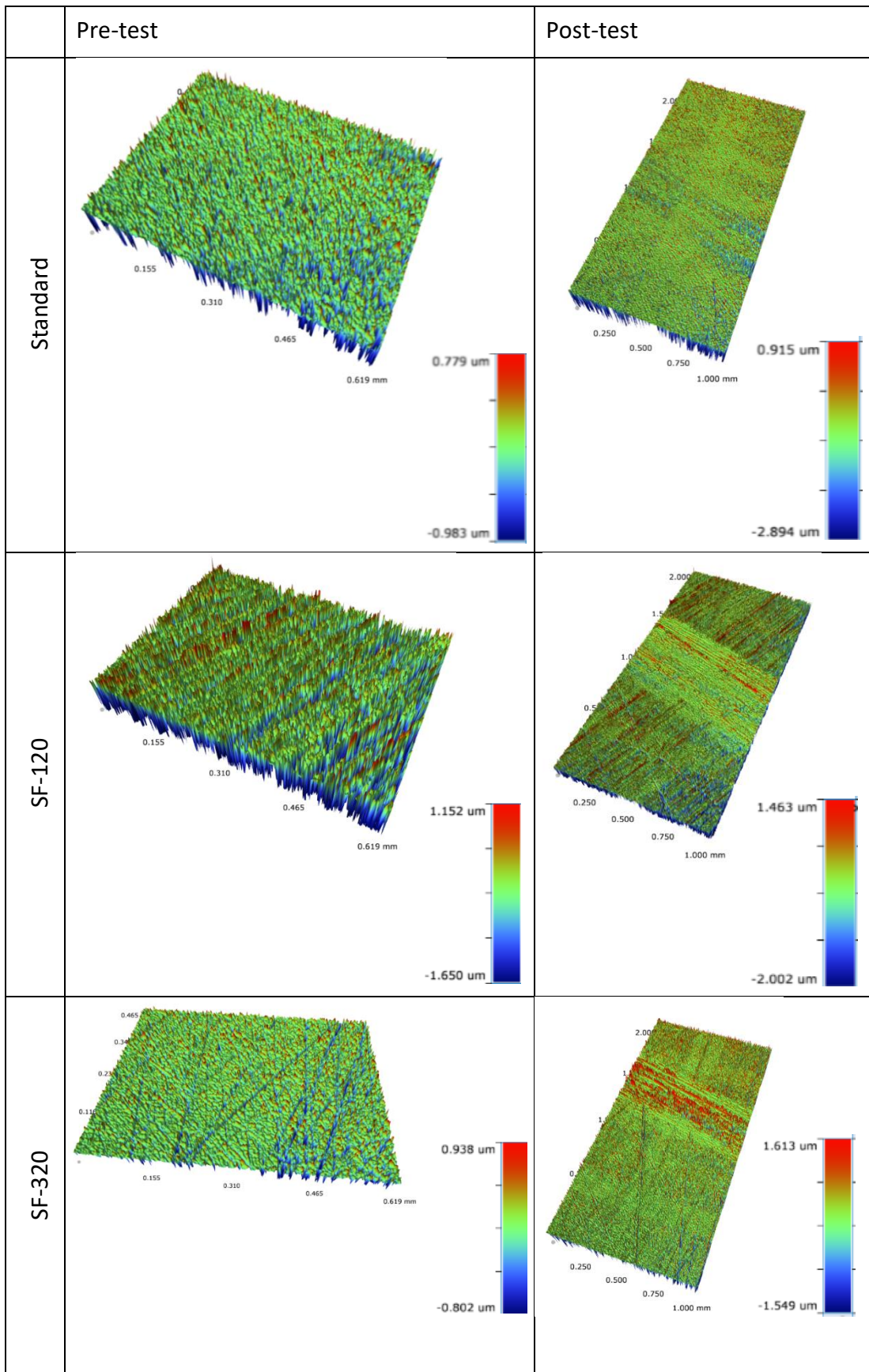
(SF-120, SF-320 and SF-600) the surface roughness value post-test is actually less than the pre-test measurement. Conversely, for the rest of the samples it can be seen that the post-test surface roughness is greater than the pre-test.

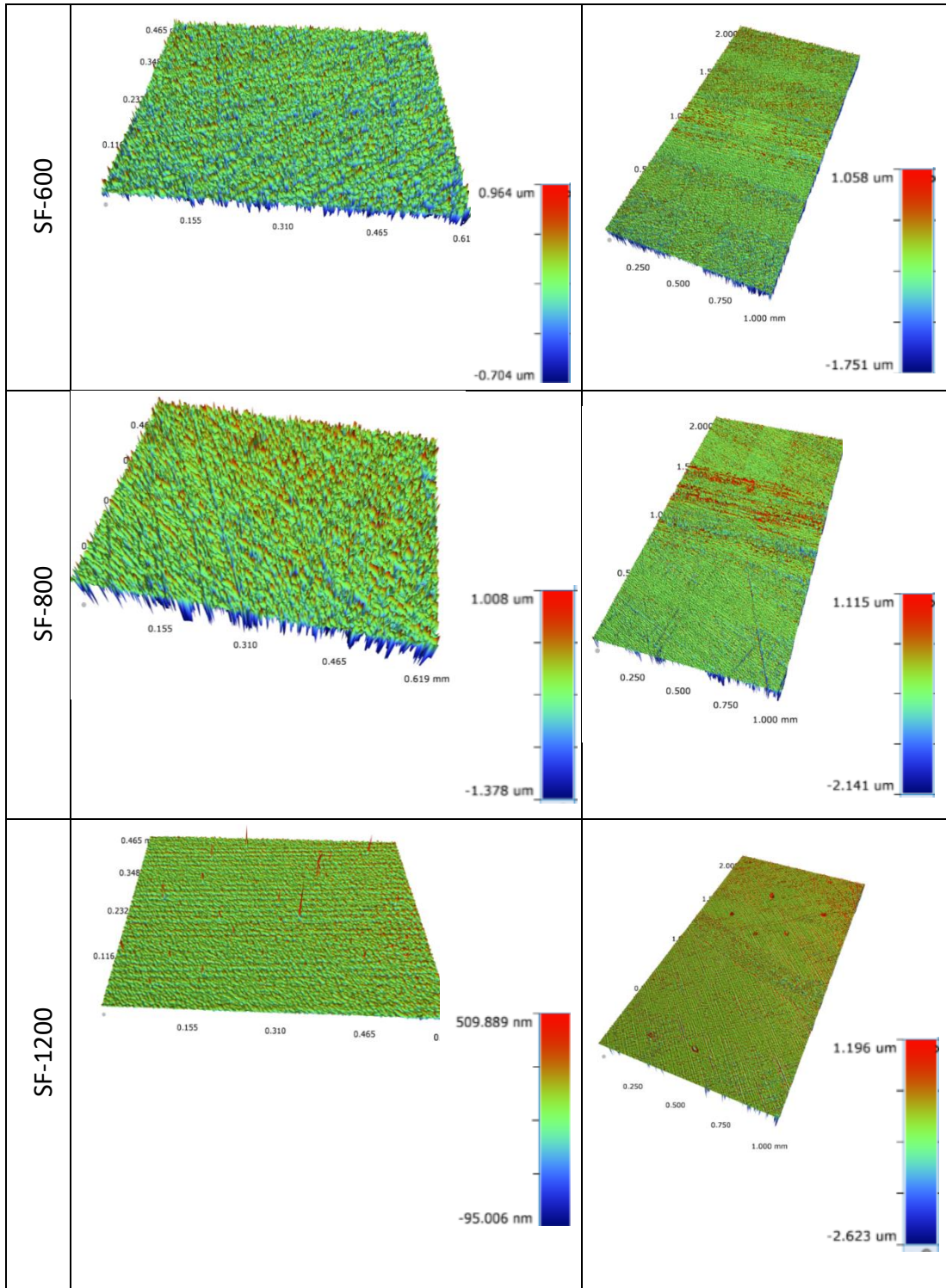
The changes in surface roughness pre- and post-test are attributed to the fact that for the rougher samples the counter ball is wearing away the asperities to form a smoother contact. Conversely, for the smooth surfaces the roughness of the counter ball is in fact wearing the smooth surface causing the surface roughness to increase.

The pre-test surface roughness of the SF-800 sample is similar to the post-test surface roughness of the SF-9 μm sample, 0.052 μm and 0.055 μm respectively. Using data shown in Figure 4.7 and Figure 4.9 the acoustic emission data can be compared. For the SF-800 sample the average RMS value for the first 5 minutes of the test is 0.028 μm . The average RMS value for the final 5 minutes of the test for the SF-9 μm sample is 0.013 μm . It can be seen that even though the surface roughnesses are similar the acoustic emission data is more than double for the SF-800 test. The exact cause of this disparity is not yet known, but it may be due to changes in contact conformity caused by wear, this would need to be fully explored in future work.

In order to visualise the effect that tribotesting had on the sample disks, white light interferometry images were taken both pre- and post-test to document the changes in surface roughness. An NPFlex (Bruker) white light interferometer was used to take the images in line with the methodology discussed in Chapter 2.

Figure 4.20 shows the images taken of the sample surfaces before and after testing; the colour map used in the images corresponds to red for peaks in the surface and blue for valleys. As previously shown in Figure 4.19, it can be seen that for the rougher samples the wear scar looks smoother than the surrounding sample surface. The opposite can also be seen for the smoother samples. For example, it can clearly be seen for SF-0.25 μm that the wear scar is considerably pronounced, approximately 1 μm higher, in comparison to the surrounding surface of the sample.





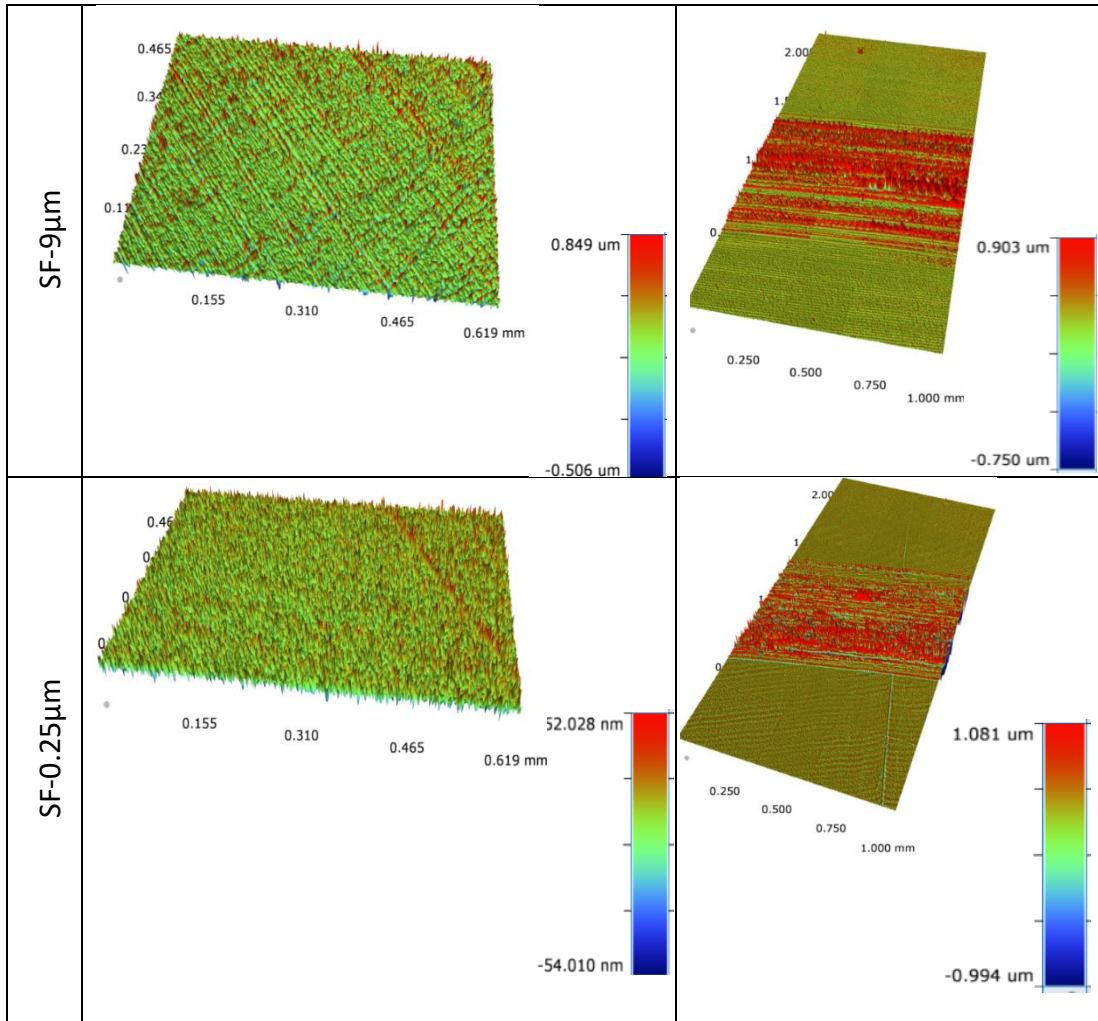


Figure 4.20 - Comparison of pre- and post-test surfaces using white light interferometry.

4.4 Summary

In this chapter the effect that initial surface roughness plays on the acoustic emission response during tribotesting has been investigated. The findings of this chapter can be summarised as follows:

- Acoustic emission sensing methodology has been used to monitor acoustic emissions in a lubricated contact
- There is a direct link between the initial surface roughness and the average coefficient of friction. This link is not present between the surface roughness and acoustic emissions.
- There is a direct link between the initial surface roughness and the maximum recorded acoustic emission value. This link is not present between the surface roughness and coefficient of friction.

Chapter 5

Monitoring MoDTC Based Tribofilm Formation and Removal Under Boundary Lubricated Conditions

Although work has been undertaken previously that looks at the acoustic emission of tribocontacts, no one has yet investigated the effect that tribochemical additives such as MoDTC have on the acoustic emission response.

When MoDTC is used as an additive in tribotests a very specific and recognisable coefficient of friction trace can be observed. The friction typically shows an initial induction period that is then followed by a drastic reduction in the friction which is maintained for the remainder of the test. This indicates that an MoS₂ tribofilm has been formed. Figure 5.1 shows a representative coefficient of friction trace from 6 experiments, data is shown as an average \pm standard error of the mean.

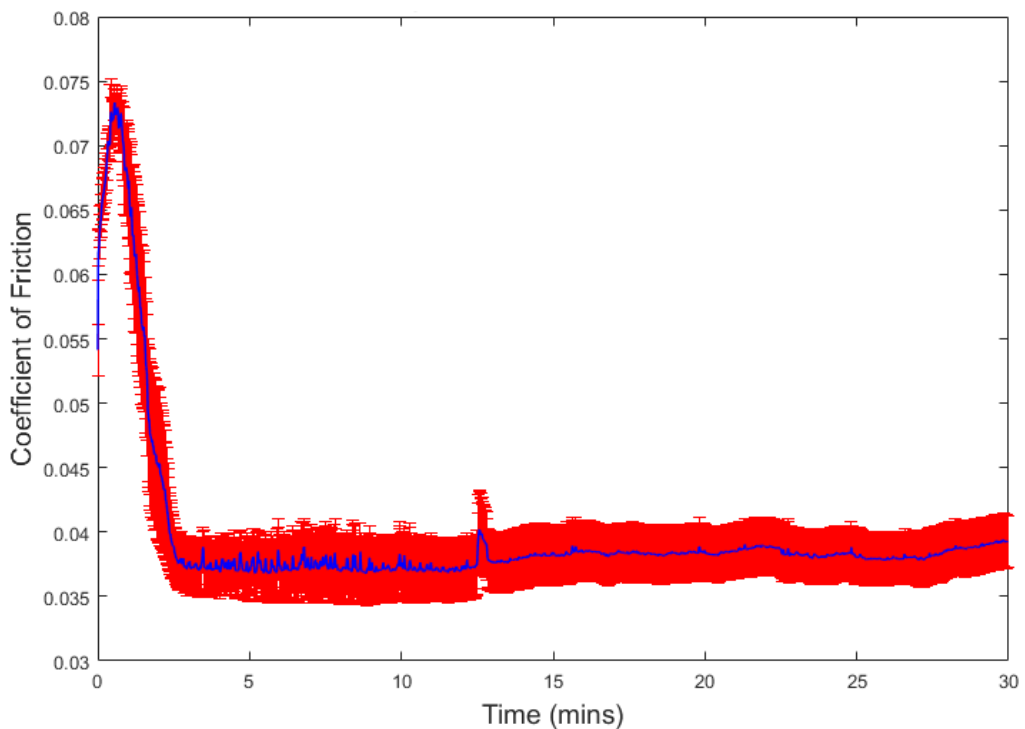


Figure 5.1 - Coefficient of friction response using PAO + 0.1 wt% MoDTC as the lubricant. 1000 RPM, 2.29 GPa, 100 °C. (Data shown as mean \pm s.e.m. n = 6).

Whilst utilising changes in the coefficient of friction is an excellent method of determining whether a MoS₂ tribofilm has been formed on test specimens, in more complex and real life systems it is not always possible to measure

instantaneous friction at the contact interface, so this methodology is limited to laboratory based testing only.

Up until now it has been very difficult to monitor tribofilm growth and removal using truly *in situ* techniques; as current methodologies require line of sight access to the interface (sapphire balls/plates) or require tribological testing to be paused so that a measurement process such as Raman spectroscopy can be performed on the sample.

The focus of the work in this chapter is to investigate for the first time the acoustic emission response to the formation and removal of MoDTC based tribofilms.

The methods used in this section are described in detail in Chapter 2. However, the key tribotest parameters used during this work are shown in Table 7 below. The parameters shown in Table 7 were chosen as they produce a consistent coefficient of friction trace that has a short induction period, this can clearly be seen in Figure 5.1.

Table 7 - Test parameters used for investigating the effect MoDTC based additives have on acoustic emission.

Test Condition	Parameters
Base oil	Polyalphaolefin
Additive Concentration	0.1 wt% MoDTC
Temperature	100 °C
Contact Pressure	2.29 GPa
Sliding Speed	1000 RPM (1.75 ms ⁻¹)
Test Duration	10 seconds – 60 minutes
Material	Disk: AISI 1074, Ball: AISI 52100
Hardness	Disk: 60-64 HRC, Ball: 60-67 HRC
Young's Modulus	190-210 GPa (ball and disk)
Roughness (R _a)	Disk: R _a = 110 nm , Ball: R _a = 10 nm
Lambda Ratio (λ)	0.25 (boundary lubrication regime)

5.1 Tribofilm Formation

As previously discussed in Chapter 1, when a MoDTC containing lubricant is used in tribological testing a very specific coefficient of friction trace can be observed. The action in which the coefficient of friction is reduced is due to the formation of MoS₂ tribofilms on the contact interface. The MoS₂ films then slide

against one another, producing considerably less friction in comparison to steel-on-steel contacts.

It is unknown at this stage what effect the presence these MoS₂ tribofilms will have on the acoustic emission response. Therefore, tests were conducted to determine whether a reduction in friction would also result in a reduction in the acoustic emission response. Multiple tests (n=6) were conducted at 1000 RPM with a load of 2.5 kg with PAO + 0.1wt % MoDTC as the lubricant.

As previously discussed, when MoDTC is used as an additive the coefficient of friction displays a consistent and recognisable trace. Across multiple tests key measurements were taken of the coefficient of friction data to quantify repeatability. Figure 5.2 shows an example coefficient of friction graph with the location of the measurements highlighted.

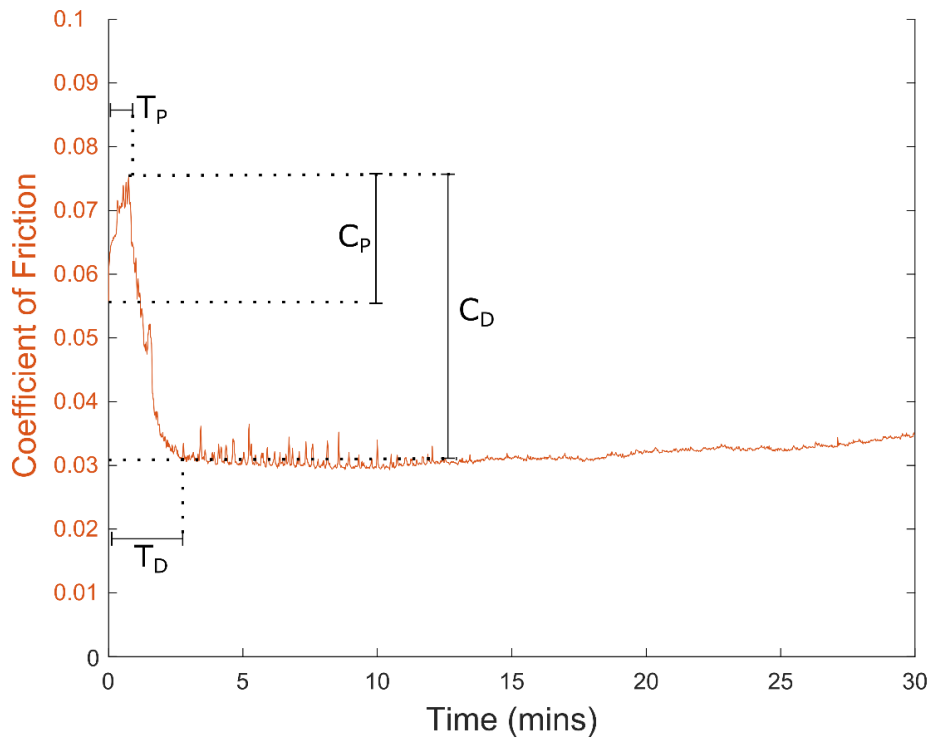


Figure 5.2 - Annotated coefficient of friction graph showing measurement parameters. T_P = Time to peak, T_D = Time to drop, C_P = Value change from start to peak, C_D = Value change from peak to drop.

Similar measurements were also taken from the acoustic emission data, Figure 5.3 shows the location of the measurements with respect to the RMS data but the same measurements were also taken from the absolute energy and hit count data.

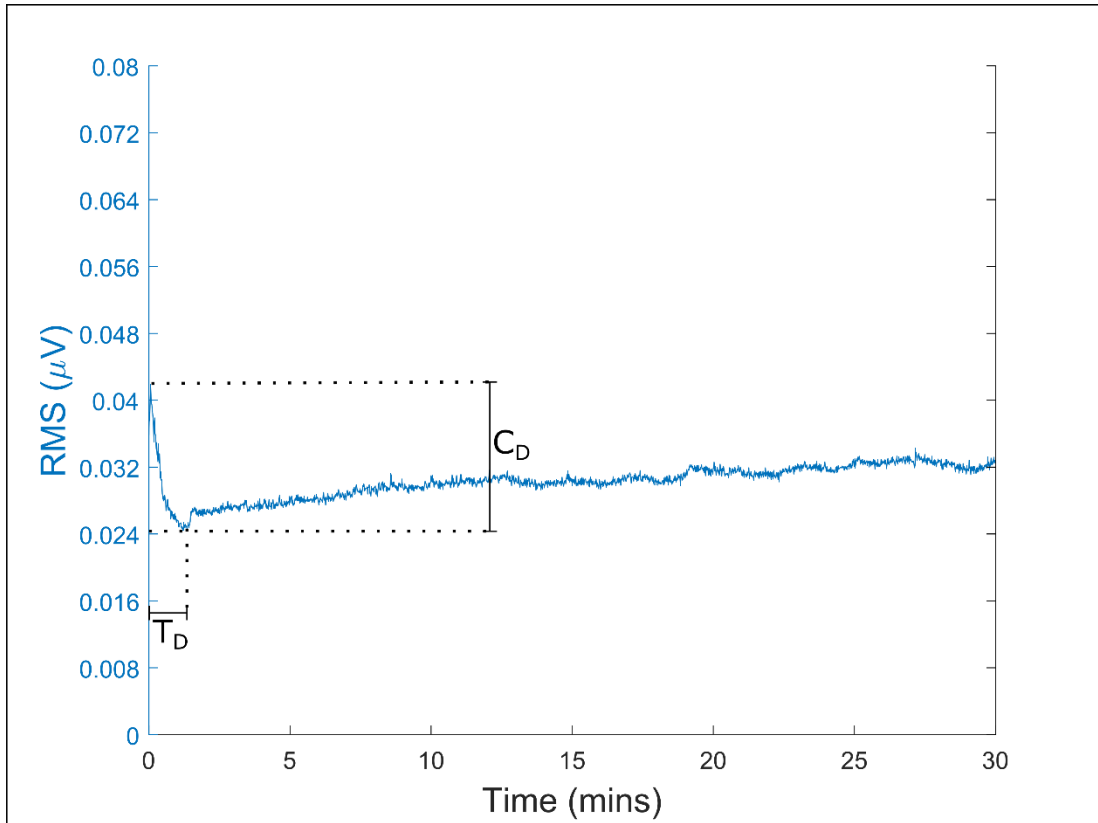


Figure 5.3 - Annotated RMS graph showing measurement parameters. T_D = Time to drop, C_D = Value change from start to drop.

It can be seen that for the coefficient of friction data there is a peak and then a drop in the data, this is measured through T_P and T_D respectively. T_D was chosen to be taken from the start of the test as opposed to the start of the peak as I wanted to ensure that the time to drop for the acoustic emission data could be directly compared to that of the coefficient of friction data.

Figure 5.4 and Figure 5.5 show the average values \pm standard error of the mean of the previously described parameters taken from multiple tests ($n=6$).

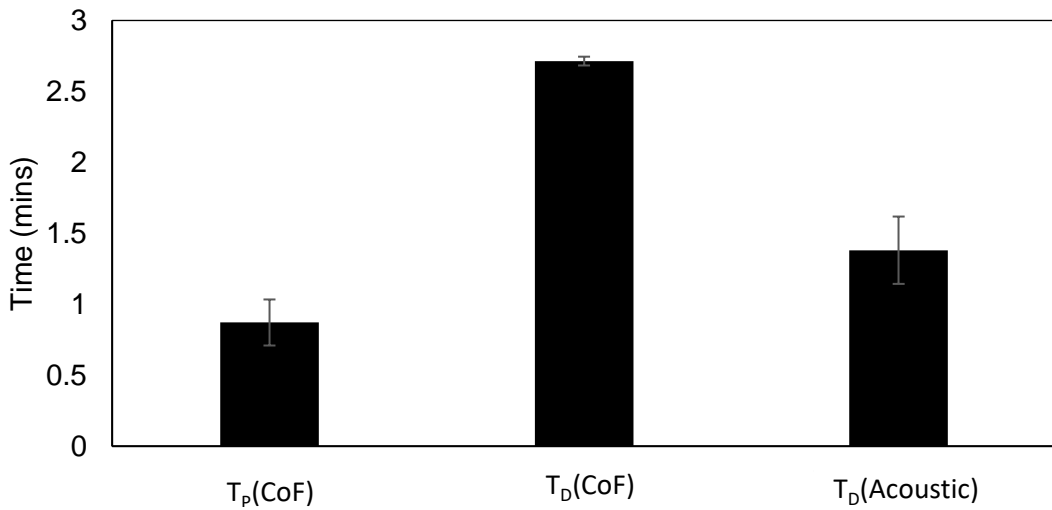


Figure 5.4 - Measurements of the time taken to reach the 'peak' (T_p) and 'drop' (T_d) for coefficient of friction and acoustic emission data. (Data is shown as mean \pm s.e.m. $n = 6$).

It can be seen in Figure 5.4 that across multiple tests the amount of time taken for the coefficient of friction to first increase and then decrease is highly repeatable. On average the time taken to reach the first peak is 52 seconds \pm 9 seconds, the time taken for the coefficient of friction to drop once a MoS_2 film has formed is 162 seconds \pm 1.86 seconds. The acoustic emission data also shows similar repeatability with an average time to drop of 88 seconds \pm 14 seconds.

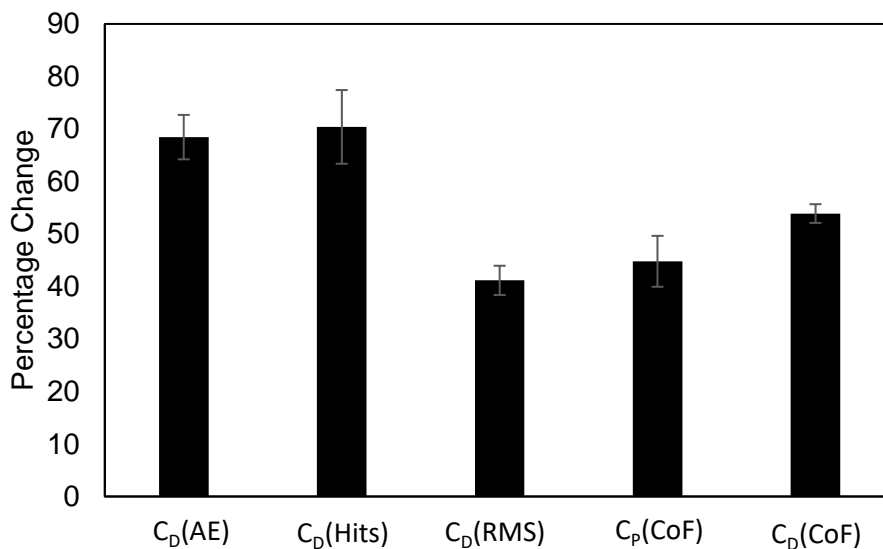


Figure 5.5 - Measurements of the percentage change in magnitude for various parameters relating to coefficient of friction and acoustic emission data. (Data is shown as mean \pm s.e.m. $n = 6$).

Figure 5.5 shows the magnitude related parameters described previously in Figure 5.2 and Figure 5.3, the data is shown as a percentage change so that all of the data can be shown on one graph.

The average percentage change in the acoustic emission data from the start to the drop is $68.4\% \pm 4.2\%$, $70.4\% \pm 7\%$ and $41.16\% \pm 2.8\%$ for absolute energy, hits, and RMS, respectively. The average percentage change from the start to the peak and the start to the drop for the coefficient of friction data is $44.8\% \pm 4.9\%$ and $53.9\% \pm 1.8\%$, respectively.

It has been shown in Figure 5.4 and Figure 5.5 that both the acoustic emission and the coefficient of friction responses are very repeatable across multiple tests. Therefore, the data from only one test will be shown as a representative example. This can be seen in Figures 5.6, 5.7 and 5.8.

The coefficient of friction shown in Figures 5.6, 5.7 and 5.8 represent the expected MoDTC curve whereby the coefficient of friction is drastically reduced following the initial induction period once the MoS₂ tribofilm has been formed. The coefficient of friction decreases dramatically from ~ 0.08 to ~ 0.04 after approximately 2 minutes. A coefficient of ~ 0.04 is sustained for the remainder of the test.

Overall, all 3 acoustic emission parameters exhibit the same trend as the coefficient of friction whereby there is an initial high value at the beginning of the test followed by a drastic reduction which is then maintained for the remainder of the test. Where the coefficient of friction and the acoustic emission data differ is during the induction period. In the very early stages of the test it can be seen that the acoustic emission parameters do not exhibit the same behaviour as the coefficient of friction, this will be explored in greater detail in Section 5.2.

The absolute energy, shown in Figure 5.6 decreases from an initial value of 4.8×10^{-4} to 1.6×10^{-4} μVs after approximately 30s. The absolute energy is seen to increase steadily to $\sim 2.4 \times 10^{-4}$ μVs after 15 minutes before levelling out at for the remainder of the test.

Figure 5.7 shows the hit count measured throughout the test and the same trend can be seen in this data as that shown for the absolute energy. The hit count decreases from an initial value of ~ 15000 to ~ 5000 in the first 30 seconds of the test. As with the absolute energy the hit count steadily increases for around 12 minutes to ~ 10000 wherein it remains steady for the duration of the test.

Finally, Figure 5.8 shows the RMS data for the test. It can be seen that the RMS signal broadly follows the same trend as the absolute energy and hit count. In the first 30 seconds the RMS signal reduces from an initial value of $\sim 0.04 \mu\text{V}$ to $\sim 0.024 \mu\text{V}$. However, the RMS signal appears to plateau at $\sim 0.032 \mu\text{V}$ at around 7 minutes. This plateau appears much earlier in the test than the absolute energy and hit count, the reasoning behind this is currently unclear.

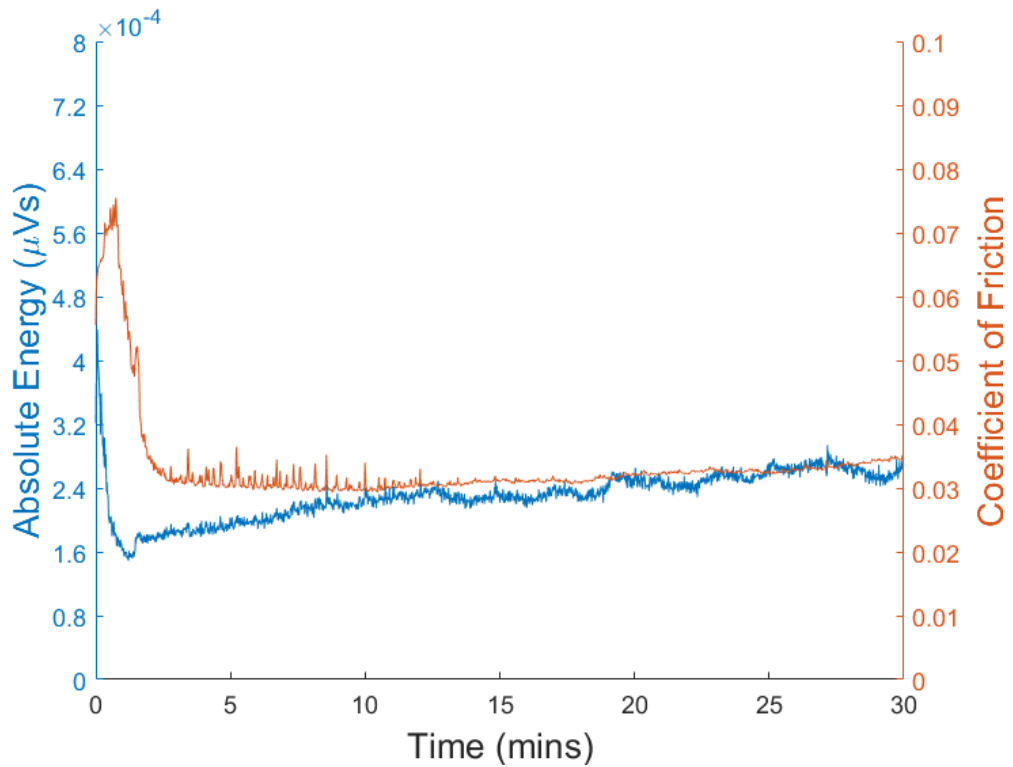


Figure 5.6 - Absolute energy and coefficient of friction data for tribotest conducted in PAO + 0.1wt% MoDTC. (Contact Pressure: 2.29 GPa, Speed: 1000 RPM and Temperature 100 °C).

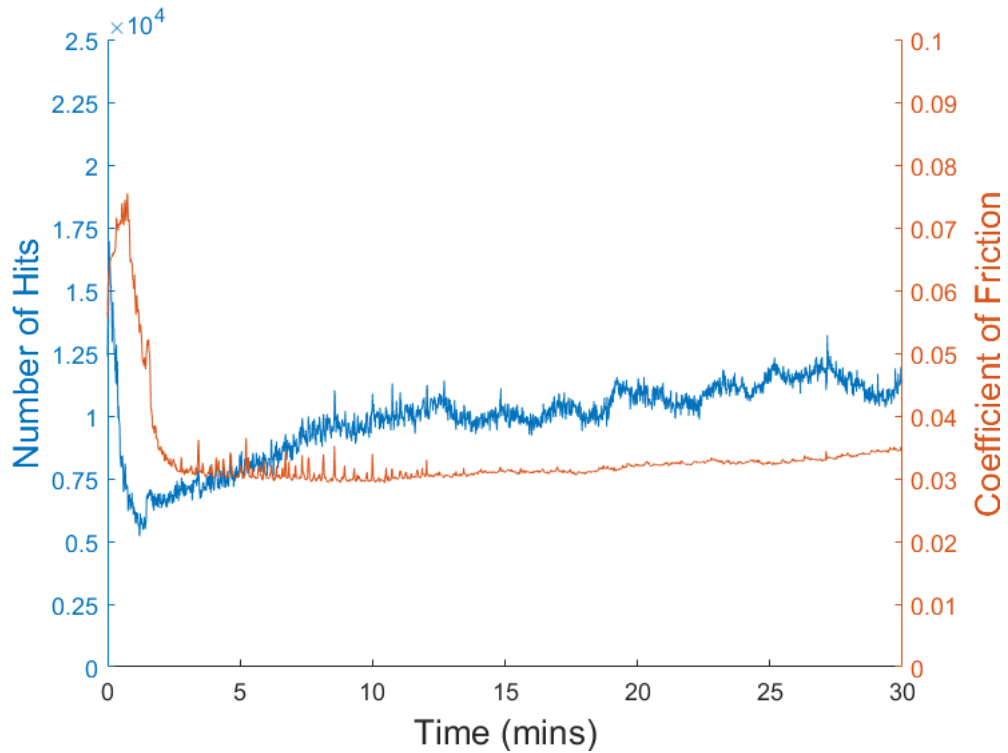


Figure 5.7 - Acoustic emission hit count and coefficient of friction data for tribotest conducted in PAO + 0.1wt% MoDTC. (Contact Pressure: 2.29 GPa, Speed: 1000 RPM and Temperature 100 °C).

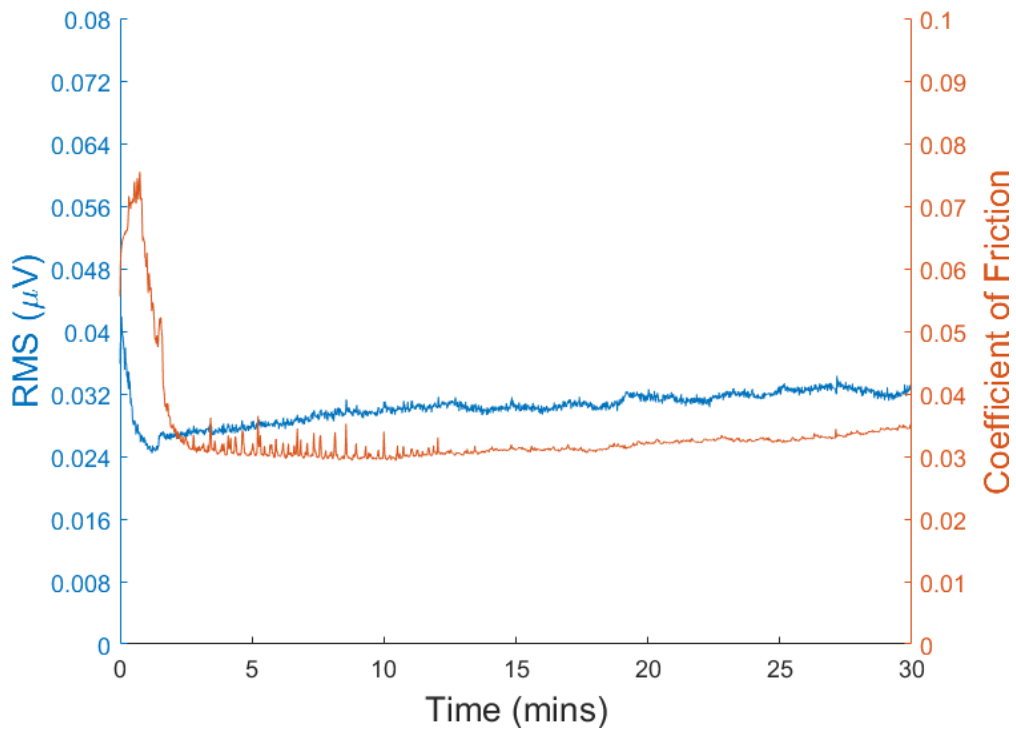


Figure 5.8 - RMS and coefficient of friction data for tribotest conducted in PAO + 0.1wt% MoDTC. (Contact Pressure: 2.29 GPa, Speed: 1000 RPM and Temperature 100 °C).

As previously discussed in Section 1.2.2.1, it is known that the reduction in the coefficient of friction is indicative of the formation of a MoS₂ tribofilm. Globally the same trend is shown in both the acoustic emission and coefficient of friction data, this indicates that there is a direct link between the acoustic emissions being produced at the interface and the formation of a MoS₂ tribofilm i.e. the formation of the tribofilm directly affects the acoustic emission response.

For all 3 acoustic emission parameters shown in Figures 5.6, 5.7 and 5.8 it can be seen that the acoustic emission signal reduces in value prior to any reduction of the coefficient of friction. If it is taken that the reduction in coefficient of friction is indicative of MoS₂ formation and that there is a direct link between the acoustic emission signal and MoS₂ formation, this data shows that the acoustic emission sensor is more sensitive to MoS₂ tribofilm formation than coefficient of friction measurements.

5.2 Early Stages of MoS₂ Tribofilm Formation

It can be seen in the previous figures that the acoustic emission response during the initial induction, whilst the tribofilm is forming, is different to that shown when the tribofilm is established. It has been shown in this work that when MoDTC is used as an additive there is a very large reduction in the acoustic emission signal at the very early stages of the test. This reduction precedes the established friction reduction that has previously been used to determine the formation of a MoS₂ tribofilm. With this in mind, a series of experiments, 7 different time points each with 3 repeats, were conducted so that the chemical composition of the tribocontact could be measured during the initial film formation period and therefore it could be determined whether the acoustic emission signal is representative of the tribofilm formation.

Test conditions for the tribotest are the same as that shown in Table 1 with the exception of test duration which are as follows: 10s, 20s, 30s, 60s, 90s, 180s and 300s.

Figure 5.9 shows the stark difference in the response times between the acoustic emission and coefficient of friction data when a tribofilm is formed. It can be seen that the acoustic emission signal starts to reduce from 0.026 μ V to 0.018 μ V at ~15s whereas the coefficient of friction starts to decrease from 0.077 to 0.037 at ~ 60s.

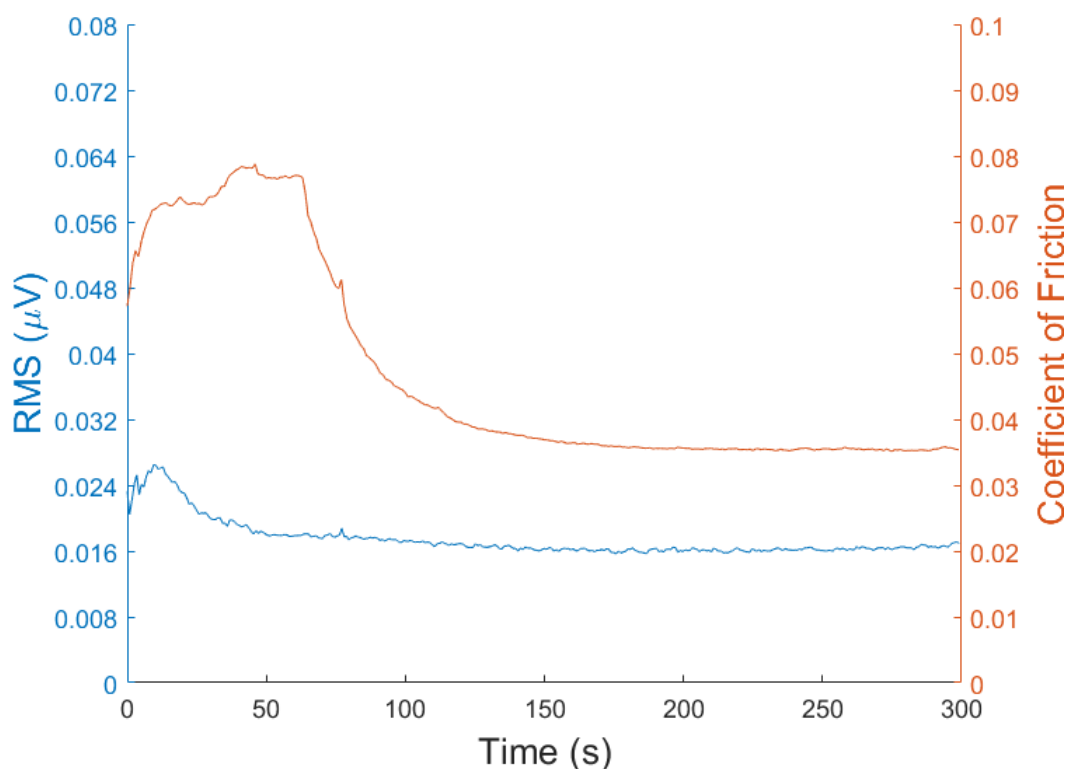


Figure 5.9 – RMS and coefficient of friction data from a test conducted using PAO + 0.1 wt% MoDTC as a lubricant. (Test duration: 300 seconds, Temperature: 100 °C, Rotational Speed: 1000 RPM, Contact Pressure: 2.29 GPa).

Raman spectroscopy analysis was used to determine the presence of MoS₂ and related reaction products formed during tribotests. After tests, samples were rinsed in heptane in an ultrasonic bath before Raman analysis. As discussed by Khaemba et al. (2016), Raman analysis can be performed on unrinsed samples, however by rinsing the samples with heptane a better signal of the MoDTC decomposition products can be observed.

As previously discussed in Section 2.4.1, Raman analysis was conducted using a Renishaw InVia spectrometer (UK). The spectrometer has a spectral resolution of 1 cm⁻¹ and a lateral resolution of 800 nm. Raman spectra were acquired with an Olympus 50x objective with a numerical aperture (N.A) of 0.75 in a backscattering configuration. All spectra were collected at 1 mW laser power with a 1 second exposure time for 10 accumulations.

Figure 5.10 shows a combination plot of each of the Raman spectra obtained from the disk wear scars from all of the experiments, for clarity each spectra has been shifted in the Y direction. An overview of how the chemical composition changes with respect to time can be observed, the spectra for

each time point and the corresponding analysis will be discussed in detail in the successive paragraphs.

It can be seen that for test durations of 60 seconds and longer, typical E_{12G} and A_{1G} MoS_2 peaks are observed at 379 cm^{-1} and 411 cm^{-1} . Typical MoS_2 peaks are not observed at test durations less than 60 seconds. Figure 5.10 also shows that there is a broad peak around 400 cm^{-1} for test durations of 30 seconds and 45 seconds, this broad peak has previously been found to be representative of amorphous sulphur-rich molybdenum, MoS_x ($x > 2$) (Khaemba et al., 2015, Wang et al., 2013).

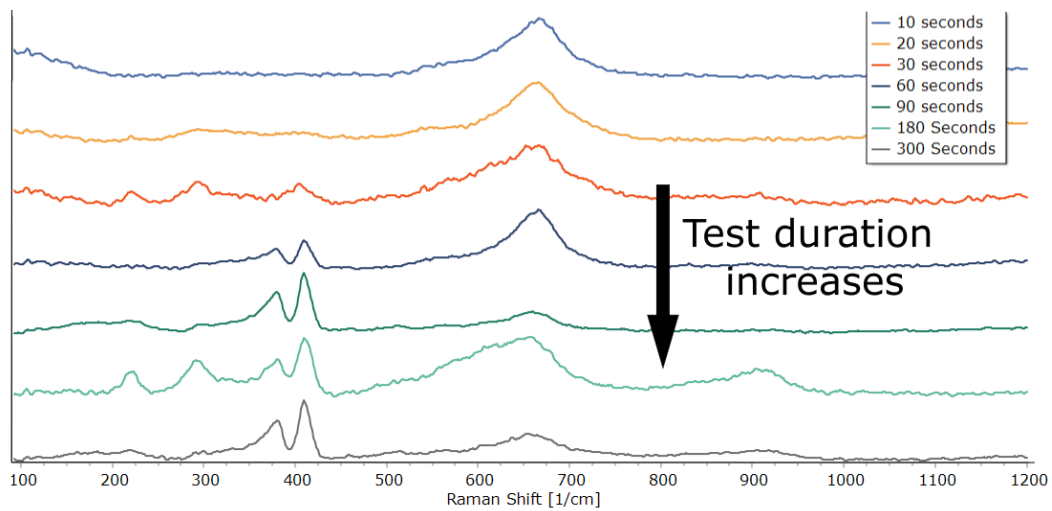


Figure 5.10 - Raman spectra obtained from disk wear scars generated at different test durations. All spectra were obtained using 1 mW laser power, 1 second exposure and 10 accumulations. The spectra are plotted on different scales and have been shifted vertically for clarity.

Figures 5.11-5.17 show the individual spectra for each time point. For each spectra the peaks present were analysed to determine the chemical composition of the wear scar at each time point.

Figure 5.11 shows a typical spectrum obtained from the disk wear scar test after 10 seconds. The spectra shows no presence of MoS₂ peaks. A peak is observed at ~670 cm⁻¹ (Fe₃O₄) (Colomban et al., 2008), the peaks at 1344 cm⁻¹ and 1599 cm⁻¹ are attributed to formation of amorphous carbon (Khaemba et al., 2015, Zabinski and McDevitt, 1996)

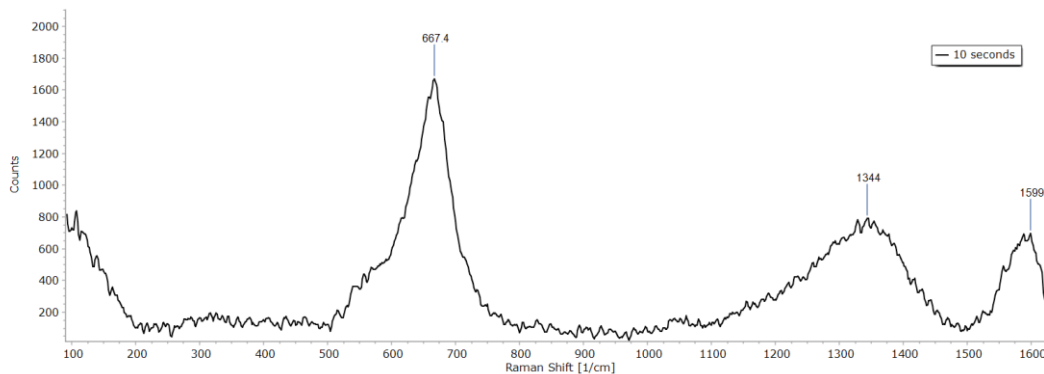


Figure 5.11 - Raman spectra obtained from sample disk after 10 second test.

Figure 5.12 shows a typical spectrum from the disk wear scar after 20 seconds. Peaks relating to Fe₃O₄ and amorphous carbon are also observed at 666 cm⁻¹ and 1353 cm⁻¹ & 1584 cm⁻¹ respectively. A broad peak is observed at 294.5

cm^{-1} this is assigned to the first order Raman mode E_{1G} of MoS_2 (Wieting, 1973, Scheuschner et al., 2015).

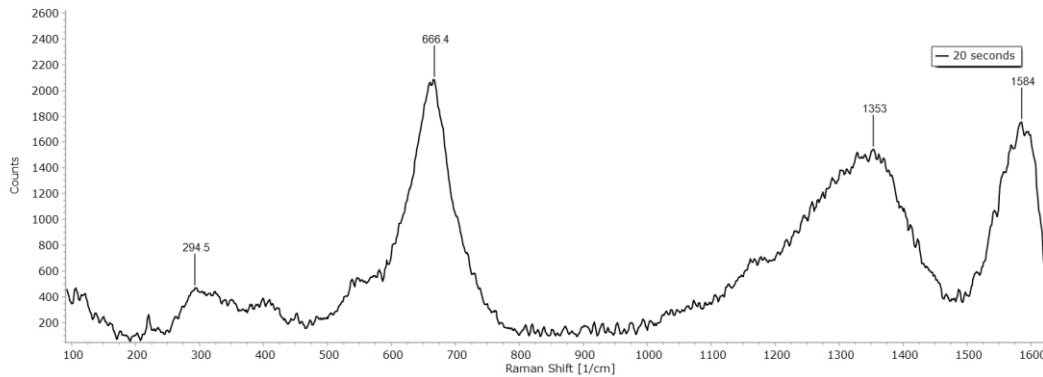


Figure 5.12 - Raman spectra obtained from sample disk after 20 second test.

Figure 5.13 shows a typical spectrum from the disk wear scar after 30 seconds. Once again peaks assigned to Fe_3O_4 and amorphous carbon are observed at 666.5 cm^{-1} and 1302 cm^{-1} & 1575 cm^{-1} respectively. A broad peak assigned to the E_{1G} mode of MoS_2 can still be seen at 293 cm^{-1} . The peak shown here at 404.1 cm^{-1} can be assigned to the A_{1G} peak of MoS_2 . The broad peak from 200 cm^{-1} – 500 cm^{-1} can also be assigned to the formation of amorphous sulphur rich molybdenum MoS_x ($x > 2$) compounds (Khaemba et al., 2015, Wang et al., 2013).

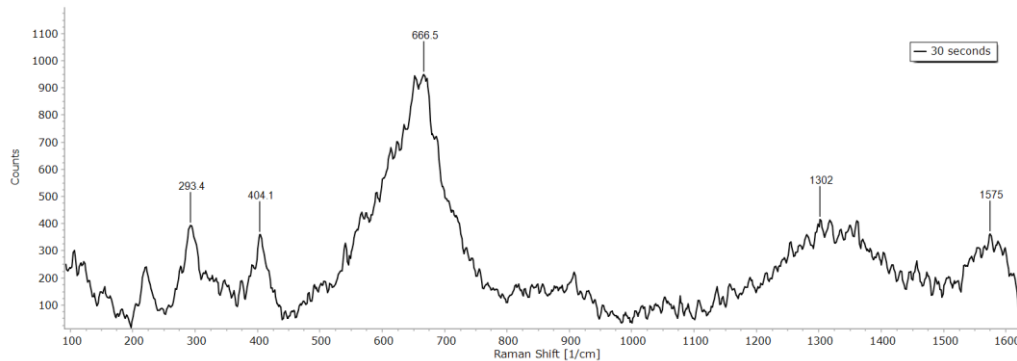


Figure 5.13 - Raman spectra obtained from sample disk after 30 second test.

Figure 5.14 shows a typical spectrum from the disk wear scar after 45 seconds. Peaks assigned to Fe_3O_4 and amorphous carbon can again be observed at 664.2 cm^{-1} and 1341 cm^{-1} & 1587 cm^{-1} respectively. The A_{1G} peak assigned to MoS_2 can still be seen at 406.2 cm^{-1} within the broad 200 cm^{-1} – 500 cm^{-1} peak assigned to the amorphous MoS_x compounds.

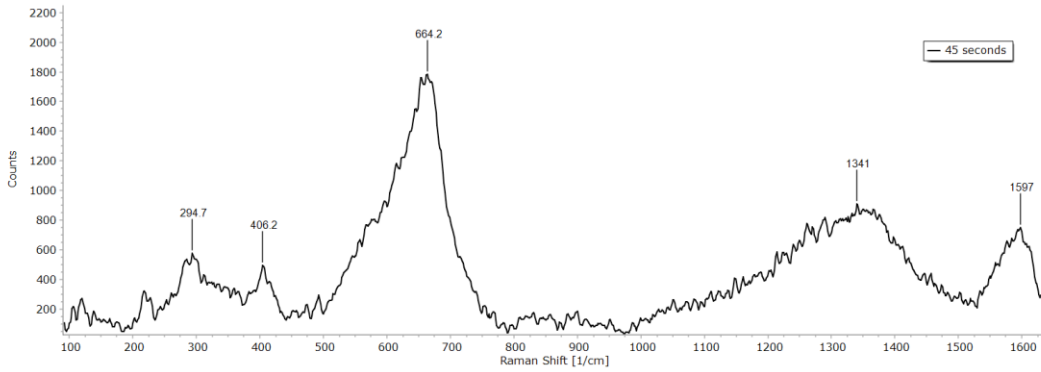


Figure 5.14 - Raman spectra obtained from sample disk after 45 second test.

Figure 5.15 shows a typical spectrum from the disk wear scar after 60 seconds. Peaks assigned to Fe_3O_4 and amorphous carbon can still be seen at 666.7 cm^{-1} and 1334 cm^{-1} & 1588 cm^{-1} respectively. Distinct MoS_2 peaks can be observed at 379.1 cm^{-1} (E_{12G} peak) and 409.8 cm^{-1} (A_{1G} peak).

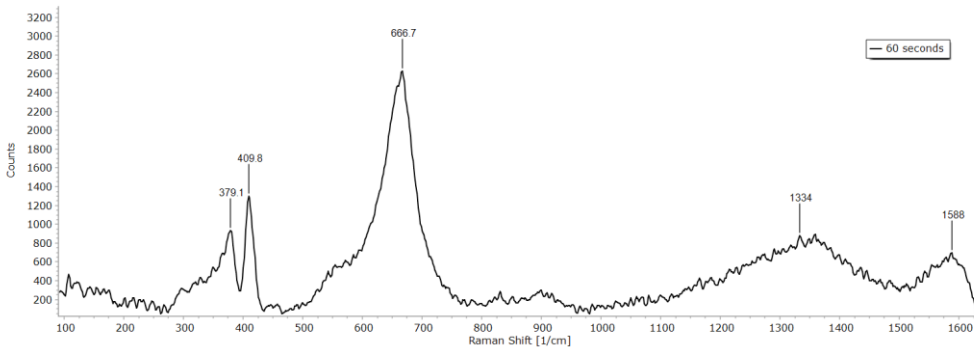


Figure 5.15 - Raman spectra obtained from sample disk after 60 second test.

Figure 5.16 shows a typical spectrum from the disk wear scar after 180 seconds. First order LA(M) peak can be seen at 222.3 cm^{-1} alongside a broad peak at 290.7 cm^{-1} which is assigned to the first order Raman mode E_{1G} . The peak assigned to Fe_3O_4 can still be seen at 657 cm^{-1} . Once again distinct MoS_2 peaks can be observed at 381 cm^{-1} (E_{12G} peak) and 410.1 cm^{-1} (A_{1G} peak). A peak assigned to FeMoO_4 can be seen at 904.9 cm^{-1} (Khaemba et al., 2016).

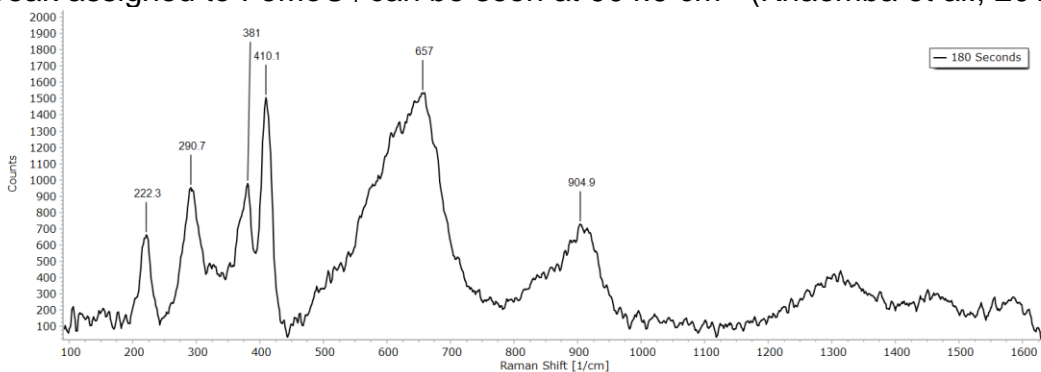


Figure 5.16 - Raman spectra obtained from sample disk after 180 second test.

Figure 5.17 shows a typical spectrum from the disk wear scar after 300 seconds. A peak assigned to the first order LA(M) can be seen at 219.3 cm^{-1} . Distinct MoS₂ peaks can be observed at 380.6 cm^{-1} (E_{12G} peak) and 409.6 cm^{-1} (A_{1G} peak). The peak assigned to Fe₃O₄ can still be seen at 653.9 cm^{-1} . A peak assigned to FeMoO₄ can be seen at 904.9 cm^{-1} and peaks assigned to amorphous carbon can once again be seen at 1334 cm^{-1} and 1588 cm^{-1} .

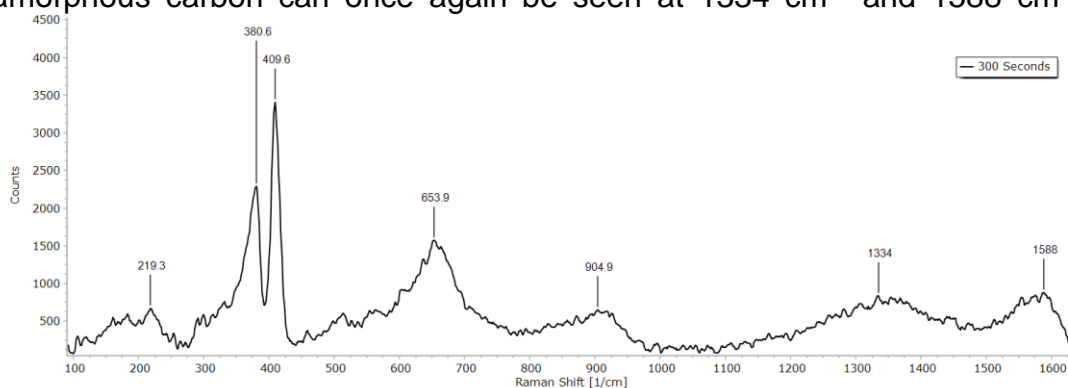


Figure 5.17 - Raman spectra obtained from sample disk after 300 second test.

Figures 5.11-5.17 show how the chemical composition of the wear scar of test disks evolves over time, this data combined with Figure 5.9 can be used to determine which point in the tribofilm development is responsible for the reductions in acoustic emission and coefficient of friction.

Figure 5.9 shows that the acoustic emission data begins to reduce at ~15 seconds and plateaus at ~30 seconds. Figure 5.12 shows spectra taken at 20 seconds, this shows peaks linked to the presence of amorphous molybdenum and sulphur. Figure 5.13 shows the Raman spectra taken at 30 seconds, both E_{1G} and A_{1G} peaks can be seen at $\sim 294\text{ cm}^{-1}$ and 404 cm^{-1} respectively. These findings are in line with Lee et al. (2010) and Li et al. (2012) who found that for few layers of MoS₂ that the A_{1G} peak blue shifts from around 409 cm^{-1} to a lower value.

In comparison, the coefficient of friction only begins to reduce at ~60 seconds and plateaus at ~120 seconds. Figure 5.15 shows the Raman spectra taken at 60 seconds, distinct MoS₂ peaks can be observed at 379.1 cm^{-1} (E_{12G} peak) and 409.8 cm^{-1} (A_{1G} peak).

Combining the above information, it can be seen that the acoustic emission signal begins to reduce when there is amorphous molybdenum and sulphur present and plateaus when the first few layers of MoS₂ begin to form. In contrast, the coefficient of friction only begins to reduce when there is a more substantial amount of MoS₂ present.

This indicates that acoustic emissions are more sensitive to the presence of MoS₂ than the coefficient of friction and that the acoustic emission sensor is capable of detecting the very small amount of MoS₂ that is present on the disk after 30 seconds.

5.3 Frequency Analysis

Whilst the traditional acoustic emission parameters of absolute energy, hits and RMS are useful in showing how the acoustic emission signal is changing along the course of the experiment, they give no insight into the frequencies of the signals that produce them. In order to determine whether changes in the tribochemical environment such as the formation of a tribofilm had a direct impact on the frequencies present in the acoustic emission signal, FFT analysis was performed approximately every 30 seconds. This allows an insight into the frequency domain of the signal and how that may change over time as the tribocontact evolves.

Figure 5.18 shows the frequency spectra taken at specific timepoints that reflect key stages in the tribofilm development such as initial formation, tribofilm development and fully established film. These time periods were taken at approximately 30 seconds, 5 minutes, 10 minutes and 30 minutes, respectively.

For the FFT taken at 30 seconds it can be seen that at a frequency of around 100 kHz there is a large peak with an amplitude of around 5×10^{-6} . It can be seen that as the test progresses the amplitude of the peak at around 100 kHz reduces to around 3×10^{-6} by the 30 minute mark. This data shows that when a MoS₂ tribofilm is present ($T > 5$ minutes) then the magnitude of the 100 kHz peak is much lower than when no tribofilm has formed.

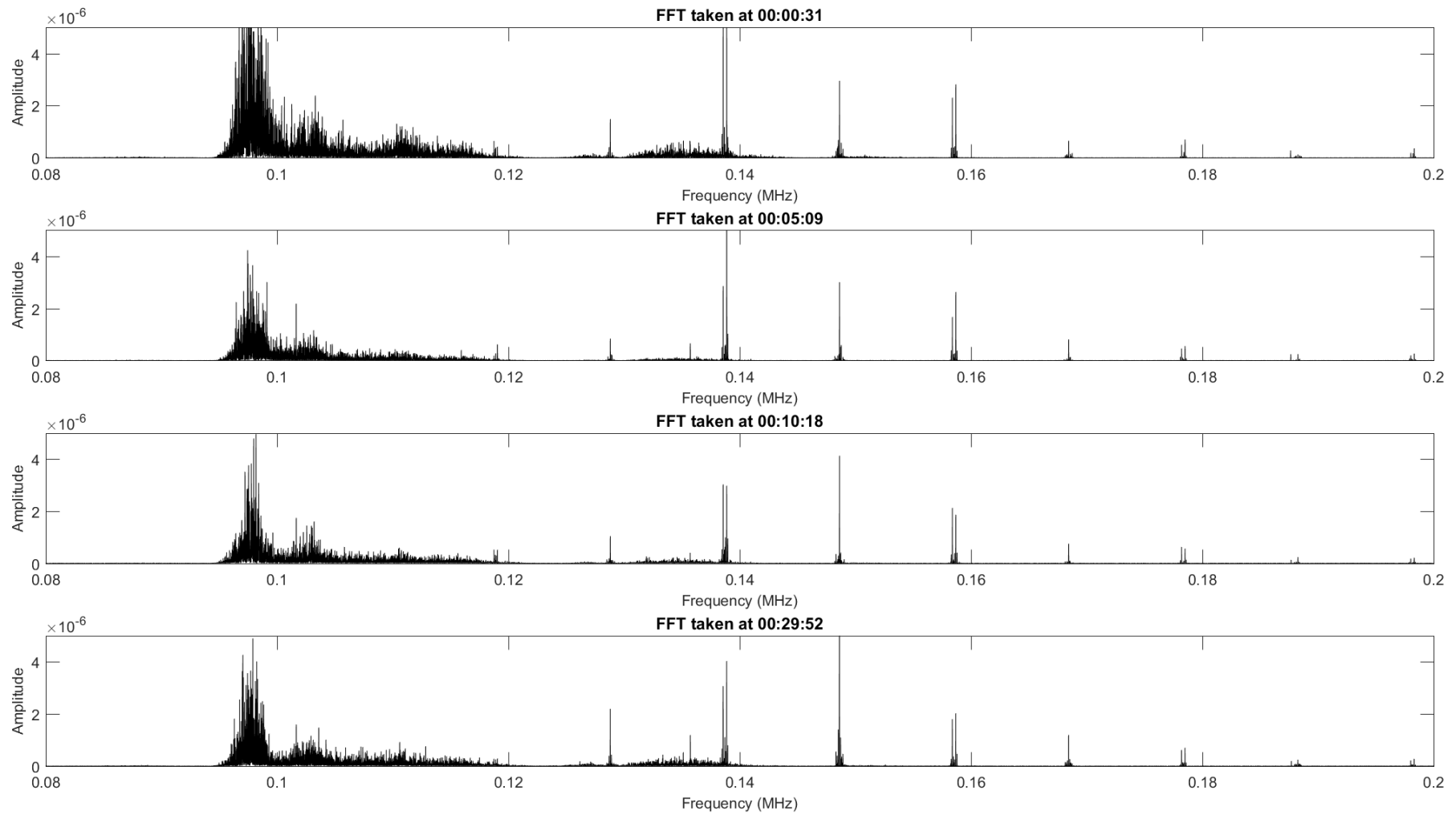


Figure 5.18 - FFT analysis taken at ~30 seconds, 5 minutes, 10 minutes and 30 minutes.

5.4 Tribofilm Removal

It is known that the MoS₂ containing tribofilm is not tenacious and without the presence of the MoDTC containing additive the tribofilm is destroyed (Morina and Neville, 2007b). The aim of this experiment is to determine whether the acoustic emission sensor is capable of detecting the removal of the tribofilm.

In this test, PAO + 0.1wt% MoDTC was used as the lubricant for the first 30 minutes with the same test parameters as in the previous experiments discussed in Section 5.1. After 30 minutes, the PAO + 0.1 wt% MoDTC was removed and replaced with PAO alone. Figure 5.19 shows the acoustic emission and coefficient of friction traces collected throughout the test. The solid vertical red line indicates the point at which the additive laden oil was replaced with pure PAO. In the first 30 minutes of the test the same trend for both acoustic emission and coefficient of friction as shown in Figure 5.8 can be seen, as such it can be determined that a MoS₂ tribofilm has successfully formed.

Figure 5.19 shows the effect of changing the lubricant once a MoS₂ tribofilm has been formed. This tribofilm formation and removal can be clearly seen and is shown both in the coefficient of friction data and the acoustic emission RMS data.

Initially, the RMS signal is aligned with the coefficient of friction data as shown previously in Figure 5.8. However, when the MoDTC additive is removed and replaced with PAO only, a very noticeable change occurs in both the coefficient of friction and RMS values. Both traces increase instantaneously to a higher value than observed when MoDTC was present in the oil. Following this, both data following broadly the same trend return to approximately the same value of coefficient of friction and RMS as prior to film formation. This indicates that the tribofilm has been successfully removed.

In Figure 5.19 it can be seen that the acoustic emission data broadly shows the same trend as the coefficient of friction data, showing the same peaks and valleys as the friction data. However, similarly to data shown in Figure 5.8, the acoustic emission data appears to exhibit these changes sooner than the coefficient of friction data.

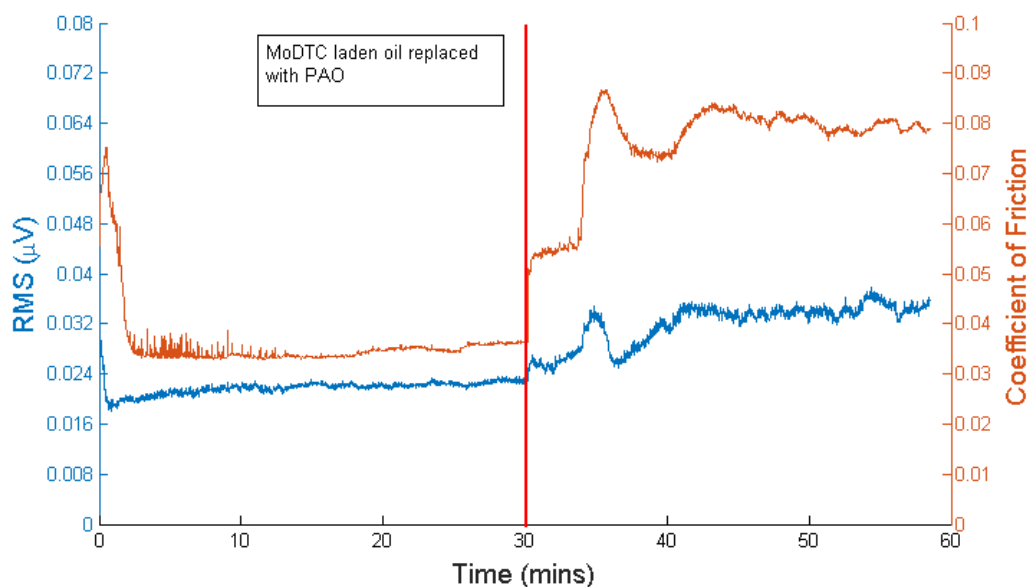


Figure 5.19 - Graph showing the acoustic emission and coefficient of friction data from a tribofilm removal test conducted in PAO + 0.1wt% MoDTC. (Test duration: 60 minutes, Temperature: 100 °C, Rotational Speed: 1000 RPM, Contact Pressure: 2.29 GPa).

Figure 5.20 shows the same data as Figure 5.19 but with an exaggerated x-axis so that the key moment when the tribofilm is removed can be further investigated.

It can be seen that both the acoustic emission and coefficient of friction data increase dramatically once the additive laden oil has been removed. For the coefficient of friction data the increase is very sudden. However, even though the acoustic emission data starts to increase slightly sooner than the coefficient of friction the rate of increase is more gradual.

It has previously been shown that the acoustic emission data is sensitive to the presence of only a few layers of MoS₂, therefore this gradual increase could be indicative of a transition period between a fully formed tribofilm and 100% tribofilm removal.

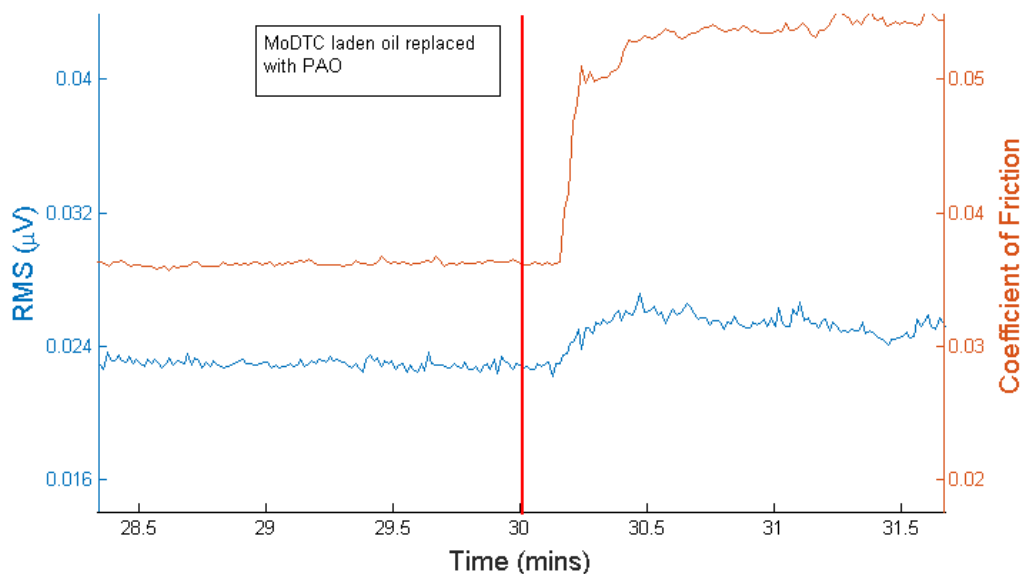


Figure 5.20 – Acoustic emission and coefficient of friction data for tribofilm removal test with exaggerated x-axis to show exact moment when the tribofilm is destroyed.

It can be seen in Figures 5.19 and 5.20 that the acoustic emission methodology implemented in this work is very much capable of detecting the removal of MoS₂ tribofilms *in situ* and in real time. It is also possible that the acoustic emission are more sensitive to MoS₂ tribofilm removal than the coefficient of friction, this is highlighted by an increased responsiveness.

5.5 Acoustic Emission and Wear

A series of tests were conducted ranging from 5 minutes to 30 minutes under the same experimental conditions shown in Table 7. After each test the diameter of the wear scar on the ball was measured using an optical microscope as discussed in Chapter 2. The wear scar diameter was then used to estimate the wear volume loss using Equation 5 (Page 52).

Figure 5.21 shows the wear volume loss for tests conducted for 5-30 minutes. It can be seen that the wear volume loss is relatively steady for tests that last between 5 and 15 minutes, after which point the amount of wear that is observed increases rapidly from $2 \times 10^{-13} \text{ m}^3$ to $5.5 \times 10^{-13} \text{ m}^3$

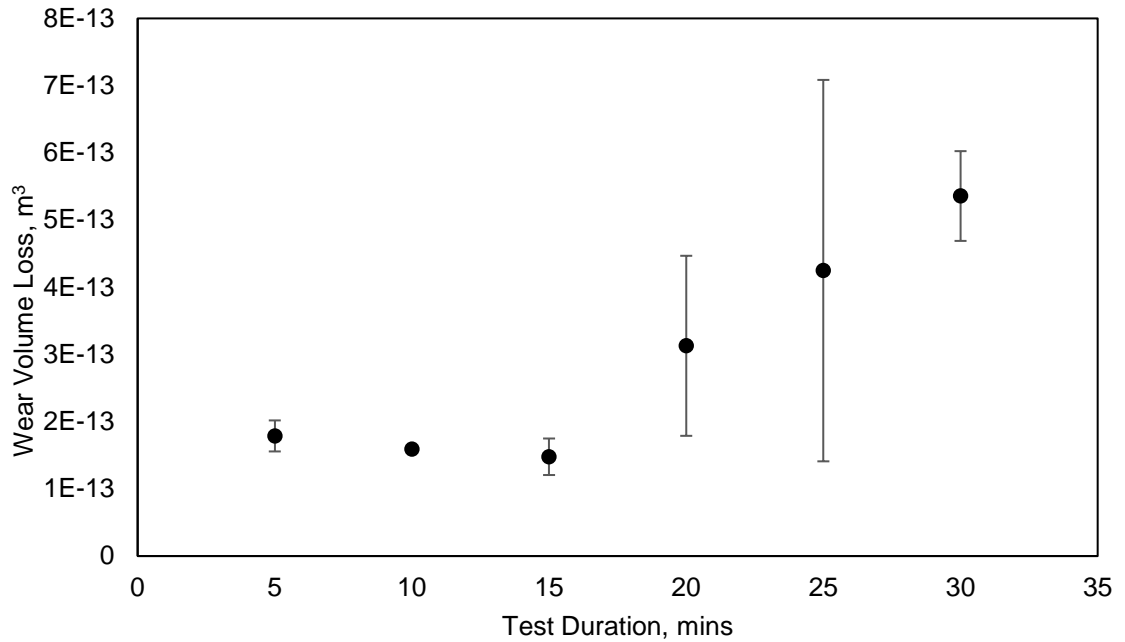


Figure 5.21 - Wear volume loss against time for tests conducted in PAO + 0.1wt% MoDTC. (Data shown as mean ± s.e.m. n≥3).

The cumulative values for each acoustic emission parameter for each test was then plotted against the corresponding wear volume loss figure in order to elucidate whether there is a relationship between the amount of wear produced and the measured acoustic emission values.

Cumulative values are taken as the integrative value of each of the parameters at each time point, for example an equation for the calculation of the cumulative RMS value can be seen below. This allows for a comparison of the real-time *in situ* acoustic emission values and post-test measured values such as the wear volume loss.

$$Cumulative\ RMS = \int RMS\ dt$$

Equation 9 - Calculation of the cumulative RMS value.

Figure 5.22 depicts the relationship between the total wear volume loss and the cumulative absolute energy values for the corresponding tests. An R² value of 0.0341 is reported, this shows that there is no correlation between the two variables.

Figure 5.23 depicts the relationship between the total wear volume loss and the cumulative hit count values for the corresponding tests. An R² value of 0.0043 is reported, this shows that there is no correlation between the two variables.

Figure 5.24 depicts the relationship between the total wear volume loss and the cumulative RMS values for the corresponding tests. An R^2 value of 0.3469 is reported, this shows that there is a very slight correlation between the two variables.

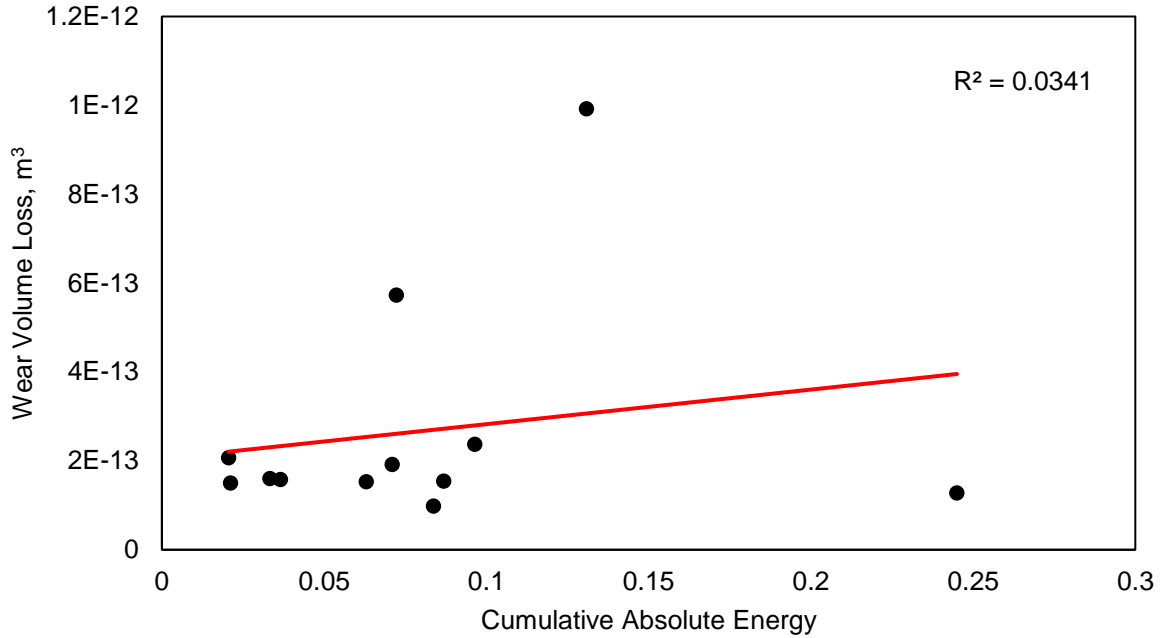


Figure 5.22 - Graph showing relationship between the wear volume loss and cumulative absolute energy (No correlation shown).

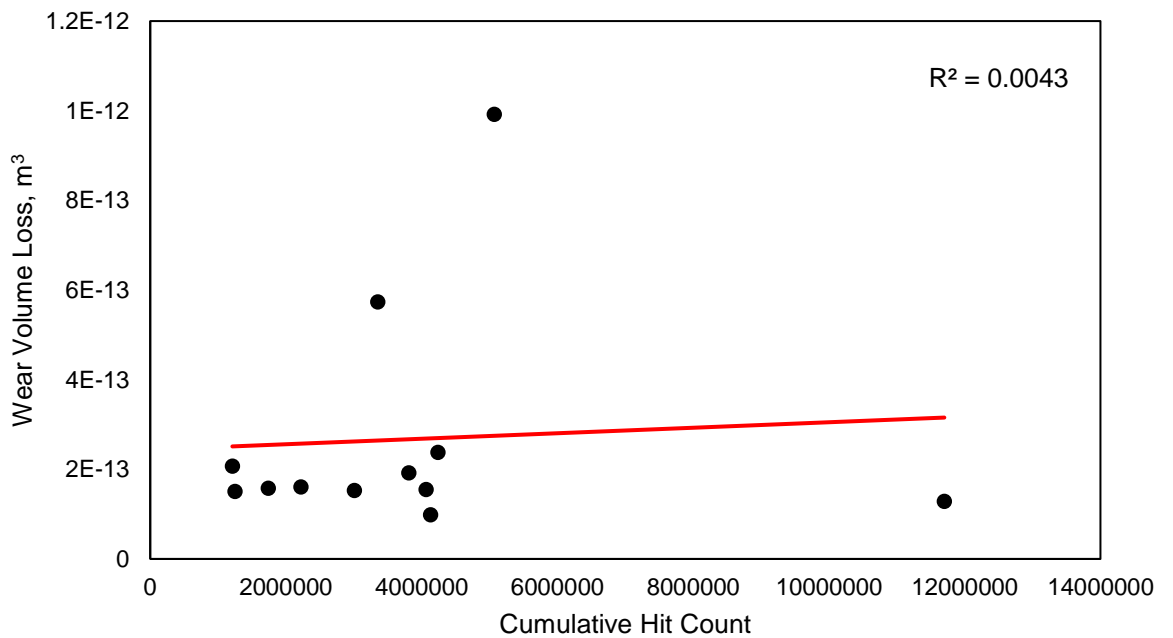


Figure 5.23 - Graph showing relationship between the wear volume loss and cumulative hit count (No correlation shown).

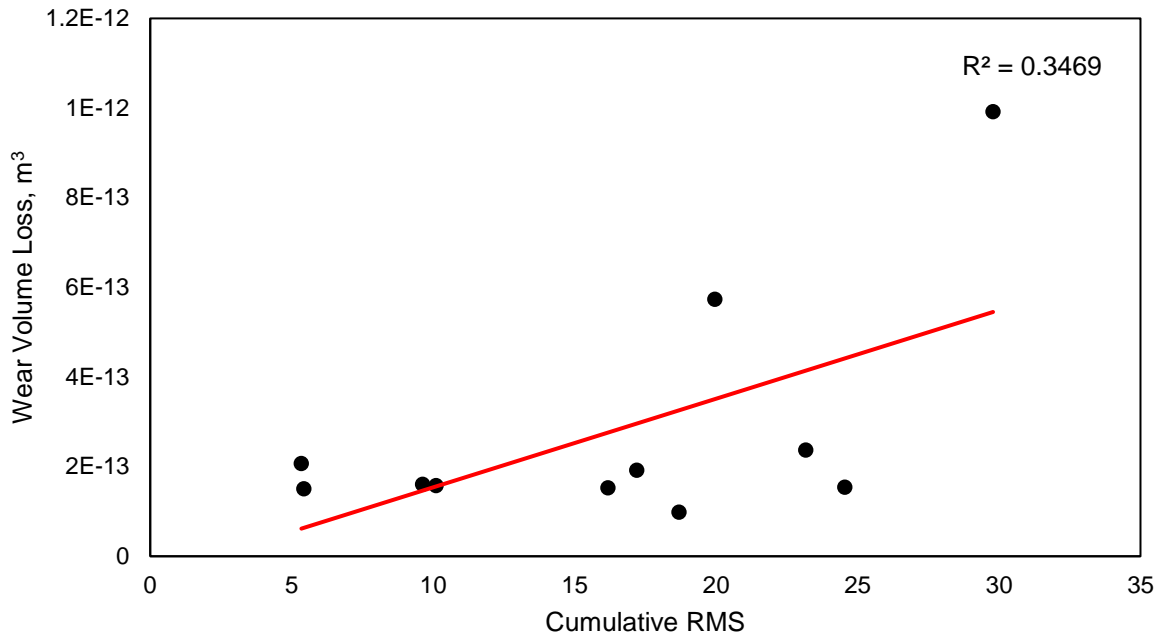


Figure 5.24 - Graph showing the relationship between the wear volume loss and cumulative RMS (No correlation shown).

Figures 5.22-5.24 show that there is little to no correlation between the amount of wear that is produced during a test and the total amount of acoustic emission that is produced. The highest correlation between the two variables comes from the cumulative RMS values, however, the R^2 value is relatively low at 0.3469. This indicates that there is no direct relationship between the measured acoustic emission signals and the amount of wear that is produced.

As discussed in Chapter 1, many authors have previously investigated the use of acoustic emissions in predicting wear with varying success. However, previous studies were conducted using dry contacts, with no one previously investigating the link between wear and acoustic emission on lubricated contacts. As such the relationship shown above was anticipated as it has previously been shown in this work that the acoustic emission data very closely resembles the coefficient of friction data and this is not directly linked with wear, especially in the presence of MoDTC.

5.6 Acoustic Emission and Coefficient of Friction

As previously discussed, a series of tests were conducted, ranging in duration from 5 minutes to 30 minutes under the same test conditions as shown in Table 7. The data at the end of these tests were then collated into a large repository of corresponding coefficient of friction and acoustic emission data. The

coefficient of friction data for multiple tests was then plotted against the corresponding acoustic emission data to determine whether there is a relationship between the acoustic emissions that are produced and the coefficient of friction. Once plotted, Pearson's correlation coefficients were used to determine statistical significance between the two sets of data.

Figure 5.25 shows the correlation between the coefficient of friction and the absolute energy. The figure shows that there is a statistically significant correlation between the two sets of data ($P < 0.0001$), with an R^2 value of 0.852 being reported. The relationship between the coefficient of friction and the absolute energy appears to fit a third-order polynomial, which is shown in red.

Figure 5.26 shows the correlation between the coefficient of friction and the hit count. The figure shows that there is a statistically significant correlation between the two sets of data ($P < 0.0001$), with an R^2 value of 0.863 being reported. The relationship between the coefficient of friction and hit count appears to fit a second-order polynomial, which is shown in red.

Figure 5.27 shows the correlation between the coefficient of friction and the RMS. The figure shows that there is a statistically significant correlation between the two sets of data ($P < 0.0001$), with an R^2 value of 0.845 being reported. The relationship between the coefficient of friction and RMS also appears to fit a second-order polynomial, which is shown in red.

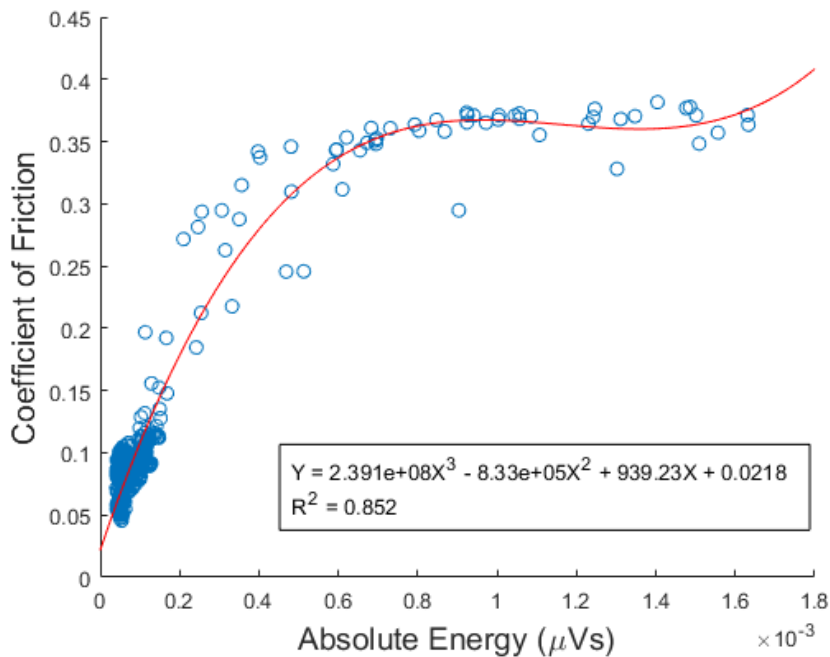


Figure 5.25 - Graph showing the significant correlation (Pearson's Correlation Coefficient, $n=2792$, $P<0.0001$) between CoF and absolute energy values with PAO + 0.1wt% MoDTC as the lubricant.

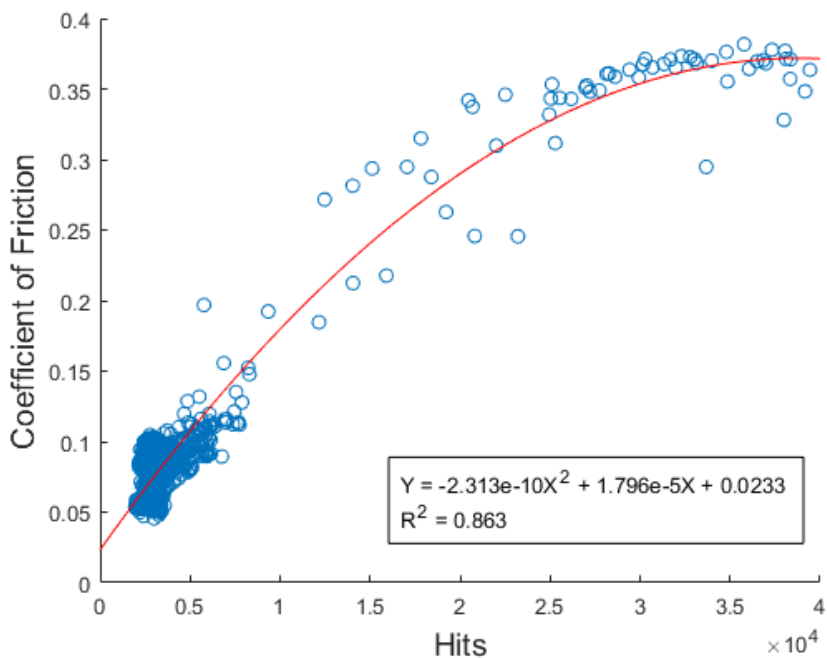


Figure 5.26 - Graph showing the significant correlation (Pearson's Correlation Coefficient, $n=2792$, $P<0.0001$) between CoF and hit count values with PAO + 0.1wt% MoDTC as the lubricant.

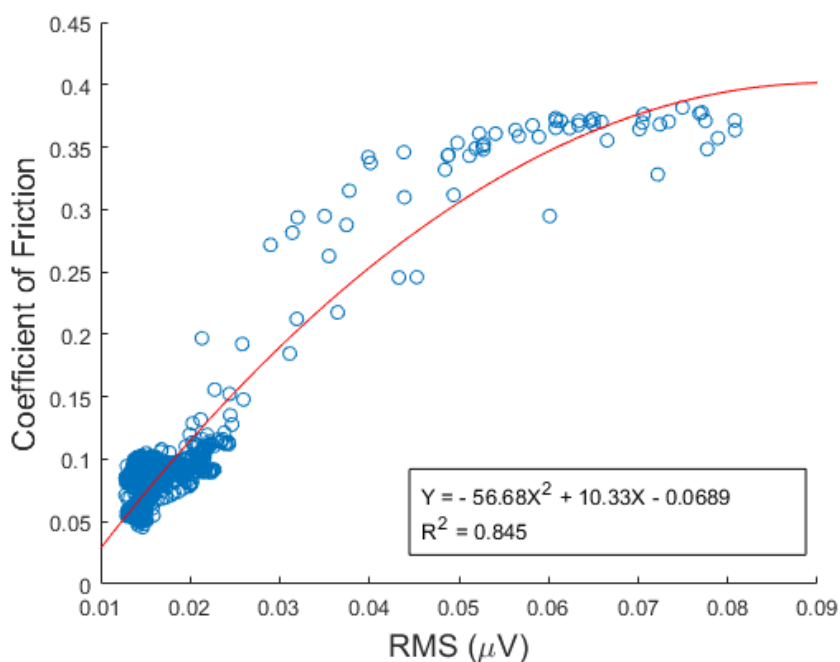


Figure 5.27 - Graph showing the significant correlation (Pearson's Correlation Coefficient, $n=2792$, $P<0.0001$) between CoF and RMS values with PAO + 0.1wt% MoDTC as the lubricant.

It can be seen in Figures 5.25-5.27 that there is a statistically significant relationship between the coefficient of friction and the acoustic emissions that are produced. This relationship, under the presence of lubricant additives, has never previously been explored by other authors in the literature. However, the behaviour of the acoustic emission signal corresponds very similarly to the coefficient of friction data and as such this relationship was anticipated.

5.7 Summary

In this chapter the *in situ* acoustic emission methodology has been used to investigate the capabilities of monitoring the point at which MoS₂ tribofilms are formed and removed. Further investigation into the tribochemical reasoning for the acoustic emission response has also been performed. The findings of this chapter can be summarised as follows:

- For the first time acoustic emission sensing methodology has been used successfully to detect the formation of MoS₂ tribofilm *in situ* and in real time.
- The acoustic emission sensor is more sensitive to the formation of MoS₂ tribofilms than current coefficient of friction methodologies.

- Reduction in acoustic emission RMS amplitude can be attributed to the presence of amorphous molybdenum and sulphur as well as the formation of a few layers of MoS₂ on the surface.
- For the first time the acoustic emission sensing methodology has been used to successfully detect the removal of MoS₂ tribofilms *in situ* and in real time.
- The frequency composition of the acoustic emission signal changes under the presence of a MoS₂ tribofilm.
- No correlation between is observed measured acoustic emission values and the wear produced during testing.
- Statistically significant correlation between measured acoustic emission values and coefficient of friction during testing.

Chapter 6

Monitoring ZDDP Based Tribofilm Formation and Removal Under Boundary Lubricated Conditions

As previously discussed in Section 1.2.2.2, ZDDP is an anti-wear additive that is known to form very tenacious tribofilms. When ZDDP is used as an anti-wear additive it has been widely reported that the coefficient of friction is increased. It is possible to determine the presence of ZDDP tribofilms post-test when wear measurements are taken or EDX analysis is performed on the wear scar.

Following on from Chapter 5, this chapter will investigate the effect that ZDDP additives have on the acoustic emission response during tribotesting. Firstly, experiments were performed to determine the acoustic emission response during ZDDP based tribofilm formation. Following this, EDX analysis was performed to categorically show that a ZDDP tribofilm had been formed. Similarly to the previous chapter, an investigation into the acoustic emission response during tribofilm removal was also performed. FFT analysis has been performed on all tests in this body of work and will be discussed. Finally, an investigation into the relationship between wear volume loss and acoustic emission response will also be performed.

Unlike MoDTC based tribofilms, there is not a specific recognisable coefficient of friction trace that can be followed to determine whether a ZDDP tribofilm has been formed. However, ZDDP film formation is directly linked to increases in the coefficient of friction that is then followed by a plateau (Taylor and Spikes, 2003, Morina et al., 2003). Figure 1 shows a representative coefficient of friction trace from 6 experiments, data is shown as an average \pm standard error of the mean. It can be seen that as the ZDDP tribofilm is formed, on average, the coefficient of friction increases to around 0.09 where it then plateaus for the remainder of the test, this correlates with work produced by Morina et al. (2006).

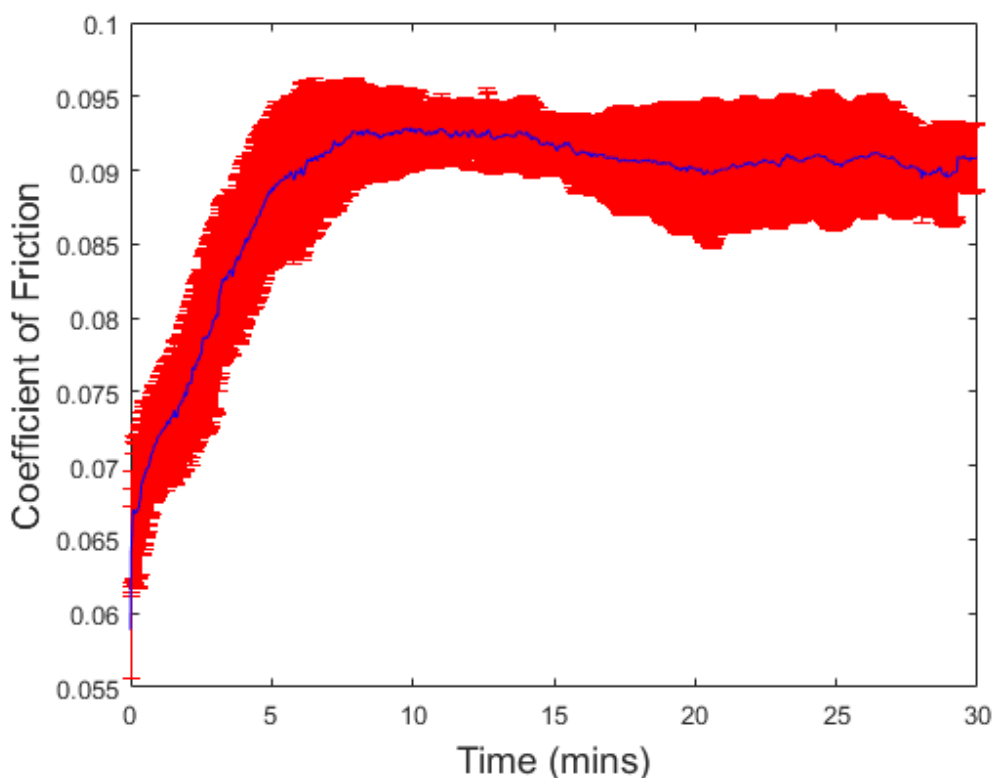


Figure 6.1 - Coefficient of friction response using PAO + 0.55 wt% ZDDP as the lubricant. 1000RPM, 2.29 GPa, 100 °C. (Data shown as mean ± s.e.m. n = 6).

It is currently not known what effect a ZDDP based tribofilm has on the acoustic emission response of the tribosystem. Therefore, the focus of the work in this chapter is to investigate for the first time the acoustic emission response to the formation and removal of ZDDP based tribofilms.

The methods used in this section are described in detail in Chapter 2. However, the key tribotest parameters used during this work are shown in Table 8 below. The parameters shown in Table 8 were chosen to replicate those used in Chapter 5 to ensure that cross additive comparisons could be made using the acoustic emission data.

Table 8 – Test parameters used for investigating the effect ZDDP based additives have on acoustic emission.

Test Condition	Parameters
Base oil	Polyalphaolefin
Additive Concentration	0.55 wt% ZDDP
Temperature	100 °C
Contact Pressure	2.29 GPa
Sliding Speed	1000 RPM (1.75 ms ⁻¹)
Test Duration	5 – 240 minutes
Material	Disk: AISI 1074, Ball: AISI 52100
Hardness	Disk: 60-64 HRC, Ball: 60-67 HRC
Young's Modulus	190-210 GPa (ball and disk)
Roughness, R _a	Disk: R _a = 110 nm , Ball: R _a = 10 nm
Lambda Ratio (λ)	0.25 (boundary lubrication regime)

6.1 Tribofilm Formation

Figure 6.1 shows that as a ZDDP tribofilm is formed the coefficient of friction increases to a point and then plateaus, it is not known however whether the acoustic emission data will replicate this trend as was shown in Chapter 5 when MoDTC tribofilms are formed. Therefore, tests were conducted to determine whether an increase in the coefficient of friction would also result in an increase in the acoustic emission response. Multiple tests (n=6) were conducted at 1000 RPM with a load of 2.5 kg with PAO + 0.55wt% MoDTC as the lubricant.

Across multiple tests key measurements were taken of the coefficient of friction data to quantify repeatability. Figure 6.2 shows an example coefficient of friction graph with the location of the measurements highlighted.

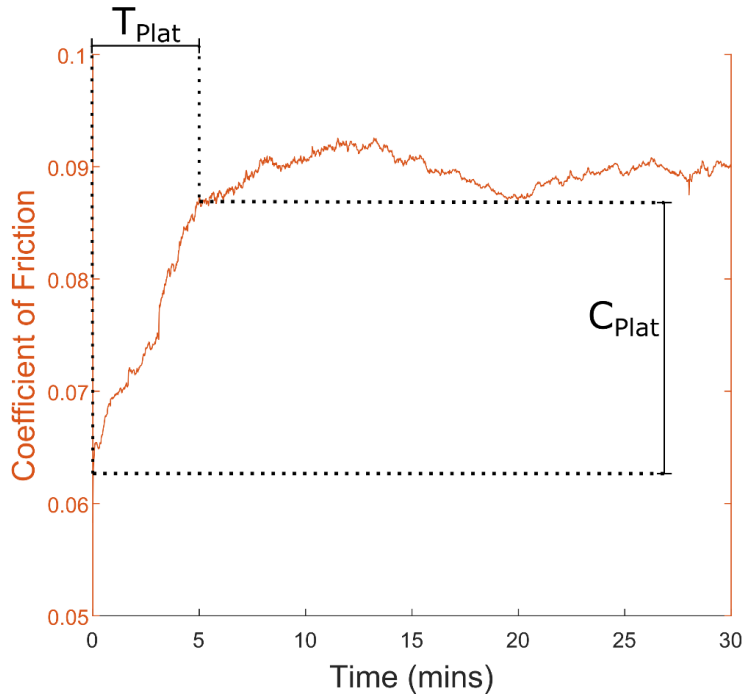


Figure 6.2 - Annotated coefficient of friction graph showing measurement parameters. T_{Plat} = Time to plateau, C_{Plat} = Value change from start to plateau.

Similar measurements were also taken from the acoustic emission data. Figure 6.3 shows the location of the measurements with respect to the RMS data but the same measurements were also taken from the absolute energy and hit count data.

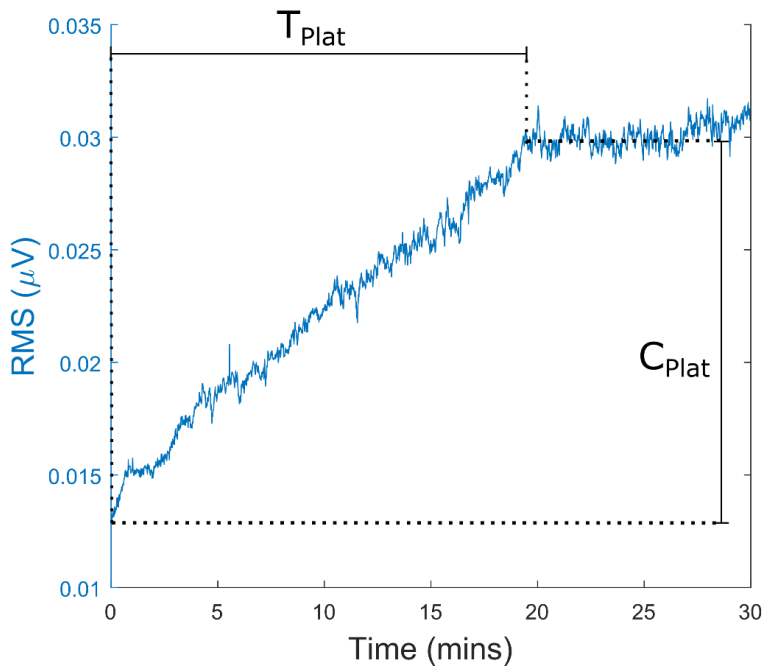


Figure 6.3 - Annotated RMS graph showing measurement parameters. T_{Plat} = Time to plateau, C_{Plat} = Value change from start to plateau.

Figure 6.4 and Figure 6.5 show the mean values \pm s.e.m. of the previously described parameters taken from multiple tests (n=6).

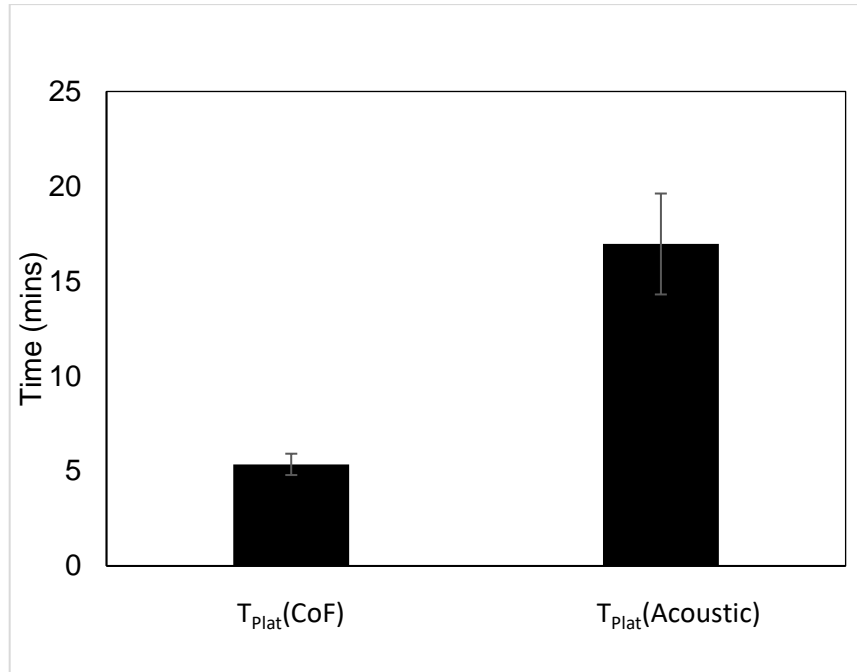


Figure 6.4 - Measurements of the time taken to reach a plateau for coefficient of friction and acoustic emission data. (Data is shown as mean \pm s.e.m. n = 6).

It can be seen in Figure 6.4 that across multiple tests the amount of time taken for the coefficient of friction to level out and reach a plateau is highly repeatable. On average the time taken for the coefficient of friction data to plateau is 5 minutes 21 seconds \pm 33 seconds. Interestingly, the acoustic emission data takes longer to plateau, on average it takes 16 minutes 57 seconds \pm 2 minutes 39 seconds.

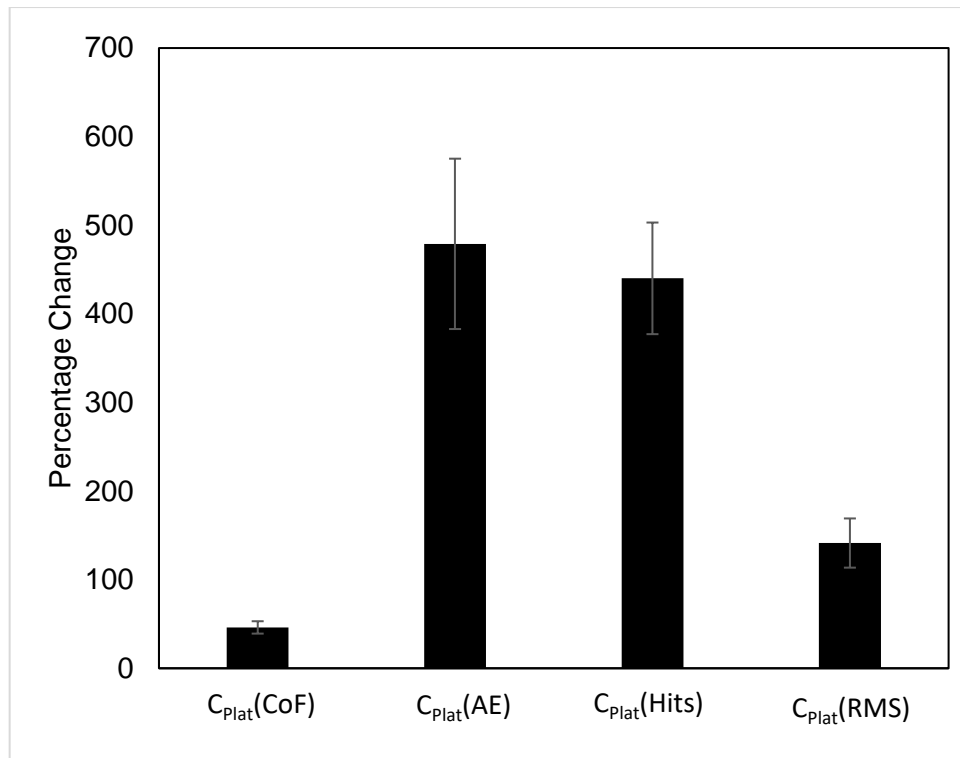


Figure 6.5 - Measurements of the percentage change in magnitude for various parameters relating to coefficient of friction and acoustic emission data. (Data is shown as mean \pm s.e.m. n = 6).

Figure 6.5 shows the magnitude related parameters described previously in Figure 6.2 and Figure 6.3, the data is shown as a percentage change from the starting value so that the data for all of the parameters can be shown on one graph.

The average percentage change in the coefficient of friction data is 46.1% \pm 6.9%. The average percentage change for the acoustic emission data from the start of the test to the plateau is 479% \pm 96%, 440% \pm 63% and 141% \pm 28% for absolute energy, hits and RMS, respectively.

It has been shown in Figure 6.4 and Figure 6.5 that both the coefficient of friction and acoustic emission responses are very repeatable across multiple tests. Therefore, the data from only one test will be shown as a representative example. This can be seen in Figures 6.6, 6.7 and 6.8.

The coefficient of friction shown in Figures 6.6, 6.7 and 6.8 show two very distinct regions. There is a very rapid increase in the CoF value from \sim 0.72 to \sim 0.96 over the first 5 minutes of the test. This is then followed by a relatively steady period for the remainder of the test in which the CoF stabilises at \sim 0.95.

This trend is not shared by the acoustic emission data, all 3 parameters show a distinctly different response than that shown by the CoF. The absolute

energy data, Figure 6.6, shows a trend whereby there is a gradual increase from $3.79 \times 10^{-5} \mu\text{Vs}$ to $0.00029 \mu\text{Vs}$ during the first 15 minutes of the test, after which the signal begins to plateau at approximately $0.00027 \mu\text{Vs}$.

Figure 6.7 shows the hit count measured throughout the test and shows the same trend as the absolute energy data. The hit count starts at ~ 2000 and then gradually increases for the first 15 minutes of the test where it then begins to plateau at ~ 15000 .

Finally, Figure 6.8 shows the RMS data for the test. It can be seen that the RMS signal broadly follows the same trend as the absolute energy and hit count. During the first 15 minutes there is a gradual increase from $\sim 0.012 \mu\text{V}$ to $\sim 0.033 \mu\text{V}$ where it remains relatively steady for the duration of the test.

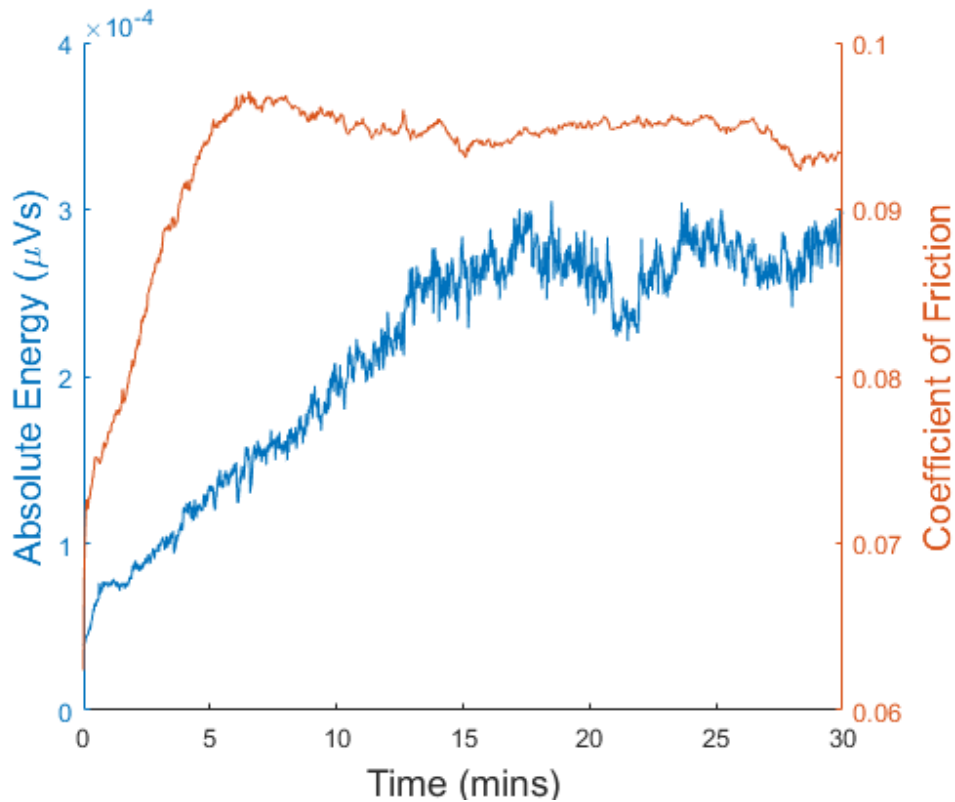


Figure 6.6 - Absolute energy and coefficient of friction data for tribotest conducted in PAO + 0.55wt% ZDDP. (Contact Pressure: 2.29 GPa, Speed: 1000 RPM and Temperature: 100 °C).

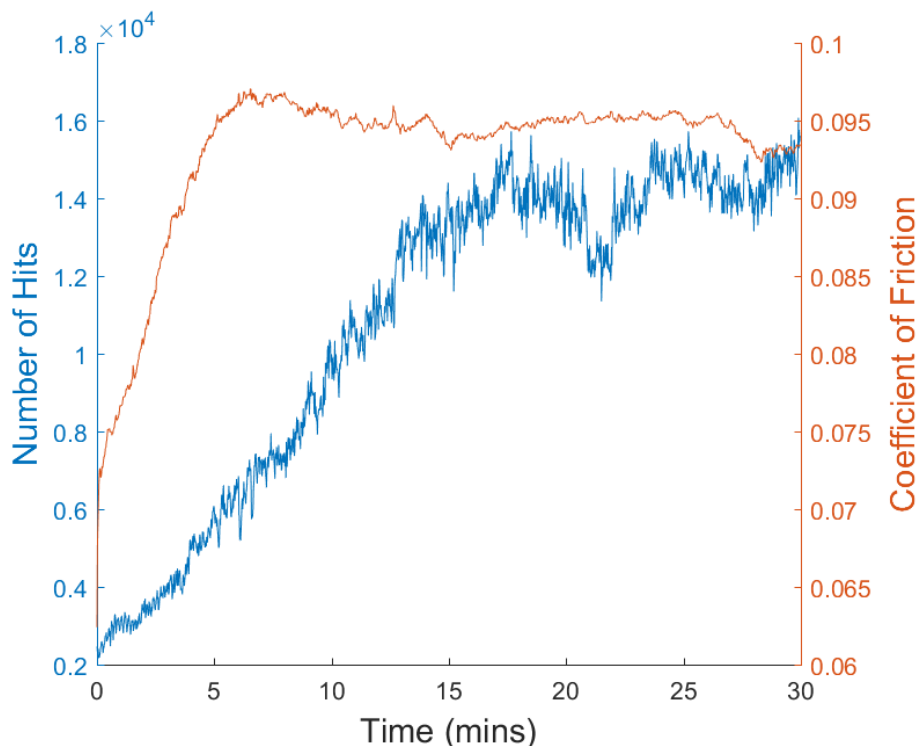


Figure 6.7 – Hit count and coefficient of friction data for tribotest conducted in PAO + 0.55wt% ZDDP. (Contact Pressure: 2.29 GPa, Speed: 1000 RPM and Temperature: 100 °C)

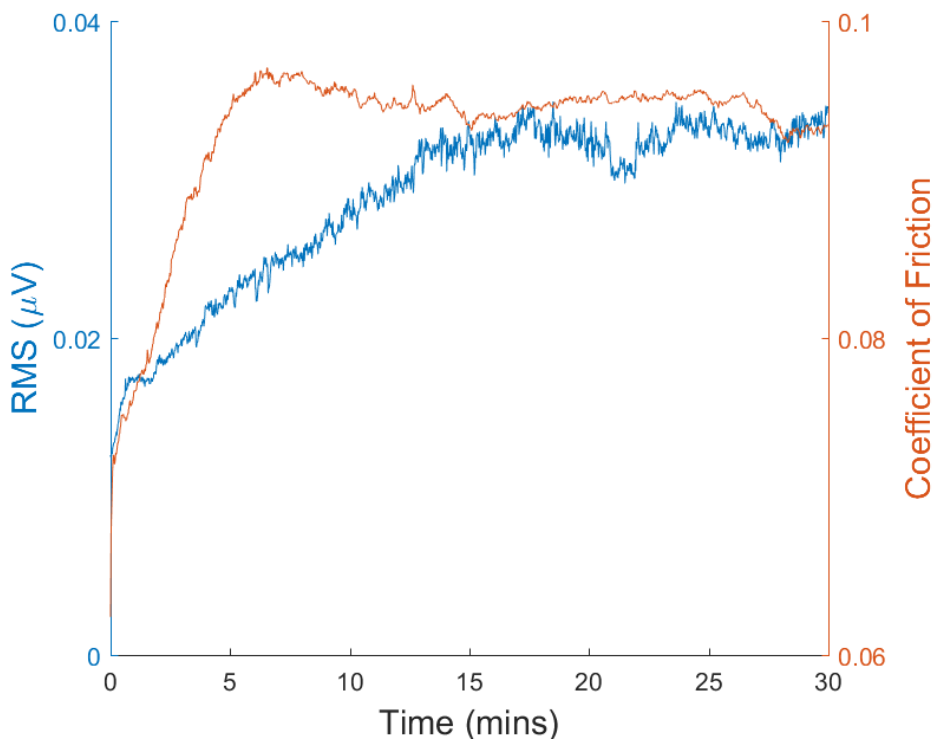


Figure 6.8 – RMS and coefficient of friction data for tribotest conducted in PAO + 0.55wt% ZDDP. (Contact Pressure: 2.29 GPa, Speed: 1000 RPM and Temperature: 100 °C).

As previously discussed in 1.2.2.2, it is known that the increase in coefficient of friction is directly related to the formation of a ZDDP tribofilm. It can also be seen that globally, a similar trend is shown by the acoustic emission data whereby the signal increases to a point and then plateaus for the remainder of the test. It is worth noting however, that whilst the acoustic emission data is also showing an increase, there is a disparity between the response of the acoustic emission signals and the coefficient of friction. The reasons for this disparity have not been fully elucidated, nevertheless the fact that the acoustic emission data follows the same global trend and begins to plateau is evidence that there is an acoustic emission response to ZDDP tribofilm formation.

6.2 Early Stages of ZDDP Tribofilm Formation

It has been shown that there is a disparity between the acoustic emission and the coefficient of friction data for tests conducted in PAO + 0.55wt% ZDDP, particularly in the very early stages of the tribotests. It is key to determine the tribochemical state of the contact during the initial stages of the test to determine whether the previously discussed low magnitude acoustic emission regions are due to chemical changes in the tribofilm or simply a by-product of running in.

Tests were conducted varying in duration from 5 to 30 minutes in length with the same tribotest parameters as shown in Table 8. After each test the disk was rinsed in heptane to remove excess oil and EDX analysis was performed on the wear scar. EDX spectra were obtained from at least 4 different locations across the wear scar. EDX analysis can be used to evaluate the composition of the entire tribofilm (Morina et al., 2006). However, as the probing depth is in excess of 1 μm the substrate will also be measured (Morina et al., 2006). In this work, the EDX analysis has been used to provide a qualitative analysis whereby the elements are identified but their true abundances are not measured.

As previously discussed in Section 2.4.2 EDX analysis was conducted using a Hitachi TM303plus benchtop SEM fitted with an Oxford Instruments Aztec EDX detector.

Percentage weight values of key elements such as zinc and phosphorous were measured across the wear scar. A ratio of Zn:P was calculated to indicate how the composition of the tribofilm varies with time. It can be seen that the average

Zn:P value at 5 minutes is ~8, this then increases as the test continues ending at approximately 10.5 when the test had been running for 30 minutes.

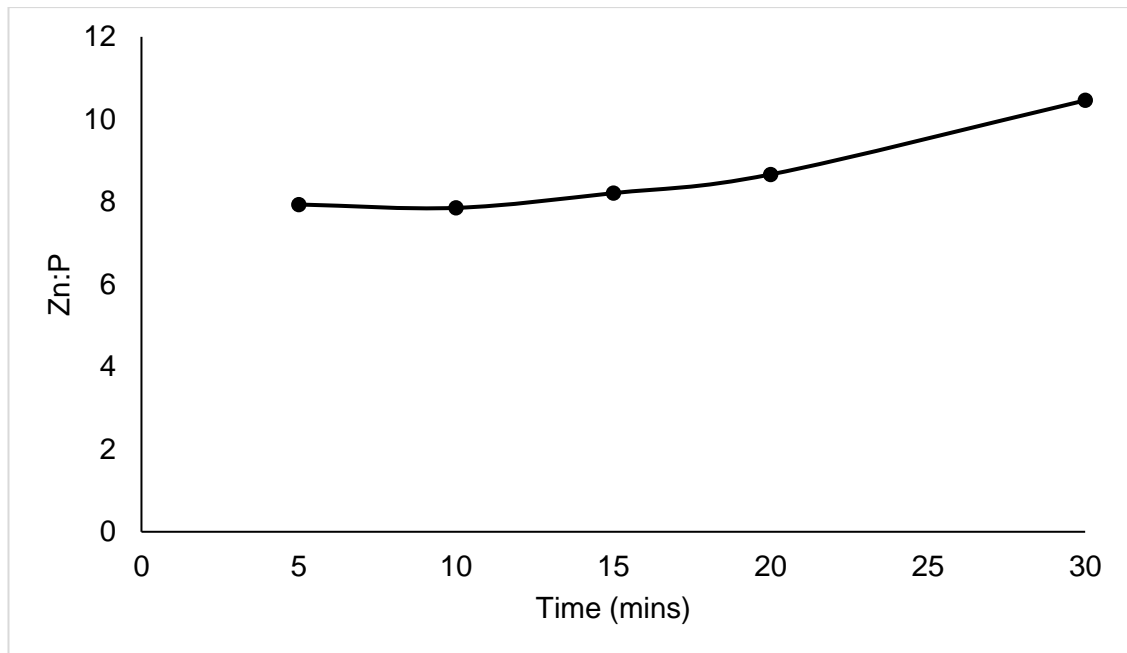


Figure 6.9 - EDX analysis data of Zn:P ratio against time.

The amount of zinc detected using the EDX analysis increases from ~4.94% to ~5.92% as the duration of the tests increases from 5 minutes to 30 minutes (data not shown). Therefore, the amount of phosphorous present in the film remains relatively constant at ~0.54% for all test durations.

The Aztec One (Oxford Instruments) EDX software has a mapping function in which the entire focal area of the microscope is measured and the presence of a number of different elements can be seen. Maps of the wear scars were taken at each time point, this allows the progression of the tribofilm formation to be visualised. Figure 6.10 shows the relative abundance of Zn and P elements within the wear scar after varying tribotest durations. On the left of the figure is the SEM image of the test surface, for all test durations except for 30 mins the tribofilm cannot be seen. However, when a map of the surface is taken, the presence of both Zn and P can clearly be seen. It is evident that as the duration of the test increases so does the quantity of both Zn and P within the wear scars.

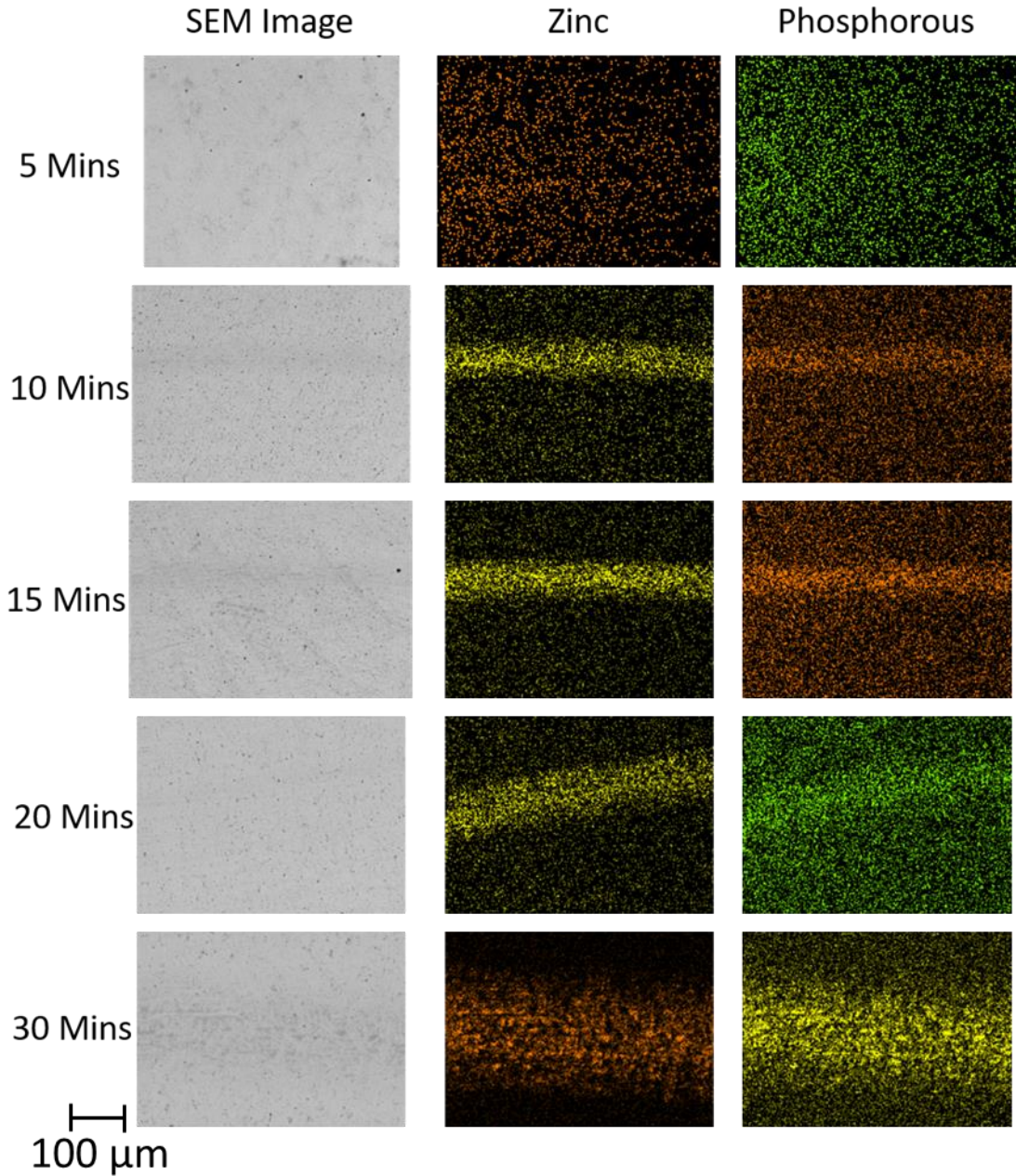


Figure 6.10 - Illustrative representation of the relative abundance of Zinc (Zn) and Phosphorus (P) elements in the wear scar of tests samples after varying tribotest durations.

By comparing both Figure 6.9 and Figure 6.10 to the coefficient of friction data shown in Figures 6.6, 6.7 and 6.8 it can be seen that at 5 minutes when the coefficient of friction begins to plateau there is a ZDDP tribofilm formed on the surface.

6.3 Frequency Analysis

As previously discussed in Section 5.3, the traditional acoustic emission parameters of absolute energy, hits and RMS do not provide any insight into how the frequencies present within the acoustic emission signal may change over the duration of the test. Therefore, throughout the data acquisition, FFT analysis was performed approximately every 30 seconds. This allows a valuable insight into the frequency domain of the signal and how that may change over time as the tribocontact evolves.

Figure 6.11 shows the frequency spectra taken at specific time points to reflect the key stages in the tribofilm development such as pre-tribofilm formation, initial formation, tribofilm development and fully established film. These time periods were taken at approximately 30 seconds, 5 minutes, 10 minutes and 30 minutes, respectively. These time points were chosen so that cross-additive comparisons could be made between the ZDDP and MoDTC data.

For the FFT at 30 seconds it can be seen that there is a sharp peak just below 100 kHz with an amplitude of around 2.5×10^{-6} . It can be seen that as the test progresses the amplitude of this peak doesn't tend to change but the breadth of the peak does. Initially at ~30 seconds, the peak only covers a tiny portion of the frequency range. As the test progresses the breadth of the peak increases and the previously identified peak can be seen covering a frequency range from 90 kHz – 115 kHz, this is also accompanied by some low level noise all the way up to 140 kHz. This data shows that as a ZDDP tribofilm develops throughout the test and the ZDDP tribofilm thickness increases, the breadth of the peak at 100 kHz also increases.

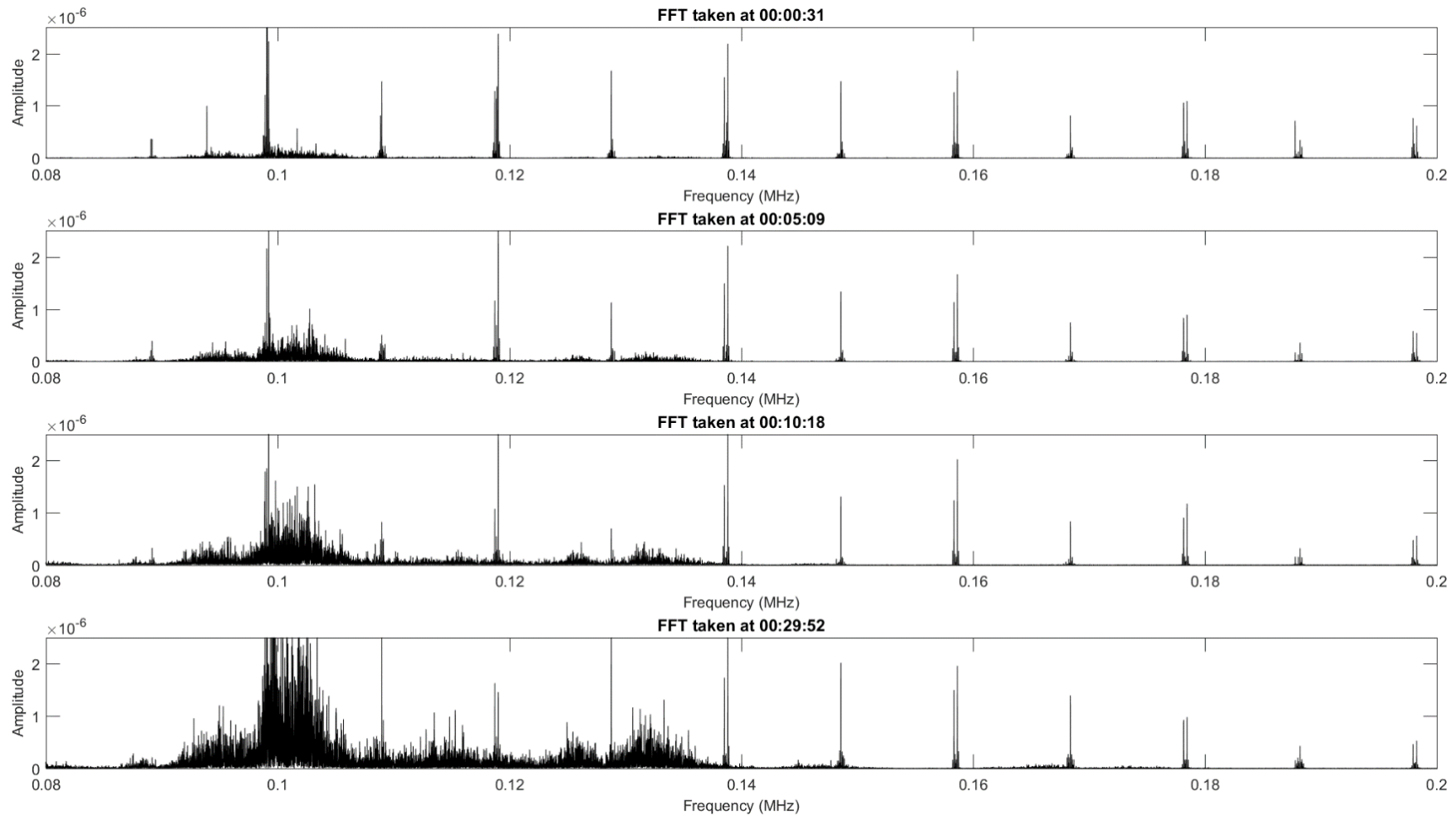


Figure 6.11 - FFT analysis taken at ~30 seconds, 5 minutes, 10 minutes and 30 minutes.

6.4 Tribofilm Removal

The aim of this experiment is to determine whether the acoustic emission sensor is capable of detecting the removal of the tribofilm. The tenacity of ZDDP based tribofilms has been widely documented and unlike the approach taken in Chapter 5, it is not simply a case of swapping the additive laden oil for base oil. A three stage approach was used to truly test the tenacity of the ZDDP tribofilm by allowing the tribofilm to develop as in previous tests, this was followed by running the test in PAO only before finally chemically removing the film using a dispersant.

In this test PAO + 0.55wt% ZDDP was used as a lubricant for the first 30 minutes of the test under the same tribotest conditions as shown in Table 8. After 30 minutes, the test was temporarily paused so that the additive laden oil could be removed and replaced with PAO alone, the test was then continued for a further 150 minutes. After 3 hours total testing time the test was once again temporarily paused and the lubricant was replaced with PAO + dispersant, the test then ran for a further 60 minutes.

Figure 6.12 shows the acoustic emission and coefficient of friction traces collected throughout the test. The solid vertical red lines indicate the points throughout the test in which the test was paused and the lubricant was changed. During the tribofilm formation stage of this test, the first 30 minutes, the acoustic emission and coefficient of friction data shows the same trends as that shown in Figure 6.8, this indicates that a ZDDP tribofilm has been formed.

When the lubricant is changed from PAO + 0.55wt% ZDDP to pure PAO it can be seen that there is a gradual increase in the coefficient of friction data and the acoustic emission data. When the pure PAO is then replaced with PAO + dispersant a very sudden and dramatic reduction in both the acoustic emission and coefficient of friction data can be seen.

This data is strongly correlated to the work produced by Fujita et al. (2005) who showed that a ZDDP tribofilm was only removed when a solution of dispersant in base oil is used and not base oil only.

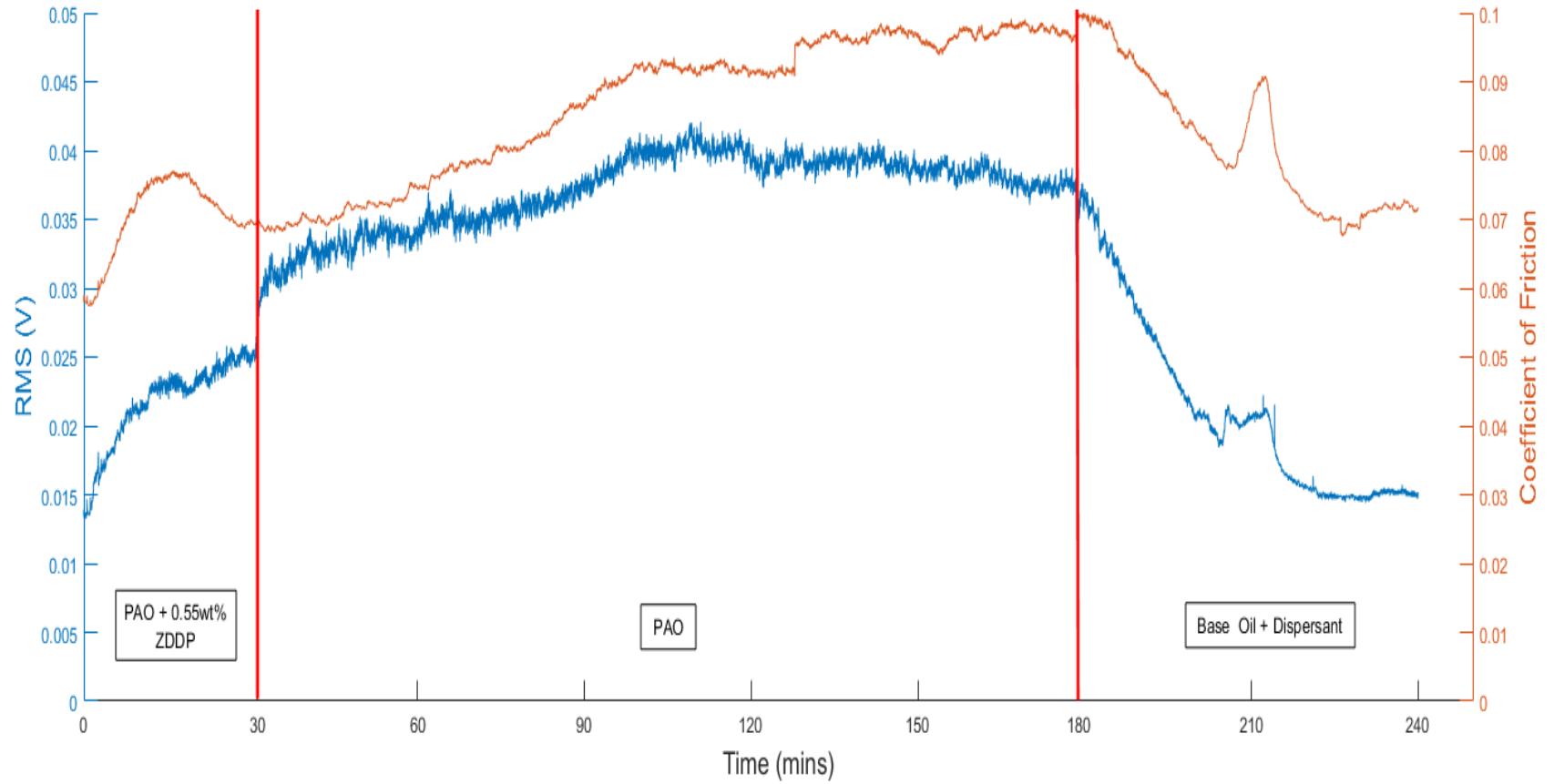


Figure 6.12 - Graph showing the acoustic emission and coefficient of friction data from a ZDDP based tribofilm removal test. (Test Duration: 240 minutes, Temperature 100 °C, Rotational Speed: 1000 RPM, Contact Pressure: 2.29 GPa).

6.5 Acoustic Emission and Wear

A series of tests were conducted ranging from 5 minutes to 30 minutes under the same experimental conditions shown in Table 8. After each test the diameter of the wear scar on the ball was measured using an optical microscope as discussed in Chapter 2. The wear scar diameter was then used to estimate the wear volume loss using Equation 5 (Page 52).

Figure 6.13 shows the wear volume loss for tests conducted for 5–30 minutes. For the first three data points, the wear volume loss is positively correlated with the test duration. However, at 20 minutes the reported wear volume loss is shown as being less than the amount of wear after 5 minutes. The remaining data points show an increase in wear volume loss correlated with increases in test duration. It is impossible for the amount of wear to be less after 20 minutes than after 5 minutes of testing. What this is showcasing is the efficacy of the anti-wear additive in action and in fact the amount of wear is relatively similar across the entire testing duration, the measured range of the data is only 3.56×10^{-14} . If this data were to be plotted on the same axis as the MoDTC wear data as shown in Figure 5.21 it would be represented by a straight line.

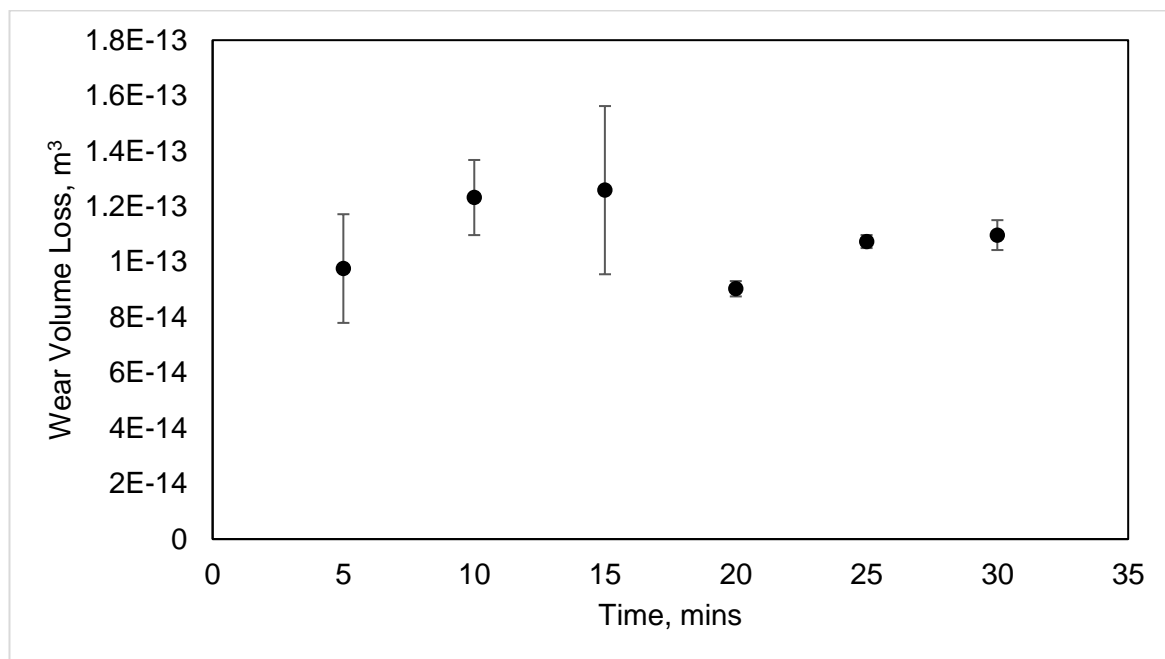


Figure 6.13 - Wear volume loss against time for tests conducted in PAO + 0.55wt% ZDDP. (Data shown as mean +/- s.e.m. n≥3).

The cumulative values for each acoustic emission parameter for each test was plotted against the corresponding wear volume loss figure to try and elucidate a relationship between the amount of wear produced and the measured acoustic emission values. Cumulative values are calculated in the same manner as shown in Chapter 5 in Equation 8. This allows for a comparison of the real-time *in situ* acoustic emission values and post-test measured wear volume loss values.

Figure 6.14 shows the relationship between the wear volume loss and the total amount of absolute energy recorded across multiple time points. An R^2 value of 0.1561 is reported, this shows that there is no correlation between the two variables.

Figure 6.15 shows the relationship between the wear volume loss and the total amount of hits recorded across multiple time points. An R^2 value of 0.199 is reported, this shows that there is no correlation between the two variables.

Figure 6.16 shows the relationship between the wear volume loss and the total magnitude of the RMS signal recorded across multiple time points. An R^2 value of 0.162 is reported, this shows that there is no correlation between the two variables.

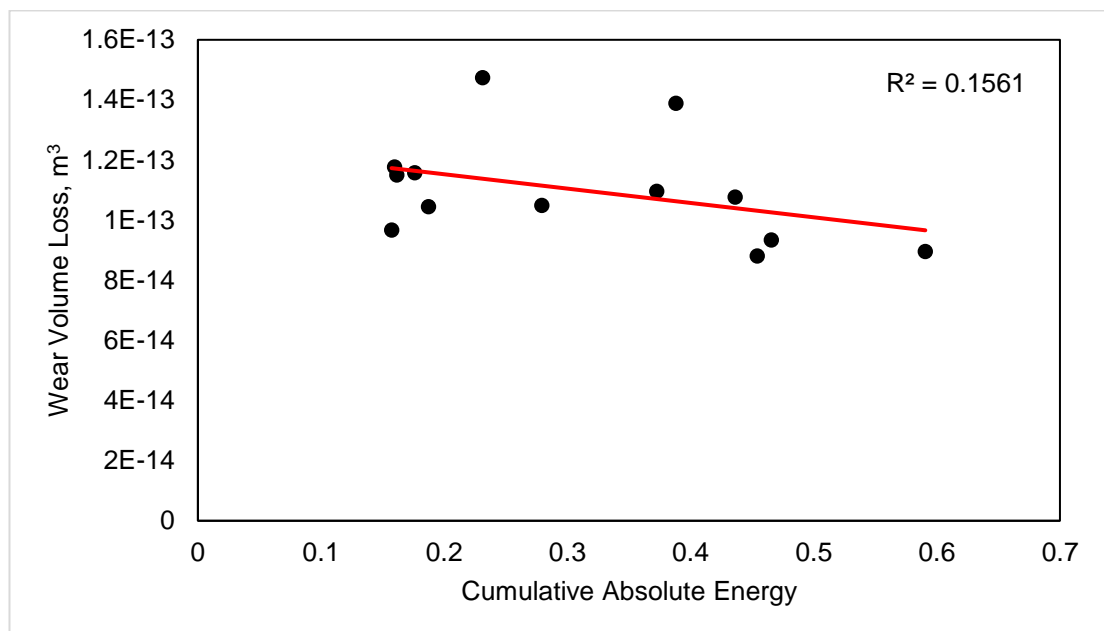


Figure 6.14 - Graph showing relationship between the wear volume loss and cumulative absolute energy (No correlation shown).

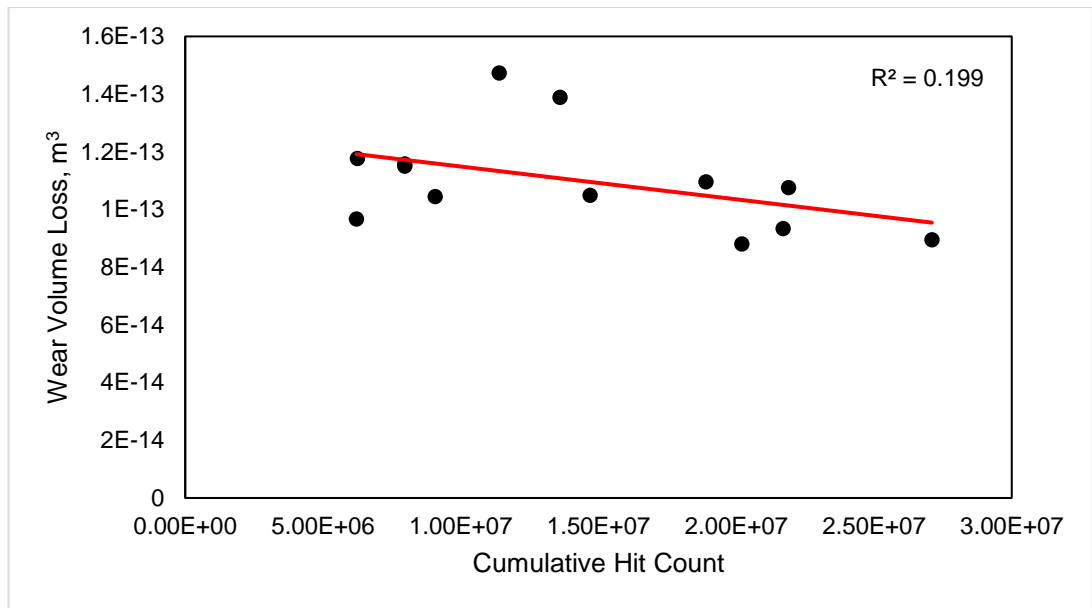


Figure 6.15 - Graph showing relationship between the wear volume loss and cumulative hit count (No correlation shown).

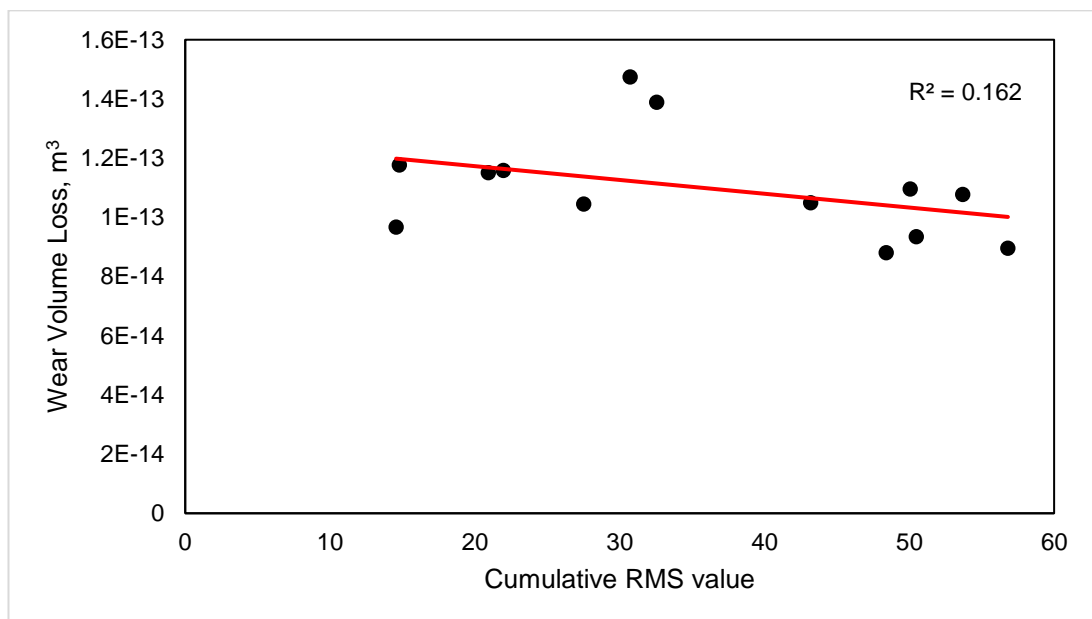


Figure 6.16 - Graph showing relationship between the wear volume loss and cumulative RMS value (No correlation shown).

Figures 6.14-6.16 show that there is little to no correlation between the amount of wear that is produced during a test and the total measured acoustic emission parameter. The highest correlation between the two variables comes from the cumulative hit count with an R^2 value of 0.199. Whilst this shows a slight correlation between the two variables, it is worth noting that the direction of the gradient is in fact negative and that would suggest that the amount of

wear actually decreases as more of the RMS value is recorded; this is physically impossible as by definition the cumulative RMS values will increase with time in the same manner as the wear volume loss.

In line with data discussed in Section 5.5 it has been shown in this chapter that the acoustic emission data very closely resembles the coefficient of friction data and this is not directly linked with wear in the presence of ZDDP. As such the relationship shown above was anticipated.

6.6 Acoustic Emission and Coefficient of Friction

As previously discussed, a series of tests were conducted, ranging in duration from 5 minutes to 30 under the same test conditions as shown in Table 1. The data at the end of these tests were then collated into a large repository of corresponding coefficient of friction and acoustic emission data. The coefficient of friction data for multiple tests was then plotted against the corresponding acoustic emission data to determine whether there is a relationship between the acoustic emissions that are produced and the coefficient of friction. Once plotted, Pearson's correlation coefficients were used to determine statistical significance between the two sets of data.

Figure 6.17 shows the correlation between the coefficient of friction and the absolute energy. The figure shows that there is a statistically significant correlation between the two sets of data ($P < 0.0001$), with an R^2 value of 0.6248 being reported.

Figure 6.18 shows the correlation between the coefficient of friction and the hit count. The figure shows that there is a statistically significant correlation between the two sets of data ($P < 0.0001$), with an R^2 value of 0.6818 being reported.

Figure 6.19 shows the correlation between the coefficient of friction and the RMS. The figure shows that there is a statistically significant correlation between the two sets of data ($P < 0.0001$), with an R^2 value of 0.6787 being reported.

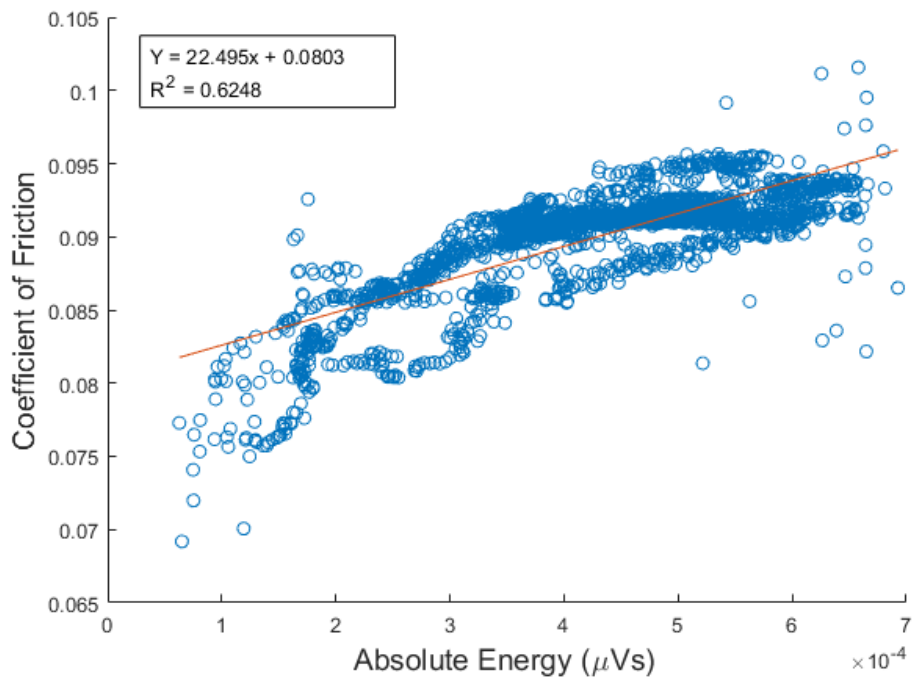


Figure 6.17 - Graph showing the significant correlation (Pearson's Correlation Coefficient, $n=2438$, $P<0.0001$) between CoF and absolute energy values with PAO + 0.55wt% ZDDP as the lubricant.

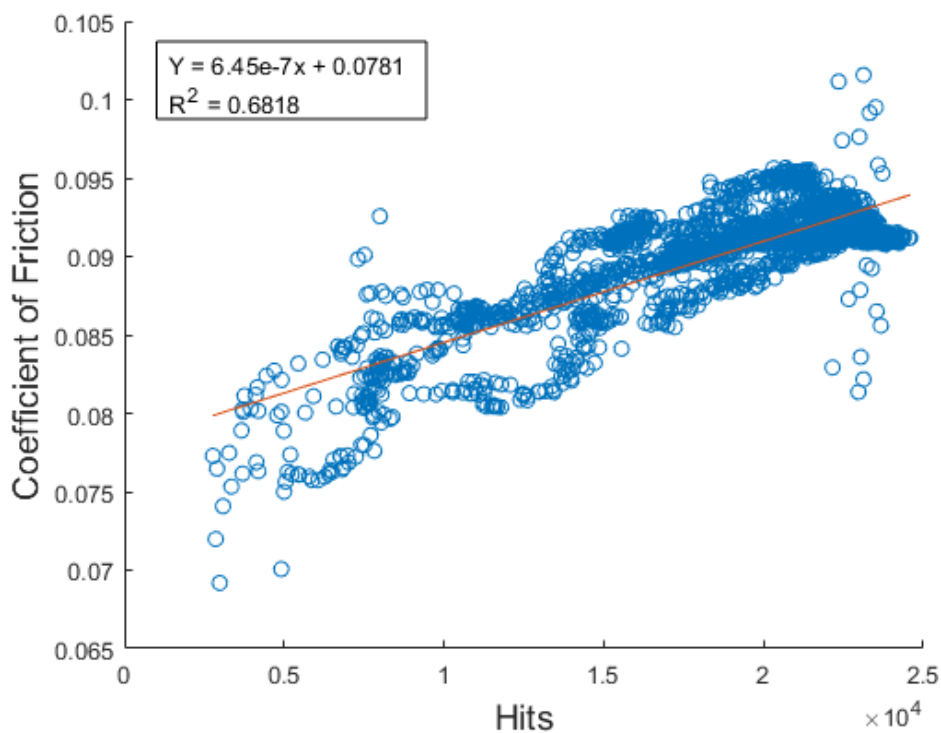


Figure 6.18 - Graph showing the significant correlation (Pearson's Correlation Coefficient, $n=2438$, $P<0.0001$) between CoF and hit count values with PAO + 0.55wt% ZDDP as the lubricant.

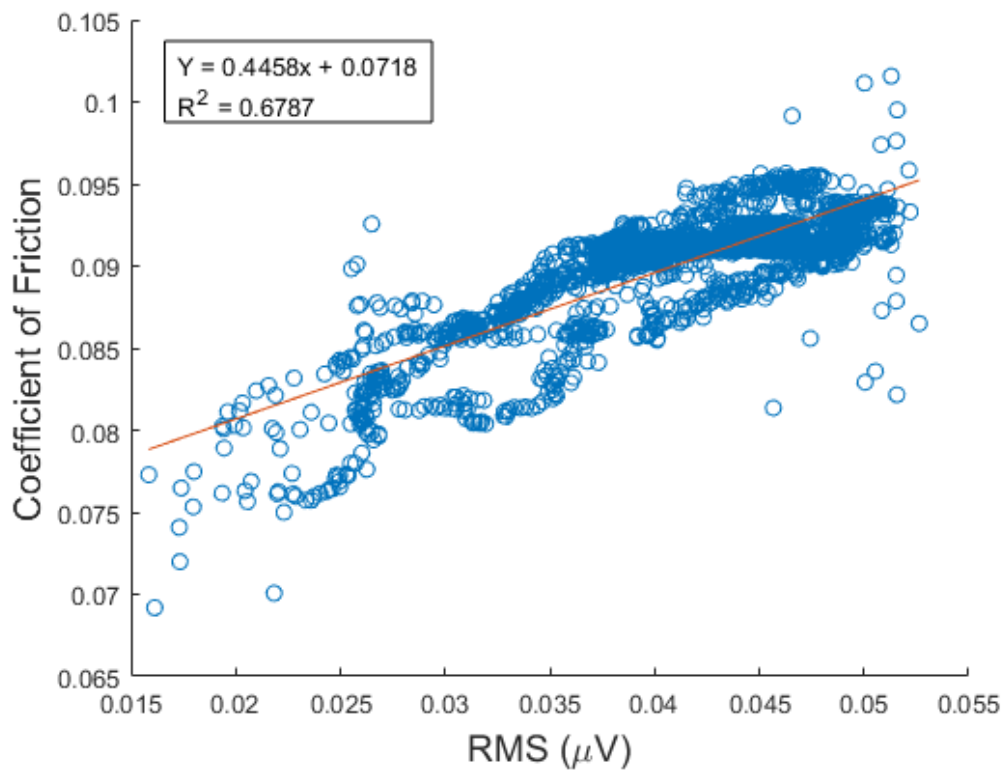


Figure 6.19 - Graph showing the significant correlation (Pearson's Correlation Coefficient, $n=2438$, $P<0.0001$) between CoF and RMS values with PAO + 0.55wt% ZDDP as the lubricant.

It can be seen from Figures 6.17-6.19 that there is a statistically significant relationship between the coefficient of friction and the acoustic emissions that are produced. This relationship, under the presence of lubricant additives, has never previously been explored by other authors in the literature. However, the behaviour of the acoustic emission signal corresponds similarly to the coefficient of friction data shown in Figures 6.6-6.8 and as such this relationship was anticipated.

6.7 Summary

In this chapter the *in situ* acoustic emission technology has been used to investigate the capabilities of monitoring the formation and removal of ZDDP based tribofilms. Further investigation into the tribochemical reasoning for the prevalent acoustic emission response has also been performed. The findings of this chapter can be summarised as follows:

- For the first time this acoustic emission sensing methodology has been used successfully to monitor the formation of a ZDDP based tribofilm *in situ* and in real time.
- Changes in the rate of change within the acoustic emission response can be attributed to changes in the atomic composition of the tribofilm.
- For the first time this acoustic emission sensing technique has been used to successfully monitor the removal of a ZDDP based tribofilm *in situ* and in real time.
- The frequency composition of the acoustic emission signal is directly influenced by tribocontact evolution.
- No correlation is observed between measured acoustic emission values and the wear produced during testing.
- Statistically significant correlation between measured acoustic emission values and coefficient of friction during testing.

Chapter 7

Discussion

Acoustic emissions have been used extensively for the condition monitoring of pressure vessels to identify cracks (Roberts and Talebzadeh, 2003, Harris and Dunegan, 1974, Gong et al., 1992, McBride et al., 1993). They have also been used to monitor tool wear in manufacturing (Hase et al., 2014, Maia et al., 2015, Liang and Dornfeld, 1989, Bhuiyan et al., 2016). The use of acoustic emission techniques has been used in tribology, primarily focusing on the wear and in particular dry contacts. To the best of my knowledge no work has been produced that investigates the acoustic emission response to different lubricant additives such as friction modifiers and anti-wear additives. This work focuses on tribochemical effects on acoustic emissions, primarily the monitoring of tribofilm formation and removal.

In this chapter, the main results obtained in this work will be discussed with regard to the available literature on acoustic emissions and tribochemistry.

Overall, the results produced in this work show that an acoustic emission sensing technology can be successfully used to monitor the formation and removal of tribofilms. This discussion will cover key questions raised in the work such as:

- The development of a bespoke data acquisition system
- The extent in which acoustic emission sensing technology can be used to monitor the formation and removal of tribofilms
- The link between acoustic emission signals and tribological phenomena such as friction and wear
- The relationship between the acoustic emission signal frequency and tribochemical phenomena
- The potential usage of this acoustic emission methodology as a predictive tool for the coefficient of friction

This chapter will also discuss limitations to the work presented.

7.1 Development of a High Speed Data acquisition System

In this work, LabVIEW has been used to develop and continuously improve a high speed data acquisition system. As previously discussed in Chapter 3, a high speed acquisition system capable of measuring at a sampling rate of greater than 5 MHz was necessary in order to avoid aliasing the acoustic emission signal.

Commercial hardware was used in this work alongside the bespoke LabVIEW based program developed by the author. The programming architecture used in this work is a queued message handler, this operates through a system of queues whereby data can be sampled and processed at different rates, ensuring efficiency in the data capture. The signal was sampled from the sensor at a very quick rate >5 MHz, the data is then processed simultaneously at a slower rate to produce the acoustic emission parameters used throughout this work.

The data acquisition system developed for this work has been continuously improved and updated in line with findings taken from tribotests; a process which would not have been possible when using a commercial system. One example of this continuous improvement is the inclusion of automated FFT analysis at pre-determined time points through the tribotest. Initially, the only way to perform a FFT analysis was at the very end of the test.

The development of the system also included the design and manufacture of the acoustic emission sensor holder; the sensor holder was designed by the author and manufactured at The University of Leeds. The purpose of this holder was to ensure that the acoustic emission signals had a direct path to the acoustic emission sensor and that the location of the sensor was repeatable. The adaptor shown in Figure 3.20 shows that the acoustic emission sensor fits inside the holder which is then directly screwed into the ball holder.

The nature of a bespoke data acquisition system ensured that it was possible to fine tune any processing parameters used for the acoustic emission measurements. Figures 3.22-3.24 show the effect that the sampling speed settings within data acquisition system have on the acoustic emission data that is measured. It was found that using a sampling time of 250 ms and an interval between samples of 1 ms that the best acoustic emission data was produced.

Figure 3.25 and Figure 3.26 show tests that were conducted in order to choose the appropriate hit count threshold and width values. All of the data produced in this work used hit count threshold and width values of 0.05 and 1 respectively. This combination of values provide a large enough hit count so that any relatively small changes can be seen in the data, but the number isn't so large as to distort the impact of any such changes.

7.2 Tribofilm Monitoring

In this work it has been shown that an acoustic emission sensing technique can be successfully used to monitor the formation and removal of tribofilms formed using both MoDTC and ZDDP additives. It was initially thought that the reduction in acoustic emission signal shown in Figures 5.6-5.8 was caused by a dampening effect caused by the formation of a tribofilm. It was thought by the author that the presence of the tribofilm could act as an acoustic impedance layer that limits the amount of acoustic emission that is released.

For this this hypothesis to be true, the same trend should also be seen when a different additive is used, such as ZDDP. Figures 6.6-6.8 show that this hypothesis is patently false. The acoustic emission signal in this data can be seen to increase as the tribofilm is forming. Therefore, it is unlikely that the presence of a tribofilm acts as an acoustic damper. Instead, it is thought that the tribofilms release acoustic emissions when acted upon in a tribocontact.

Whilst the coefficient of friction and acoustic emission parameters do appear to broadly show the same trend it can be seen there are disparities in the response times of the acoustic emission and coefficient of friction data. For tests conducted in PAO + 0.1wt% MoDTC it can be seen that the acoustic emission signal reduces in value much sooner than the coefficient of friction signal. The cause of this reduction can be attributed to the presence of a small number of layers of MoS₂ on the sample surface as shown by the Raman spectra in Figure 5.13. It is believed that the presence of only a small amount of MoS₂ is enough to cause the acoustic emission signal to reduce prior to any discernible changes to the coefficient of friction.

Conversely, for tests conducted in PAO + 0.55wt% ZDDP there is a large disparity in the time taken for the acoustic emission and coefficient of friction data to plateau. It is generally considered that a ZDDP tribofilm has formed when the coefficient of friction plateaus at around 0.1. Figure 6.4 shows the average time taken for the coefficient of friction and acoustic emission data to

plateau. It can be seen that it takes approximately three times longer for the acoustic emission data to reach a steady state on average. The cause of this disparity has yet to be fully elucidated. However, it is possible that the coefficient of friction is directly affected as soon as ZDDP is present on the surface whereas the acoustic emission signal only plateaus when a tribofilm is fully formed. Further, it is worth noting the striking resemblance that the acoustic emission data has with graphs of ZDDP tribofilm thickness over time as reported by Shimizu and Spikes (2016) and Zhang and Spikes (2016) shown in Figure 7.1 and Figure 7.2.

Figure 7.1 shows the mean ZDDP tribofilm thickness for varying slide-roll ratios as reported by Shimizu and Spikes (2016). The slide-roll ratio of a pure sliding contact such as that used in this work is 200%. Therefore, it is the dashed green line in Figure 7.1 that is most applicable to this work. It can be seen that the rate at which the tribofilm grows is not constant throughout the test and that there appears to be two different regimes. It is worth noting that in this work ZDDP tribofilms formed successfully within 30 minutes as opposed to the 90 minutes for the data in the figure below. The reason for the accelerated growth in this work is due to the higher contact pressure, 2.2 GPa, compared with 0.82 GPa for the data shown in Figure 7.1.

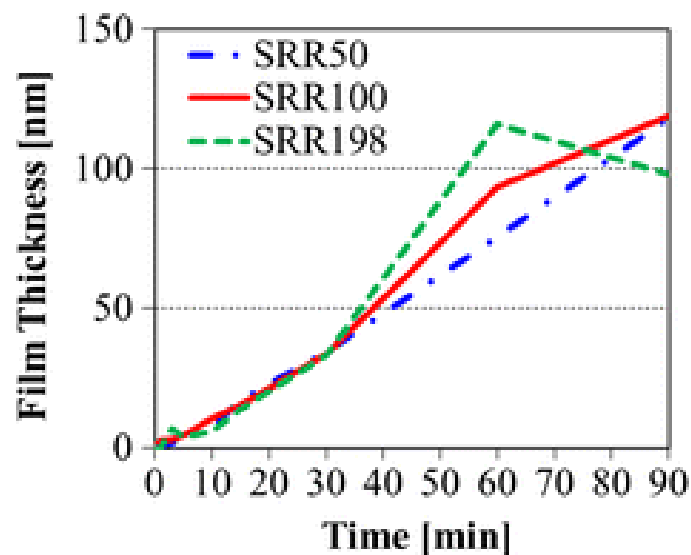


Figure 7.1 – Mean ZDDP tribofilm thickness for varying slide-roll ratios. Taken from Shimizu and Spikes (2016).

Figure 7.2 shows the ZDDP film thickness for tests conducted under various loads and temperatures reported by Zhang and Spikes (2016). The tribotest parameters for ZDDP tests conducted in this work are ~54 N load, 100 °C temperature and 30 minutes duration, the closest data shown in Figure 7.2 to

this data is the orange line with circular markers (55 N, 120 °C). Focusing on only the first 30 minutes it can be seen that there are two distinct regimes with regards to the rate of tribofilm growth, the gradient of the curve is much steeper earlier on in the test.

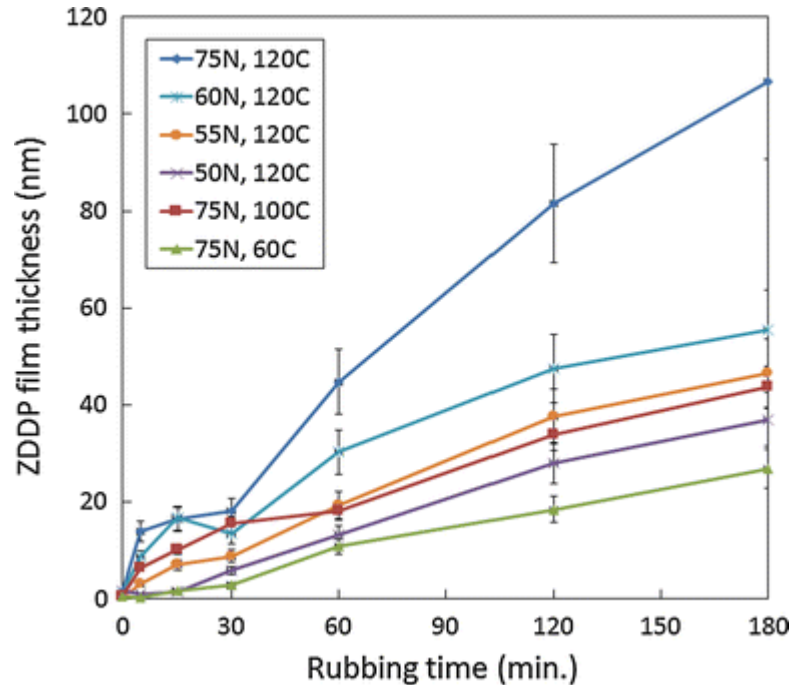


Figure 7.2 – ZDDP film thickness for various load and temperature configurations. Taken from Zhang and Spikes (2016)

Both Figure 7.1 and Figure 7.2 show that when a ZDDP tribofilm grows, initially the film grows quicker before plateauing. This is a very similar trend to that shown in the acoustic emission data for this work, as such it is possible that the two distinct regions shown in Figures 6.6, 6.7 and 6.8 is a corollary of the tribofilm thickness.

Figure 5.20 and Figure 6.12 show the acoustic emission and coefficient of friction data for the formation and removal of both MoDTC and ZDDP tribofilms. The removal of the tribofilm for both additives results in a dramatic change in the acoustic emission and coefficient of friction data back towards pre-tribofilm formation values. As such, the dramatic changes are taken as evidence that the tribofilm in question has been removed. It is therefore possible to use acoustic emission monitoring to indicate the time at which a MoDTC or ZDDP based tribofilm is destroyed.

7.3 Acoustic Emission and Friction

It has been shown throughout this work that the acoustic emission data broadly shows the same trend as the coefficient of friction data, the exact cause of this correlation is not fully defined but two possible reasons are discussed below.

The average acoustic emission values were taken during the final five minutes of multiple tests in order to compare the magnitude of the data. Figures 7.3-7.5 show a comparison between the average acoustic emission values for tests conducted in PAO only, PAO + 0.1 wt% MoDTC and PAO + 0.55wt% ZDDP. It can be seen that for all three parameters the magnitude of the ZDDP data is higher than the MoDTC and PAO data. The ZDDP data is between 1.83 and 4.17 times the MoDTC data for RMS and hit count data respectively.

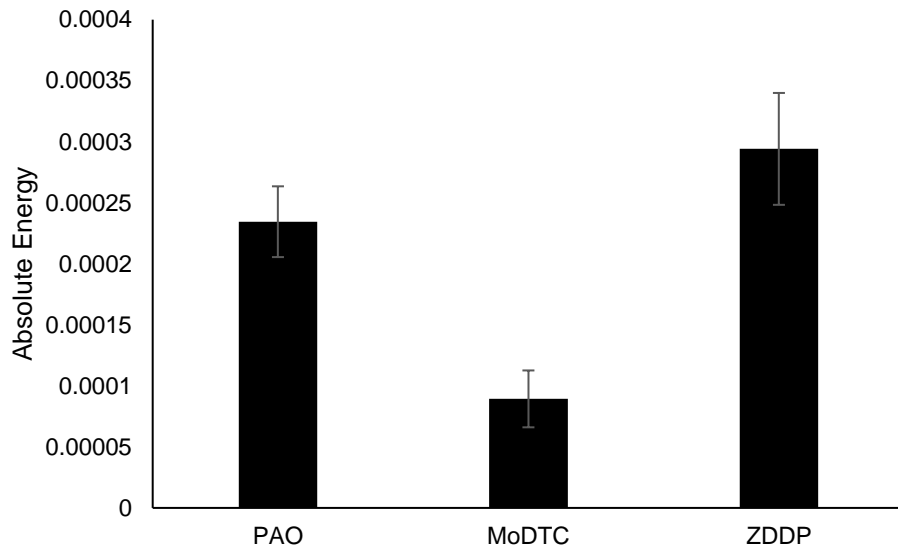


Figure 7.3 – Comparison between the magnitude of absolute energy values taken in the last 5 minutes of the test between MoDTC and ZDDP data. (Data shown as mean ± s.e.m. n=3).

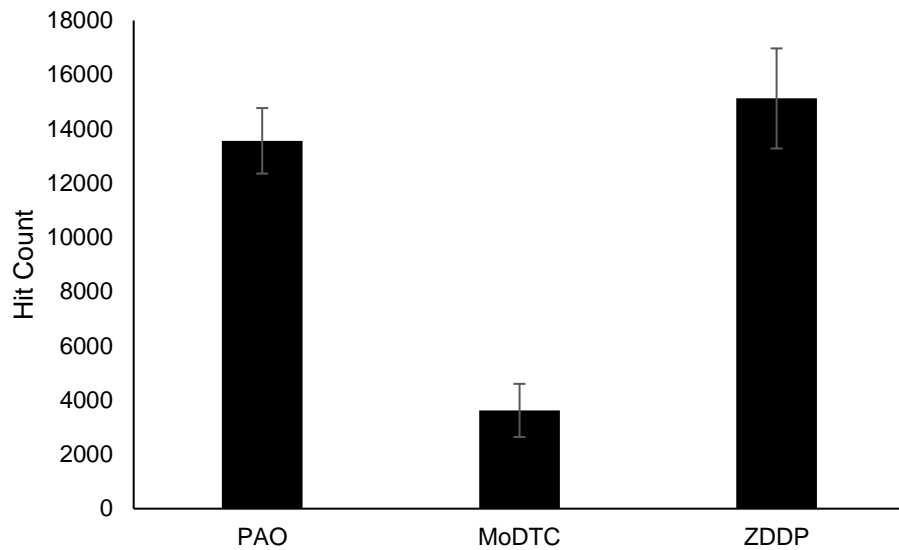


Figure 7.4 - Comparison between the magnitude of hit count values taken in the last 5 minutes of the test between MoDTC and ZDDP data. (Data shown as mean ± s.e.m. n=3).

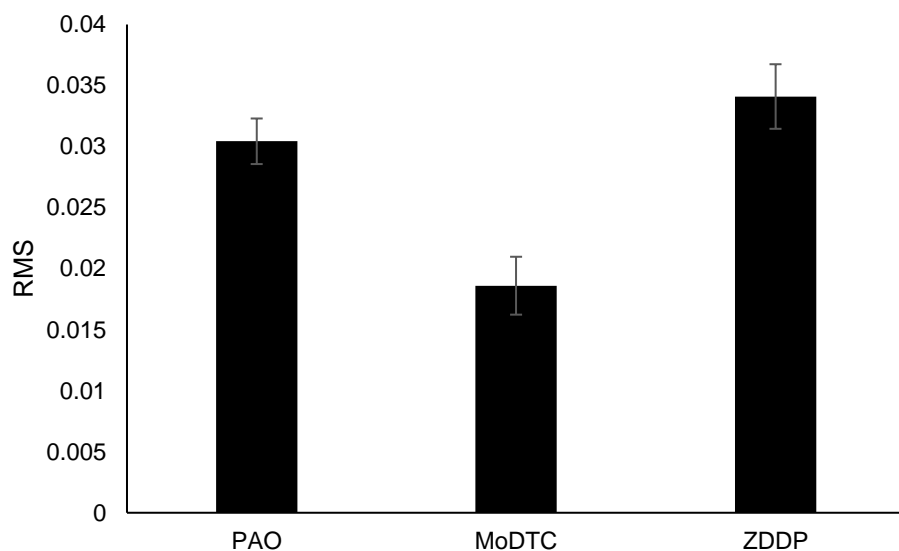


Figure 7.5 - Comparison between the magnitude of RMS values taken in the last 5 minutes of the test between MoDTC and ZDDP data. (Data shown as mean ± s.e.m. n=3).

The cause of this variance in magnitude between PAO, MoDTC and ZDDP data is yet to be fully elucidated. However, it is the author's view that the difference in the signal magnitude is directly linked to the morphology of the counterface surface, either substrate or the tribofilm.

One morphological parameter that could be responsible for the difference in magnitudes for the acoustic emission data is the surface roughness of the contact. Topolovec-Miklozic et al. (2001) measured the topography of various

tribofilms using AFM and they reported that the RMS roughness of ZDDP and MoDTC tribofilms are 30 nm and 17 nm respectively.

However, in this work the surface roughness of the standard steel samples used was measured to be ~100 nm. As such the surface roughness data does not fully correlate with the acoustic emission data when also considering the steel substrate. It is worth considering that in this work the surface roughness data shown in Figures 4.15-4.18 indicates that the initial surface roughness directly impacts the acoustic emission signal for tribotests conducted in PAO only. It is possible that this relationship holds true with regards to the surface roughness of the tribofilm but the relationship does not translate between the presence or lack thereof of a tribofilm.

Alternatively, a more likely morphological parameter that may be responsible for the differences in magnitudes for the acoustic emission data is the hardness of the contact; either the tribofilm or the steel substrate itself when considering tests undertaken in PAO only. The hardness of the steel sample disks is 1.54 GPa. Bec et al. (1999) reported that the hardness of a ZDDP tribofilm is 2 GPa, this value has also been used by Ghanbarzadeh et al. (2016) in a semi-deterministic wear model of ZDDP tribofilms. Further research undertaken by Bec et al. (2004) reported that the hardness of a MoDTC tribofilm is typically in the range of 0.4-0.5 GPa. Therefore, the relationship between relative hardness of each counterface is very similar to the relationship between the magnitude of the acoustic emission data.

In order to aid clarity, the previously discussed hardness values, taken from the literature, have been plotted against the absolute energy data to highlight any correlation between their values. This can be seen in Figure 7.6.

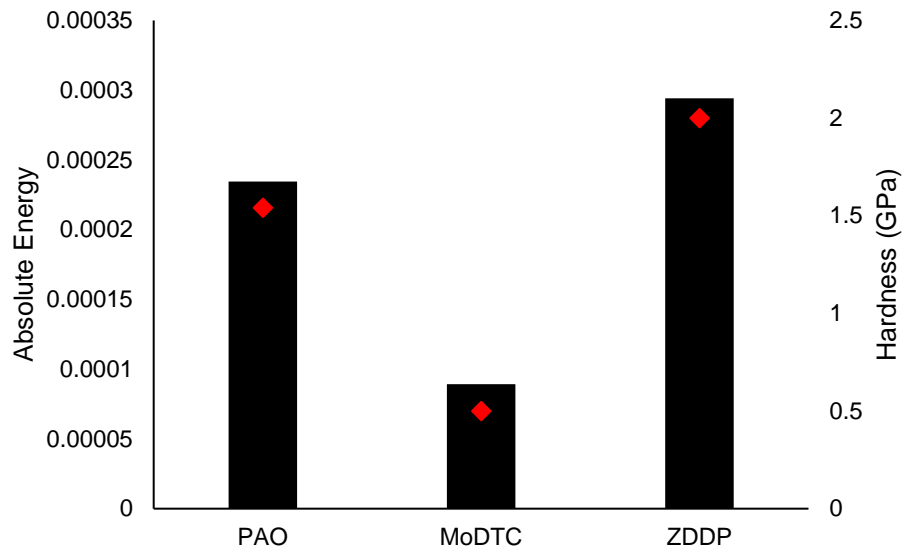


Figure 7.6 – Combination plot of absolute energy data (black bar) and reported hardness values (red diamond) for the steel plate, MoDTC tribofilm and ZDDP tribofilm.

Figure 7.6 shows that when plotted on separate axes there is a large correlation between the acoustic emission data and the hardness. It can be seen that as the hardness increases so does the magnitude of the acoustic emission data.

Whilst it is not known what exactly causes the variations in the magnitudes of the acoustic emission signals, the above scenarios provide a viable solution that warrant further investigation.

7.4 Acoustic Emission and Wear

In this work it has been shown that there is no direct link between the acoustic emission and wear volume loss. It can be seen in Figures 5.22-5.24 and Figures 6.14-6.16 that there is little to no correlation between the total amount of acoustic emissions produced throughout the tests and the wear volume loss.

Matsuoka (2001) showed that the amount of wear on hard disk drives could be estimated using acoustic emissions. Further to this, acoustic emissions have been used extensively in the monitoring of tool wear (Liang and Dornfeld, 1989, Sampath and Vajpayee, 1986, Cho and Komvopoulos, 1997). Whilst it is clear that in the literature acoustic emissions have been used to monitor/measure wear it remains unclear as to why the same relationship hasn't been recorded in this work.

There are many differences between the published literature on acoustic emissions and wear and this work. One of these differences could be the reason for no correlation between acoustic emission and wear. All of the tests conducted in this work took place with a lubricated contact, both with and without the presence of additives. Conversely, whilst Sun et al. (2005) showed a link between the integrated RMS signal and wear, their work was conducted on dry contacts. Boness and McBride (1991) showed a link between the integrated RMS signal and the total wear, however their work was conducted on a ball and cylinder tribometer and the lubricants used were heavy and light paraffin. Matsuoka (2001) developed a method for predicting the wear of hard drive disks, however the loads and materials used in their work is not representative of the tribosystems used in this work.

7.5 Frequency Analysis

As previously discussed, an acoustic emission signal consists of two separate domains, frequency and time. The time domain concerns the way in which the acoustic emission signal changes in amplitude over time. Whereas, the frequency domain, as the name suggests, is used to investigate the frequencies present in the acoustic emission signal at a specific time point. In order to gain insight into the frequency domain a FFT is performed on the raw acoustic emission data.

The FFT data shown in Section 5.3 and Section 6.3 demonstrate the way in which the frequency of the acoustic emission data changes as the tribofilms develop; FFT analysis was also performed on tests conducted in PAO only under the same tribotest conditions (data not shown). Three key measurements have been taken of the FFT data, these are the Peak Centre, Peak Width and Peak Amplitude, the way in which these measurements were taken are illustrated in Figure 7.7.

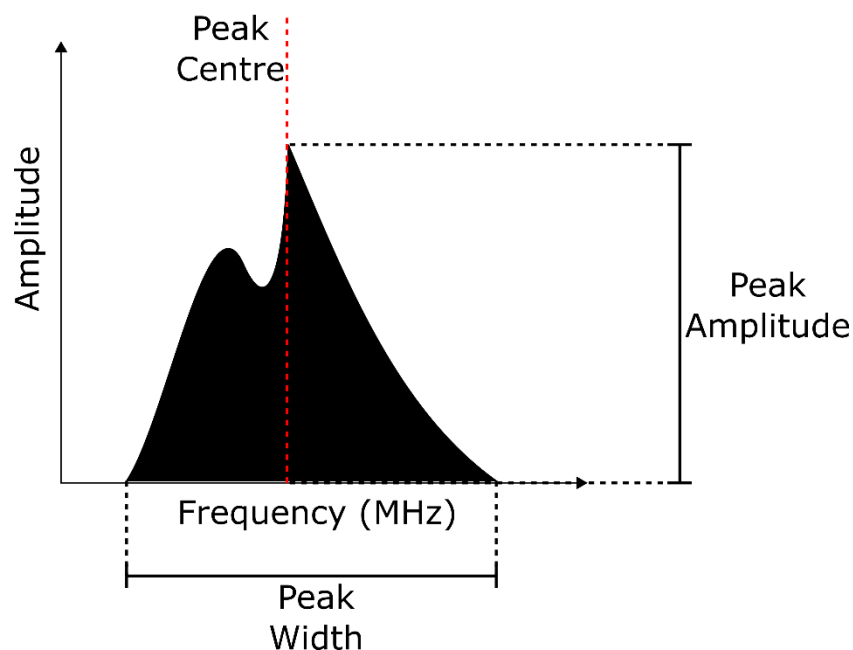


Figure 7.7 – Schematic indicating the three key measurements taken from the FFT data.

Figures 7.8-7.10 show the three measurement parameters explained in Figure 7.7 for tests conducted in PAO only, PAO + 0.1 wt% MoDTC and PAO + 0.55 wt% ZDDP. The figures show data from three time points, 5 minutes, 10 minutes and 30 minutes in order to assess how the frequency data changes as the tests continue and a tribofilm develops.

Figure 7.8 shows the peak centre values taken at 5, 10 and 30 minutes for tests conducted in PAO only, PAO + 0.1 wt% MoDTC and PAO + 0.55 wt% ZDDP. It can be seen that for all three additives there is very little change in the centre location throughout the duration of the test. It is also worth noting that all three lubricants have roughly the same value for peak centre at ~0.1 MHz.

Figure 7.9 shows the peak width values taken at 5, 10 and 30 minutes for tests conducted in PAO only, PAO + 0.1 wt% MoDTC and PAO + 0.55 wt% ZDDP. Similarly to the peak centre data, it can be seen that there are little changes to the width values over time. However, for PAO only, there is a very slight decrease in width as the test duration increases. Notably, whilst there is no major change in the width over time for the MoDTC data, the width itself is considerably lower than the PAO and ZDDP data.

Figure 7.10 shows the peak amplitude values taken at 5, 10 and 30 minutes for tests conducted in PAO only, PAO + 0.1 wt% MoDTC and PAO + 0.55 wt% ZDDP. For the PAO data there is no change to the peak amplitude throughout the test duration, it stays at around 6.5×10^{-7} . The MoDTC data shows the

highest amplitude of all of the data, starting at 9.27×10^{-6} at 5 minutes. There is a clear reduction in the MoDTC peak amplitude as the tribofilm is formed, it reduces from its initial high starting value to 8.16×10^{-6} and 6.66×10^{-6} at 10 and 30 minutes respectively. Finally, the ZDDP data shows the opposite trend to the MoDTC data, the peak amplitude increases as the tribofilm is formed. Initially starting at 4.6×10^{-7} for the 5 minute FFT, it can then be seen to increase at both the 10 and 30 minute data points to 1.57×10^{-6} and 3.56×10^{-6} respectively. This behaviour is to be expected as the increased amplitude of the peak frequency correlates directly to the magnitude of the time-domain acoustic emission parameters. This response is comparable to data shown in Figure 7.6.

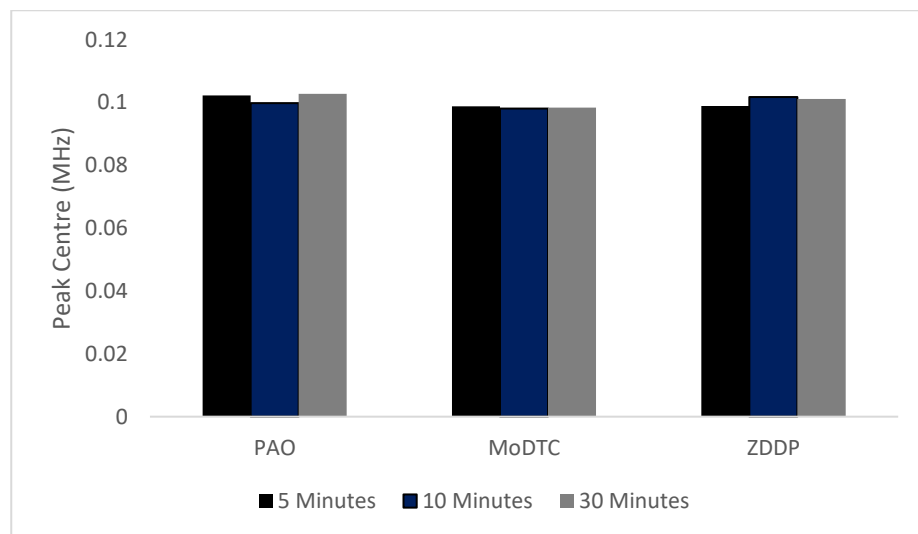


Figure 7.8 - Comparison of peak centre values of FFT data from various time points during tests conducted in PAO, PAO + 0.1 wt% MoDTC and PAO + 0.55 wt% ZDDP.

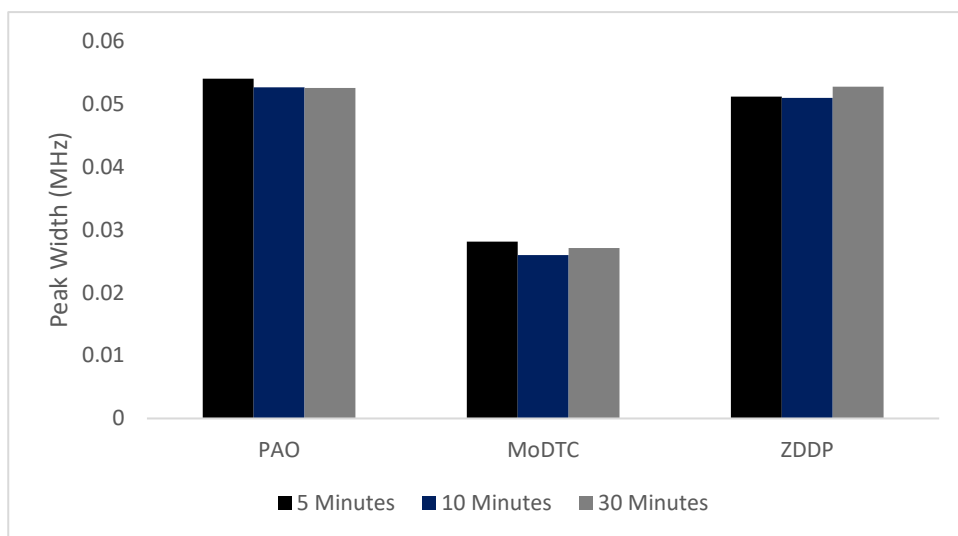


Figure 7.9 - Comparison of peak width values of FFT data from various time points during tests conducted in PAO, PAO + 0.1 wt% MoDTC and PAO + 0.55 wt% ZDDP.

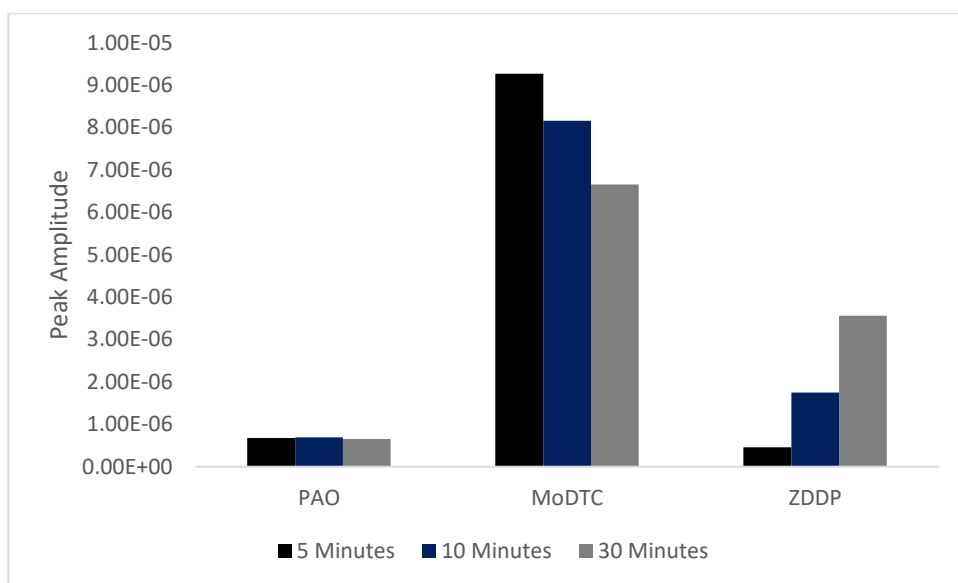


Figure 7.10 - Comparison of peak amplitudes of FFT data from various time points during tests conducted in PAO, PAO + 0.1 wt% MoDTC and PAO + 0.55 wt% ZDDP.

This work has shown that the frequency domain of the acoustic emission data is a very important aspect of the overall signal. Figure 7.10 clearly shows very different magnitudes and behaviours present in the acoustic emission frequency domain depending upon the additives present in the lubricant. The exact cause of the differing frequencies present in the acoustic emission data is yet to be fully understood. It is possible that the presence of certain frequencies may be additive specific and act as a 'fingerprint' for that additive.

Future work may lead to it being possible to analyse the acoustic emission frequency domain to identify the presence of lubricant additives in a contact.

7.6 Acoustic Emission as an *in situ* Real Time Methodology

It has previously been discussed in Chapter 1 that there are a number of *in situ* measurement methods available, each with their own positives and negatives. The novel approach taken in this work with regards to acoustic emission and tribochemistry has identified that acoustic emission technology can be successfully used to monitor the formation and removal of tribofilms in real time and *in situ*.

There are multiple ways in which this work could be adapted going forward, one way would be to utilise the technique to monitor more complex contacts throughout the entirety of a test. As such, it would be possible to identify changes in the state of the tribocontact without having to stop a test and measure the relevant parameter. This work could also be adapted to be used as an on-line monitoring tool that would identify when a tribofilm has formed or has been removed.

7.7 Using Acoustic Emissions as a Predictive Tool for the Coefficient of Friction

In Chapter 5 and 6, results showed that there is a statistically significant relationship between the coefficient of friction and the measured acoustic emission value.

It is possible that by manipulating this relationship the coefficient of friction can be predicted using only the acoustic emission data. Figures 5.25-5.27 and 6.17-6.19 established that there is a significant relationship between the acoustic emission data and the coefficient of friction. The correlation between the coefficient of friction and the acoustic emission is as high as 0.863 and 0.6818 for the MoDTC and ZDDP data respectively.

For both additives, it is the hit count data that is most highly correlated to the coefficient of friction. As such, going forward only the hit count data will be used to establish a predictive tool. A polynomial relationship was identified for the MoDTC data whereas a linear relationship can be seen for the ZDDP data. For the polynomial data, the equation of the curve of best fit can be used to predict future coefficient of friction values. Similarly for the ZDDP data, a line

of linear regression will be used to quantify the relationship between the hit count and the coefficient of friction. The line of linear regression can be used to establish an equation of the form $\mu = mH_c + C$ where μ is the coefficient of friction and H_c is the hit count.

Figure 5.26 shows the correlation between the coefficient of friction and the hit count for tribotests conducted in PAO + 0.1wt% MoDTC. The equation of the curve can be manipulated into a predictive equation shown below.

Equation 10 - Predictive coefficient of friction for 0.1wt% MoDTC.

$$\mu = -2.313 \times 10^{-10}H_c^2 + 1.796 \times 10^{-5}H_c + 0.0233.$$

Figure 6.18 shows the correlation between the coefficient of friction and the hit count for tribotests conducted in PAO + 0.55wt% ZDDP. The equation of the curve can be manipulated into a predictive equation shown below.

Equation 11 - Predictive coefficient of friction equation for 0.55 wt% ZDDP.

$$\mu = 6.45 \times 10^{-7}H_c + 0.0781.$$

It has already been established that the magnitude of the acoustic emission signal when ZDDP was used as an additive is considerably higher than when MoDTC is used. This is also reflected in the equation of the linear regression for the ZDDP data as the constant for H_c is two orders of magnitude smaller than in the MoDTC data. Therefore, it can be seen that there is not just one equation that can be used to link the acoustic emission and coefficient of friction data. Each tribosystem has to be considered separately, as it is possible that there are additive specific constants that can be used to estimate the coefficient of friction.

The hypothesis is that from the equation of the line of best fit or linear regression, it is then possible to estimate the instantaneous friction value from a real-time hit count value, giving an real-time *in situ* friction estimate.

Figure 7.11 shows the measured and predicted coefficient of friction values for a test conducted in PAO + 0.1 wt% MoDTC. It can be seen that by using Equation 10 the instantaneous coefficient can be accurately estimated in real time using only the measured hit count signal.

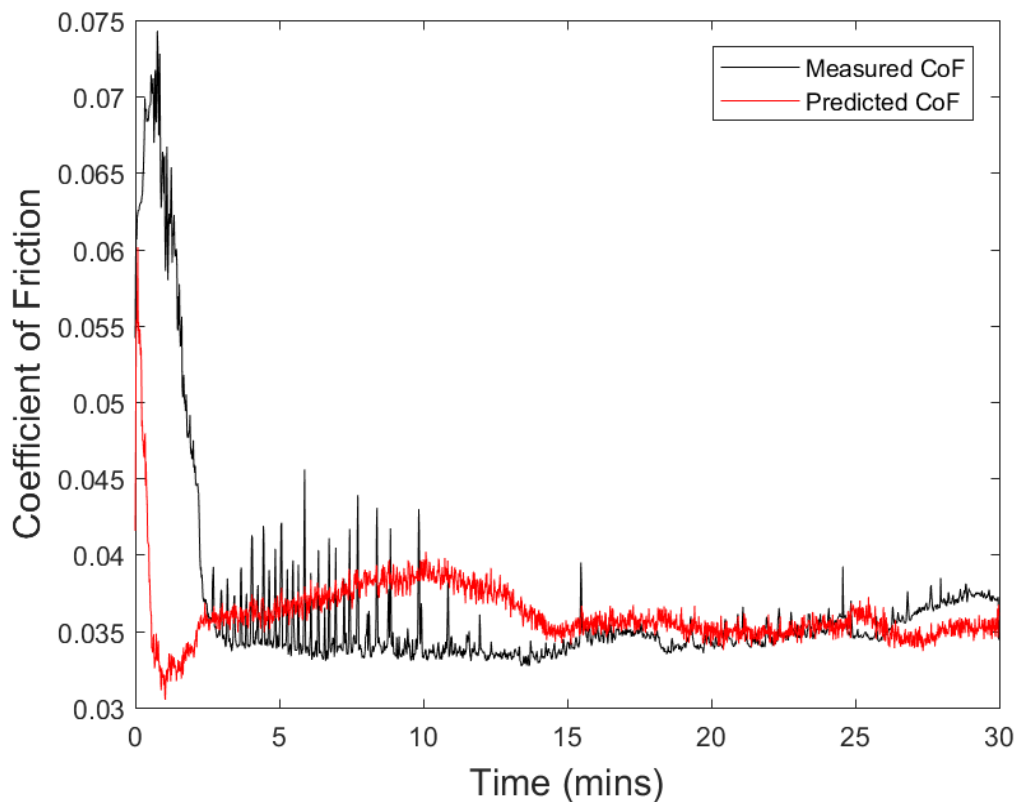


Figure 7.11 - Measured and predicted coefficient of friction values for a tribotest conducted in PAO + 0.1 wt% MoDTC.

Figure 7.11 shows that the predicted coefficient of friction value matches well to the measured value once a tribofilm has been formed. However, this method does not accurately predict the coefficient of friction prior to film formation, due to the disparity between the acoustic emission and CoF data as previously discussed in Section 5.1. Whereby the acoustic emission value decreases prior to the coefficient of friction under the presence of only a few layers of MoS₂. This leads the two values to not match up during the beginning of the test prior to tribofilm formation. The average percentage difference was then calculated for the final 5 minutes of the test. The percentage difference between predicted and measured coefficient of friction across all tests was found to be -6.92%.

The same approach can be taken using the equation for ZDDP data. Figure 7.12 shows the measured and predicted coefficient of friction values for a test conducted in PAO + 0.55 wt% ZDDP. It can be seen that by using Equation 11 above, the instantaneous coefficient of friction can be estimated in real time using only the measured hit count signal.

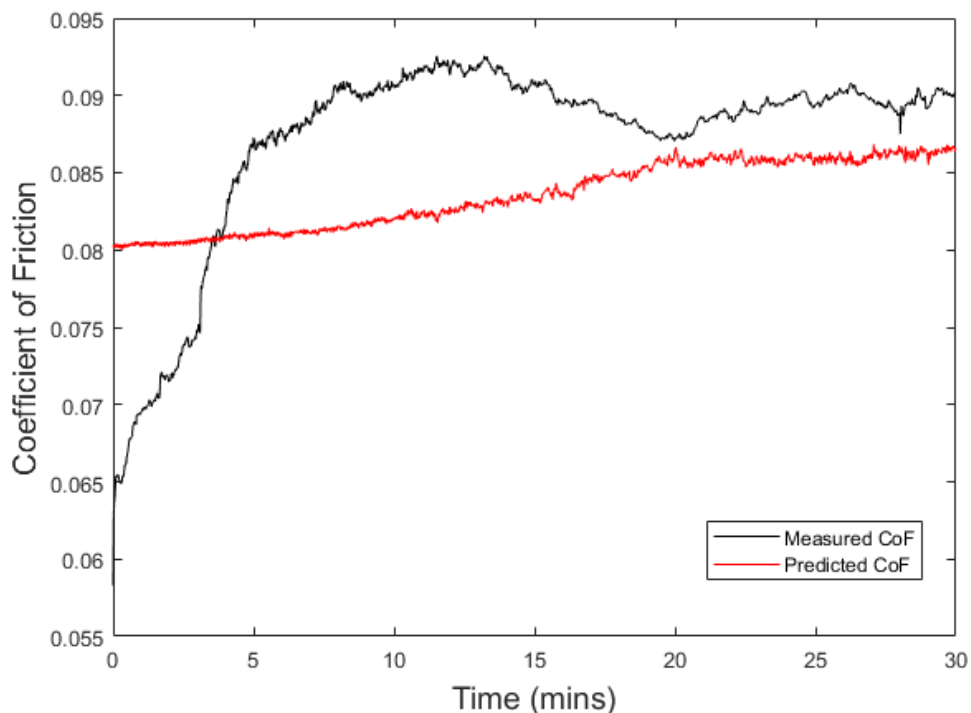


Figure 7.12 - Measured and predicted coefficient of friction values for a tribotest conducted in PAO + 0.55 wt% ZDDP.

It can be seen in Figure 7.12 that the estimated coefficient of friction bears very little resemblance to the measured coefficient of friction prior to approximately 15 minutes. From 15 minutes onwards, the predicted and measured coefficient of friction data show very similar values, 0.0861 and 0.0898 respectively. As previously discussed in Section 6.1, it is believed that the ZDDP tribofilm has formed once the signals have plateaued, therefore it can be seen that the acoustic emission signal can be used to predict the coefficient of friction when a ZDDP tribofilm has formed. The average percentage difference was then calculated for the final 5 minutes of the test. The percentage difference between predicted and measured coefficient of friction across all tests was found to be -4.12%.

These two examples show clearly that acoustic emissions can be used as a predictive tool to estimate the coefficient of friction. This proposed methodology, whilst in its infancy, shows that it is possible to estimate the coefficient of friction without using mechanical means such as a load cell. There is a wide range of possibilities for which this methodology could be applied, such as the estimation of the coefficient of friction of complex tribosystems where the application of a load cell is impractical.

Chapter 8

Conclusion and Future Work

8.1 Conclusion

In this thesis, commercial acoustic emission sensors have been used for the first time to monitor the effect of surface roughness and tribochemistry on acoustic emission response for lubricated steel on steel contacts.

A bespoke data acquisition system has been developed to manage the vast amounts of raw data in real time whilst simultaneously processing the signals into key acoustic emission parameters. The data acquisition system offers significant scalability in the future due to the inherent open environment a bespoke system offers.

It has been shown that the initial surface roughness of the steel samples has a very large impact on the acoustic emission response for contacts lubricated with PAO. There is a trend shown between the initial surface roughness and the average coefficient of friction that is not seen between the initial surface roughness and the average acoustic emission data. Conversely, there is also a correlation present between the maximum acoustic emission value and the initial surface roughness that is not present in the coefficient of friction data.

For steel contacts lubricated with PAO + 0.1% MoDTC it has been shown for the first time that acoustic emission sensors can be used to monitor tribofilm formation *in situ* and in real time. The acoustic emission offers a more sensitive response to the presence of MoS₂ and shows a decrease in magnitude in advance of any effect on coefficient of friction. This reduction in acoustic emission response is associated with the formation of only a few layers of MoS₂ as identified by Raman spectroscopy. For the first time it has also been shown that the removal of MoS₂ tribofilms can be monitored via acoustic emissions in real time and *in situ*.

For tribotests conducted with PAO + 0.55wt% ZDDP as the lubricant it has been shown that acoustic emission sensors can also be used to monitor the formation of ZDDP based tribofilms *in situ* and in real time. The presence of a ZDDP tribofilm was determined using EDX analysis and the two different regimes shown in the acoustic emission data is attributed to the chemical composition of the tribofilm. It has also been shown for the first time that the

removal of a ZDDP based tribofilm can be detected and monitored using acoustic emissions.

The frequency domain of the acoustic emission data has been investigated at various time-points during experiments, it was found that key characteristics of the frequency spectra such as magnitude changed as the tribofilm developed. This was shown to be true for both MoDTC and ZDDP additives, although the responses observed were completely different.

It has been shown for both MoDTC and ZDDP additives that there is no correlation between measured acoustic emission data and the wear produced during testing. However, it has also been demonstrated that there is a highly statistically significant relationship between the acoustic emission parameters and the measured coefficient of friction.

The relationship between the coefficient of friction and acoustic emission signal is very highly correlated (maximum R^2 value of 0.863), it has also been demonstrated that the acoustic emission signal can be used to predict the coefficient of friction in real time and *in situ* using only the acoustic emission sensor, located away from the contact interface.

8.2 Future Work

8.2.1 Software Development

This work has shown for the first time that a high speed data acquisition system developed in LabVIEW is capable of monitoring the formation and removal of tribofilms in real time. The intrinsic sophistication associated with the architecture of the LabVIEW data acquisition system means that measurement parameters can be expanded upon in future iterations to meet the complexity and needs of future studies. Future work would focus on incorporating more sophisticated data processing techniques such as wavelet transforms and short-time Fourier Transforms. Both of these techniques allow changes in the frequency domain over time to be visualised.

8.2.2 Experimental

This work has shown that acoustic emission sensing methodologies can successfully be used to monitor the formation and removal of MoDTC and ZDDP tribofilms. However, there is a lot of work that can be undertaken to take the research further.

In order to provide cross additive comparison, only one set of tribological parameters was chosen for all tribotests in this work. Going forward, it would be worthwhile varying things such as additive concentration, contact pressure, temperature and sliding speed to investigate the full capabilities of the acoustic emission methodology. Further to this, a unidirectional HSPOD tribometer was used for all of the experiments shown in this work, the effect of a reciprocating contact would be of great interest for future work as it is currently not known what effect this would have on the acoustic emission.

The cause of acoustic emission signals in a tribological context needs to be fully elucidated, whilst it is thought that the hardness of the tribocontact is directly linked to the amplitude of the acoustic emission signal it has not been verified. Future work will focus on definitively establishing this link through the use of materials/systems of defined hardness.

It has long been established that there is a synergistic relationship between MoDTC and ZDDP when both are present in a lubricant. As such the acoustic emission implications of MoDTC/ZDDP ratio would be investigated similarly to the work conducted by Morina et al. (2006) where the tribological implications were investigated.

Further work is also needed to fully establish whether the frequency domain of acoustic emission signals can be used as a 'fingerprint' to identify the lubricant additive.

Finally, the use of acoustic emission signals to predict the coefficient of friction *in situ* and in real time is very promising. Further work is needed to demonstrate the robustness of this relationship and explore the extent in which it can be used.

Bibliography

- AGHABABAEI, R., WARNER, D. H. & MOLINARI, J.-F. J. N. C. 2016. Critical length scale controls adhesive wear mechanisms. *7*, 11816.
- AKTARY, M., MCDERMOTT, M. T. & MCALPINE, G. A. 2002. Morphology and nanomechanical properties of ZDDP antiwear films as a function of tribological contact time. *Tribology letters*, *12*, 155-162.
- AKTARY, M., MCDERMOTT, M. T. & TORKELESON, J. 2001. Morphological evolution of films formed from thermooxidative decomposition of ZDDP. *Wear*, *247*, 172-179.
- ARCHARD, J. & HIRST, W. 1956. The wear of metals under unlubricated conditions. *J Proceedings of the Royal Society of London. Series A. Mathematical*, *236*, 397-410.
- ARCHARD, J. F. 1953. Contact and rubbing of flat surfaces. *Journal of Applied Physics*, *24*, 981-988.
- AXÉN, N., JACOBSON, S. & HOGMARK, S. 2001. Friction and Wear Measurement Techniques.
- BANCROFT, G., KASRAI, M., FULLER, M., YIN, Z., FYFE, K. & TAN, K. H. 1997. Mechanisms of tribochemical film formation: stability of tribo- and thermally-generated ZDDP films. *Tribology Letters*, *3*, 47-51.
- BEC, S., TONCK, A., GEORGES, J.-M., COY, R., BELL, J. & ROPER, G. 1999. Relationship between mechanical properties and structures of zinc dithiophosphate anti-wear films. *Proceedings of the Royal Society of London. Series A: Mathematical, Physical Engineering Sciences*, *455*, 4181-4203.
- BEC, S., TONCK, A., GEORGES, J.-M. & ROPER, G. W. 2004. Synergistic effects of MoDTC and ZDTP on frictional behaviour of tribofilms at the nanometer scale. *Tribology Letters*, *17*, 797-809.
- BENABDALLAH, H. S. & AGUILAR, D. A. 2008. Acoustic Emission and Its Relationship with Friction and Wear for Sliding Contact. *Tribology Transactions*, *51*, 738-747.
- BERGMAN, F., HEDENQVIST, P. & HOGMARK, S. 1997. The influence of primary carbides and test parameters on abrasive and erosive wear of selected PM high speed steels. *Tribology International*, *30*, 183-191.
- BHUIYAN, M., CHOUDHURY, I. A., DAHARI, M., NUKMAN, Y. & DAWAL, S. 2016. Application of acoustic emission sensor to investigate the frequency of tool wear and plastic deformation in tool condition monitoring. *Measurement Science and Technology*, *92*, 208-217.
- BHUSHAN, B. 2000. *Modern tribology handbook, two volume set*, CRC press.
- BHUSHAN, B., GUPTA, B. K. & AZARIAN, M. H. 1995. Nanoindentation, microscratch, friction and wear studies of coatings for contact recording applications. *Wear*, *181-183*, 743-758.
- BONESS, R., MCBRIDE, S. & SOBCZYK, M. 1990. Wear studies using acoustic emission techniques. *Tribology International*, *23*, 291-295.
- BONESS, R. J. 1993. Measurements of wear and acoustic emission from fuel-wetted surfaces. *Wear*, *162-164*, 703-705.
- BONESS, R. J. & MCBRIDE, S. L. 1991. Adhesive and abrasive wear studies using acoustic emission techniques. *Wear*, *149*, 41-53.

- BONGAERTS, J., DAY, J., MARRIOTT, C., PUDNEY, P. & WILLIAMSON, A.-M. J. J. O. A. P. 2008. In situ confocal Raman spectroscopy of lubricants in a soft elastohydrodynamic tribological contact. *Journal of Applied Physics*, 104, 014913.
- CANN, P. M., SPIKES, H. A. & HUTCHINSON, J. 1996. The Development of a Spacer Layer Imaging Method (SLIM) for Mapping Elastohydrodynamic Contacts. *Tribology Transactions*, 39, 915-921.
- CHO, C.-W. & LEE, Y.-Z. 2000. Wear-life evaluation of CrN-coated steels using acoustic emission signals. *Surface Coatings Technology*, 127, 59-65.
- CHO, S.-S. & KOMVOPOULOS, K. 1997. Correlation between acoustic emission and wear of multi-layer ceramic coated carbide tools. *Journal of Manufacturing Science*, 119, 238-246.
- CHUNG, K.-H. & KIM, D.-E. J. T. L. 2003. Fundamental investigation of micro wear rate using an atomic force microscope. 15, 135-144.
- COLOMBAN, P., CHERIFI, S. & DESPERT, G. 2008. Raman identification of corrosion products on automotive galvanized steel sheets. *Journal of Raman Spectroscopy*, 39, 881-886.
- DAWCZYK, J., MORGAN, N., RUSSO, J. & SPIKES, H. 2019. Film Thickness and Friction of ZDDP Tribofilms. *Tribology Letters*, 67, 34.
- DOWSON, D. 1998. *History of Tribology*, Wiley.
- ENNACEUR, C., LAKSIMI, A., HERVE, C. & CHERFAOUI, M. 2006. Monitoring crack growth in pressure vessel steels by the acoustic emission technique and the method of potential difference. *International Journal of Pressure Vessels Piping*, 83, 197-204.
- ESWARA-MOORTHY, S. K., BALASUBRAMANIAN, P., VAN MIERLO, W., BERNHARD, J., MARINARO, M., WOHLFAHRT-MEHRENS, M., JÖRISSEN, L., KAISER, U. J. M. & MICROANALYSIS 2014. An in situ SEM-FIB-based method for contrast enhancement and tomographic reconstruction for structural quantification of porous carbon electrodes. *Microscopy and Microanalysis*, 20, 1576-1580.
- FAN, Y., GU, F. & BALL, A. 2010. Modelling acoustic emissions generated by sliding friction. *Wear*, 268, 811-815.
- FUJITA, H., GLOVNEA, R. & SPIKES, H. 2005. Study of zinc dialkyldithiophosphate antiwear film formation and removal processes, part I: experimental. *Tribology Transactions*, 48, 558-566.
- FUJITA, H. & SPIKES, H. 2004. The formation of zinc dithiophosphate antiwear films. *Proceedings of the Institution of Mechanical Engineers, Part J: Journal of Engineering Tribology*, 218, 265-278.
- FUJITA, H. & SPIKES, H. 2005. Study of zinc dialkyldithiophosphate antiwear film formation and removal processes, part II: kinetic model. *Tribology Transactions*, 48, 567-575.
- FURUSTIG, J., DOBRYDEN, I., ALMQVIST, A., ALMQVIST, N. & LARSSON, R. 2016. The measurement of wear using AFM and wear interpretation using a contact mechanics coupled wear model. *Wear*, 350-351, 74-81.
- G. KALHARA, P., D. JAYASINGHEARACHCHID, V., H. A. T. DIAS, A., C. RATNAYAKE, V., JAYAWARDENA, C. & KURUWITAARACHCHI, N.

2017. *TreeSpirit: Illegal logging detection and alerting system using audio identification over an IoT network*.
- GÅHLIN, R. & JACOBSON, S. 1998. A novel method to map and quantify wear on a micro-scale. *Wear*, 222, 93-102.
- GENG, Z., PUHAN, D. & REDDYHOFF, T. 2019. Using acoustic emission to characterize friction and wear in dry sliding steel contacts. *Tribology International*, 134, 394-407.
- GHANBARZADEH, A., PARSAEIAN, P., MORINA, A., WILSON, M. C., VAN EIJK, M. C., NEDELCU, I., DOWSON, D. & NEVILLE, A. 2016. A semi-deterministic wear model considering the effect of zinc dialkyl dithiophosphate tribofilm. *Tribology Letters*, 61, 12.
- GLOVNEA, R., FORREST, A., OLVER, A. & SPIKES, H. 2003. Measurement of sub-nanometer lubricant films using ultra-thin film interferometry. *Tribology Letters*, 15, 217-230.
- GOHAR, R. & RAHNEJAT, H. 2012. *Fundamentals of tribology*.
- GOLAN, Y., SEITZ, M., LUO, C., MARTIN-HERRANZ, A., YASA, M., LI, Y., SAFINYA, C. R. & ISRAELACHVILI, J. 2002. The X-ray surface forces apparatus for simultaneous X-ray diffraction and direct normal and lateral force measurements. *Review of Scientific Instruments*, 73, 2486-2488.
- GOLDSTEIN, J. I., NEWBURY, D. E., MICHAEL, J. R., RITCHIE, N. W., SCOTT, J. H. J. & JOY, D. C. 2017. *Scanning electron microscopy and X-ray microanalysis*, Springer.
- GONG, Z., NYBORG, E. & OOMMEN, G. 1992. Acoustic emission monitoring of steel railroad bridges. *Materials Evaluation*, 50.
- GRIERSON, D., FLATER, E. & CARPICK, R. 2005. Accounting for the JKR–DMT transition in adhesion and friction measurements with atomic force microscopy. *Journal of Adhesion Science Technology*, 19, 291-311.
- GROSSIORD, C., MARTIN, J. M., LE MOGNE, T. & PALERMO, T. 1998. In situ MoS₂ formation and selective transfer from MoDPT films. *Surface and Coatings Technology*, 108-109, 352-359.
- GUNSEL, S., SPIKES, H. & ADERIN, M. 1993. In-situ measurement of ZDDP films in concentrated contacts. *Tribology Transactions*, 36, 276-282.
- HANCHI, J. & KLAMECKI, B. E. 1991. Acoustic emission monitoring of the wear process. *Wear*, 145, 1-27.
- HARRIS, D. & DUNEGAN, H. 1974. Continuous monitoring of fatigue-crack growth by acoustic-emission techniques. *Experimental Mechanics*, 14, 71-81.
- HASE, A., MISHINA, H. & WADA, M. 2012. Correlation between features of acoustic emission signals and mechanical wear mechanisms. *Wear*, 292-293, 144-150.
- HASE, A., WADA, M., KOGA, T. & MISHINA, H. 2014. The relationship between acoustic emission signals and cutting phenomena in turning process. *The International Journal of Advanced Manufacturing Technology*, 70, 947-955.
- HISAKADO, T. & WARASHINA, T. 1998. Relationship between friction and wear properties and acoustic emission characteristics: iron pin on hardened bearing steel disk. *Wear*, 1-7.

- HOLM, R. 2013. *Electric contacts: theory and application*, Springer Science & Business Media.
- HOSHINO, K., YAGISHITA, K., TAGAWA, K. & SPIKES, H. 2012. Tribological properties of sulphur-free antiwear additives zinc dialkylphosphates (ZDPs). *SAE International Journal of Fuels Lubricants*, 5, 504-510.
- HUTCHINGS, I. & SHIPWAY, P. 2017a. Chapter 3 - Friction. In: HUTCHINGS, I. & SHIPWAY, P. (eds.) *Tribology (Second Edition)*. Butterworth-Heinemann.
- HUTCHINGS, I. & SHIPWAY, P. 2017b. *Tribology: friction and wear of engineering materials*, Butterworth-Heinemann.
- HUTCHINGS, I. M. 2016. Leonardo da Vinci's studies of friction. *Wear*, 360-361, 51-66.
- IDZIAK, S. H., KOLTOVER, I., DAVIDSON, P., RUTHS, M., LI, Y., ISRAELACHVILI, J. N. & SAFINYA, C. R. 1996. Structure under confinement in a smectic-A and lyotropic surfactant hexagonal phase. *Physica B: Condensed Matter*, 221, 289-295.
- IDZIAK, S. H., SAFINYA, C. R., HILL, R. S., KRAISER, K. E., RUTHS, M., WARRINER, H. E., STEINBERG, S., LIANG, K. S. & ISRAELACHVILI, J. N. 1994. The X-ray surface forces apparatus: structure of a thin smectic liquid crystal film under confinement. *Science* 264, 1915-1918.
- JIAA, C. L. & DORNFELD, D. A. 1990. Experimental studies of sliding friction and wear via acoustic emission signal analysis. *Wear*, 139, 403-424.
- JOST, H. P. 1966. *Lubrication: Tribology; Education and Research; Report on the Present Position and Industry's Needs (submitted to the Department of Education and Science by the Lubrication Engineering and Research) Working Group*, HM Stationery Office.
- KANO, M., MABUCHI, Y., ISHIKAWA, T., SANO, A. & WAKIZONO, T. 1999. The effect of ZDDP in CVT fluid on increasing the traction capacity of belt-drive continuously variable transmissions. *Lubrication Science*, 11, 365-377.
- KEITH, J. H. 2010. *Design of a pin-on-disk tribometer with in situ optical profilometry*. University of Florida.
- KHAEMBA, D. N., NEVILLE, A. & MORINA, A. 2015. A methodology for Raman characterisation of MoDTC tribofilms and its application in investigating the influence of surface chemistry on friction performance of MoDTC lubricants. *Tribology Letters*, 59, 38-38.
- KHAEMBA, D. N., NEVILLE, A. & MORINA, A. 2016. New insights on the decomposition mechanism of Molybdenum DialkyldiThioCarbamate (MoDTC): a Raman spectroscopic study. *RSC Advances*, 6, 38637-38646.
- KHAN, T., TAMURA, Y., YAMAMOTO, H., MORINA, A. & NEVILLE, A. 2016. Friction and wear mechanisms in boundary lubricated oxy-nitrided treated samples. *Wear*, 368, 101-115.
- KHRUSCHOV, M. M. 1974. Principles of abrasive wear. *Wear*, 28, 69-88.
- KRICK, B. A., VAIL, J. R., PERSSON, B. N. & SAWYER, W. G. J. T. L. 2012. Optical in situ micro tribometer for analysis of real contact area for contact mechanics, adhesion, and sliding experiments. 45, 185-194.

- KUSTAS, F. M., SCHWARTZBERG, J. N., CARPENTER, S. H., HEIPLE, C. R. & ARMENTROUT, D. L. 1994. Acoustic emission monitoring of diamond-like carbon coating degradation during sliding wear. *Surface and Coatings Technology*, 67, 1-7.
- LAEDRE, S., KONGSTEIN, O. E., OEDEGAARD, A., SELAND, F. & KAROLIUSSEN, H. 2013. In situ and ex situ contact resistance measurements of stainless steel bipolar plates for PEM fuel cells. *ECS Transactions*, 50, 829-839.
- LE MOGNE, T., MARTIN, J.-M. & GROSSIORD, C. 1999. Imaging the chemistry of transfer films in the AES/XPS analytical UHV tribotester. *Tribology Series*. Elsevier.
- LEE, C., YAN, H., BRUS, L. E., HEINZ, T. F., HONE, J. & RYU, S. 2010. Anomalous lattice vibrations of single-and few-layer MoS₂. *ACS Nano*, 4, 2695-2700.
- LI, H., ZHANG, Q., YAP, C. C. R., TAY, B. K., EDWIN, T. H. T., OLIVIER, A. & BAILLARGEAT, D. 2012. From bulk to monolayer MoS₂: evolution of Raman scattering. *Advanced Functional Materials*, 22, 1385-1390.
- LI, X. 2002. A brief review: acoustic emission method for tool wear monitoring during turning. *International Journal of Machine Tools and Manufacture*, 42, 157-165.
- LI, Y.-R., PEREIRA, G., LACHENWITZER, A., KASRAI, M. & NORTON, P. R. 2008. Studies on ZDDP Thermal Film Formation by XANES Spectroscopy, Atomic Force Microscopy, FIB/SEM and ³¹P NMR. *Tribology Letters*, 29, 11-22.
- LIANG, S. & DORNFELD, D. 1989. Tool wear detection using time series analysis of acoustic emission. *Journal of Engineering for Industry*, 111, 199-205.
- LIM, S. & BRUNTON, J. 1985. A dynamic wear rig for the scanning electron microscope. *Wear*, 101, 81-91.
- LINGARD, S. & NG, K. K. 1989. An investigation of acoustic emission in sliding friction and wear of metals. *Wear*, 130, 367-379.
- LINGARD, S., YU, C. W. & YAU, C. F. 1993. Sliding wear studies using acoustic emission. *Wear*, 162-164, 597-604.
- LIU, J., NOTBOHM, J. K., CARPICK, R. W. & TURNER, K. T. J. A. N. 2010. Method for characterizing nanoscale wear of atomic force microscope tips. 4, 3763-3772.
- LUO, X., HAYA, H., INABA, T., SHIOTANI, T. & NAKANISHI, Y. 2004. Damage evaluation of railway structures by using train-induced AE. *Construction Building Materials*, 18, 215-223.
- MAIA, L. H. A., ABRAO, A. M., VASCONCELOS, W. L., SALES, W. F. & MACHADO, A. R. 2015. A new approach for detection of wear mechanisms and determination of tool life in turning using acoustic emission. *Tribology International*, 92, 519-532.
- MARTIN, J. M. 1999. Antiwear mechanisms of zinc dithiophosphate: a chemical hardness approach. *Tribology Letters*, 6, 1-8.
- MATSUOKA, K. 2001. In-Situ wear monitoring of slider and disk using acoustic emission. *Journal of Tribology*, 123, 175-180.

- MAW, W., STEVENS, F., LANGFORD, S. & DICKINSON, J. 2002. Single asperity tribochemical wear of silicon nitride studied by atomic force microscopy. *Journal of Applied Physics*, 92, 5103-5109.
- MCBRIDE, S., HONG, Y. & POLLARD, M. 1993. Enhanced fatigue crack detection in aging aircraft using continuous acoustic emission monitoring. *Review of Progress in Quantitative Nondestructive Evaluation*. Springer.
- MECHEFSKE, C. & SUN, G. Monitoring sliding wear using acoustic emission. International Congress on Condition Monitoring, 2001.
- MIYAKE, S. & KANEKO, R. 1992. Microtribological properties and potential applications of hard, lubricating coatings. *Thin Solid Films*, 212, 256-261.
- MORHAIN, A. & MBA, D. 2003. Bearing defect diagnosis and acoustic emission. *Proceedings of the Institution of Mechanical Engineers, Part J: Journal of Engineering Tribology*.
- MORINA, A. & NEVILLE, A. 2007a. Tribofilms: aspects of formation, stability and removal. *Journal of Physics D: Applied Physics*, 40, 5476-5487.
- MORINA, A. & NEVILLE, A. 2007b. Understanding the composition and low friction tribofilm formation/removal in boundary lubrication. *Tribology International*.
- MORINA, A., NEVILLE, A., GREEN, J. H. & PRIEST, M. 2003. Assessing friction, wear and film formation characteristics in formulated lubricants in severe to moderate boundary lubrication conditions. In: DOWSON, D., PRIEST, M., DALMAZ, G. & LUBRECHT, A. A. (eds.) *Tribology Series*. Elsevier.
- MORINA, A., NEVILLE, A., PRIEST, M. & GREEN, J. H. 2006. ZDDP and MoDTC interactions in boundary lubrication—The effect of temperature and ZDDP/MoDTC ratio. *Tribology International*, 39, 1545-1557.
- MORTIER, R. M., ORSZULIK, S. T. & FOX, M. F. 2010. *Chemistry and technology of lubricants*, Springer.
- NATIONAL INSTRUMENTS. 2019a. Acquiring an Analog Signal: Bandwidth, Nyquist Sampling Theorem and Aliasing. Available: <http://www.ni.com/en-gb/innovations/white-papers/06/acquiring-an-analog-signal--bandwidth--nyquist-sampling-theorem-.html>.
- NATIONAL INSTRUMENTS. 2019b. Understanding FFTs and Windowing. Available: <http://download.ni.com/evaluation/pxi/Understanding%20FFTs%20and%20Windowing.pdf>.
- NATIONAL INSTRUMENTS. 2019c. What is LabVIEW. Available: <http://www.ni.com/en-gb/shop/labview.html>.
- NDT RESOURCE CENTER. 2019. *Introduction to Acoustic Emission Testing* [Online]. Available: https://www.nde-ed.org/EducationResources/CommunityCollege/Other%20Methods/AE/AE_Equipment.htm [Accessed].
- NYQUIST, H. 1928. Thermal agitation of electric charge in conductors. *Physical review*, 32, 110.
- OHTSU, M. 1996. The history and development of acoustic emission in concrete engineering. *Magazine of concrete research*, 48, 321-330.

- OHTSU, M. Quantitative AE techniques standardized for concrete structures. *Advanced Materials Research*, 2006. Trans Tech Publ, 183-192.
- OYARCE, A., HOLMSTRÖM, N., BODÉN, A., RANDSTRÖM, S. & LINDBERGH, G. J. E. T. 2009. In-situ Measurements of Contact Resistance and In-situ Durability studies of Steels and Coatings to be used as Bipolar Plates in PEMFCs. 25, 1791-1801.
- PATTON, S. T. & BHUSHAN, B. 1996. Micromechanical and tribological characterization of alternate pole tip materials for magnetic recording heads. *Wear*, 202, 99-109.
- PENKOV, O., KHADEM, M., NIETO, A., KIM, T.-H. & KIM, D.-E. 2017. Design and construction of a micro-tribotester for precise in-situ wear measurements. *Micromachines*, 8, 103.
- PEPPER, S. V. 1974. Auger analysis of films formed on metals in sliding contact with halogenated polymers. *Journal of Applied Physics*, 45, 2947-2956.
- PHYSICAL ACOUSTICS. 2019. *WSA - 100 - 1000 kHz Wideband AE Sensor* [Online]. Available: <http://www.physicalacoustics.com/by-product/sensors/WSa-100-1000-kHz-Wideband-AE-Sensor>. [Accessed].
- PIRAS, F. M., ROSSI, A. & SPENCER, N. 2002a. In situ Attenuated Total Reflection (ATR) spectroscopic analysis of tribological phenomena. *Tribology Series*. Elsevier.
- PIRAS, F. M., ROSSI, A. & SPENCER, N. D. 2002b. Growth of tribological films: in situ characterization based on attenuated total reflection infrared spectroscopy. *Langmuir*, 18, 6606-6613.
- PRIEST, M. 2014. MECH5570M Introduction to Tribology.
- RABE, R., BREGUET, J.-M., SCHWALLER, P., STAUSS, S., HAUG, F.-J., PATSCHEIDER, J. & MICHLER, J. 2004. Observation of fracture and plastic deformation during indentation and scratching inside the scanning electron microscope. *Thin Solid Films*, 469, 206-213.
- RAI, Y. 2015. *In-situ Interface Chemical Characterisation of a Boundary Lubricated Contact*. University of Leeds.
- RATOI, M., BOVINGTON, C. & SPIKES, H. 2003. In situ study of metal oleate friction modifier additives. *Tribology Letters*, 14, 33-40.
- RATOI, M., NISTE, V. B., ALGHAWEL, H., SUEN, Y. F. & NELSON, K. 2014. The impact of organic friction modifiers on engine oil tribofilms. *Rsc Advances*, 4, 4278-4285.
- RAVI, D. & SETHURAMIAH, A. 1995. Acoustic emission in dynamic compression and its relevance to tribology. *Tribology International*.
- ROBERTS, T. M. & TALEBZADEH, M. 2003. Acoustic emission monitoring of fatigue crack propagation. *Journal of Constructional Steel Research*, 59, 695-712.
- SAEIDI, F., SHEVCHIK, S. & WASMER, K. 2016. Automatic detection of scuffing using acoustic emission. *Tribology International*, 94, 112-117.
- SAMPATH, A. & VAJPAYEE, S. On-line tool wear prediction using acoustic emission. *Emerging Trends in Manufacturing: Proceedings of the 12th All India Machine Tool Design and Research Conference* Tata McGraw-Hill, 1986. 269-272.

- SATO, T., ISHIDA, T., JALABERT, L. & FUJITA, H. 2012. Real-time transmission electron microscope observation of nanofriction at a single Ag asperity. *Nanotechnology*, 23, 505701.
- SAWYER, W. G. & WAHL, K. J. 2008. Accessing inaccessible interfaces: in situ approaches to materials tribology. *MRS bulletin*, 33, 1145-1150.
- SCH, J., SCHNEIDER, T. & SANTNER, E. 1998. Development of a combined AFM-tribometer test rig. *Tribotest*, 4, 345-353.
- SCHARF, T. & SINGER, I. 2003. Monitoring transfer films and friction instabilities with in situ Raman tribometry. *Tribology Letters*, 14, 3-8.
- SCHEUSCHNER, N., GILLEN, R., STAIGER, M. & MAULTZSCH, J. 2015. Interlayer resonant Raman modes in few-layer MoS₂. *Physical Review B*, 91, 235409.
- SHIMIZU, Y. & SPIKES, H. A. 2016. The influence of slide-roll ratio on ZDDP tribofilm formation. *Tribology Letters*, 64, 19.
- SHIOTANI, T., OHTSU, M. & IKEDA, K. 2001. Detection and evaluation of AE waves due to rock deformation. *Construction Building Materials*, 15, 235-246.
- SHIOTANI, T., SHIGEISHI, M. & OHTSU, M. 1999. Acoustic emission characteristics of concrete-piles. *Construction Building Materials*, 13, 73-85.
- SINGER, I., DVORAK, S., WAHL, K. & SCHARF, T. 2002. Third body processes and friction of solid lubricants studied by in situ optical and Raman tribometry. *Tribology Series*. Elsevier.
- SPENCER, A., DOBRYDEN, I., ALMQVIST, N., ALMQVIST, A. & LARSSON, R. 2013. The influence of AFM and VSI techniques on the accurate calculation of tribological surface roughness parameters. *Tribology International*, 57, 242-250.
- SPIKES, H. 1999. Thin films in elastohydrodynamic lubrication: the contribution of experiment. *Proceedings of the Institution of Mechanical Engineers, Part J: Journal of Engineering Tribology*, 213, 335-352.
- SPIKES, H. 2004. The history and mechanisms of ZDDP. *Tribology Letters*, 17, 469-489.
- SPIKES, H. & CANN, P. 2001. The development and application of the spacer layer imaging method for measuring lubricant film thickness. *Proceedings of the Institution of Mechanical Engineers, Part J: Journal of Engineering Tribology*, 215, 261-277.
- STACHOWIAK, G. & BATCHELOR, A. W. 2004. *Experimental methods in tribology*, Elsevier.
- STACHOWIAK, G. & BATCHELOR, A. W. 2013. *Engineering tribology*, Butterworth-Heinemann.
- STEVENSON, H., PARKES, M., AUSTIN, L., JAGGARD, M., AKHBARI, P., VAGHELA, U., WILLIAMS, H., GUPTA, C. & CANN, P. 2018. The development of a small-scale wear test for CoCrMo specimens with human synovial fluid. *Biotribology*, 14, 1-10.
- SUN, J., WOOD, R. J. K., WANG, L., CARE, I. & POWRIE, H. E. G. 2005. Wear monitoring of bearing steel using electrostatic and acoustic emission techniques. *Wear*, 259, 1482-1489.

- TAYLOR, L. J. & SPIKES, H. A. 2003. Friction-Enhancing Properties of ZDDP Antiwear Additive: Part I—Friction and Morphology of ZDDP Reaction Films. *Tribology Transactions*, 46, 303-309.
- TOPOLOVEC-MIKLOZIC, K., CANN, P. & SPIKES, H. 2001. *The use of AFM to study lubricant films*.
- TOPOLOVEC-MIKLOZIC, K., FORBUS, T. R. & SPIKES, H. 2008. Film forming and friction properties of overbased calcium sulphonate detergents. *Tribology Letters*, 29, 33-44.
- TOPOLOVEC-MIKLOZIC, K., FORBUS, T. R. & SPIKES, H. A. 2007. Film thickness and roughness of ZDDP antiwear films. *Tribology Letters*, 26, 161-171.
- TORBACKE, M., RUDOLPHI, Å. K. & KASSFELDT, E. 2014. *Lubricants: introduction to properties and performance*, John Wiley & Sons.
- UNNIKRISHNAN, R., JAIN, M. C., HARINARAYAN, A. K. & MEHTA, A. K. 2002. Additive–additive interaction: an XPS study of the effect of ZDDP on the AW/EP characteristics of molybdenum based additives. *Wear*, 252, 240-249.
- VAJPAYEE, S. & SAMPATH, A. Acoustic emission as an indirect parameter for tool monitoring. *Proceedings of Manufacturing International*, 1988. 321-325.
- VALLEN SYSTEME GMBH 2017. Acoustic Emission Sensors - Specification.
- WAHL, K. J. & SAWYER, W. G. 2008. Observing Interfacial Sliding Processes in Solid–Solid Contacts. *MRS Bulletin*, 33, 1159-1167.
- WANG, J., LOCKWOOD, A., PENG, Y., XU, X., BOBJI, M. & INKSON, B. 2009. The formation of carbon nanostructures by in situ TEM mechanical nanoscale fatigue and fracture of carbon thin films. *Nanotechnology*, 20, 305703.
- WANG, L. & WOOD, R. J. K. 2009. Acoustic emissions from lubricated hybrid contacts. *Tribology International*, 42, 1629-1637.
- WANG, Y., CONG, C., QIU, C. & YU, T. 2013. Raman spectroscopy study of lattice vibration and crystallographic orientation of monolayer MoS₂ under uniaxial strain. *Small*, 9, 2857-2861.
- WIETING, T. 1973. Long-wavelength lattice vibrations of MoS₂ and GaSe. *Solid State Communications*, 12, 931-935.
- WIETING, T. J. & VERBLE, J. L. 1971. Infrared and Raman Studies of Long-Wavelength Optical Phonons in Hexagonal MoS₂. *Physical Review B*, 3, 4286-4292.
- YAHIAOUI, M., PARIS, J. Y. & DENAPE, J. 2015. Correlation between Acoustic Emission Signals and Friction Behavior under Different Sliding Configurations and Materials Pairs. *Key Engineering Materials*, 640, 21-28.
- YAMAMOTO, Y. & GONDO, S. 1989. Friction and Wear Characteristics of Molybdenum Dithiocarbamate and Molybdenum Dithiophosphate. *Tribology Transactions*, 32, 251-257.
- ZABINSKI, J. S. & MCDEVITT, N. T. 1996. Raman Spectra of Inorganic Compounds Related to Solid State Tribochemical Studies. WRIGHT LAB WRIGHT-PATTERSON AFB OH.
- ZHANG, J. & SPIKES, H. 2016. On the mechanism of ZDDP antiwear film formation. *Tribology Letters*, 63, 24.

ZHANG, J., YAMAGUCHI, E. & SPIKES, H. 2014. The Antagonism between Succinimide Dispersants and a Secondary Zinc Dialkyl Dithiophosphate. *Tribology Transactions*, 57, 57-65.